

UNIVERSITY OF BIRMINGHAM



The aerodynamics of a container freight train

David Soper

A thesis submitted to the University of Birmingham for the degree of
DOCTOR OF PHILOSOPHY

School of Civil Engineering
University of Birmingham
April 2014

UNIVERSITY OF
BIRMINGHAM

University of Birmingham Research Archive

e-theses repository

This unpublished thesis/dissertation is copyright of the author and/or third parties. The intellectual property rights of the author or third parties in respect of this work are as defined by The Copyright Designs and Patents Act 1988 or as modified by any successor legislation.

Any use made of information contained in this thesis/dissertation must be in accordance with that legislation and must be properly acknowledged. Further distribution or reproduction in any format is prohibited without the permission of the copyright holder.

Abstract

This research aims to characterise the aerodynamic flow around a container freight train and investigate how changing the container loading configuration affects the magnitude of aerodynamic forces measured on a container. Experiments were carried out using a 1/25th scale moving model freight train at the University of Birmingham's TRAIN rig facility. The model was designed to enable different container loading configurations and train lengths to be tested. A series of experiments to measure slipstream velocities and static pressure were undertaken to assess the influence of container loading configuration. Experiments to measure aerodynamic loads on a container were carried out using an on-board pressure monitoring system built into a specifically designed measuring container. A collation of full scale freight data from previous studies provided a tool to validate model scale data.

Analysis of freight data found it was possible to present slipstream results as a series of flow regions. Clear differences in slipstream development and aerodynamic load coefficients were observed for differing container loading configurations. Velocity and pressure magnitudes measured in the nose region were larger than values observed previously. For container loading efficiencies higher than 50% boundary layer growth stabilises rapidly, however, for less than 50% continual boundary layer growth was observed until after 100m when stabilisation occurs. Velocities in the lateral and vertical directions have magnitudes larger than previously observed; increasing the overall magnitude by $\sim 10\%$. Comparison of model and full scale data showed good agreement, indicating Reynolds number independence. An analysis of TSI safety limits found results lie close to, but do not break, existing limits. Aerodynamic load coefficients were compared with previous studies and shown to be characteristic of typical values measured for a 30° yaw angle; however, differences between static wind tunnel and moving model results were discovered.

Acknowledgements

I wish to express my gratitude to my supervisors Prof. Chris J. Baker and Prof. Mark Sterling for allowing me the opportunity to undertake this research and for their support throughout the study. I have greatly benefitted from their knowledge of wind engineering and vehicle aerodynamics, drawing upon their experience and understanding of technical details relating to experimental wind engineering. I would also like to express my sincere gratitude for helping me deal with the hardships I encountered during the first few months of my studies. I would like to thank Dr. Andrew D. Quinn and Dr. Hassan Hemida for their advice, encouragement and valued discussions throughout my studies. Furthermore, I would like to express my sincere thanks to Dr. Andrew D. Quinn for allowing me to utilise the freight experimental data from Uffington and for patiently discussing any issues I encountered when analysing the data. I feel fortunate to have had the opportunity to have been supervised by and to work alongside the team of academics in the wind engineering group at the University of Birmingham.

I acknowledge the University of Birmingham Centre for Rail Research and Education for providing financial support during my PhD studies.

There are a number of people that have provided invaluable help and support during this project. During the time I have spent at the University of Birmingham these people have not only provided an important contribution to the completion of this study but also whose friendship I value deeply and without whom I would not have been able to enjoy my time in Birmingham as much. I am thankful to Dr. Tim Gilbert, Mr. Matt Haines, Mr. Dominic Flynn, Mr. Nainesh Patel, Mr. Martin ‘hit it with a hammer’ Gallagher and Mr. Justin Morden. I am also thankful to Dr. Sarah Jordan, whose knowledge of the TRAIN rig and ever willingness to have a chat and put the world to rights has been invaluable, and Dr. Francesco Dorigatti, whose expertise in the TRAIN rig crosswind generator has proved to be an invaluable source of knowledge on many an occasion. I am very grateful to all the people who have spared a day or two to assist in

the work carried out at the TRAIN rig and to Mr. Mani Entezami the ‘creator’ of the on-board data logger utilised as part of this research. I would like to thank Mr. Mike Vanderstam and the technicians of the Civil Engineering Laboratory of the University of Birmingham for their assistance with any technical problems that arose during my studies. I wish to thank Derwent Patterns Ltd. for their invaluable contribution of making my ideas come to fruition and constructing the TRAIN rig model freight train. Their technical knowledge and expertise in model making for the TRAIN rig ensured that the novel freight train design was a success. I am indebted to Mr. Terry Johnson and RSSB for their support and for kindly sharing industry insight to enable me to understand the potential applications of my research. Finally, I would like to give my sincere thanks to the RTC business park canteen for continually pushing the boundaries of culinary expertise and coming up with daily delights to keep us going through Derby’s harsh winters.

Lastly I would like to thank my friends and family. Mum and Dad you have always been amazing, supporting all my studies and ambitions. My sister, Danielle, you are always a constant and an ever dependable pillar; I thank you for always cheering me up. Finally a massive thank you to Katie Armstrong for all the support and encouragement, especially in these final few months of writing.

Contents

1	Introduction	1
1.1	Outline of studies	1
1.2	Research background	1
1.3	Research motivation	3
1.4	Research aims and objectives	5
1.5	Structure of the thesis	7
2	Literature review	11
2.1	Introduction	11
2.2	Freight research	12
2.3	Slipstreams	15
2.3.1	TSI and EN standards	15
2.3.2	UK standards	16
2.3.3	Passenger slipstreams	17
2.3.3.1	Upstream and nose region	19
2.3.3.2	Boundary layer region	21
2.3.3.3	Tail and wake region	23
2.3.4	Freight Slipstreams	24
2.3.5	Associated aerodynamics	25
2.3.5.1	Bluff Body Aerodynamics	26
2.3.5.2	Building Aerodynamics	27

2.3.6	Summary of slipstream research	27
2.4	Crosswinds	29
2.4.1	Atmospheric boundary layers	29
2.4.2	Crosswind relative to a moving vehicle	32
2.4.3	Aerodynamic loads on vehicles	36
2.4.4	Suitability of a vehicle travelling in crosswind conditions	39
2.4.4.1	TSI and EN standards	39
2.4.4.2	UK standards	42
2.4.5	Further implications on crosswind safety	44
2.4.6	Summary of crosswind research	47
3	Slipstream experiment setup	49
3.1	Introduction	49
3.2	Model scale experiment methodology	50
3.2.1	TRAIN rig facility	50
3.2.2	TRAIN rig model	52
3.2.2.1	Motivation for model design	52
3.2.2.2	Model development	54
3.2.2.3	Model chassis and trailing wheel system	56
3.2.2.4	Model containers and loading consists	59
3.2.3	Experiment setup	59
3.2.3.1	Coordinate system and measuring positions	59
3.2.3.2	Trackside instrumentation	61
3.2.4	Experiment methodology	66
3.3	Full scale experiment methodology	67
3.3.1	Uffington test site	67
3.3.2	Experiment setup	68
3.3.2.1	Coordinate system and measuring positions	68
3.3.2.2	Trackside instrumentation	71

3.3.3	Experiment Methodology	75
3.3.4	Measured train types	76
4	Slipstream data processing methodology	79
4.1	Introduction	79
4.2	Data conversion	80
4.2.1	Model scale data conversion	80
4.2.2	Full scale data conversion	81
4.3	Non-dimensionalised variables	82
4.4	Data alignment	84
4.5	Uncertainty analysis	85
4.6	Wavelet analysis	87
4.6.1	From Fourier transforms to Wavelet analysis	88
5	Slipstream data analysis, results and discussion	91
5.1	Introduction	91
5.2	Ensemble averaging	92
5.3	Coefficient of pressure	98
5.3.1	Train side	98
5.3.2	Train roof	102
5.4	Normalised ensemble longitudinal component of velocity U	108
5.4.1	Train side	108
5.4.2	Train roof	110
5.5	Normalised ensemble components of velocity V and W	116
5.6	Detailed consideration of the flow within specific flow regions	121
5.6.1	Nose region	121
5.6.2	Boundary layer region	123
5.6.2.1	Velocity profiles	123
5.6.2.2	Displacement thickness	124

5.6.2.3	Turbulence intensity	131
5.6.2.4	Autocorrelation	134
5.6.3	Tail and wake region	139
5.6.4	Wavelet analysis	143
5.6.4.1	Wavelet analysis of TRAIN rig data	143
5.7	Assessing the effect of train speed	152
5.8	Full scale results	153
5.8.1	Validation of model scale results	154
5.8.1.1	Coefficient of pressure	154
5.8.1.2	Normalised ensemble longitudinal component of velocity U	155
5.8.2	TSI analysis	157
5.8.3	UK safety position analysis	163
5.9	Discussion	165
5.9.1	Reynolds number effect	165
5.9.2	Safety limits and positions	166
5.9.3	General concluding remarks	167
6	Aerodynamic load experiment setup	170
6.1	Introduction	170
6.2	TRAIN rig crosswind generator	171
6.2.1	Flow characterisation	172
6.3	TRAIN rig model	179
6.3.1	On-board pressure measuring system	179
6.3.1.1	Data logger	180
6.3.1.2	Pressure transducers	184
6.3.1.3	Pressure taps and loading consists	185
6.3.1.4	On-board reference pressure system	193
6.3.1.5	Light detector	193

6.4	Experiment setup	194
6.4.1	Coordinate system and measuring positions	194
6.4.2	Trackside instrumentation	195
6.4.2.1	Cobra probes	195
6.4.2.2	Photoelectric position finders	195
6.4.2.3	Light sensor	196
6.4.2.4	Ambient condition monitors	198
6.5	Experiment methodology	198
7	Aerodynamic load experiment processing methodology	201
7.1	Introduction	201
7.2	Processing methodology	202
7.2.1	Quasi-steady methodology	202
7.2.2	Modified methodology	204
7.2.3	Modifications for this study	208
7.2.3.1	Modifications to crosswind methodology	208
7.2.3.2	Modifications for open air experiments	209
7.3	Data conversion	210
7.3.1	Photoelectric position finders and light detector data	210
7.3.2	Pressure transducer data	212
7.3.3	Cobra probe data	214
7.4	Non-dimensionalised variables	216
7.4.1	Pressure coefficient measured through the crosswind	217
7.4.2	Pressure coefficient measured through the open air	217
7.5	Aerodynamic forces and moments	218
7.6	Uncertainty analysis	223
7.6.1	Mean pressure coefficients	223
7.6.2	Aerodynamic load coefficients	224

8	Aerodynamic load analysis, results and discussion	225
8.1	Introduction	225
8.2	Open air results and analysis	226
8.2.1	Surface pressure distribution	226
8.2.2	Analysis of surface pressure distribution	242
8.2.2.1	Lead face	242
8.2.2.2	Side faces	243
8.2.2.3	Roof	243
8.2.2.4	Rear face	244
8.2.3	Overall aerodynamic load coefficients	244
8.3	Crosswind results and analysis	249
8.3.1	Surface pressure distribution	249
8.3.2	Analysis of surface pressure distribution	266
8.3.2.1	Lead face	266
8.3.2.2	Windward face	267
8.3.2.3	Roof	268
8.3.2.4	Leeward face	269
8.3.2.5	Rear face	270
8.3.3	Overall aerodynamic load coefficients	271
8.4	Discussion	276
8.4.1	Reynolds number effect	276
8.4.2	Uncertainty analysis	277
8.4.3	General concluding remarks	278
9	Conclusions and recommendations for further work	282
9.1	Introduction	282
9.2	Conclusions	282
9.3	Recommendations for further work	293
	References	296

A Instrumentation calibration	309
A.1 Introduction	309
A.2 TFI Cobra probe calibration	310
A.2.1 Calibration process	310
A.2.2 Cobra probe comparison results	312
A.2.2.1 Stationary results	312
A.2.2.2 Transient results	313
A.2.2.3 Conclusions	313
A.2.3 Cobra probe calibration results	315
A.2.3.1 Stationary results	315
A.2.3.2 Transient results	315
A.2.3.3 Conclusions	317
A.3 Gill Instruments R3-50 ultrasonic anemometer calibration	319
A.4 Sensor Technics HCLA12X5PB calibration	319
A.4.1 Calibration process	319
A.4.2 Nominal linear calibration (NLC)	322
A.4.3 Actual cubic calibration (ACC)	322
A.4.4 Discussion	325
A.5 Honeywell 164PC01D37 calibration	326
B Uncertainty analysis	327
B.1 Introduction	327
B.2 Uncertainty analysis methodology	327
B.2.1 Bias limit	328
B.2.2 Random uncertainty	329
B.2.3 Total uncertainty	329
B.3 Slipstream uncertainty analysis	329
B.3.1 Slipstream velocities	330
B.3.1.1 Bias limit	330

B.3.1.2	Random uncertainty	331
B.3.1.3	Total uncertainty	331
B.3.2	Static pressure	333
B.3.2.1	Bias limit	333
B.3.2.2	Random uncertainty	334
B.3.2.3	Total uncertainty	335
B.4	Aerodynamic load uncertainty methodology	337
B.4.1	Mean pressure coefficients	337
B.4.1.1	Bias limit	337
B.4.1.2	Random uncertainty	338
B.4.1.3	Total uncertainty	338
B.4.2	Aerodynamic load coefficients	342
C	Preliminary model scale experiments	344
C.1	Introduction	344
C.2	Experiment setup	344
C.2.1	Slipstream experiment	345
C.2.2	Aerodynamic load experiment	346
C.3	Preliminary experiment results	347
C.3.1	Slipstream experiment	347
C.3.2	Aerodynamic load experiment	350
C.4	General concluding remarks	354
D	Ensemble sensitivity analysis	356
D.1	Introduction	356
D.2	Ensemble averaging methodology	357
D.2.1	Correlation coefficient	359
D.2.2	Standard deviation method	359
D.3	Cobra probe ensemble analysis	361

D.3.1	Correlation coefficient results	361
D.3.2	Standard deviation results	363
D.4	Pressure transducer ensemble analysis	364
D.4.1	Correlation coefficient results	365
D.4.2	Standard deviation results	366
D.5	Full scale ensemble analysis	366
D.6	Discussion	369
D.6.1	Moving ensemble size	369
D.6.2	Full scale vs model scale	370
D.6.3	General concluding remarks	371
E	Author's publications	373
E.1	Introduction	373

List of Figures

1 Introduction

- 1.1 A photograph of an overturned passenger train on Leven Viaduct, Cumbria, 1903. 4
- 1.2 Photograph showing detached containers blown from flatbed freight wagons travelling along the West Coast Mainline, Cheddington UK, on the 1st March 2008. 5

2 Literature review

- 2.1 Deutsche Bahn high speed passenger ICE2 model train at the TRAIN rig facility. 17
- 2.2 A generic atmospheric boundary layer profile. 30
- 2.3 Reference coordinate system for an onset wind. 32
- 2.4 Resultant wind velocity diagram with respect to a moving train. 33
- 2.5 A vertical profile of the mean wind relative to a moving vehicle. 34
- 2.6 A vector diagram to show mean wind velocity relative to a moving vehicle for a) a nominal mean wind b) relative mean wind fluctuations. . . 35
- 2.7 The reference system used for calculating load coefficients on the discretised container surface. 38
- 2.8 Generic characteristic wind curve (CWC) to consider yaw angle and resultant wind velocity. 40
- 2.9 Generic time history of wind speed for a Chinese hat wind scenario. . . 41

3 Slipstream experiment setup

- 3.1 The TRAIN rig facility. 51
- 3.2 Schematic images of the TRAIN rig test room, track bed structure and the track layout. 51
- 3.3 A schematic of the TRAIN rig propulsion and braking mechanisms. . . 53

3.4	A comparison of images showing the TRAIN rig Class 66 and FEA-B wagon models to the real vehicles.	55
3.5	The dimensions of the model scale Class 66 locomotive and FEA-B wagons.	57
3.6	The couplings between vehicles on the TRAIN rig freight model.	58
3.7	The TRAIN rig chassis for the freight model.	58
3.8	Diagrams to show the loading configurations to be tested at the TRAIN rig.	60
3.9	The coordinate system defined for the slipstream experiments at the TRAIN rig.	61
3.10	Series 100 Cobra probe key elements and dimensions.	63
3.11	The TFI interface unit and the reference pressure positioning underneath the TRAIN rig apparatus.	64
3.12	Photoelectric position finders to measure the model speed and the ambient condition monitors.	66
3.13	A map of the position of the Uffington test site and village in Oxfordshire, and a photo of the old Great Western Railway (GWR) station.	69
3.14	The proposed HOPS vehicle and the RRV MEWP test vehicle used in the experiments at Uffington, Oxfordshire.	70
3.15	Gill Instrumentation R3-50 ultrasonic anemometer key elements and dimensions.	73
3.16	The pressure probe and mounting used for the Uffington experiments.	74
3.17	A series of images to illustrate different wagon types recorded at Uffington, Oxfordshire.	77
4	Slipstream data processing methodology	
4.1	TFI .ap file format.	81
4.2	Illustration of how the data is aligned to the point at which pressure crosses the x-axis between the maximum positive and negative pressure peaks.	85
5	Slipstream data analysis, results and discussion	
5.1	Run to run variability in 25 runs of data for consist 5 for the 101.25m train.	93
5.2	A series of figures to illustrate the process of ensemble averaging using normalised longitudinal velocity U	94
5.3	An illustration of the effect of increasing ensemble size on the ensemble average for U	95

5.4	Coefficient of pressure for freight consists 1 to 5 for train lengths 101.25m, measured at train speed 20m/s for probes 2, 3 and 4 at the side of the train.	99
5.5	Coefficient of pressure for freight consists 1, 3 and 5 for train lengths 181.25m, measured at train speed 20m/s for probes 2, 3 and 4 at the side of the train.	103
5.6	Coefficient of pressure for freight consists 1 to 5 measured at train speed 20m/s for probe 1 above the train roof.	104
5.7	Coefficient of pressure for freight consists 1, 3 and 5 for train lengths 181.25m, measured at train speed 20m/s for probes 1, 5 and 6 above the train roof.	106
5.8	Normalised ensemble longitudinal component of velocity U for freight consists 1 to 5 for train lengths 101.25m, measured at train speed 20m/s for probes 2, 3 and 4 at the side of the train.	107
5.9	Normalised ensemble longitudinal component of velocity U for freight consists 1, 3 and 5 for train lengths 181.25m, measured at train speed 20m/s for probes 2, 3 and 4 at the side of the train.	111
5.10	Normalised ensemble longitudinal component of velocity U for freight consists 1 to 5 measured at train speed 20m/s for probe 1 above the train roof.	112
5.11	Normalised ensemble longitudinal component of velocity U for freight consists 1, 3 and 5 for train lengths 181.25m, measured at train speed 20m/s for probes 1, 5 and 6 above the train roof.	115
5.12	Normalised ensemble longitudinal components of velocity V and W for the 181.25m train with freight consists 1 and 5 measured at train speed 20m/s for probes 2, 3 and 4 at the side of the train.	117
5.13	Normalised ensemble longitudinal components of velocity V and W for the 181.25m train with freight consists 1 and 5 measured at train speed 20m/s for probe 1, 5 and 6 above the train roof.	118
5.14	A series of figures illustrating the overall magnitude in relation to the normalised ensemble longitudinal components of velocity U for freight consist 5 measured at train speed 20m/s for probes 1 to 4.	119
5.15	Normalised ensemble longitudinal component of velocity U and normalised ensemble deviations for train consists 1, 2, 3, 4, 5 in the nose region for probes 1, 2, 3 and 4.	123
5.16	The development of velocity U profiles along the train side in the boundary layer.	125

5.17	The development of velocity U profiles above the train roof.	126
5.18	Displacement thickness (m) along the train length.	128
5.19	A comparison of displacement thickness (m) for consist 5 above the train roof and at the train side.	130
5.20	Displacement thickness (m) above the train roof.	131
5.21	Turbulence intensity at train side for all consists tested.	132
5.22	Turbulence intensity above the train roof for all consists tested.	134
5.23	Autocorrelation for the normalised ensemble longitudinal component of velocity U at train side for all consists tested.	136
5.24	The wake region for the normalised ensemble longitudinal component of velocity U at train side for all consists tested.	141
5.25	The far wake region (100m from the train end) for the normalised en- semble longitudinal component of velocity U for all consists tested. . .	142
5.26	A series of wavelet plots for normalised longitudinal component of ve- locity U for consists 1, 3 and 5 at probe position 1.	144
5.27	A series of wavelet plots for normalised longitudinal component of ve- locity U for consists 1, 3 and 5 at probe position 2.	145
5.28	A series of wavelet plots for normalised longitudinal component of ve- locity U for consists 1, 3 and 5 at probe position 3.	146
5.29	A series of wavelet plots for normalised longitudinal component of ve- locity U for consists 1, 3 and 5 at probe position 4.	147
5.30	A wavelet plot for normalised longitudinal component of velocity U for consist 1 at probe position 1 with extended x-axis.	148
5.31	Coefficient of pressure and normalised ensemble longitudinal component of velocity U for freight consist 1 measured at train speeds 25m/s and 20m/s for probes 1, 2 and 3.	150
5.32	Coefficient of pressure and normalised ensemble longitudinal component of velocity U for freight consist 5 measured at train speeds 25m/s and 20m/s for probes 1, 2 and 3.	151
5.33	A comparison of coefficient of pressure for model and full scale data. . .	155
5.34	A comparison of normalised ensemble longitudinal component of velocity U for model and full scale data.	156
5.35	A comparison of normalised longitudinal component of velocity U for individual runs and the ensemble at model scale and the equivalent full scale data.	157
5.36	A comparison of normalised longitudinal velocity U for all train types at full scale.	158

5.37	Maximum 1 second moving average velocities and the position where the value was recorded for train speed $V_{train}=33.5\text{m/s}$	162
5.38	Maximum velocities and the position where the value was recorded for train speed $V_{train}=33.5\text{m/s}$ for consist 3 at the UK trackside safety position.	164
 6 Aerodynamic load experiment setup		
6.1	The TRAIN rig crosswind generator with the Class 66 hauled container freight train.	171
6.2	A schematic of the TRAIN rig crosswind generator.	173
6.3	A schematic of the TRAIN rig crosswind generator.	174
6.4	A comparison of horizontal wind profiles for the streamwise mean velocity $\overline{u_{cwg}}$, the lateral mean velocity $\overline{v_{cwg}}$ and the vertical mean velocity $\overline{w_{cwg}}$ for the original crosswind generator flow characterisation and the retested points.	176
6.5	A comparison of horizontal wind profiles for the mean differential static pressure $\overline{\Delta P_{ST}}$ for the original crosswind generator flow characterisation and the retested points.	177
6.6	A comparison of horizontal wind profiles for the streamwise $I_{u_{cwg}}$, lateral $I_{v_{cwg}}$ and vertical $I_{w_{cwg}}$ turbulence intensities.	177
6.7	The data logger circuit boards and rechargeable battery.	181
6.8	The data logger control software.	181
6.9	Images to show how the data logger and on-board equipment is positioned and setup within the measuring container.	183
6.10	The measuring container external features.	184
6.11	An image and schematic of a miniaturised differential pressure transducer.	185
6.12	The pressure tapping shown from inside and outside the measuring container.	186
6.13	Diagrams of the container loading configurations and efficiencies to be tested at the TRAIN rig.	188
6.14	Pressure tapping positions on loops 1 to 4 for consist 1.	189
6.15	Pressure tapping positions on loops 5 to 8 for consist 1.	190
6.16	Pressure tapping positions on loops 1 to 8 for consist 4.	191
6.17	Pressure tapping positions on loops 1 to 8 for consist 6.	192
6.18	The coordinate system defined for the crosswind experiments at the TRAIN rig.	194

6.19	The Cobra probe in position within the crosswind generator and the pressure tubing to vent the reference of port out of the flow underneath the rig.	196
6.20	Images of the equipment under the TRAIN rig, the ‘Sick’ photoelectric position finders and the light source positions.	197
7	Aerodynamic load experiment processing methodology	
7.1	A vector diagram to show mean wind velocity relative to a moving vehicle for a) a nominal mean wind b) relative mean wind fluctuations. . .	204
7.2	Positions of photoelectric position finders and light sources in the crosswind test zone.	210
7.3	Time histories recorded by the on-board data logger for a single run. . .	213
7.4	An example of a crosswind velocity u_{loc} time history recorded by the reference Cobra probe.	215
7.5	The method of discretising the container geometry.	219
7.6	Pressure tapping positions and associated discretised area to each tapping point.	221
7.7	The reference systems used for calculating load coefficients on the discretised container surface.	222
8	Aerodynamic load analysis, results and discussion	
8.1	Examples of the typical evolution of pressure coefficient as the train travels within the open air section for consist 1 loop 2.	227
8.2	Examples of the typical evolution of pressure coefficient as the train travels within the open air section for consist 4 loop 2.	228
8.3	Examples of the typical evolution of pressure coefficient as the train travels within the open air section for consist 6 loop 2.	229
8.4	Mean surface pressure coefficient distribution with associated uncertainty error bounds for consist 1 loops 1, 2 and 3.	232
8.5	Mean surface pressure coefficient distribution with associated uncertainty error bounds for consist 1 loops 4, 5 and 6.	233
8.6	Mean surface pressure coefficient distribution with associated uncertainty error bounds for consist 1 loops 7 and 8.	234
8.7	Mean surface pressure coefficient distribution with associated uncertainty error bounds for consist 4 loops 1, 2 and 3.	236
8.8	Mean surface pressure coefficient distribution with associated uncertainty error bounds for consist 4 loops 4 and 5.	237

8.9	Mean surface pressure coefficient distribution with associated uncertainty error bounds for consist 4 loop 8.	238
8.10	Mean surface pressure coefficient distribution with associated uncertainty error bounds for consist 6 loops 1, 2 and 3.	239
8.11	Mean surface pressure coefficient distribution with associated uncertainty error bounds for consist 6 loops 4 and 5.	240
8.12	Mean surface pressure coefficient distribution with associated uncertainty error bounds for consist 6 loop 8.	241
8.13	Estimated values for the aerodynamic load coefficients C_X , C_Y , C_Z , C_{M_X} and $C_{M_{X,lee}}$ in the open air test section.	245
8.14	Examples of the typical evolution of pressure coefficient as the train travels within the crosswind generator for consist 1 loop 2.	250
8.15	Examples of the typical evolution of pressure coefficient as the train travels within the crosswind generator for consist 4 loop 2.	251
8.16	Examples of the typical evolution of pressure coefficient as the train travels within the crosswind generator for consist 6 loop 2.	252
8.17	Mean surface pressure coefficient distribution with associated uncertainty error bounds for consist 1 loops 1, 2 and 3.	256
8.18	Mean surface pressure coefficient distribution with associated uncertainty error bounds for consist 1 loops 4, 5 and 6.	257
8.19	Mean surface pressure coefficient distribution with associated uncertainty error bounds for consist 1 loops 7 and 8.	258
8.20	Mean surface pressure coefficient distribution with associated uncertainty error bounds for consist 4 loops 1, 2 and 3.	260
8.21	Mean surface pressure coefficient distribution with associated uncertainty error bounds for consist 4 loops 4 and 5.	261
8.22	Mean surface pressure coefficient distribution with associated uncertainty error bounds for consist 4 loop 8.	262
8.23	Mean surface pressure coefficient distribution with associated uncertainty error bounds for consist 6 loops 1, 2 and 3.	263
8.24	Mean surface pressure coefficient distribution with associated uncertainty error bounds for consist 6 loops 4 and 5.	264
8.25	Mean surface pressure coefficient distribution with associated uncertainty error bounds for consist 6 loops 8.	265
8.26	Estimated values for the aerodynamic load coefficients C_Y , C_Z , C_{M_X} and $C_{M_{X,lee}}$ in the crosswind test section.	272

8.27	A comparison of $C_{M_{X,lee}}$ for consists 1, 4 and 6 with RSSB data measured for just the loaded container. Results are measured about the leeward container base edge reference system for a yaw angle of 30°	275
A Instrumentation calibration		
A.1	The University of Birmingham downburst simulator.	311
A.2	A comparison of University of Birmingham Cobra probes within a stationary flow.	312
A.3	A comparison of University of Birmingham Cobra probes within a transient flow.	314
A.4	A comparison of a stationary flow to assess the calibration of Cobra probes used at the TRAIN rig.	316
A.5	A comparison of a transient flow to assess the calibration of Cobra probes used at the TRAIN rig.	317
A.6	Standard deviation of individual runs with respect to the ensemble mean for Cobra probes in a stationary and transient flow.	318
A.7	Pressure calibration raw data as measured by the Betz manometer and on-board pressure measuring system.	321
A.8	Nominal linear calibration error $E_{NLC,k}$ associated with each pressure transducer.	323
A.9	Actual cubic calibration error $E_{ACC,k}$ associated with each pressure transducer.	324
B Uncertainty analysis		
B.1	The bias limit, random uncertainties and total uncertainties for slip-stream velocity measurements at model and full scale.	332
B.2	The bias limit, random uncertainties and total uncertainties for slip-stream static pressure measurements at model and full scale.	336
B.3	The bias limit, random uncertainties and total uncertainties for consist 1 in the open air and crosswind test sections.	339
B.4	The bias limit, random uncertainties and total uncertainties for consist 4 in the open air and crosswind test sections.	340
B.5	The bias limit, random uncertainties and total uncertainties for consist 6 in the open air and crosswind test sections.	341
C Preliminary model scale experiments		

C.1	Nose region coefficient of pressure data for an individual run plotted with the voltage data from the nose region position finder.	348
C.2	Coefficient of pressure and normalised ensemble longitudinal velocity U results from the preliminary experiments.	349
C.3	Examples of the typical evolution of pressure coefficient as the train travels within the crosswind generator.	352
C.4	Examples of the typical evolution of pressure coefficient as the train travels within the crosswind generator.	353
 D Ensemble sensitivity analysis		
D.1	Correlation coefficient differences relative to a changing ensemble size. .	362
D.2	Standard deviation analysis results for original data set $\overline{\sigma_{\bar{c}_N}}$ and the bootstrap method $\overline{\sigma_{\bar{c}_N}^{BS}}$	363
D.3	Standard deviation analysis results for original data set $\overline{\sigma_{\bar{c}_N}}$ and the bootstrap method $\overline{\sigma_{\bar{c}_N}^{BS}}$	364
D.4	Correlation coefficient differences relative to a changing ensemble size. .	365
D.5	Standard deviation analysis results for original data set $\overline{\sigma_{\bar{c}_N}}$ and the bootstrap method $\overline{\sigma_{\bar{c}_N}^{BS}}$	367
D.6	Standard deviation analysis results for original data set $\overline{\sigma_{\bar{c}_N}}$ and the bootstrap method $\overline{\sigma_{\bar{c}_N}^{BS}}$ for the full and model scale nose region data for U and C_p	368

List of Tables

2	Literature review	
2.1	Equations to calculate lee side roll moment coefficients for freight trains.	44
3	Slipstream experiment setup	
3.1	Slipstream measuring positions and the consists and train lengths tested at those positions.	62
3.2	The tension required for each consist to achieve the desired train speed.	67
3.3	Slipstream measuring positions and instrumentation used at those positions for the full scale experiments.	70
3.4	Train types and lengths recorded at Uffington.	78
4	Slipstream data processing methodology	
4.1	A table of mean and maximum total uncertainties for slipstream velocities and static pressure for each container loading configuration tested at model scale for the 181.25m train and mean values at full scale. . . .	86
5.1	Mean, maximum and minimum ensemble sizes, as well as the percentage of time steps with a ensemble size greater or equal to 20.	97
5	Slipstream data analysis, results and discussion	
5.2	Nose coefficient of pressure peaks measured on a trackside hoarding placed 1.4m from the centre of track and 0.25m above the top of the rail.	100
5.3	Autocorrelation integral time and length scales for all consists tested. .	138
5.4	A table showing TSI calculation results for both model and full scale freight trains at train speeds $V_{train}=33.5\text{m/s}$ and $V_{train}=40\text{m/s}$	161
5.5	TSI calculation results for a 0.35 second moving average filter for both model and full scale freight trains at train speeds $V_{train}=33.5\text{m/s}$	162

5.6	A table showing changes to the UK trackside safety position and train speed in relation to maximum values recorded for a high speed passenger train of 17m/s.	164
5.7	A table showing changes to the UK platform safety position and train speed in relation to the suggested platform safety limit of 11m/s. . . .	165
6	Aerodynamic load experiment setup	
6.1	Spanwise averages for the horizontal wind profile.	178
6.2	The tension required to achieve the desired train speed needed for each consist in each experiment test section.	200
7	Aerodynamic load experiment processing methodology	
7.1	Dimensions for the different area sizes of the container discretised geometry.	220
7.2	A table of mean and maximum total uncertainties for mean pressure coefficients for all consists tested in the aerodynamic load experiments.	224
7.3	A table of mean total uncertainties for aerodynamic load coefficients. .	224
8	Aerodynamic load analysis, results and discussion	
8.1	Mean pressure coefficients and the standard deviation for consist 1 in the open air test section, on all vertical loops with taps 1 to 9.	231
8.2	Mean pressure coefficients and the standard deviation for consist 4 in the open air test section, on all vertical loops with taps 1 to 9.	235
8.3	Mean pressure coefficients and the standard deviation for consist 6 in the open air test section, on all vertical loops with taps 1 to 9.	235
8.4	Aerodynamic load coefficients for consists 1, 4 and 6 C_X , C_Y , C_Z , C_{M_X} and $C_{M_{X,lee}}$ with respect to a container and track reference system in the open air test section.	245
8.5	Mean pressure coefficients and the standard deviation for consist 1 on all vertical loops for taps 1 to 9.	255
8.6	Mean pressure coefficients and the standard deviation for consist 4 on all vertical loops for taps 1 to 9.	259
8.7	Mean pressure coefficients and the standard deviation for consist 6 on all vertical loops for taps 1 to 9.	259
8.8	Aerodynamic load coefficients for consists 1, 4 and 6 C_Y , C_Z , C_{M_X} and $C_{M_{X,lee}}$ with respect to a container and track reference system in the crosswind test section.	272

A Instrumentation calibration

- A.1 Zero offset voltages $\text{Vol}_{0,k}$ for pressure transducers PT1-PT14. 320
- A.2 Actual cubic calibration factors C_1 , C_2 and C_3 324

B Uncertainty analysis

- B.1 A table of measuring instrument accuracies for the slipstream velocity experiments. 331
- B.2 A table of mean and maximum bias, random and total uncertainties for slipstream velocities for each container loading configuration at model scale and mean values at full scale. 332
- B.3 A table of measuring instrument accuracies for the slipstream static pressure experiments. 334
- B.4 A table of mean and maximum bias, random and total uncertainties for slipstream static pressure for each container loading configuration at model scale and mean values at full scale. 335
- B.5 A table of measuring instrument accuracies for the aerodynamic load experiments. 338
- B.6 A table of mean and maximum bias, random and total uncertainties for mean pressure coefficients. 342
- B.7 A table of mean total uncertainties for aerodynamic load coefficients. . 343

C Preliminary model scale experiments

- C.1 Cobra probe measuring positions for the slipstream preliminary experiments. 346

Nomenclature

Principal symbols

\bar{u} Mean value of all resultant air speed measurements in the x - y plane (m/s)

$\Delta P(t)$ Differential pressure (Pa)

$\tilde{\mathbf{d}}$ Vector perpendicular to the longitudinal axis X

\mathbf{n} Normal unit vector

\mathbf{V} Instantaneous wind velocity field (m/s)

$\text{Vol}(t)$ Voltage time history (Volts)

Vol_0 Zero offset voltage (Volts)

$\overline{u_{wind}}$ Mean wind velocity in the streamwise flow direction (m/s)

A Davis equation coefficient

a Coefficient

A_{ref} Vehicle reference area (m²)

B Davis equation coefficient

b Common power

C Davis equation coefficient

c Speed of sound (m/s)

C_ξ Non-dimensional force coefficient for $\xi = X, Y, Z$

C_{M_ξ} Non-dimensional moment force coefficient for $\xi = X, Y, Z$

$C_{Mx,lee}$	Aerodynamic rolling moment coefficient about the leeward rail
C_P	Coefficient of pressure
f	Signal frequency (Hz)
F_ξ	Aerodynamic forces for $\xi = X, Y, Z$ (N)
f_{samp}	Sampling frequency (Hz)
H_{ref}	Vehicle reference height (m)
I_ξ	Turbulence intensities defined for the fluctuating velocity components u , v and w
K_{NLC}	Nominal linear calibration factor (Pa)
L_{CW}	Crosswind test section length (m)
L_{ref}	Vehicle reference length (m)
L_{us}	Characteristic length scale of ultrasonic anemometer (m)
m	Coefficient for calculating rolling moment coefficient. $m = \theta/100$ (degrees)
M_R	Restoring moment (Nm)
M_ξ	Aerodynamic moment forces for $\xi = X, Y, Z$ (N)
M_{over}	Overtopping moment (Nm)
$M_{X,lee}$	Aerodynamic rolling moment about the leeward rail (Nm)
N_{samp}	Sample number
P	Actual surface pressure at any point (Pa)
$P(t)$	Instantaneous static pressure (Pa)
P_0	Static reference pressure (Pa)
P_{AMB}	Ambient room pressure (Pa)
P_{AMB}	Atmospheric pressure (Pa)

P_{cf}	Pressure transducer calibration factor
P_{ST}	Wind static pressure (Pa)
Q	Vertical force of the wheel on the rail (N)
q	Dynamic pressure (Pa)
R	Specific gas constant (J/(kgK))
r	Individual run
s	Wavelet scale parameter
s_N	Spanwise position in crosswind generator
St	Strouhal number
t	Time (s)
T_{room}	Temperature of room (Kelvin)
t_{samp}	Sample time (s)
u'_{wind}	Turbulent fluctuations in wind velocity in the x direction (m/s)
$U(t)$	Normalised ensemble velocity in the longitudinal direction
$u(t)$	Instantaneous velocity in the longitudinal direction (m/s)
u_*	Surface friction velocity (m/s)
$U_r(t)$	Normalised velocity per run in the longitudinal direction
$u_{2\sigma}$	TSI limit velocity value (m/s)
U_∞	Normalised free stream velocity
U_{res}	Resultant velocity in the horizontal x - y plane (m/s)
u_{wind}	Onset natural wind velocity (m/s)
v'_{wind}	Turbulent fluctuations in wind velocity in the y direction (m/s)
$V(t)$	Normalised ensemble velocity in the lateral direction

$v(t)$	Instantaneous velocity in the lateral direction (m/s)
$V_r(t)$	Normalised velocity per run in the lateral direction
V_{max}	Maximum operational line speed (m/s)
V_{rel}	Relative velocity (m/s)
V_{train}	Train speed (m/s)
v_{us}	Flow speed along the ultrasonic anemometer transducer axis (m/s)
v_{wind}	Natural wind velocity in the lateral direction (m/s)
w'_{wind}	Turbulent fluctuations in wind velocity in the z direction (m/s)
$W(t)$	Normalised ensemble velocity in the vertical direction
$w(t)$	Instantaneous velocity in the vertical direction (m/s)
$W_r(t)$	Normalised velocity per run in the vertical direction
x	Distance in the longitudinal direction (m)
y	Distance in the lateral direction (m)
y'	Distance in the lateral direction from train side (m)
Y_{lat}	Lateral guiding force of a wheel exerted on the rail measured in a wheelset based reference frame (N)
z	Distance in the vertical direction (m)
z'	Distance in the vertical direction from train side (m)
z_0	Surface roughness length (m)
Re	Reynolds number

Greek Symbols

β	Onset natural wind angle (degrees)
δ^*	Displacement thickness (m)

κ	Von Kármán constant (~ 0.41)
ν	Kinematic viscosity (m^2/s)
ρ	Air density (kg/m^3)
σ	Standard deviation
Θ	Resultant yaw angle (degrees)
θ	Yaw angle (degrees)
φ	Velocity potential function

Subscripts

0	Zero offset voltage
ACC	Actual cubic calibration
AMB	Atmospheric value
BIAS	Bias limit
BS	Bootstrap method
cf	Calibration factor
CWG	Crosswind test section
i	Index of the individual pressure tap on each loop
j	Index of the individual pressure tap loop
k	Index of the individual on-board pressure transducers
LG_ξ	Light gate position where $\xi=1,2$
loc	Local value
NLC	Nominal linear calibration
nose	Nose of train
OA	Open air test section

r	Data from one run (one train passage)
ref	Reference
rel	Relative (to the train)
res	Resultant
RND	Random uncertainty
room	Variable measured in the test room
samp	Individual sample
SW	Spanwise average
TOT	Total uncertainty
train	Train
wind	Wind

Abbreviations

ABL	Atmospheric boundary layer
AeroTRAIN	Aerodynamics Total Regulatory Acceptance for the Interoperable Network (project)
AOA	Aerodynamics in Open Air
BR	British Rail
BSI	British Standards Institute
CFD	Computational fluid dynamics
CRWC	Characteristic reference wind curve
CWC	Characteristic wind curve
CWG	Crosswind generator
DB	Deutsche Bahn

FFT	Fast Fourier transform
FOC	Freight operating company
GRP	Glass-fibre reinforced plastic
HOPS	High Output Plant System
HPP/LPP	High/low pressure port of differential pressure transducers
HS1	High Speed 1
HS2	High Speed 2
HWP	Horizontal wind profile
ISO	International Shipping Organisation
LD	On-board light beam detector
LES	Large eddy simulation
LG1/LG2	Trackside vehicle speed detectors
LS1/LS2	Trackside light sources
OLE	Overhead Line Equipment
RANS	Reynolds-averaged Navier-Stokes
RAPIDE	Railway Aerodynamics of Passing Interactions with Dynamic Effects (project)
RMS	Root mean square
RRV MEWP	Mobile elevated working platform road rail vehicle
RSSB	Rail Safety and Standards Board
RWTA	Real World Train Aerodynamics (project)
TFI	Turbulent Flow Instrumentation Ltd.
TRAIN rig	Transient Aerodynamic Investigation rig
TSI	Technical Specifications for Interoperability
VWP	Vertical wind profile

Chapter 1

Introduction

1.1 Outline of studies

This thesis presents an experimental investigation carried out to analyse the aerodynamics of freight trains, undertaken as part of the author's PhD studies. The details and results of these experiments form the main body of this thesis. Preliminary versions of the results in this thesis have been published and presented in a series of conference papers, included in appendix E.

1.2 Research background

The rail freight industry in the UK is a growing sector with increasing volumes of international trade, coupled with a gradual return from road to rail transportation. It is estimated that the growth rate in container transportation by rail from British ports between 2001 and 2005 was 5%, indicating the importance of efficient freight distribution for the British economy (Woodburn, 2008). The UK government has set out aims to double the volume of freight cargo transported by rail on the UK rail network by 2030 (DfT, 2007).

Efficiency studies into increased volumes of freight trains within an already overstretched network, primarily focused on passenger transportation, recommend building new and reopening closed railway lines, while developing faster and longer trains (Gibson, 2003; Woodburn, 2008). New infrastructure developments are expensive and would take several years to complete. Capacity could be increased by lengthening freight trains, however this may lead to slower trains, due to locomotive power, creating further congestion within the rail network. The final option to increase freight operational speeds would be simpler to implement and lead to increased route capacity. This option, however, has implications on efficiency and safety, as the movement of a vehicle causes deformation in the surrounding air, creating transient aerodynamic effects.

The airflow around a moving vehicle is called a slipstream (Baker et al., 2001). A slipstream extends from upstream of the train nose into the wake beyond the train tail. Slipstreams associated with high speed trains can create highly turbulent non-stationary air flows, with pressure and velocity magnitudes capable of interacting and potentially destabilising trackside objects and people (Jordan et al., 2009). However, slipstream magnitudes are highly dependent on train type, speed, and the distance from the train side.

Concerns over the possibility of slipstream induced incidents have led to a number of studies into the effects of slipstreams, mainly for high speed passenger trains (Baker et al., 2001; Pope, 2006; Sterling et al., 2008; Baker et al., 2013b). Results show the flow can be divided into a number of regions along the train. Individual results were shown to be highly variable, as the flow is dominated by large scale turbulent structures, thus the technique of ensemble averaging is required when studying train slipstreams (Sterling et al., 2008). Results from these studies have led to the development of the Technical Specifications for Interoperability (TSI); a series of standards on train aerodynamics giving limiting values for slipstream velocities, allowing for interoperability of trains across national boundaries in Europe (TSI, 2008). Although some freight

research has been included in these studies, a thorough study of freight slipstream development and appropriate guidelines written in relation to rail freight is yet to be undertaken. Freight slipstream studies have tended to be conducted by rail authorities following incidents, focused on defining appropriate safety guidelines (Temple and Johnson, 2008).

Transient air flows created by vehicle movement when coupled with naturally turbulent crosswinds can create a series of steady and unsteady aerodynamic forces and moments (Dorigatti, 2013). These aerodynamic loads can potentially induce significant changes to vehicle dynamic behaviour, possibly compromising stability. A train will overturn when the contribution of the aerodynamic rolling moment about the leeward rail, generated by a crosswind, is large enough to overcome the restoring moment associated with the train weight (Gawthorpe, 1994; RSSB, 2009). The investigation of crosswind effects on rail vehicles has been the subject of a number of studies concerned with the inherent risks of vehicle overturning and track instability (Gawthorpe, 1994; Andersson et al., 2004; Alam and Watkins, 2007a,b; Baker and Sterling, 2009). Research has predominantly focused on passenger trains due to the possible impact of loss of life if a vehicle were to overturn (Raghunathan et al., 2002). However, in light of the recent container freight crosswind incidents (section 1.3) there have been series of investigative national safety reports commissioned and published (RAIB, 2009; ATSB, 2008; TSI, 2008), leading to fundamental research projects focused on freight in crosswind conditions (Alam and Watkins, 2007a; Hemida and Baker, 2010; RSSB, 2012).

1.3 Research motivation

Induced slipstream forces can interact with trackside objects. In the last forty years there have been twenty four train slipstream incidents, the majority caused by freight trains. Although no fatalities, only minor injuries have occurred, thirteen of these incidents have involved a pushchair. In one incident a braked pushchair was drawn by

the slipstream 3m towards a freight train, hitting the moving train and thrown across the platform into two passengers (Temple and Johnson, 2008). In other incidents three people have been blown over by freight trains passing station platforms (Temple and Johnson, 2008).

Research has shown slipstream velocities increase with train speed, therefore following efficiency study guidelines and increasing freight train speeds will also increase the risk of destabilising trackside objects. Understanding slipstream development allows appropriate safety guidelines to be published. Current safety measures include announcements of oncoming trains, platform warning signs and yellow lines indicating a safe distance from which to stand behind as an oncoming non-stopping train approaches (Temple and Johnson, 2008; Jordan et al., 2009).

Transient air flows created by vehicle movement when coupled with outside effects such as crosswinds can also have serious consequences. As early as 1903 there have been reported cases of trains blown over or off railway structures (Gawthorpe, 1994). Figure 1.1 shows a photograph of an overturned passenger train on a viaduct in Cumbria in 1903. The train was overturned by a crosswind with gust speeds of up to 55m/s.



Figure 1.1: A photograph of an overturned passenger train on Leven Viaduct, Cumbria, 1903 due to crosswinds with gust speeds of up to 55m/s. In the local signal box a cup anemometer set to sound an alarm at 30m/s gust speed still exists (Gawthorpe, 1994).

More recently in two separate incidents on the 1st March 2008 a total of seven containers were blown from flatbed freight wagons travelling along the West Coast Mainline, UK, shown in figure 1.2. The effects of slipstream velocities coupled with strong gusty crosswind conditions and a failure of equipment was found to be the incidents cause (RAIB, 2009).



Figure 1.2: Photograph showing detached containers blown from flatbed freight wagons travelling along the West Coast Mainline, Cheddington UK, on the 1st March 2008.

On 11th November 2008 in Loongana, Western Australia an intermodal freight train derailment occurred after being hit by a wind induced ball of dust while travelling into a storm. Authorities concluded that the loading of double stack containers in high wind conditions and slipstream induced forces were the cause of the accident (ATSB, 2008). Similarly on a bridge in Ohio, USA in February 2003 and January 2008 a double stacked container train encountered wind gusts of 22m/s causing the derailment of wagons off the bridge (ATSB, 2008).

Although such incidents are rare it highlights the possibility and importance of understanding aerodynamic flows around freight trains; however, it is shown in chapter 2 that there is very little research on characterising flow around freight trains. This study will provide a foundation within the field of rail aerodynamics, creating a detailed characterisation and understanding of the influencing factors on how the flow around a container freight train develops.

1.4 Research aims and objectives

The main aim of this research was to characterise the aerodynamic flow around a container freight train and investigate how changing the container loading configuration

affects the magnitude of aerodynamic forces measured on a container. To accomplish this aim a novel experimental study using a 1/25th scale container freight train was carried out at the Transient Aerodynamic Investigation (TRAIN) rig, owned and operated by the University of Birmingham. A series of detailed research objectives were developed to guide the study:

1. Carry out a thorough literature review on the aerodynamics of freight trains and bluff body vehicles to assess how the field of freight train aerodynamics would most benefit from a focused model scale experimental study.
2. Develop a moving model container freight train suitable for working at the TRAIN rig facility. The model should be able to have an interchangeable container loading configuration. A model container must be developed to include an on-board stand-alone pressure measuring system for measuring the surface pressure distribution on the container surface during moving model tests in both an open air and crosswind situation.
3. Develop a test methodology for undertaking TRAIN rig moving model experiments to measure slipstream velocities and static pressure, as well as aerodynamic loads on a container surface in an open air and crosswind situation. The methodology should be designed to confirm to codes of practice where necessary.
4. Undertake a series of moving model experiments in the open air to assess the influence of container loading configuration on slipstream development.
5. Collate together all previous full scale freight data sets. Carry out a comparison of model and full scale data to validate the TRAIN rig experiments and create a foundation of freight data to assess the suitability of TSI methodologies.
6. Undertake a series of moving model experiments in an open air and crosswind situation to measure the pressure distribution on a container surface to assess the influence of container loading configuration.

7. Provide a data set of moving model container freight data for slipstream and aerodynamic loads to be used as a benchmark for CFD simulations.

The research aim and objectives will be reviewed in chapter 9 to assess how the study has addressed the aims and objectives; providing a series of recommendations to how further developments to this study would benefit the research field of freight train aerodynamics.

1.5 Structure of the thesis

The structure of the thesis and content of the sections are organised as follows:

1. Chapter 2 presents a review of relevant literature for the study of slipstream development and aerodynamic loading effects on a container freight train. A discussion of the fundamental properties of slipstream research and atmospheric boundary layers is given. Analysing previous studies focused on understanding development and effects of transient air flows created by trains, knowledge is drawn together to provide the foundations from which to build upon for this experimental study, fulfilling the requirements of objective 1. The lack of experimental data and understanding of aerodynamic development of a freight is highlighted as the motivation for the present research. The methodology of quantifying slipstream and aerodynamic loads by rail authorities is discussed in relation to developing a framework from which to test the model freight train. Finally, studies from other fields of bluff body research are analysed, drawing upon relevant findings and discussing application for freight.
2. In chapter 3 the experiment methodology developed for the slipstream tests is discussed in relation to fulfilling the requirements of objectives 2 and 3. The TRAIN rig facility is described. The development of the TRAIN rig freight model is described in relation to objective 2. The experiment variables and coordinate

system are introduced. The experiment instrumentation employed in this study and the setup of such equipment is described in detail. The associated experiment methodologies adopted for the full and model scale tests are introduced.

3. Chapter 4 introduces the data processing methodology adopted for analysing the slipstream experiment data. The method of calculating non-dimensional coefficients is discussed in relation to both model and full scale data sets. An analysis of experimental uncertainty is carried out for assessing the accuracy of results presented in this study. Finally, an introduction to the process of wavelet analysis is given in relation to a discussion undertaken in chapter 5.
4. Chapter 5 presents and discusses the results of the ensemble non-dimensional velocity and static pressure measurements within freight slipstreams. An in depth analysis of slipstream flow in a series of flow regions at train side and above the train roof is carried out. By comparing results for different container loading configurations an assessment of the influencing factors on slipstream flow development is discussed. Model scale results are validated by making comparisons between full and model scale data, with conclusions drawn on the suitability of using model scale experiments to understand freight slipstream development, meeting the requirements of objective 5.
5. Chapter 6 presents the experiment methodology developed for the aerodynamic load study in relation to fulfilling the requirements of objectives 2 and 3. The TRAIN rig facility crosswind generator is described, and results from a flow characterisation test presented. Further development of the TRAIN rig freight model to include an on-board surface pressure monitoring system is described in relation to objective 2. The experiment variables and coordinate system are introduced. Instrumentation employed in carrying out this study and the setup of such equipment is described in detail. The associated experiment methodologies adopted for the aerodynamic load tests are introduced.

6. Chapter 7 introduces the data reduction and processing methodology adopted for analysing the aerodynamic load experiment data. The method of calculating non-dimensional coefficients for pressure and aerodynamic loads is discussed in relation to both the open air and crosswind test sections. Ensemble analysis is discussed in relation to each test section; reducing the crosswind data down to a set of key conditions. An analysis of experimental uncertainty is carried out for assessing the accuracy of results presented in this study.
7. Chapter 8 presents and discusses the results of the mean non-dimensional surface pressure distribution and the aerodynamic loads from both the open air and crosswind test sections. By comparing results for different container loading configurations an assessment of the influencing factors leading to increased magnitudes of aerodynamic loads is discussed.
8. Chapter 9 presents the main outcomes of the research, summarised within the framework of the aims and objectives presented in chapter 1. Recommendations for further developments to the study are also discussed.

A series of appendices to this thesis develop further aspects of the research presented:

1. Appendix A discusses the calibration performed for the Cobra probes and differential pressure transducers used in this study. The methodologies used to calibrate the different instrumentation employed in the model and full scale experiments are introduced and implemented.
2. Appendix B presents a discussion of the uncertainty associated with experimental data presented in this study. Estimate values for total error were given for the slipstream velocity and static pressure measurements, as well as surface pressure and aerodynamic load coefficients for a freight train running through an open air and crosswind situation.
3. Appendix C introduces a series of preliminary experiments designed and conducted to test the TRAIN rig facility and freight model, while analysing the

suitability of the slipstream and aerodynamic load experiment setups for different loading efficiencies. By analysing results of a series of preliminary experiments it was possible to make small amendments to the experiment methodologies for application within this study.

4. Appendix D develops further the analysis of the ensemble averaging method discussed in chapter 5 and 8. By analysing data collected in this study it is possible to assess the suitability of ensemble requirements from the TSI standards.
5. Preliminary versions of the results in this thesis have been published and presented in a series of conference papers:

- A conference paper for the 2013 International Workshop on Railway Aerodynamics (Soper et al., 2013a).
- A conference paper for the 2013 European and African Conference on Wind Engineering (Soper et al., 2013b).
- Two conference papers for the 2014 First international conference in numerical and experimental aerodynamics of road vehicles and trains (Soper et al., 2014).

The latter are included in appendix E.

The data set created as part of this study has been used to validate a series of CFD simulations published and presented at the 2013 University of Birmingham 4th annual BEAR PGR conference (Flynn et al., 2013). In addition to the main research carried out for this study the author has assisted in an external consultancy experimental project outside of the main context of the research presented in this study. The findings from this project were presented to the company for which the consultancy was performed; however, the findings are unpublished at the time of writing.

Chapter 2

Literature review

2.1 Introduction

This chapter presents a review of relevant literature for the study of slipstream development and aerodynamic loading effects on a container freight train. The review draws together knowledge from previous studies focused on understanding development and effects of transient air flows created by trains, providing the foundations for this experimental study on a container freight train. Section 2.2 introduces topics of freight research relevant to developing an understanding of vehicle induced slipstreams, including aspects of drag calculation in respect to vehicle aerodynamics. Section 2.3 describes the effects of train slipstreams and discusses the methodology of how they are quantified by rail authorities in sections 2.3.1-2.3.2. As a thorough study of freight slipstreams has not previously been carried out, an introduction to passenger slipstream research is given in section 2.3.3. The methodology and results of these studies are examined in relation to application for this study. The slipstream can be divided into a series of flow regions; each flow region is discussed in detail in sections 2.3.3.1-2.3.3.3. Section 2.3.4 introduces previous full scale experiments undertaken to determine velocity time histories of a freight train; examining how slipstream results differ to a high speed passenger train. Section 2.3.5 assesses other fields of bluff body research, drawing upon relevant

findings and discussing application for freight slipstream research. Finally conclusions are drawn in section 2.3.6 on slipstream research and how developments can be made by this study for the understanding of freight slipstream development.

Section 2.4 introduces the effects that crosswinds can create on a train to develop an understanding of why research on this topic is relevant to the rail industry. To thoroughly study crosswinds, firstly a discussion regarding the fundamental nature of atmospheric boundary layers is presented in section 2.4.1. This knowledge is developed to consider crosswind effects relative to a vehicle (section 2.4.2), with a view to understanding forces and moments exerted on a vehicle moving through a crosswind (section 2.4.3). As in section 2.3.1, safety limits and calculation methodologies are discussed in sections 2.4.4.1-2.4.4.2. Section 2.4.5 examines further implications on crosswind safety by examining studies which take different approaches to crosswind stability, as well as studies from other fields of bluff body research, drawing upon relevant findings and discussing application for freight crosswind research. Finally conclusions are drawn on crosswind research and how developments can be made by this study for the understanding of aerodynamic load stability in relation to a freight train, in section 2.4.6.

2.2 Freight research

As early as the 1930's experiments in train motion and running resistance were conducted for the determination of economic speeds, loads of train working and fuel consumption (Andrews, 1954). Research into aerodynamic properties of bluff bodies has developed from mainly aircraft to all types of vehicles. A bluff body refers to an object that when placed in a flow has leading edge separation with large regions of flow separation creating drag; where pressure drag components are much larger than skin friction drag (Cooper, 1993).

In America and Australia, where rail freight is moved across large distances, research

on drag reduction methods and running resistance calculation can potentially create huge savings for companies. The introduction of computer programmes to calculate loading efficiency of container freight trains at shipping yards in America has increased loading efficiency by nearly 30%, reducing fuel consumption by 1gal/mile per train (Lai and Barkan, 2006).

For economic reasons open top wagons are most useful for loading loose commodities, such as coal or ballast. When loaded, goods create a rough surface affecting flow over the top surface, however, when unloaded open top wagons cause large flow disturbances, dramatically increasing drag. High drag coefficients are created by air flows over the leading wagon face, along inside faces of body sides and into the trailing end wall (Donnelly and Butcher, 1990). Covering open top wagons dramatically reduces drag by up to 42% (Watkins et al., 1992). However fitting partial covers at an angle, optimally 37.5° with respect to the wagon sides, and implementing internal baffle plates, to stabilise internal vortices, also provides large drag reductions while offering greater economic sustainability (Watkins et al., 1992; Saunders et al., 1993).

A number of studies have developed models to calculate running resistance to assist with experimental data and computational fluid dynamics (CFD) results in the optimisation of train design (Rochard and Schmid, 2000). Running resistance can be divided into five items (Lukaszewicz, 2009).

- Mechanical rolling resistance on tangent track, due to mechanical energy dissipation in vehicle, track, and the contact areas between wheels and track.
- Mechanical curve resistance, which is the increment in rolling resistance as a train is rounding a curve.
- Aerodynamic drag.
- Grade resistance, as ascending a grade a train will experience a resistive force due to gravity.

- Inertia resistance, can be interpreted as the additional tractive effort required for acceleration due to the effect of inertia.

The Davis equation is an approximation for the resistance force (Bernsteen, 1979),

$$R = A + BV_{rel} + CV_{rel}^2 \quad (2.1)$$

where V_{rel} is the train speed relative to the surrounding air (m/s) and A (N), B (N s/m) and C (N s²/m²) are calculated by fitting coefficients to running resistance curves obtained from experiment results defined for individual environments, such as open space or tunnels. To calculate resistance experimentally, either deceleration against time while a vehicle is coasting (a coast down test) or the tractive effort needed to maintain a constant velocity at various speeds over a working range are measured (Rochard and Schmid, 2000). Coefficients A and B relate to mechanical resistance and C the aerodynamic resistance (Rochard and Schmid, 2000). From equation 2.1 it is clear at low speeds mechanical resistance terms are dominant, however as train speed is increased the aerodynamic resistance term becomes increasingly dominant.

Increases in computing power have made the study of vehicle aerodynamics by CFD more accessible. In line with industrial needs a number of studies have analysed drag effects of open top wagons (Golovanevskiy et al., 2012), container wagons (Hemida and Baker, 2010; Flynn et al., 2013; Östh and Krajnović, 2013) and locomotives (Paul et al., 2009). Large differences in flow development and drag coefficients were observed between a single wagon and a series of wagons within a train consist (Östh and Krajnović, 2013). Although computational power has increased many of these studies lack experimental data for validation. However, Flynn et al. (2013) compared flow over a container freight train using a Detached Eddy Simulation (DES) to results presented in this study, finding good agreement in general.

2.3 Slipstreams

2.3.1 TSI and EN standards

Slipstreams are created as air is dragged by the movement of a train due to fluid viscosity (Baker et al., 2001). The study of slipstreams is important for understanding possible interactions with objects and people. The European Railway Agency for the Trans-European Rail network set standards for slipstreams in the Technical Specifications for Interoperability (TSI), to allow interoperability throughout the European rail network, such as High Speed 1 (TSI, 2008; CEN, 2009). The TSI report states that a train operating at 200 km/h should not cause slipstream velocities higher than 15.5 m/s at 1.2 m above the platform at a distance 3.0 m from the centre of the track. For open track a train running at 190-249 km/h should not cause velocities exceeding 20.0 m/s at 0.2 m above top of rail and 3.0 m from the centre of the track (TSI, 2008).

TSI methodology for a straight open ballasted track calculates a limit velocity $u_{2\sigma}$. The TSI states tests should be carried out on track where the distance from the top of rail to the cess is 0.75 ± 0.25 m and at least 20 independent measurements taken in ambient wind speeds of less than 2 m/s at least 15 seconds before the train passes (TSI, 2008). In general slipstream measurements should be taken close to the maximum operational line speed V_{max} with a least 50% of measurements within $\pm 5\%$ of V_{max} and 100% within $\pm 10\%$ of V_{max} . The TSI value is calculated for a set whole train passing event, defined as starting 1 second before the train nose and 10 seconds following the train tail, filtered using a 1 second moving average filter (TSI, 2008). The TSI limit velocity $u_{2\sigma}$ is then calculated as (TSI, 2008),

$$u_{2\sigma} = \bar{u} + 2\sigma \quad (2.2)$$

where \bar{u} is the mean value of all resultant air speed measurements in the x - y plane, and σ is the standard deviation.

European codes of practice EN 14067-4 (BSI, 2005) outline limits for aerodynamic loads on trackside structures created by pressure loading amplitudes. The codes are developed from experimental and theoretical work and include methodologies to assess loads either experimentally or by numerical assessment, providing formulae for assessing loads on a range of structures (BSI, 2005).

Slipstream research has predominantly focused on passenger trains in line with development of faster more aerodynamically efficient trains and network upgrades (Raghu-nathan et al., 2002). Indeed, the TSI focuses on trains travelling at speeds of 200km/h plus, much faster than freight speeds of 120km/h. The majority of freight slipstream studies have been conducted in conjunction with passenger studies.

2.3.2 UK standards

UK standards for slipstream velocities have been developed in line with a series of slipstream incidents in the past 40 years. Small studies focussed on measuring maximum slipstream velocities, and not characteristics of flow development, have been carried out in relation to defining appropriate safety guidelines (BR, 1982, 1993a,b). A platform and trackside safety position are defined in UK standards, however maximum permissible slipstream velocities measured at these positions are not defined. The trackside worker safety condition is defined as a distance of 2m from the centre of track for a train speed of less than 45m/s. Studies found at this position passenger trains created a maximum 1 second moving average slipstream velocity of 17m/s 1m above the top of rail (Temple and Johnson, 2008). Similarly the UK ‘yellow line’ platform safety position was introduced as a passenger safety measure following slipstream incidents (BR, 1982). The platform yellow line safety position is defined as 1.5m from the platform edge (2.95m from centre of track) for a passenger train passing at speeds up to 55m/s. Studies showed for passenger trains recorded at this position a maximum 1 second moving average slipstream velocity of 11m/s, measured at 1m above the platform

level, was created (Temple and Johnson, 2008). Other UK slipstream safety measures include warning signs and platform announcements to inform passengers or trackside workers of an approaching train.

2.3.3 Passenger slipstreams

To investigate flows caused by the movement of passenger trains a number of European Union led studies have been undertaken. Projects such as the RAPIDE project (railway aerodynamics of passing interactions with dynamic effects) and AeroTRAIN (aerodynamics within a total regulatory acceptance interoperable network), have been carried out by rail authorities in conjunction with vehicle manufacturers and academic establishments to collect data experimentally and numerically in order to quantify flows (Schulte-Werning et al., 1999; Baker et al., 2001; Temple and Johnson, 2008; Sterling et al., 2008; Gil et al., 2008).

RAPIDE led experimental studies compared both full (Schulte-Werning et al., 1999; Temple and Dalley, 2001) and model scale (Baker et al., 2001) data sets, creating a foundation of knowledge for passenger train slipstream development and the formulation of specific flow regions created within high speed passenger train slipstreams.



Figure 2.1: Deutsche Bahn high speed passenger ICE2 model train at the TRAIN rig facility.

Baker et al. (2001) conducted 1/25th scale moving model experiments using a German high speed passenger ICE2 train at the TRAIN rig facility in Derby, UK. The TRAIN rig is a purpose built testing facility for examining the transient aerodynamics of moving vehicles. The advantage of using a moving model rig over a typical stationary wind

tunnel is the ability to correctly simulate relative motion between the vehicle and the ground/structures or crosswind simulation. The model ICE2 train consisted of a tapered leading and trailing power vehicle and two intermediate carriages separated by inter-carriage gaps, shown in figure 2.1. Total train length was 4.2m (105m at full scale) and measurements were made at a train speed of 32 ± 1 m/s. Slipstream longitudinal (measured in the direction of travel) and lateral (measured from the centre of the track) velocities were measured using hot film anemometers at varying distances from the train side for an open track situation (i.e. no platform). The experiment was repeated twenty times at each measuring position and ensemble averages created. Results showed slipstreams could be divided into four flow regions.

- Upstream and nose region - characterised by an increase in flow velocity before the front of the vehicle leading to a localised velocity peak lasting around 0.1-0.2 seconds duration; generally considered an inviscid region.
- Boundary layer region - highly turbulent region growing along the side of the vehicle. Turbulent gusts within the boundary layer lasting for 0.1 seconds duration.
- Near wake region - a large velocity peak due to turbulent flow and possible vortex shedding lasting 0.15 seconds close to the train, however 0.3-0.4 seconds 20-30m downstream of the train.
- Far wake region - characterised by turbulent flow with shedding vortices induced by the train.

Boundary layers were found to grow faster on train sides than the roof, with equilibrium reached along the first carriage (Baker et al., 2001). Maximum slipstream velocities were found in the near wake. Slipstream velocities increased with train speed and decreased with distance from the train side.

Sterling et al. (2008) cross examined full and model scale ICE2 data recorded as part of the RAPIDE project. Flow regions seen previously were found, however an additional velocity peak was discovered at the train tail. Baker et al. (2001) had concluded flow

accelerations were large at the vehicle nose but small elsewhere. In comparison to full scale data Sterling et al. (2008) showed this result not to hold. The passage of the vehicle nose creates an acceleration and deceleration of the flow. Sterling et al. (2008) showed there is also an acceleration resulting in a velocity peak at the vehicle tail, thought to be caused by vortex shedding, the measuring of which is dependent on the phase. Due to ensemble averaging and phase dependent vortex shedding the tail peak was previously missed. At the train tail, due to shape, either a large separation bubble or two counter rotating vortices extending far into the wake are created (Muld, 2010). Specific design of the train nose or tail can reduce the intensity of vortices (Baker, 2010).

Research focused on key flow regions has allowed an understanding of the fundamental nature of flow within these regions to be developed in recent years (Sanz-Andrés et al., 2003; Jordan et al., 2009; Baker et al., 2012, 2013a,b).

2.3.3.1 Upstream and nose region

The upstream and nose regions are characterised by an increase in flow velocities before the vehicle, reaching a localised peak at the nose. A static pressure fluctuation is observed about the vehicle nose, with a positive then negative peak, before stabilising to zero in the boundary layer region. The magnitude of these peaks is dependent on flow separation at the train nose (Baker et al., 2012). Sanz-Andrés et al. (2003) developed the assumption that flow can be considered as inviscid in the nose region to present an analytical solution for velocity around the vehicle nose using potential flow theory. By modelling the vehicle nose as a simple moving source within a frame of reference about the vehicle, the longitudinal velocity measured by a stationary observer is defined as,

$$u = -\frac{V_{train}A_{ref}}{4\pi} \frac{x}{(x^2 + y^2 + z^2)^{\frac{3}{2}}} \quad (2.3)$$

where x , y and z are distances in the longitudinal, lateral and vertical direction respectively. V_{train} is the train speed and A_{ref} is the vehicle cross-sectional area. Similarly the static pressure coefficient in the nose region can be defined as (Sanz-Andrés et al., 2004),

$$C_p = - \left(\frac{U_{res}}{V_{train}} \right)^2 - \frac{2}{V_{train}^2} \frac{\partial \varphi}{\partial t} \quad (2.4)$$

where the static pressure coefficient C_p is defined as the static pressure p divided by the dynamic pressure ($q = 0.5\rho U_{res}^2$), where U_{res} is the resultant velocity in the horizontal x - y plane. φ is a velocity potential function and ρ is the air density, defined as (TSI, 2008),

$$\rho = \frac{P_{AMB}}{RT_{room}} \quad (2.5)$$

where the gas constant $R = 287\text{J}/(\text{kg K})$ and T_{room} is the temperature measured in Kelvin.

Baker et al. (2012) adopted the assumption of inviscid velocity and pressure fluctuations in the nose region by applying Bernoulli's equation to find a relationship between the coefficient of pressure and normalised slipstream velocities in open air,

$$C_p = 1 - (1 - U)^2 - V^2 - W^2 \quad (2.6)$$

where U , V and W are slipstream velocities in the longitudinal, lateral and vertical directions normalised by train speed V_{train} . Analysing model scale experiment results conducted at the TRAIN rig, using a series of rail vehicles ranging from a high speed passenger Class 390 to a Class 158 two-car multiple unit, Baker et al. (2012) found W was in general small and could be neglected, while U and V are sufficiently similar to assume,

$$C_p \approx 2U \quad (2.7)$$

Considering a wall placed next to the track, using potential flow theory the pressure coefficient can be represented as an image source on the other side of the wall, thus

the coefficient of pressure measured on the wall is defined as,

$$C_p \approx 4U \quad (2.8)$$

These models can be adapted to predict forces on pedestrians and trackside objects. The application of potential flow theory assumes flow is inviscid and irrotational. This dictates no flow separation at the train nose, which in reality is unrealistic, especially in relation to freight vehicles.

2.3.3.2 Boundary layer region

Boundary layer growth is observed between the nose and tail region of the train. In general boundary layer thickness is related to train nose shape, number of carriages/inter-carriage gaps and surface roughness (Baker et al., 2013a). However, Baker et al. (2001) illustrated for a high speed passenger train an equilibrium state of boundary layer stabilisation is reached along the first carriage. Boundary layer flow is characterised as highly turbulent and three-dimensional, featuring pressure gradients around changes in vehicle geometry. CFD studies have shown that turbulence is generated in geometrically rough regions including bogies (Sterling et al., 2008), inter-carriage gaps (Hemida et al., 2010) and upper body corners/roof edges (Diedrichs et al., 2004). Turbulence generated at bogie height moves up the vehicle side, impinging with flow above the train roof (Brockie and Baker, 1990). Thus, boundary layer growth is seen to occur faster at train side in comparison to above the roof (Baker et al., 2001).

Analysis techniques adopted for characterising flow within the boundary layer region are generally based on slipstream velocities. Plotting velocities at increasing distance from the train side depicts boundary layer profiles (Baker et al., 2001). Integrating velocities across the boundary layer profile with respect to the vehicle reference system

calculates the displacement thickness,

$$\delta^* = \int_{y=0}^{\infty} \left(1 - \frac{U}{U_{\infty}}\right) dy \quad (2.9)$$

where U_{∞} is the free stream velocity outside the boundary layer normalised by train speed V_{train} . The displacement thickness measures the amount by which the mass carried in the boundary layer lies below the uniform flow; thus the distance by which a wall would have to be displaced to maintain the same mean flow rate in the absence of a boundary layer (Durbin and Medic, 2007; Kundu and Cohen, 2010).

Spatial variation between a moving train and the air surrounding that body is called shear; shear produces turbulence (Davidson, 2004). In a turbulent region velocity can be thought of as composed of two parts; an average velocity component and a component representing fluctuations about the mean. Turbulence intensity is a measure of the strength of the turbulent fluctuations about the mean, defined as the ratio of the standard deviation of the ensemble velocity to the ensemble mean (Davidson, 2004).

$$I = \frac{\sigma_u(x)}{(1 - (U(x)))} \quad (2.10)$$

where $U(x)$ is the longitudinal component of slipstream velocity normalised by train speed V_{train} (defined in chapter 4). Sterling et al. (2008) found that flow around a freight train is more distorted with higher normalised velocities and turbulence levels than for a passenger train. Comparison of trackside and platform data showed boundary layers form rapidly at trackside with higher turbulence intensities, due to exposed bogies (Sterling et al., 2008). It is clear that for geometrically bluff vehicles, such as freight train, increases in slipstream velocities create a thicker boundary layer with an increasing displacement thickness, with regions of higher turbulence intensity.

2.3.3.3 Tail and wake region

For an aerodynamically shaped passenger train the highest transient slipstream velocities occur in the tail region before decaying into the wake (Sterling et al., 2008; Baker et al., 2013a). A static pressure fluctuation similar to the nose region occurs at the train tail, but reversed with a negative followed by a positive peak. Generally peak static pressure magnitudes are lower than the nose region due to differences in the flow separation. As discussed, at the train tail due to vehicle shape, either a large separation bubble or two counter rotating vortices extending far into the wake are created (Muld, 2010). Baker (2001) found by analysing the Strouhal number that flow structures could be identified in the wake region. The Strouhal number is a dimensionless number to describe oscillating flow mechanisms and can be applied to a vortex shedding frequency f ,

$$St = \frac{f L_{ref}}{V_{train}} \quad (2.11)$$

where L_{ref} is a characteristic length. Strouhal numbers calculated in the train wake were between 0.05 and 0.4 (Baker, 2010). Baker (2001) identified separated shear layers created by boundary layer detachment and longitudinal helical vortices shed with a characterised frequency, as shown by Sterling et al. (2008). Flow structures influencing wake patterns are dependent on tail shape and flow properties of the boundary layer region; specific train design can reduce the intensity of vortices (Baker, 2010).

Baker et al. (2013a) observed similarity of velocity decay in the far wake region between different passenger train types. By modelling velocity decay using a power law type equation,

$$U = a(x)^b \quad (2.12)$$

where x is the longitudinal position of the train, Baker et al. (2013a) found for passenger trains a common power of $b = -0.5$ could be applied.

2.3.4 Freight Slipstreams

Freight slipstream studies have tended to be conducted by rail authorities following incidents. These studies focus on maximum slipstream velocities, not characteristics of slipstream development, in relation to defining appropriate safety guidelines (BR, 1982, 1993a,b). In 2002 English, Welsh and Scottish Railway (EWS) commissioned a study into freight slipstreams after requesting an increase in operational line speeds from 120km/h to 145km/h. Tests showed maximum velocities in the slipstream increased with train speed and length (BR, 2002).

The British Rail studies set research foundations, however there is little analysis of slipstream development or flow structures. These issues have been approached within high speed passenger train research and characteristic flow regions defined; some of these studies have included freight data (Temple and Dalley, 2001; Sterling et al., 2008).

In 2001 a series of full scale container freight tests were conducted on the West Coast Mainline, UK. The train consisted of a British Rail Class 92 locomotive with thirty four flatbed wagons, loaded with forty six containers in a configuration with a sixty percent loading efficiency (Temple and Dalley, 2001). All containers were 2.438m wide, 2.59m high, and 6.096m long except for ten wagons at the rear loaded with 12.192m long containers. The train was travelling at 120km/h (33.6m/s) and had a total length of 703.5m. Slipstream velocities were recorded with sonic anemometers at trackside (2m from the centre of track and 1m above the rail head) and platform level (3m from the centre of track and 2.25m above the rail head) (Temple and Dalley, 2001).

Analysis found flow around a freight train is more distorted and boundary layers develop faster, with higher normalised velocities and turbulence levels, than for a passenger train (Temple and Dalley, 2001). Maximum velocities were found in the boundary layer region not the near wake as with a passenger train. No velocity peak is observed at the rear of the freight train, unlike a high speed passenger train (Sterling et al., 2008),

hypothesised to be related to the difference in vehicle shape between the aerodynamically efficient tail of a passenger train and the shear end of a container (Baker, 2010). Comparison of trackside and platform data showed boundary layers form rapidly at trackside due to exposed bogies whereas at platform level slipstream velocities increase gradually to a constant level, due to platform shielding effects (Sterling et al., 2008).

In 2012 full scale freight measurements were collected as part of a University of Birmingham/Network Rail project. The experiment was carried out at an open air trackside position in Uffington, Oxfordshire. The freight results from this project are presented within this study. The project aim was take measurements to assess whether safety limits are breached for trackside workers working in a High Output Plant System (HOPS), for the installation of overhead line equipment (OLE), when a train passes at full operational line speeds (Baker and Quinn, 2012). The report found freight trains created higher slipstream velocity and pressure magnitudes than passenger trains, however trackside worker safety limits were not broken for a HOPS deck height of 2.95m above the cess (Baker and Quinn, 2012). It was, however, suggested that further experiments should be undertaken to assess the possibility of slipstreams causing movement of equipment placed on the HOPS deck (Baker and Quinn, 2012). The full scale Uffington data presented in Baker and Quinn (2012) will be analysed further in chapter 5, to validate model scale experimental data and analyse the suitability of the TSI methodology in relation to a container freight train.

2.3.5 Associated aerodynamics

Section 2.3.4 discussed previous studies conducted in relation to freight train slipstream development. This section will focus on associated fields of research which can be adapted for the purpose of freight train aerodynamics. This section will include research of fluid flow over surface mounted cuboids and buildings within an urban street canyon.

2.3.5.1 Bluff Body Aerodynamics

Container transportation is a growing sector of rail freight, and one which poses many aerodynamic issues due to the characteristic bluff shape. The study of flow over cuboid shapes, either surface or non-surface mounted can give indications to flows created over containers attached to a flatbed wagon. The study of cubes mounted closely in a line can be considered a similar problem aerodynamically to a series of containers loaded onto the flatbed wagons of a freight train. The studies discussed span a large range in Reynolds number $Re=10^4$ to $Re=10^6$; considered to be highly turbulent flow. The range includes the Reynolds numbers of both the model and full scale experimental data presented in this study.

CFD studies of single surface mounted cubes indicate upstream of the object there is a horseshoe vortex, affecting flow around the object. Flow separation emanates from leading container edges, creating separation regions at the cube sides (Castro and Robins, 1977; Paterson and Apelt, 1990; Shah and Ferziger, 1997; Zajackowski and Peltier, 2011). Behind the cube there is a region of recirculation and reattachment (Zajackowski and Peltier, 2011). Drag on the object is caused by a difference in pressure at the front and rear faces; little viscous drag is formed at cube side due to reversed flow (Shah and Ferziger, 1997).

Developing the situation further to include multiple objects in a line, Stoesser et al. (2003) concluded that flow separated in front of the first cube creating a horse shoe vortex, which is displaced by flow separation at the cube sides and a series of horse-shoe vortices in front of the following cubes. Separation also occurs at cube corners and edges, however, reattachment occurs soon after. Behind each cube there is a recirculation region, with an arch vortex close to the object wall (Castro and Robins, 1977; Stoesser et al., 2003).

2.3.5.2 Building Aerodynamics

For container freight trains with a high loading efficiency, generally, the space between loaded containers is smaller than the height of a loaded container. This situation is similar to an urban canyon, in which the size of a street separating two buildings is generally less than or equal to the height of the buildings. Wind and pollution dispersion within an urban setting can be modelled using CFD, inputting experimental data from weather stations and pollution characteristics (Ahmad et al., 2005). The situation is modelled similarly to a series of surface mounted cubes in a line. If the gap between buildings is small, the wakes behind buildings are disrupted and eddies can form in the space. If the object height is greater than the gap between two objects a circulatory vortex is established inside the space between objects, due to the shear layer at roof level. This creates a ‘skimming flow’ over the objects (Oke, 1988).

For trains with a high container loading efficiency the space between containers will be less than the height of a container. This can be considered like a urban canyon situation with ‘skimming flow’. Within the inter-container region there will be a series of trapped vortices and large pressure differences to the outside flow. For trains with a low container loading efficiency in front of each container a horseshoe vortex will be created, with a recirculation region behind the container. The flow will separate off leading edges and corners of the container, reattaching further downstream. A large pressure difference will be created between the leading and trailing face of the container.

2.3.6 Summary of slipstream research

Through examining existing freight slipstream research studies it has been possible to draw together previous knowledge to assess how the field of freight train aerodynamics would most benefit from a focused model scale experimental study. It is clear that previous freight studies have tended to focus on drag reduction in relation to minimising

fuel consumption. Although the Davis approximation to bluff body drag includes an aerodynamic term, the field of slipstream research has focused on high speed passenger trains, in relation to improved rail networks and increasing train speeds. Freight slipstream research has been undertaken, but generally in small studies focused on defining new safety standards following an incident (Temple and Johnson, 2008) or included in passenger studies as a point of reference and comparison (Sterling et al., 2008). As discussed, the development of a high speed passenger train slipstream has been the focus of a number of studies, aiming to define key flow characteristics (Baker et al., 2001; Pope, 2006; Sterling et al., 2008; Baker et al., 2013b). Results show the flow can be divided into a number of regions along the train, however individual results were shown to be highly variable, as flow is dominated by large scale turbulent structures. Results from these studies have led to the development of the Technical Specifications for Interoperability (TSI); a set of laws including methodologies of how to measure train aerodynamics and providing limit values for slipstream velocities, allowing for interoperability of trains across national boundaries in Europe (TSI, 2008). Although some freight research has been included in these studies, a thorough study of freight slipstream development and appropriate guidelines written in relation to rail freight is yet to be undertaken.

The literature review indicates that a focused freight study is needed to characterise the slipstream development for a common freight type, chosen to be container freight in this study. Previous freight studies have tended to include numerous freight types with minimal ensemble sizes. This indicates that it is important to focus on a number of key container loading configurations to create data sets with a suitable ensemble size to analyse the effects of container loading configuration on the flow development. The review indicates that there is a gap in the research in understanding how freight trains fit within the TSI methodology. Constructing a suitable freight experimental study will enable an analysis using the TSI methodology, to assess the suitability of the methodology in relation to freight slipstream development.

2.4 Crosswinds

The investigation of crosswind effects on rail vehicles has been the subject of a number of studies concerned with the inherent risks of vehicle overturning and track instability (Gawthorpe, 1994; Andersson et al., 2004; Alam and Watkins, 2007a,b; Baker and Sterling, 2009). A train will overturn when the contribution of the aerodynamic rolling moment about the leeward rail generated by a crosswind is large enough to overcome the restoring moment associated with the train weight (Gawthorpe, 1994; RSSB, 2009). Other effects include loss of ride quality through enhanced suspension vibrations (Cooper, 1984) and pantograph displacement due to wind induced lateral deflection of a train (Andersson et al., 2004; Baker and Sterling, 2009).

Crosswind research has predominantly focused on passenger trains due to the possible impact of loss of life if a vehicle were to overturn and, as with slipstream studies, in line with development of faster more aerodynamically efficient trains and network upgrades (Raghunathan et al., 2002). However, in light of the recent container freight crosswind incidents there have been series of investigative national safety reports commissioned and published (RAIB, 2009; ATSB, 2008), leading to fundamental research projects focused on freight in crosswind conditions (Alam and Watkins, 2007a; Hemida and Baker, 2010; RSSB, 2012). In addition, the study of past crosswind related accidents can allow new methods of prevention to be considered (Gawthorpe, 1994).

2.4.1 Atmospheric boundary layers

The study of wind induced forces on a vehicle is dependent on an understanding of the natural wind to which the vehicle is exposed. An atmospheric boundary layer (ABL) is created in lower layers of the earth's atmosphere by friction developing between a mass of moving air and the earth's surface (Garratt, 1994). The general ABL formation can be estimated as a logarithmic velocity profile, as shown in figure 2.2. Flow is characterised by a shear in the moving air, caused by the friction exerted between the

wind and earth's surface, creating a turbulent flow with vertical and horizontal velocity components induced by the earth's topography. The wind speed has zero velocity at the ground, due to the no slip condition, and an increasing wind velocity with increased height above the ground (Garratt, 1994).

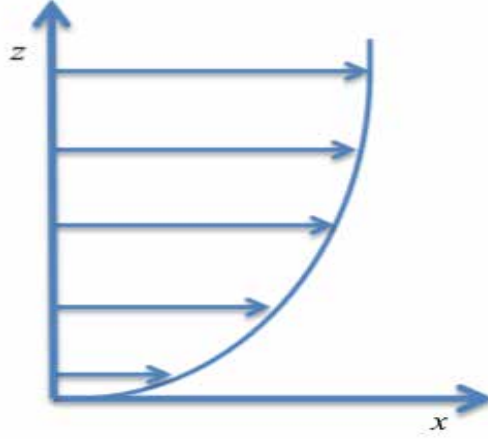


Figure 2.2: A generic atmospheric boundary layer profile.

The instantaneous wind velocity field can be considered as a composition of the mean flow and a series of turbulent fluctuations. In general a series of assumptions are made to apply this decomposition and define the frame of reference adopted for considering a crosswind in this study (Dorigatti, 2013):

1. Flow is stationary within a sufficiently long time interval.
2. The mean wind velocity depends only on the height above the ground.
3. Wind direction does not change over small heights.

The instantaneous wind velocity field \mathbf{V} at a time t relative to a height z above the ground can be defined as (George, 2004; Dorigatti, 2013),

$$\mathbf{V}(x, y, z, t) = \overline{u_{wind}}(z)\mathbf{i} + [u'_{wind}(x, y, z, t)\mathbf{i} + v'_{wind}(x, y, z, t)\mathbf{j} + w'_{wind}(x, y, z, t)\mathbf{k}] \quad (2.13)$$

where \mathbf{i} , \mathbf{j} , \mathbf{k} are unit vectors associated with flow directions x , y and z respectively, as defined in figure 2.3. $\overline{u_{wind}}$ is the mean flow in the streamwise flow direction and

u'_{wind} , v'_{wind} and w'_{wind} are turbulent fluctuations relating to flow directions x , y and z respectively. The mean wind speed is only dependent on height z . Considering the logarithmic wind profile, the mean flow can be approximated as (Blackadar and Tennekes, 1968),

$$\overline{u_{wind}}(z) = \frac{u_*}{\kappa} \ln \left(\frac{z}{z_0} \right) \quad (2.14)$$

where u_* is the surface friction velocity, κ is the Von Kármán constant (~ 0.41) and z_0 the surface roughness length, dependent on topography. Turbulent fluctuations, however, depend on time t and position in a three dimensional space (x, y, z) , as shown in equation 2.13. By the process of Reynolds decomposition the mean of turbulent fluctuations is zero (Reynolds, 1895). A similar definition to equation 2.10, for turbulence intensity relating to velocity components of the wind, can be defined as the ratio of the standard deviation of fluctuating velocity components to the mean wind speed. Considering a natural wind as a horizontally homogeneous flow allows the turbulence intensities for each component of velocity to be defined as,

$$I_u(z) = \frac{\sigma_u(z)}{\overline{u_{wind}}(z)} \quad (2.15)$$

$$I_v(z) = \frac{\sigma_v(z)}{\overline{u_{wind}}(z)} \quad (2.16)$$

$$I_w(z) = \frac{\sigma_w(z)}{\overline{u_{wind}}(z)} \quad (2.17)$$

Turbulence intensities are dependent on surface topography and decrease as height above a surface is increased. Natural winds considered for this study generally have a turbulence intensity of 10%-30%.

In Dorigatti (2013) the development of boundary layer theory is taken further for the purpose of designing the crosswind simulator utilised in this study; defining how turbulent length scales and the power spectral density of a flow are calculated. These quantities are important when modelling a crosswind flow to ensure the simulated wind has relevant length scales and spectral components in relation to the flow which it is

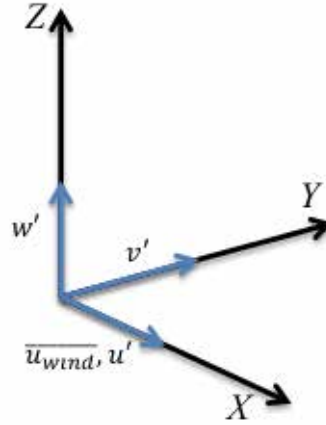


Figure 2.3: Reference coordinate system for an onset wind.

modelling. As the crosswind simulator is used as a tool within this study and not developed further, these definitions are not redefined here.

2.4.2 Crosswind relative to a moving vehicle

For a vehicle moving through a natural wind the relative wind velocity to the vehicle is defined as the resultant combination of the onset wind velocity and the vehicle speed. Figure 2.4 illustrates a train moving through a natural wind. The resultant wind velocity is dependent on the natural wind speed, wind angle relative to the train, and the train speed. The resultant wind velocity V_{rel} can be defined as,

$$V_{rel} = \sqrt{[\overline{u_{wind}}(z)\sin\beta]^2 + [V_{train} + \overline{u_{wind}}(z)\cos\beta]^2} \quad (2.18)$$

with a resultant yaw angle,

$$\theta = \arctan\left(\frac{\overline{u_{wind}}(z)\sin\beta}{V_{rel} + \overline{u_{wind}}(z)\cos\beta}\right) \quad (2.19)$$

where β is the natural wind angle. The natural onset wind velocity u_{wind} is measured in the undisturbed flow upstream of the vehicle, to negate any influence from the

vehicle slipstream. In previous railway applications the reference onset wind velocity is measured at a reference height of 3m above the ground (Baker and Sterling, 2009; RSSB, 2009, 2012; Dorigatti, 2013), a convention also adopted for this study.

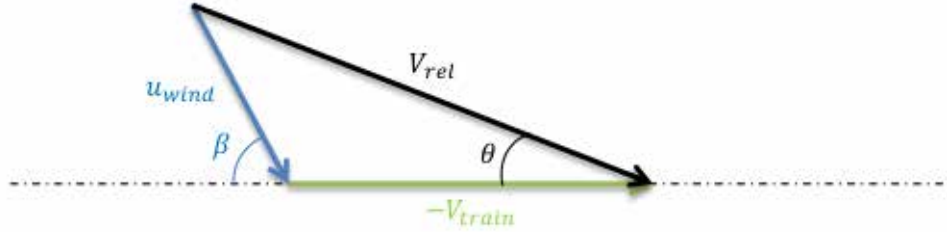
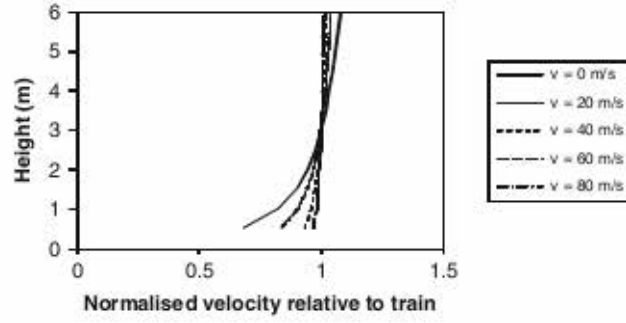


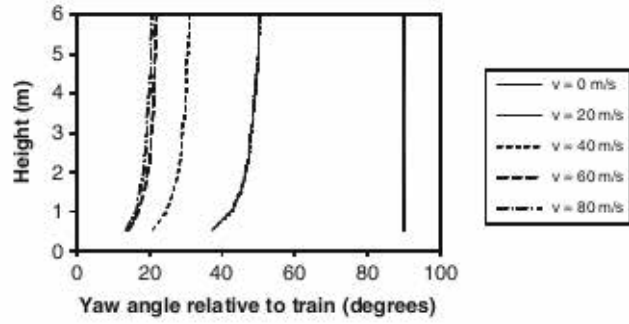
Figure 2.4: Resultant wind velocity diagram with respect to a moving train.

As discussed, an atmospheric boundary layer can be considered as a logarithmic profile close to the earth's surface. Considering equations 2.14 and 2.18, the resultant wind velocity \bar{V}_{rel} as a function of z is a skewed logarithmic profile. Baker (2010) carried out a study to assess the effect of a natural wind in relation to a moving train over flat ground ($z_0 = 0.03\text{m}$) with varying train speeds. By assuming a wind angle normal to the train track and a logarithmic wind profile with wind speed 20m/s measured 3m above the ground Baker (2010) calculated the resultant wind velocity, yaw angle and turbulence intensity profiles, shown in figure 2.5. Results show at low train speeds the velocity profile has a typical ABL form with a large degree of variation in velocity and high turbulence intensity across the train height ($\sim 4\text{m}$). Conversely as train speed is increased the velocity and yaw angle profiles become uniform across the vehicle height, exhibiting low turbulence intensity (Baker, 2010). In relation to modelling a freight train travelling at a relatively low train speed, in comparison to a passenger train, these results imply that tests should not be carried out in a low turbulence wind tunnel, and velocity shear should be simulated.

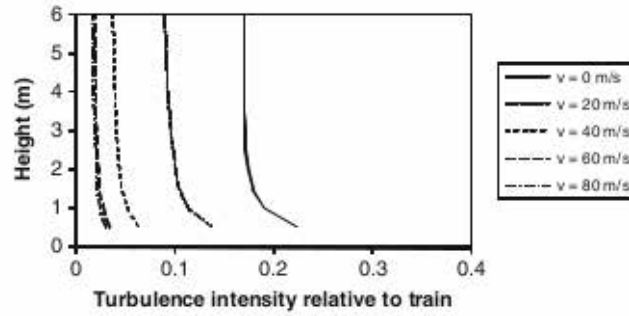
Dorigatti (2013) discussed the influence of a train travelling with a varying train speed through a natural wind with varying wind speed and angle. Many crosswind studies use a fixed wind speed and angle relative to a stationary train (Alam and Watkins,



(a) Normalised relative wind velocity



(b) Relative yaw angle



(c) Turbulence intensity

Figure 2.5: A vertical profile of the mean wind relative to a moving vehicle for a wind speed $\overline{u_{wind}} = 20\text{m/s}$ measured at a height of 3m, at a wind angle of $\beta = 90^\circ$ for a surface roughness length of $z_0 = 0.03\text{m}$. Figure a) shows the normalised relative wind velocity, b) relative yaw angle and c) turbulence intensity relative to the train (Baker, 2010)

2007b; Baker and Sterling, 2009). Applying the assumptions of a wind angle normal to the track and wind measurements taken at a height of 3m above the ground, Dorigatti (2013) perturbed equation 2.18 (as shown in figure 2.6) to assess the influence of inhomogeneity within the resultant wind velocity variables. Sensitivity analysis showed long time scale fluctuations in the resultant wind velocity had an influence on the forces exerted on the train. Introducing a modified methodology, to account for a spanwise varying onset reference wind velocity and a changing train speed, gave comparable results to the quasi-steady methodology but reduced the influence of long time scale fluctuations. The resultant wind velocity defined in equation 2.18 is therefore redefined for a inhomogeneous flow in a horizontal plane as (Dorigatti, 2013),

$$V_{rel} = \sqrt{\overline{u_{wind}}^2 + [V_{train} - \overline{v_{wind}}]^2} \quad (2.20)$$

where v_{wind} is the natural wind velocity in the lateral direction.

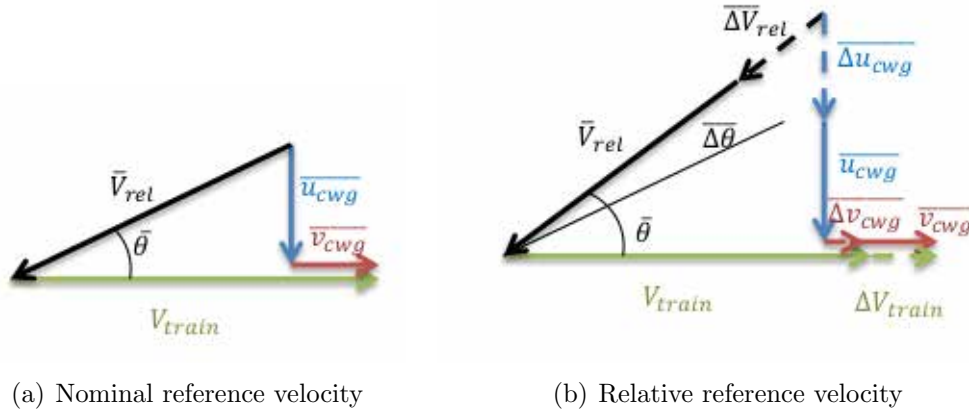


Figure 2.6: A vector diagram to show mean wind velocity relative to a moving vehicle for a) a nominal mean wind b) relative mean wind fluctuations¹.

The influence of a vehicle slipstream when coupled with a natural wind can also increase the resultant velocity subjected to the vehicle. Following container freight crosswind

¹In figure 2.6 and equation 2.20 the v_{wind} component is included to account for variations in the lateral component of the onset wind, see chapter 7. In figure 2.6(b) the variations in reference velocity components can be both larger and smaller than the mean values.

incidents (RAIB, 2009), Hemida and Baker (2010) conducted a CFD study of a 1/20th scale flatbed wagon loaded with a container, in the middle of a multi-wagon freight train subjected to a crosswind at a 90° yaw angle, with boundary conditions to simulate motion along a track. Hemida and Baker (2010) found vortex sheets shedding from the wagon bottom and the container roof in the leeward flow field. A comparison of a stationary and a moving vehicle test case showed little difference in the velocity distribution over the wagon, or the time average side force. However, significant effects were observed in the wake region to the time averaged pressure and subsequently the time averaged lift force.

2.4.3 Aerodynamic loads on vehicles

As a train moves through a natural wind it is subjected to a surface pressure distribution creating a series of steady and unsteady aerodynamic forces and moments acting on the vehicle (Baker, 2010). A number of studies have analysed vehicle surface pressure distributions to calculate, by discrete integration, the forces acting on a vehicle travelling through a crosswind (Sanquer et al., 2004; Quinn et al., 2007; Dorigatti, 2013). The surface pressure distribution can be presented in terms of a series of non-dimensionalised pressure coefficients,

$$C_P = \frac{P - P_0}{\frac{1}{2}\rho V_{rel}^2} \quad (2.21)$$

where P is the actual surface pressure at any point on the vehicle and P_0 is the static reference pressure. Air density ρ is calculated as in equation 2.5.

Considering figure 2.3 it is possible to resolve the aerodynamic loads acting on the

vehicle by defining forces and moments with respect to the vehicle coordinate system,

$$F_\xi = \frac{1}{2} C_\xi \rho A_{ref} V_{rel}^2 \quad \text{where } \xi = X, Y, Z \quad (2.22)$$

$$M_\xi = \frac{1}{2} C_{M_\xi} \rho A_{ref} L_{ref} V_{rel}^2 \quad \text{where } \xi = X, Y, Z \quad (2.23)$$

where A_{ref} and L_{ref} are the vehicle reference area and reference length, generally taken for train applications to be the nominal side area of one coach and nominal height (Baker and Sterling, 2009). C_ξ and C_{M_ξ} are the non-dimensional coefficients defined for each component ($\xi = X, Y, Z$) of forces and moments respectively.

Generally in vehicle aerodynamics the lateral, vertical and rolling moment forces (side, lift and roll moments respectively) are used to analyse the risk of possible wind induced vehicle overturning (Sanquer et al., 2004; Quinn et al., 2007; Baker and Sterling, 2009; RSSB, 2009, 2012). Non-dimensionalised aerodynamic coefficients for the side and lift forces, and the rolling moment about the centre of track (x-axis in figure 2.4) and leeward rail, are given as (Dorigatti, 2013),

$$C_Y = \frac{F_Y}{\frac{1}{2} \rho V_{rel}^2 A_{ref}} \quad (2.24)$$

$$C_Z = \frac{F_Z}{\frac{1}{2} \rho V_{rel}^2 A_{ref}} \quad (2.25)$$

$$C_{M_X} = \frac{M_X}{\frac{1}{2} \rho V_{rel}^2 A_{ref} L_{ref}} \quad (2.26)$$

$$C_{M_{X,lee}} = \frac{M_{X,lee}}{\frac{1}{2} \rho V_{rel}^2 A_{ref} L_{ref}} \quad (2.27)$$

where F_Y , F_Z are side and lift forces respectively and M_X , $M_{X,lee}$ are rolling moment forces about the x-axis and leeward rail respectively.

Sanquer et al. (2004) and Quinn et al. (2007) developed a method to estimate relative non-dimensional force coefficients through integrating surface pressure coefficients on a discretised geometry of a vehicle surface. Discretised areas were formed by creating a rectangle centred on each surface pressure measuring point, extending halfway to

neighbouring measuring point or to the vehicle edges. The overall load coefficients are defined as (Quinn et al., 2007; Dorigatti, 2013),

$$C_Y = \frac{\sum_i \overline{C_{P_{ij}}} A_{ij} (\mathbf{n}_{ij} \cdot \mathbf{y})}{A_{ref}} \quad (2.28)$$

$$C_Z = \frac{\sum_i \overline{C_{P_{ij}}} A_{ij} (\mathbf{n}_{ij} \cdot \mathbf{z})}{A_{ref}} \quad (2.29)$$

$$C_{M_X} = \frac{\sum_i \overline{C_{P_{ij}}} A_{ij} \|\mathbf{d}_{ij} \times \mathbf{n}_{ij}\|}{A_{ref} H_{ref}} \mathbf{x} \quad (2.30)$$

$$C_{M_{X,lee}} = \frac{\sum_i \overline{C_{P_{ij}}} A_{ij} \|\tilde{\mathbf{d}}_{ij} \times \mathbf{n}_{ij}\|}{A_{ref} H_{ref}} \mathbf{x} \quad (2.31)$$

where $\overline{C_{P_{ij}}}$ is the mean ensemble pressure coefficient for each pressure measuring point ij , associated with discretised area A_{ij} . \mathbf{n}_{ij} is the normal unit vector associated with discretised area A_{ij} (directed inwards into the body), and \mathbf{x} , \mathbf{y} and \mathbf{z} are the unit vectors associated with axes X , Y and Z (Dorigatti, 2013). \mathbf{d}_{ij} and $\tilde{\mathbf{d}}_{ij}$ are vectors perpendicular to the longitudinal axis X and leeward rail, directed from each measuring point on the vehicle surface (Dorigatti, 2013).

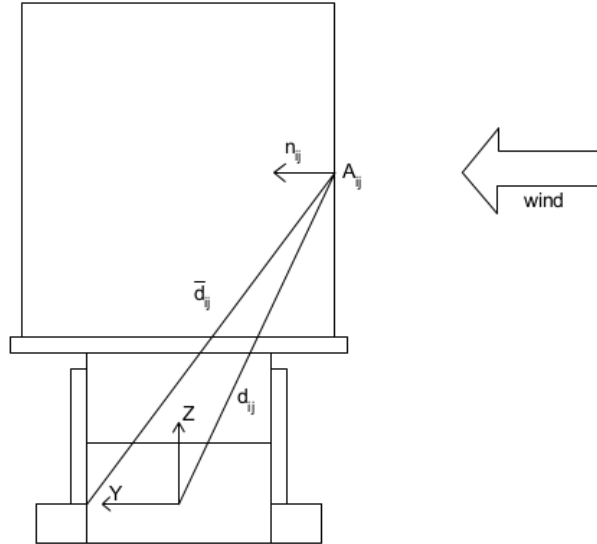


Figure 2.7: The reference system used for calculating load coefficients on the discretised container surface.

Many freight trains are composed of containers or other objects loaded onto flatbed or sunken floor wagons. Loads are usually attached by the object weight and hinged

spigots. Studies on crosswind effects for freight tend to focus on container freight, considered the highest risk due to the relatively light weight nature when empty or tare (Peters, 1993; Alam and Watkins, 2007b; Hemida and Baker, 2010). Peters (1993) undertook a study for the German railway system (Deutsche Bahn) in relation to proposed speed increases, to 200km/h, for freight trains. Drag, side and lift forces were calculated for varying yaw angles (0° to 90° in increments of 10°) using a 1/7th scale model of a 13.9m flatbed wagon loaded with a 12.192m container in a wind tunnel. As discussed, increased train speeds enhance the resultant crosswind, which in turn affects the forces measured on train (Peters, 1993; Gawthorpe, 1994). It was shown that all absolute forces and moments acting on a container increased continuously with Reynolds number (Peters, 1993).

2.4.4 Suitability of a vehicle travelling in crosswind conditions

2.4.4.1 TSI and EN standards

Leading European transport authorities introduced projects, such as Aerodynamics in Open Air (AOA), to develop methods to assess safety risks for trains and track infrastructure in crosswind conditions, by determining aerodynamic forces and moments (Baker and Sterling, 2009). The European Railway Agency for the Trans-European Rail network set TSI guidelines on crosswind safety (TSI, 2008; CEN, 2009). The EU methodology for assessing crosswind stability is presented in terms of a Class 1 high speed train; defined as rolling stock having a maximum speed equal to or greater than 250km/h. To meet TSI crosswind requirements a comparison of a vehicles characteristic wind curve (CWC), which describes the critical wind conditions for wheel unloading for the most wind sensitive carriage of a train, and the characteristic reference wind curves (CRWC), specified by the TSI methodology, is calculated (TSI, 2008). If the CWC is equal or higher than the CRWC then a train is deemed acceptable in terms of crosswind stability.

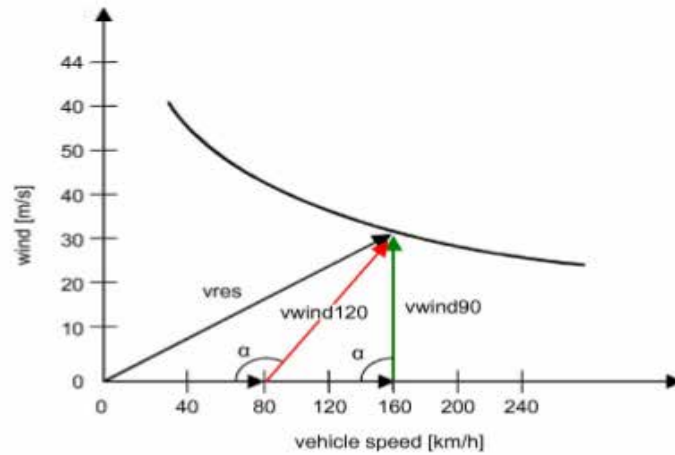


Figure 2.8: Generic characteristic wind curve (CWC) to consider yaw angle and resultant wind velocity (TSI, 2008).

The CWC relates train speed and wind speed, as shown in figure 2.8. Therefore, given a specific train speed the CWC can be used to calculate the ‘maximum natural wind speed that the train can withstand before a characteristic limit for wheel unloading is exceeded’ (TSI, 2008). The characteristic limit is specified as 90% wheel unloading occurring at any bogie. The CWC is calculated by firstly undertaking a series of model scale wind tunnel experiments to measure forces and moments on the vehicle subject to a series of yaw angles (from 0° to 70° in 5° steps). The model should be modelled accurately, including all key vehicle features and mounted on a five component dynamometer balance for an open air and embankment setup, modelled with a twin track and ballast shoulder (TSI, 2008). The onset wind velocity is modelled as a ‘Chinese hat’ scenario (figure 2.9), a time invariant gust wind profile. The Chinese hat is used as an approximation to a turbulent natural wind in the proximity of a local maximum velocity peak (TSI, 2008).

The vehicle dynamics are modelled using a 3D time dependent multi-body numerical simulation (MBS) to reproduce train behaviour under crosswind effects. The simulation models train body, bogies and wheel sets, including masses, inertias and centre of gravity. Suspension and wheel contact dynamic characteristics are also modelled but track irregularities are not. The MBS is validated through full scale on track data.

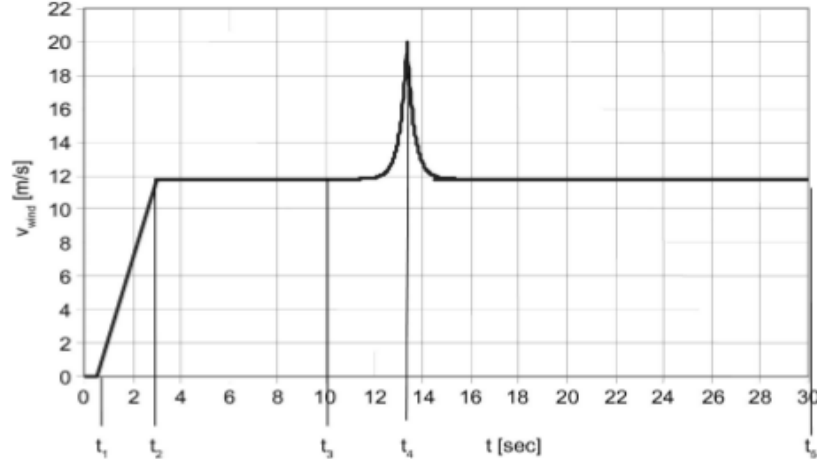


Figure 2.9: Generic time history of wind speed for a Chinese hat wind scenario (TSI, 2008).

The MBS is used to calculate forces and moments (TSI, 2008),

$$F_{\xi}(t) = \frac{1}{2} \overline{C}_{\xi}(\theta(t)) \rho A_{ref} V_{rel}^2(t) \quad (2.32)$$

$$M_{\xi}(t) = \frac{1}{2} \overline{C}_{\xi}(\theta(t)) \rho A_{ref} H_{ref} V_{rel}^2(t) \quad (2.33)$$

where $\xi = X, Y, Z$ and resultant velocity and yaw angle are respectively,

$$V_{rel} = \sqrt{[\overline{u}_{wind}(t) \sin \beta]^2 + [V_{train} + \overline{u}_{wind}(t) \cos \beta]^2} \quad (2.34)$$

$$\theta(t) = \arctan \left[\frac{\overline{u}_{wind}(t) \sin \beta}{V_{train} + \overline{u}_{wind}(t) \cos \beta} \right] \quad (2.35)$$

The coefficient terms $\overline{C}_{\xi}(\theta(t))$ are the force and moment coefficients calculated by the model scale wind tunnel experiments. The MBS calculated forces and moments are then used to calculate a set of Q -forces at each wheel, where Q is the vertical force of the wheel on the rail. By defining a maximum value for Q for a specific train it is possible to calculate a maximum train speed for each wind speed and wind angle, thus creating a CWC to compare against the CRWC.

Guidelines state limiting values and corresponding methods for Class 1 tilting trains and Class 2 trains (defined as rolling stock having a maximum speed of at least 190km/h

but less than 250 km/h) is an open issue. If a train does not meet standards set by the TSI then a series of proofing tests are needed to ascertain crosswind safety on a specific route. The UK maximum freight line speed is 120km/h, falling below the limits defined in the TSI methodology. Baker (2013) has questioned the TSI methodology, highlighting inconsistencies and inadequacies in the approach adopted in relation to the level of complexity and uncertainties associated to calculation variables.

2.4.4.2 UK standards

The UK equivalent standard GM/RT 2142 (RSSB, 2009), in combination with the code of practice GC/RT 5521 (RSSB, 2001) and recommendations in GM/RC 2542 (RSSB, 2012) give guidelines and limiting values for freight trains. The assessment of a train's crosswind stability calculates the intrinsic roll over wind speed, defined as 'the wind speed which is just sufficient to cause 100% unloading of the wheels on the windward side of the vehicle, when the vehicle is running in its tare condition at its maximum design operating speed on straight track' (RSSB, 2009). The intrinsic roll over wind speed for a train should not be less than:

- a) 36.5m/s for vehicles designed to carry people, including passengers and crew.
- b) 30.8m/s for freight and other vehicles not designed to carry people.

The limit value is a reference wind speed, not a maximum wind speed, for a straight track situation, ensuring that a vehicle is safe to operate in UK prevailing wind conditions (RSSB, 2009). The standard provides different methods of calculation for both passenger and freight vehicles; subsequently only the freight calculation will be considered for this study. RSSB (2009) states the reference freight vehicle as a freightliner loaded with empty containers; chosen because of the relative light weight per unit side area and safe history of operation over exposed routes in the UK. RSSB (2012) recommended a change to the reference vehicle to the FEA-B flatbed wagon loaded with a 12.192m and 6.096m container. Recommendations to change the limit value to 26.7

m/s for freight and other vehicles not designed to carry people were made following a series of wind tunnel experiments using the new adopted vehicle and a HYA coal hopper wagon (RSSB, 2012).

The intrinsic roll over wind speed is calculated by modelling the train as a two dimensional (three mass) system considering the point at which instability occurs for resultant yaw angles in the range $\theta = 10^\circ$ to 40° ,

$$M_{over} = M_R \quad (2.36)$$

where M_{over} denotes overturning moment and M_R the restoring moment, both taken about the leeward rail. The restoring moment is calculated with respect to vehicle weight, taking into account vehicle mass and the moment due to body lateral and roll displacements, created by movement in the suspension system. The overturning moment is calculated as (RSSB, 2009),

$$M_{over} = M_{X,lee}(\theta) = \frac{1}{2} C_{Mx,lee}(\theta) \rho A_{ref} H_{ref} V_{rel}^2 \quad (2.37)$$

The overturning condition in equation 2.37 can be rearranged to determine the resultant wind speed relative to the train,

$$V_{rel} = \sqrt{\frac{M_R}{\frac{1}{2} C_{Mx,lee}(\theta) \rho A_{ref} H_{ref}}} \quad (2.38)$$

Thus by figure 2.4 it is possible to evaluate the intrinsic roll over wind speed as,

$$u_{wind} = \frac{V_{rel}(\sin(\theta))}{\sin(\beta)} \quad (2.39)$$

These conditions can be modified to include centrifugal forces for vehicles moving on curves (Gawthorpe, 1994). The difficulty with these equations is calculating the aerodynamic rolling moment coefficient, which must be estimated from experiments or

numerical simulation. RSSB (2009) defines a series of equations to estimate the lee rail rolling moment coefficient for both leading (locomotive) and tailing (wagons) vehicles, shown in table 2.1. The equations are based on yaw angle θ , such that $m = \theta/100$.

Vehicle type	Aerodynamic lee rail rolling moment coefficient equation
Locomotive	$C_{Mx,lee}(\theta) = \begin{cases} -5.1418m^3 + 3.4488m^2 + 1.1410m & \text{for } m \leq 0.6 \\ 0.816 & \text{for } m > 0.6 \end{cases}$
Wagons	$C_{Mx,lee}(\theta) = \begin{cases} 2m & \text{for } m \leq 0.5 \\ 1.0 & \text{for } m > 0.5 \end{cases}$

Table 2.1: Equations to calculate lee side roll moment coefficients for freight trains.

Unloading of windward wheels or the inside rail of a curve is usually largest for the leading vehicle for high speed trains, due to the nature of construction and high loads on the front vehicle. However, for freight trains the leading vehicle is usually the heaviest so trailing vehicles are more susceptible to overturning (Andersson et al., 2004). In many cases other factors such as centrifugal forces in curves, suspension deflections and uneven track surfaces all lead to destabilisation of vehicles, which when coupled with crosswinds can cause overturning (Gawthorpe, 1994; Andersson et al., 2004). For trains travelling on conventional cant deficiencies the mean roll moment coefficient is extrapolated from table 2.1. When operating above conventional cant deficiencies peak moment coefficients, obtained through experimental data, are used.

2.4.5 Further implications on crosswind safety

A vehicle is more likely to experience overturning forces when subjected to a sudden gust of wind rather than a constant wind force (Andersson et al., 2004). The topography of many rail routes includes sections with differing severity of gust risk, including tunnel exits or exiting sheltered areas of track, such as cuttings. The timescale of a gust

when coupled with dynamic roll characteristics of a vehicle can create unloading of the windward side wheels and a risk of overturning (Andersson et al., 2004). Gust build-up time is important to the force applied to a vehicle; a build-up of less than 1 second can result in a large unloading force, however for build-up greater than 1 second the force is considered constant (Andersson et al., 2004). Build-up time is dependent on characteristics of wind velocity, which is in turn dependent on topography. Throughout the atmospheric boundary layer topography influences the wind; at ground level wind velocity is zero, and at higher altitudes there is a decreased influence of topography thus increased velocities. Wind speed increases quicker over smooth than rough surfaces.

Railway structures can also have an influence on the over turning risk. As bridges are elevated the wind velocity at track level will be dependent on the wind velocity profile (Krönke and Sockel, 1994). Mass continuity implies that the perpendicular component of wind velocity to the track will increase on embankments, highest close to track level and decreasing with increasing height above track level (Baker, 1985; Andersson et al., 2004). Experiments by Baker (1985) found that 3m above track level on an embankment of 8m experienced a 68% increased wind velocity in relation to a flat ground situation, and a 12m embankment an increase of 81%. Gawthorpe (1994) cited that knowledge of specific routes and cooperation between the Met Office and rail authorities could help design defences or provide early warning systems to help prevent accidents from occurring.

The stochastic nature of wind speeds will always create possibility for crosswind accidents (Andersson et al., 2004; Baker et al., 2011). Due to route topography only 1-2km sections may be at risk of gust conditions capable of overturning, therefore as tunnels have similar a length, Andersson et al. (2004) developed a risk analysis method usually applied to tunnels to a crosswind situation. Andersson et al. (2004) used risk analysis models for a section of track in Sweden and put forth possible risk reducing measures. The use of wind shielding from fences or trees, lower embankments and creating wind warning systems linked to meteorological information, to provide

speed reductions based on wind speed, were all found to decrease the risk of vehicle overturning.

Complex data sets obtained from real time computational simulations can be used to calculate wind loading force coefficients. Baker et al. (2011) developed a programme to simulate the motion of a Class 365 and a container freight train in tare condition to create worst case conditions. Wind loadings derived from wind tunnel and computational simulations were applied to a vehicle dynamics model ‘Vampire’. Vampire allows detailed descriptions of vehicle suspension, track irregularities and nonlinear modelling of wheel to rail contact. Combined with user inputted crosswind data the programme creates a simulation of wheel to rail forces, position of contact with rail and detailed behaviour of vehicle bodies (Baker et al., 2011). The ratio of lateral force to the vertical force at any wheel, Y_{lat}/Q (derailment quotient) is analysed, where Q is as defined in section 2.4.4.1 and Y_{lat} is the lateral guiding force of a wheel exerted on the rail measured in a wheel set based reference frame (TSI, 2008; Baker et al., 2011). The level of unloading at any wheel is defined as the ratio of actual load to static load at the wheel, $\Delta Q/Q$ (Baker et al., 2011). The derailment quotient measures the ratio of lateral forces leading to flange climbing and vertical forces; calculated using the coefficient of friction and flange angle (Baker et al., 2011). Vampire showed $\Delta Q/Q$ is reached before the derailment quotient Y_{lat}/Q . For a laden freight train $\Delta Q/Q$ and Y_{lat}/Q were low for all wind conditions and no derailment occurred. However, for a train in tare the simulation showed derailment occurred for higher crosswind speeds of 25m/s, below the revised limit suggested by RSSB (2012), and the limit of $\Delta Q/Q$ was exceeded for crosswinds of 17m/s.

Many rail vehicles including freight locomotives are powered by electrical overhead wires and a pantograph mounted on the locomotive roof. In crosswind situations overhead wires can oscillate and the pantograph can experience unusual lift forces, which may in turn cause damage and disruption to the rail network (Gawthorpe, 1994; Baker and Sterling, 2009).

Throughout Europe only single stack container freight trains are viable due to gauge limitations. However, in the USA and Australia double stack container trains are widely used. In essence a double stack container train consists of one or more locomotives (dependent on train weight) and a series of flatbed wagons loaded with two shipping containers; one placed on top of the other. The stability of a freight train is affected by aerodynamic forces from crosswinds, centrifugal forces and gravitational forces due to track cant (Andersson et al., 2004; Alam and Watkins, 2007b). Each double stack container on a wagon increases the side surface area making the wagon more susceptible to crosswind effects. Alam and Watkins (2007a,b) investigated the effect of double stack containers travelling through a crosswind situation for Australian railways. Using two different 1/15th scale double stack wagon models in a wind tunnel, with steady wind speeds and varying yaw angles, experiments were conducted to calculate forces acting on the model, using a six-component force sensor attached to the train mounting. Results showed side force and rolling moment coefficients increased as yaw angle increased to 75° , stabilising thereafter. Side force increased with increased side area. Lift force was shown to increase up to a yaw angle of 30° then decrease thereafter. Overturning was shown to be possible even at relatively low wind speeds, depending on the yaw angle and train speed, agreeing with previous crosswind studies (Krönke and Sockel, 1994; RSSB, 2012). Alam and Watkins (2007a) cited a possible dependence on container loading configuration and efficiency for aerodynamic forces; however, no additional experiments were conducted to test this theory.

2.4.6 Summary of crosswind research

Analysis of existing studies has shown the field of freight aerodynamic load research to be a more active area of research than freight slipstream development. Incidents such as those in 2008 have led to a series of investigative national safety reports commissioned and published (RAIB, 2009; ATSB, 2008), leading to fundamental research projects focused on freight in crosswind conditions (Alam and Watkins, 2007a; Hemida

and Baker, 2010; RSSB, 2012). Although freight research has been carried out, like slipstream research, crosswind research has predominantly focused on passenger trains due to the possible impact of loss of life if a vehicle were to overturn and, as with slipstream studies, in line with development of faster more aerodynamically efficient trains and network upgrades (Raghunathan et al., 2002). However, unlike slipstream safety standards, freight trains are included in the UK standards for crosswind effects on rail vehicles. Although the standards provide limits on crosswind stability, much of the research is focused on the vehicle and load overturning as a system, and not load detachment, as witnessed in previous crosswind incidents (ATSB, 2008).

The literature review indicates that a focused freight study is needed to understand the influence of aerodynamic loads on an item loaded onto a freight train; chosen to be a container in this study. By assessing the influence of running in an open air and crosswind situation a comparison to previous studies and safety standards can be made in relation to a vehicle and load system, as well as analysing effects of load detachment. Previous freight studies have tended to include numerous freight types with minimal ensemble sizes. This indicates that it is important to focus on a number of key container loading configurations to create data sets, with a suitable ensemble size, to analyse the effects of container loading configuration on the flow development. By conducting a moving model study it will be possible to compare results with previous wind tunnel studies and assess any influences created by vehicle motion.

Chapter 3

Slipstream experiment setup

3.1 Introduction

Chapter 3 describes the experiment setup and methodology adopted for the slipstream development research. Section 3.2 introduces the model scale slipstream experiment design and methodology undertaken at the TRAIN rig facility; outlining the facility features in section 3.2.1 and the motivation and development of the model design in section 3.2.2. Section 3.2.3.1 defines the coordinate system used for both model and full scale experiments. The model scale trackside instrumentation, including measuring probes, position finders and ambient condition monitors are described in section 3.2.3.2 and the experiment methodology is discussed in section 3.2.4.

Similarly 3.3 discusses the full scale experiment design and methodology undertaken at Uffington. The Uffington test site is introduced in section 3.3.1, and previous Uffington research carried out is discussed in relation to site suitability for slipstream experiments. Sections 3.3.2 and 3.3.3 describe the full scale experiment setup, including trackside instrumentation, and the experiment methodology respectively. Section 3.3.4 gives an overview of all the trains which passed the test site during the experiment and how specific trains have been chosen for this study.

3.2 Model scale experiment methodology

3.2.1 TRAIN rig facility

The TRainsient Aerodynamic INvestigation (TRAIN) rig is a purpose built testing facility in Derby for examining the transient aerodynamics of moving vehicles. The facility, owned by The University of Birmingham, is situated at the RTC Business Park, London Road, Derby; once the home of British Rail Research (Baker et al., 2001). The TRAIN rig consists of a 155m long testing room in which three 150m test tracks are situated. The test room is joined onto a control room from which the facility is safely operated, and a workshop for general repairs and experiment apparatus construction.

The TRAIN rig offers the possibility to measure slipstream velocities, static pressure pulses and pressures acting on the train or trackside structures in a 12m long open air test section. The effects of crosswinds at various yaw angles and ground simulations can also be modelled using a purpose built 6.35m long crosswind generator. A 23m long tunnel is also installed for the measurement of vehicle aerodynamics in tunnel confines. The advantage of a moving model rig over a typical stationary wind tunnel is the ability to correctly simulate the relative motion between the vehicle and the ground/structures or crosswind simulation (Baker et al., 2001).

The rig fires 1/25th scale model trains down three 150m straight track at speeds up to 75m/s, dependent on model weight, using two identical mechanical propulsion systems. The track on which a vehicle travels is mounted on a concrete deck supported by 1.2m high concrete pillars, between which the propulsion system is mounted.

Models are accelerated using a pre-tensioned elastic bungee cord system, ensuring the model acceleration occurs very rapidly; thus the model is travelling at the specified testing speed within a 50m firing section (figures 3.3 and 3.1(a)). The elastic bungee cord system is attached to the model vehicle by means of a firing rope and chassis. As



(a) TRAIN rig firing zone



(b) TRAIN rig open air testing zone and tunnel

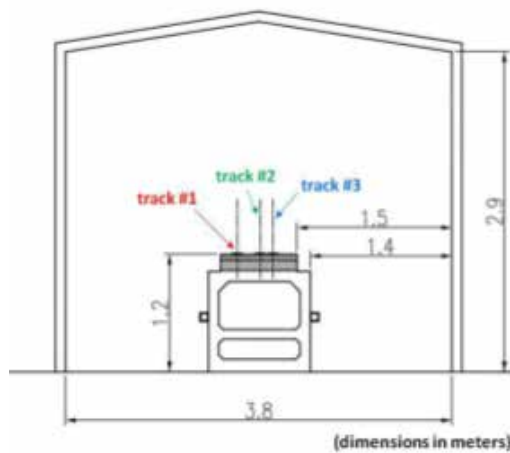


(c) TRAIN rig crosswind generator

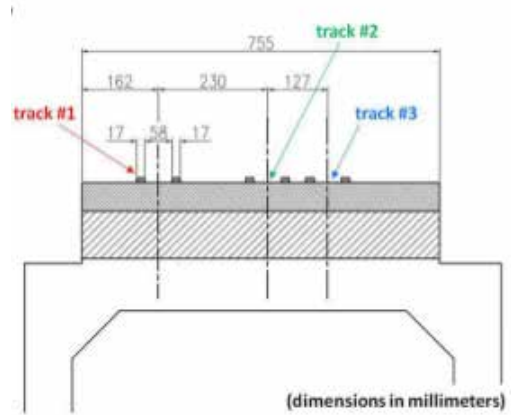


(d) TRAIN rig braking zone

Figure 3.1: The TRAIN rig facility. Figures 3.1(a)-3.1(d) show the firing and braking zones in the testing room, as well as the open air and crosswind test sections and the tunnel installation.



(a) TRAIN rig test room dimensions



(b) TRAIN rig track dimensions

Figure 3.2: Schematic images of the TRAIN rig test room and track bed structure 3.2(a) and the track layout 3.2(b) (Dorigatti, 2013). The dimensions in 3.2(a) are given in metres, whereas the dimensions in 3.2(b) are given in millimeters.

the firing carriage (figure 3.3) is retracted, by an electronic winch controlled from the control room, tension is applied to the system until a pre-specified tension is reached. The firing rope is in turn kept in tension via a retracting rope attached to the model by an elastic band and cable tie. When fired, the firing carriage is released from the tensioned bungee which pulls the firing rope through a geared pulley system, applying a force to the model and thus breaking the elastic band, setting the model in motion (figure 3.3).

Once in motion the model is free from any propulsion devices, allowing free motion with minimal constraints on model design. However, due to aerodynamic drag and friction, a small decrease in vehicle speed occurs between the firing and braking section. For the models tested in this experimental campaign an average speed decrease of 0.05m/s per m has been estimated for an average train speed of 20m/s through the open air testing section (figures 3.1(b) and 3.1(c)).

Following the 50m test section the model is decelerated using a friction device in a 50m braking section. The braking device uses a piston dragged through a deformable polyurethane tube which is attached to a rope which attaches to the train chassis during the braking phase (section 3.2.2.3 and figure 3.3). This method of braking ensures slow dissipation of model energy creating a gentle deceleration, minimising possible damage to the model. If the primary brake fails, a secondary brake by means of a second braking rope secured to the ground is setup, however this creates a much more severe braking motion and is avoided. At each end of the TRAIN rig tracks are blocks of deformable foam acting as a last resort braking method.

3.2.2 TRAIN rig model

3.2.2.1 Motivation for model design

A moving model was developed to simulate container loading configurations seen at full scale (section 3.3.4). Unlike focusing on a specific high speed passenger train the term

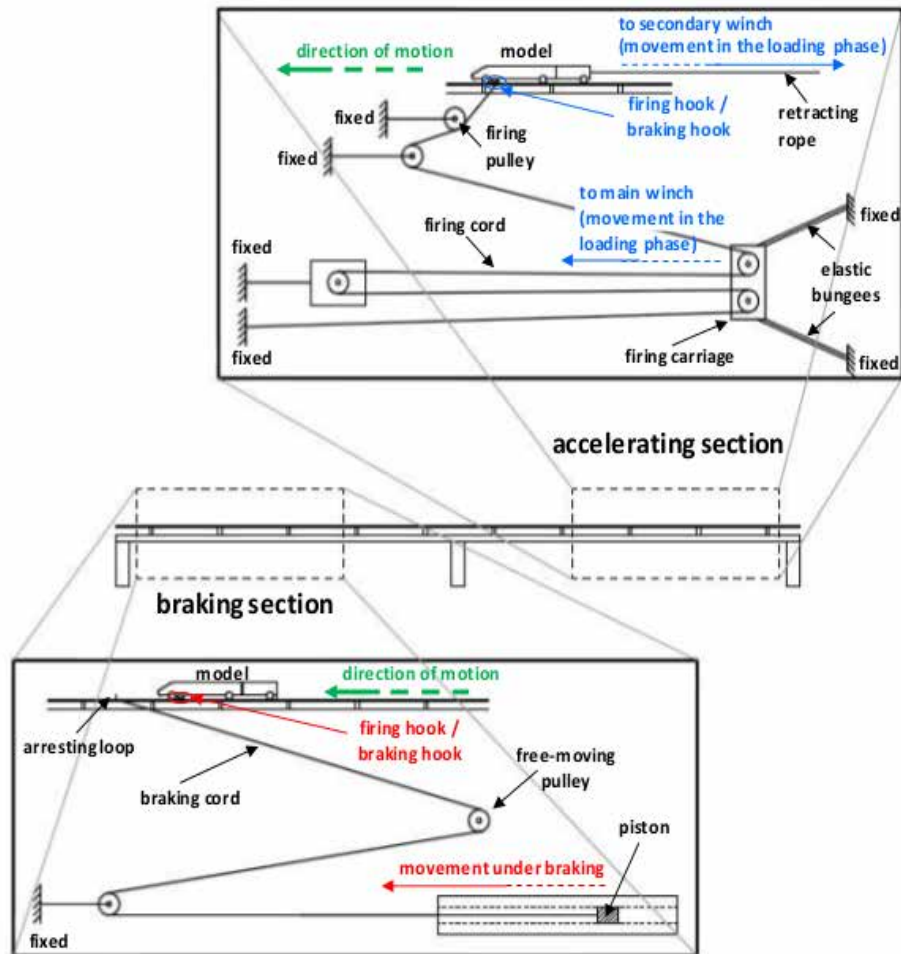


Figure 3.3: A schematic of the TRAIN rig propulsion and braking mechanisms (Dorigatti, 2013).

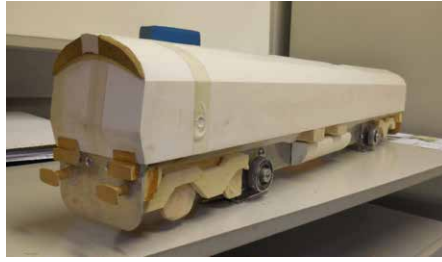
‘freight train’ applies to many different train types. For this study the term ‘freight train’, unless otherwise stated, refers to a series of flatbed wagons loaded with shipping containers hauled by a Class 66 locomotive. Container freight is one of the largest sectors of freight transported in the UK and the choice for this study offers relative ease for modelling purposes.

The British Rail/ EMD Class 66 locomotive was chosen for this study to reflect widespread use across the UK rail network. Introduced in 1998 to the UK, the Class 66 locomotive is operated by all UK freight operating companies (FOCs), apart from Mendip Rail who operate Class 59 locomotives (the Class 66 development vehicle with essentially the same body work) (Fox et al., 2008). Previous model scale experiments which focused on loading pressures on trackside buildings and structures highlighted much higher magnitudes for the Class 66 locomotive than either the Class 158 or Class 390 passenger trains (Baker et al., 2012). The Class 66 locomotive was chosen for this study to build upon knowledge developed in Baker et al. (2012) and provide data for comparison with full scale measurements of freight recorded from predominately Class 66 hauled freight routes.

3.2.2.2 Model development

An existing 1/25th scale Class 66 model was modified to include a long flat aluminium plate to simulate FEA-B flatbed wagons, with bogies and undercarriage equipment modelled using balsa wood. The Class 66 model was designed as a simplified version of the full scale locomotive, including main body shape, nose and tail features (such as buffers and guard plates) and simplified underbody features (figure 3.4). The Class 66 main body is modelled using glass-fibre reinforced plastic (GRP) with an average thickness of 2mm. The FEA-B wagons are modelled as a wagon twin set with simplified underbody features, again modelled in balsa wood (figure 3.4).

Two train lengths were tested as part of these model scale slipstream experiments.



(a) TRAIN rig Class 66 model



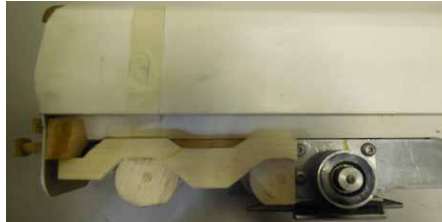
(b) Class 66



(c) TRAIN rig FEA-B wagons model - twin set



(d) FEA-B wagon - twin set



(e) TRAIN rig Class 66 bogie



(f) Class 66 bogie



(g) TRAIN rig FEA-B wagon bogie



(h) FEA-B wagon bogie

Figure 3.4: A comparison of images showing the TRAIN rig Class 66 and FEA-B wagon models to the real vehicles. The differences between modelled balsa wood bogies for the Class 66 and FEA-B wagon and full scale bogies are also shown (Bartlett, 2014; Read, 2014).

Initially a model length of 4.05m was developed, with the existing Class 66 of length 0.85m and four FEA-B flatbed wagons of individual length 0.8m (figure 3.5). At full scale this gives a total train length of 101.25m. The choice of initially simulating four wagons reflected the maximum length of previous TRAIN rig models of 4m. Unlike other models at the TRAIN rig this design is not built around a central spine, rather the rigidity of the aluminium plate, which was required to be 4mm thick so as not to twist under the action of firing and braking the model. As model weight is an important factor in relation to the tension required to create a specific train speed a conservative approach was taken, following consultation with the model makers Derwent Patterns Ltd of Derby. Therefore a train length of 4.05m was chosen to be within the capable working range of the TRAIN rig.

Following a first series of experiments the model length was reassessed and a similar series of experiments were undertaken using a model length of 7.25m; with existing Class 66 of length 0.85m and eight FEA-B wagons of individual length 0.8m. At full scale this gives a total train length of 181.25m. A feature of this model is the ability to detach the simulated wagons from the Class 66 via the use of a series of couplings (figure 3.6).

3.2.2.3 Model chassis and trailing wheel system

The model is mounted on a specially designed chassis and trailing wheel system, designed to spread model weight out evenly, providing stability and a structure by which to fire/brake the model. The Class 66 model is mounted onto the chassis (figure 3.7(a)), while four/eight (depending on model length) sets of trailing wheels are attached at varying distances along the flat plate (figure 3.4(c)).

The chassis is essentially an aluminium box section mounted with two sets of wheels and two horns, one for firing and one for braking (figure 3.7). The firing and braking ropes end in a reinforced loop designed to be attached to the chassis horns during

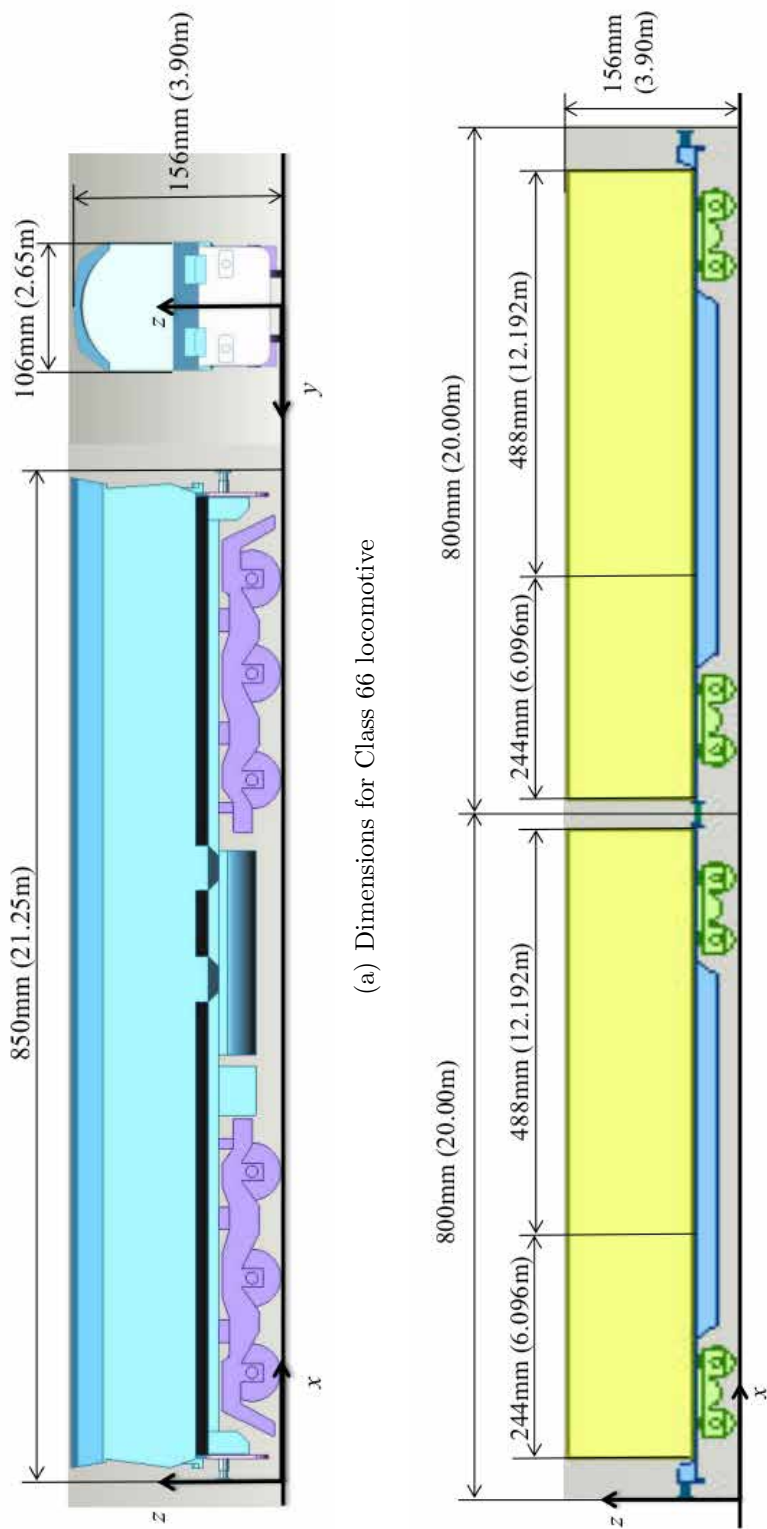
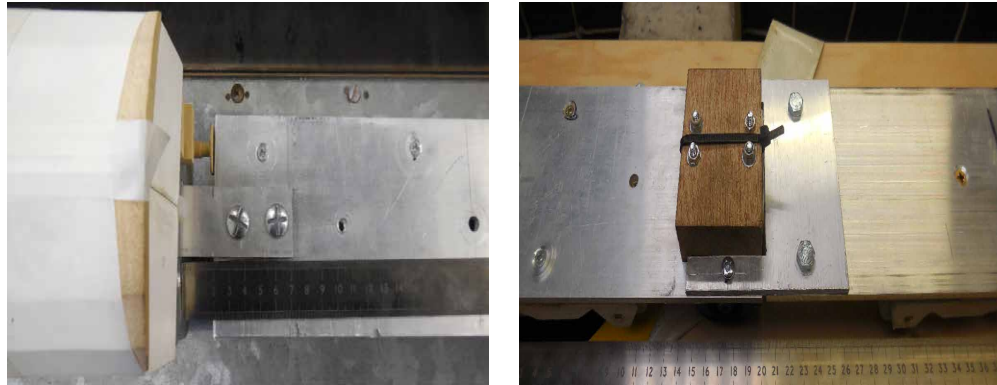
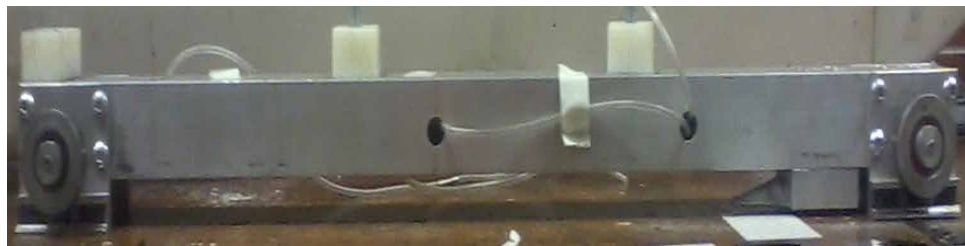


Figure 3.5: The dimensions of the model scale Class 66 locomotive and FEA-B wagons at the TRAIN rig.



(a) Coupling between Class 66 and FEA-B wagon (b) Coupling between two sets of four FEA-B wagons

Figure 3.6: The couplings between vehicles on the TRAIN rig freight model.



(a) TRAIN rig chassis



(b) TRAIN rig chassis wheels



(c) TRAIN rig chassis horns

Figure 3.7: The TRAIN rig chassis for the freight model.

either the firing (rear horn) or braking (front horn) sequences. The chassis and trailing wheels axle plate onto which the wheel is mounted extends below the radius of the wheel and the head of the rail to an L-shaped skid plate (figure 3.7(b)). This feature allows the train to move along the track in a longitudinal direction but negates lateral and vertical motion.

3.2.2.4 Model containers and loading consists

To simulate different container loading configurations, a series of detachable scale containers were designed to standard International Shipping Organisation (ISO) container sizes 12.192m x 2.438m x 2.590m (40 foot) and 6.096m x 2.438m x 2.590m (20 foot) (ISO, 2006). Twelve scale 6.096m containers, and eight 12.192m containers have been built and are arranged as five different container loading consists with varying loading efficiencies (figure 3.8). FEA-B wagons are arranged in a ‘twin-set’ configuration, i.e. two wagons are continually coupled together, therefore loading consists are chosen to be repeating patterns every two wagons. The consists have been chosen to represent loading efficiencies ranging from 100% to 0% loaded, while also allowing for comparison with full scale data (section 3.3.4). Containers are attached to the model via threaded holes drilled in the flat aluminium plate through which a bolt from the base of the container is secured.

3.2.3 Experiment setup

3.2.3.1 Coordinate system and measuring positions

A coordinate system is defined (figure 3.9) such that the x-axis is aligned in the direction of travel, with the origin taken to be when the train nose passes the measuring point, indicated by the pressure ‘zero-crossing’ created between positive and negative pressure peaks in the train nose region (see section 4.4). The y-axis is the horizontal plane



Figure 3.8: A series of diagrams to show the loading configurations to be tested at the TRAIN rig. Consists 1, 3 and 5 are also tested for the eight wagon train length, i.e. the loading patterns are repeated over the next four wagons.

Probe number	Cobra Probe positions		Consists tested	
	Height (mm)	Distance from track centre (mm)	101.25m	181.25m
1	4500	0	1,2,3,4,5	1,3,5
2	2250	1750	1,2,3,4,5	1,3,5
3	2250	2375	1,2,3,4,5	1,3,5
4	2250	3000	1,2,3,4,5	1,3,5
5	5100	0	5	1,3,5
6	5700	0	5	1,3,5
7	200	3000		1,3,5
8	1000	2000		1,3,5

Table 3.1: Slipstream measuring positions and the consists and train lengths tested at those positions. All dimensions are given as the relative full scale measurements in mm.

a frequency response of 2000 Hz, making it ideal for the measurement of turbulent flow fields. The accuracy of measurements are generally to within $\pm 0.5\text{m/s}$ and $\pm 1^\circ$ for velocity and direction respectively, and the probe remains relatively accurate to greater than 30% turbulence intensity (TFI, 2011). The differential static pressure is approximately accurate to $\pm 5\text{Pa}$ (TFI, 2011).

The Cobra probe is supplied fully calibrated, however the probe must be statically calibrated every six months or following large changes in temperature (TFI, 2011). The static calibration determines the voltage to pressure scaling factors used by internal pressure transducers (TFI, 2011). Prior to the experiments at the TRAIN rig two probes were returned to TFI, due to damage, for a full recalibration. Appendix A describes a series of experiments undertaken to compare all the University of Birmingham Cobra probes before and after the recalibration of the damaged probes. The results show all the probes used in the TRAIN rig experiments fell within the calibration and accuracy bounds outlined by TFI.

The Cobra Probe outputs voltage data proportional to pressures on the probe head, which are converted to three components of velocity data by TFI Device Control software using a pre-determined calibration. The software allows the user to input values for air temperature and atmospheric pressure into the calibration formulae. The TFI Device Control software is used on a standard laptop computer connected via USB

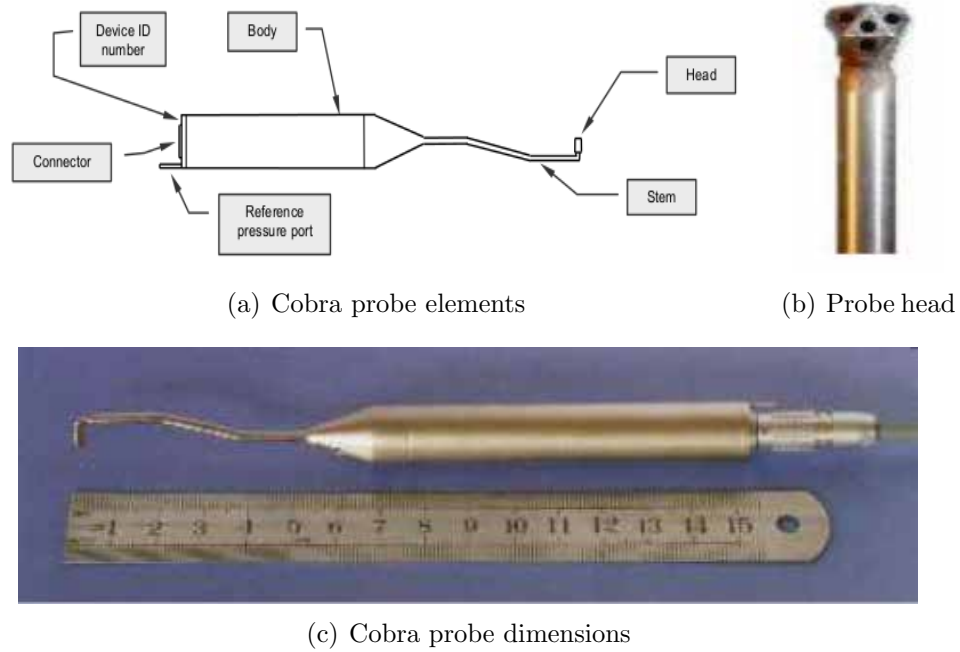


Figure 3.10: Series 100 Cobra probe key elements and dimensions (TFI, 2011).

cables to the TFI data loggers, which are in turn connected to the probes with TFI supplied cables. For each measurement the Cobra probe was ‘zeroed’, using the TFI software, before the train was fired. This ensured measurements are made in relation to a still air situation.

A drawback to the Cobra Probe is a ± 45 degree cone of acceptance, limiting the range of flow detection. If flow is outside the cone of acceptance, data outputted is replaced by a zero (see section 5.2). The Cobra probe is also fitted with a transducer with a range of operation specified by the user when purchasing the probe. For the probes used in these experiments a maximum velocity cap is applied for velocities above 30m/s. If the flow is beyond the range of operation the software will crash and no data will be collected.

The probe is set up such that the central measuring hole is placed at the specified measuring position (table 3.1). The central measuring hole is in the centre of the Cobra probe head, which has a diameter of 4mm. The probe is setup by measuring to the bottom face of the probe head adding or subtracting 2mm to ensure the central

measuring hole is at the measuring position (figure 3.9). The probes are setup at the beginning of each test day, with measuring positions and alignment checked to an accuracy of $\pm 1\text{mm}$ and $\pm 2^\circ$ respectively.

The Cobra probes are mounted on supports by specifically designed probe holders or clamp stands. These allow for yaw and pitch angle rotation, as well as displacement along the vertical and lateral axis until the probe is in the correct measuring position. Probe supports are fixed to the ground and isolated from mechanical vibrations which may be caused by TRAIN rig motion. All joints and connection points in the apparatus supports have 3mm thick rubber washers to dampen any remaining effects of mechanical vibrations. The reference pressure port from the rear of the Cobra probe must be vented to a location out of the flow itself so as to not allow flow induced pressure fluctuations to interfere with the reference pressure (TFI, 2011). In this case tubing from the reference pressure port was guided underneath the TRAIN rig apparatus (figure 3.11(b)).



(a) TFI interface unit



(b) Cobra probe reference pressure position

Figure 3.11: The TFI interface unit and the reference pressure positioning underneath the TRAIN rig apparatus.

3.2.3.2.2 Photoelectric position finders The model speed was altered by pre-determining the tension in the firing cable, which in turn was altered for different loading efficiencies in relation to model weight. Model speed was measured using a series of opposing ‘Sick’ photoelectric position finders and reflectors along the TRAIN

rig trackside. The position finders can be used to calculate train speed to an accuracy of $\pm 0.1\text{m/s}$. The position finders were separated by 1m and 2m about a central lateral position located at $x = 0$, in line with the probes measuring head (figure 3.12(a)). The position finders are linked to bespoke interface units which calculate train speed based on the distance between linked position finders and the time taken for each beam to be broken. The speed calculated by each pair of position finders is outputted on the interface unit screen and manually inputted into an Excel spreadsheet after every run.

3.2.3.2.3 Light sensor A light source and detector were positioned at the trackside in line with the Cobra probe measuring head to act as a position finder for the train nose in the Cobra probe data files, to justify the choice of data alignment method (section 4.4). The light sensor consists of a torch with 1mm slitted cover and a Vishay Intertechnology Inc. phototransistor sensor (VISHAY-TEPT5600) (Vishay, 2011). The phototransistor sensor was powered by a Caltek Industrial Ltd. power supply unit (PSD 30/3B) (BST, 2007), and connected with shielded three core wire and a coaxial connector to the TFI data logger and monitored by the TFI device control. The outputted signal is $\sim 5\text{V}$ until broken by the train when it would fall to 0V. The signal was monitored and recorded alongside Cobra probe signals and used in the data processing stage to align Cobra probe data with the train nose.

3.2.3.2.4 Ambient condition monitors Ambient conditions were monitored using an Oregon Scientific BAR208HGA weather station to measure temperature and relative humidity to a resolution of $\pm 1^\circ\text{C}$ and $\pm 1\%$, with an accuracy of $\pm 2^\circ\text{C}$ and $\pm 10\%$ respectively. A GBP3300 Digital Barometer measured atmospheric pressure to a resolution of $\pm 1\text{mb}/100\text{Pa}$ with an accuracy of $\pm 200\text{Pa}$. Sensors to measure ambient conditions were placed on a TRAIN rig supporting pillar next to the experiment setup (figure 3.12(b)). Ambient condition measurements were recorded before each run manually into an Excel spreadsheet.

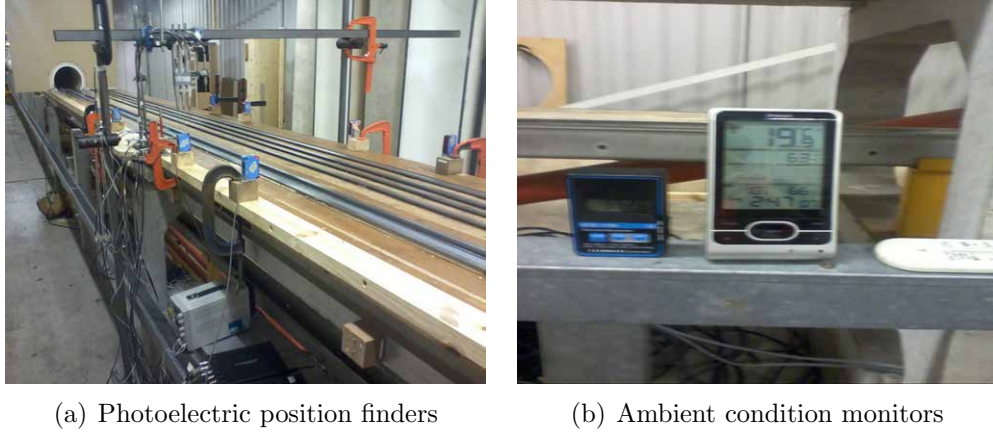


Figure 3.12: Photoelectric position finders to measure the model speed and the ambient condition monitors.

3.2.4 Experiment methodology

The TRAIN rig model scale slipstream experiments entailed taking Cobra probe measurements for a series of runs for each train consist. In general 25 repeats were undertaken to create ensemble averages in line with TSI standards (TSI, 2008). The number of repeats was only altered during a series of preliminary experiments (appendix C) when train speed was beyond the capable operational range of the Cobra probes, causing the Cobra probe software to crash.

A train speed $V_{train} = 20 \pm 0.5 \text{ m/s}$ was adopted for these experiments to create slipstream velocities within the capable range of the Cobra probes. To achieve this train speed a series of preliminary firings to find the launching tension required was completed. The tension required is dependent on model weight and thus varies between loading efficiencies and model lengths (table 3.2).

For a 1/25th scale model travelling at 20m/s with a characteristic height of 0.156m the Reynolds number is defined as,

$$\text{Re} = \frac{V_{train} L_{ref}}{\nu} = \frac{20 * 0.156}{0.000015} = 2.2 \times 10^5 \quad (3.1)$$

This Reynolds number value is below a typical value for a full scale train, $\text{Re} = 8 \times 10^6$.

Consist number	Tension required (kN)	
	101.25m	181.25m
1	7.60	8.65
2	7.40	×
3	7.50	8.55
4	7.53	×
5	7.44	8.40

Table 3.2: The tension required for each consist to achieve the desired train speed $V_{train} = 20\text{m/s}$. The difference in tension required for differing train lengths are also shown.

BSI (2005) states that slipstream experiments carried out with a model train should be conducted for a Reynolds number larger than 2.5×10^5 , to ensure values are representative of full scale measurements. It was not possible to test at a Reynolds number of 2.5×10^5 due to model fragility and instrumentation limits, as discussed in appendix C. In sections 5.6.2.4 and 5.7 the differences in slipstream development created by altering the Reynolds number will be analysed. In general values for slipstream velocity and pressure magnitudes at model scale are within $\pm 3\%$ of full scale measurements, meeting the requirements specified by BSI (2005).

A sampling frequency of 2500Hz was chosen for these experiments to avoid signal aliasing and provide a resolution of measurements every 8mm along the TRAIN rig model, corresponding to every 0.2m at full scale. To allow the TRAIN rig firing process to be completed a sampling time of 20 seconds was chosen.

3.3 Full scale experiment methodology

3.3.1 Uffington test site

Full scale experiments were carried out at an open air trackside position in Uffington, Oxfordshire. The freight slipstream study was completed in conjunction with a University of Birmingham/Network Rail project, while also providing an initial test case for the Real World Train Aerodynamics project (RWTa); a project to assess the

aerodynamic properties of a Class 43 HST passenger train. The site is that of the old Uffington railway station situated on the Great Western Main Line, shown in figure 3.13. The site, once at the junction between the Great Western Main Line and the Faringdon Railway branch line, is used as an access point and storage depot for Network Rail maintenance.

The site layout consists of a section of twin track with a shallow 0.3m ballast shoulder either side. To the north of the site there is a large flat gravel area with a temporary welfare unit from which measurements could be monitored. Access is provided by a ramp from a bridge over the railway to the east of the site; a small section of the gravel area was reserved away from the experiment for parking road vehicles.

The Uffington test site was chosen to measure slipstream velocities and pressures for a University of Birmingham run Network Rail project. Measurements were made in relation to assessing whether safety limits were breached for trackside workers working in a High Output Plant System (HOPS) for the installation of Overhead Line Equipment (OLE) when a train passes all full operational line speeds (Baker and Quinn, 2012). The report found freight trains created higher slipstream velocity and pressure magnitudes than passenger trains, however trackside worker safety limits were not broken for a HOPS deck height of 2.95m above the cess (Baker and Quinn, 2012). It was however suggested that further experiments should be undertaken to assess the possibility of slipstreams causing movement of equipment placed on the HOPS deck (Baker and Quinn, 2012).

3.3.2 Experiment setup

3.3.2.1 Coordinate system and measuring positions

The coordinate system used for model scale slipstream experiments is also adopted for the full scale experiments (figure 3.9). The experiment was designed in relation to



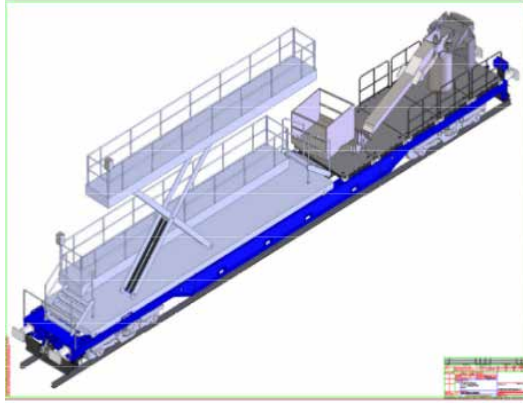
(a) Map showing Uffington test site



(b) Photograph of Uffington old railway station

Figure 3.13: A map of the position of the Uffington test site (circled in red) and village in Oxfordshire (Microsoft-Corporation, 2013) and a photo of the old Great Western Railway (GWR) station (Uffington, 2012).

the Network Rail project assessing maximum slipstream loadings on a HOPS vehicle. Slipstream velocities were measured at a series of positions on a stationary trackside vehicle as well as fundamental TSI trackside positions.



(a) HOPS vehicle



(b) RRV MEWP

Figure 3.14: The proposed HOPS vehicle and the RRV MEWP test vehicle used in the experiments at Uffington, Oxfordshire.

To simulate a HOPS vehicle on a twin section of track a RB25-KLLSX type mobile elevated working platform road rail vehicle (RRV MEWP) (SRS Sjlanders AB) was positioned next to the up track to the north of the experimental site (Baker and Quinn, 2012). The RRV MEWP has two workers' baskets, of which the more open sided one was raised to a base height of 2.95m above the cess (2.65m above the top of rail), approximately the proposed position of the HOPS basket (figure 3.14). Table 3.3 shows RRV MEWP measuring positions as well as TSI equivalent trackside measuring positions and the measuring instrumentation used at each position.

Probe number	Probe positions		Instrumentation
	Height (mm)	Distance from track centre (mm)	
Basket 1	4300	4000	ultrasonic anemometer
Basket 2	2800	4000	ultrasonic anemometer
Trackside V1	700	3000	ultrasonic anemometer
Trackside P1	1000	2000	pressure probe
Trackside P2	1000	2000	pressure probe

Table 3.3: Slipstream measuring positions and instrumentation used at those positions for the full scale experiments conducted at Uffington, Oxfordshire.

For this study the basket position data is neglected due to interactions between the

slipstream and basket not modelled at model scale. Although not modelled, it is assumed the influence of the relatively shallow 0.3m ballast shoulder on slipstream velocities should be negligible in line with previous studies (Sterling et al., 2008), therefore positions Trackside V1, P1 and P2 are analysed.

3.3.2.2 Trackside instrumentation

3.3.2.2.1 Ultrasonic anemometers Slipstream velocities were measured using Gill Instruments R3-50 ultrasonic anemometers (Gill, 2013). The R3-50 ultrasonic anemometer is specifically designed for scientific research and capable of measuring three components of velocity and flow direction in real time. These anemometers are frequently used for making high accuracy wind speed and direction measurements at weather stations.

The anemometer can measure velocity flow fields in a range of 0-45m/s with a resolution of 0.01m/s at a sampling frequency of 50Hz, with an accuracy to less than 1% RMS (Gill, 2013). Wind direction is measured within the range 0-359° with a resolution of 1° to an accuracy of $\pm 1^\circ$ RMS (Gill, 2013).

The ultrasonic anemometer outputs digital data proportional to the time taken for sonic pulses to pass between a pair of transducers (figure 3.15), recorded at a frequency of 100Hz (Gill, 2013). Pulse times depend on the distance between transducers, speed of sound and the flow speed along the transducer axis (Gill, 2013),

$$T = \frac{L_{us}}{c + v_{us}} \quad (3.2)$$

The speed of sound is in turn dependent on temperature, pressure and particle content in the measured air; thus the same anemometer can be used to estimate air temperature (Gill, 2013). To find the flow speed between transducers, each transducer is alternated as a transmitter and receiver, so pulses travel in both directions, leading to the flow

speed and speed of sound equations respectively (Gill, 2013),

$$v_{us} = 0.5L_{us} \left(\frac{1}{t_1} - \frac{1}{t_2} \right) \quad (3.3)$$

$$c = 0.5L_{us} \left(\frac{1}{t_1} + \frac{1}{t_2} \right) \quad (3.4)$$

where L_{us} is the distance between transducers and t_1 and t_2 are pulse times. In still air pulse time for each transducer is the same, $t_1 = t_2$, thus no flow, whereas within a slipstream the movement of air increases pulse time. The R3-50 has three pairs of opposing transducers in three different axes, creating time data converted by Gill Instrumentation software to three components of velocity data and flow direction, using a custom calibration provided with the anemometer (Gill, 2013). The device control software is used on a standard laptop computer connected via serial cables to the anemometers.

The anemometer is mounted on a 50mm diameter metal pole fixed to a 750mm diameter secure metal base, such that the anemometer vertical axis is that of the centre of the base, which is positioned at the lateral measuring position from the centre of track. The anemometer height is adjusted so the centre of the measuring head is at the specified measuring position (table 3.3). The method of mounting the anemometer allows for yaw angle rotation as well as displacement along the vertical axis, while ensuring the anemometer remains securely fixed at the measuring position throughout the test.

3.3.2.2.2 Pressure probes Experiment analysis methods rely on a series of pressure probes used as train position finders in the continuous data set and an additional method to calculate train speed. The probe is essentially a vertically mounted covered metal tube with a small open hole in the end to measure static pressure (figure 3.16) (Moran and Hoxey, 1979). Inside the probe casing the tube is connected directly to a Honeywell 164PC01D37 differential pressure transducer to record static pressure (Honeywell, 2013). The reference pressure side of the transducer is connected to a 20m

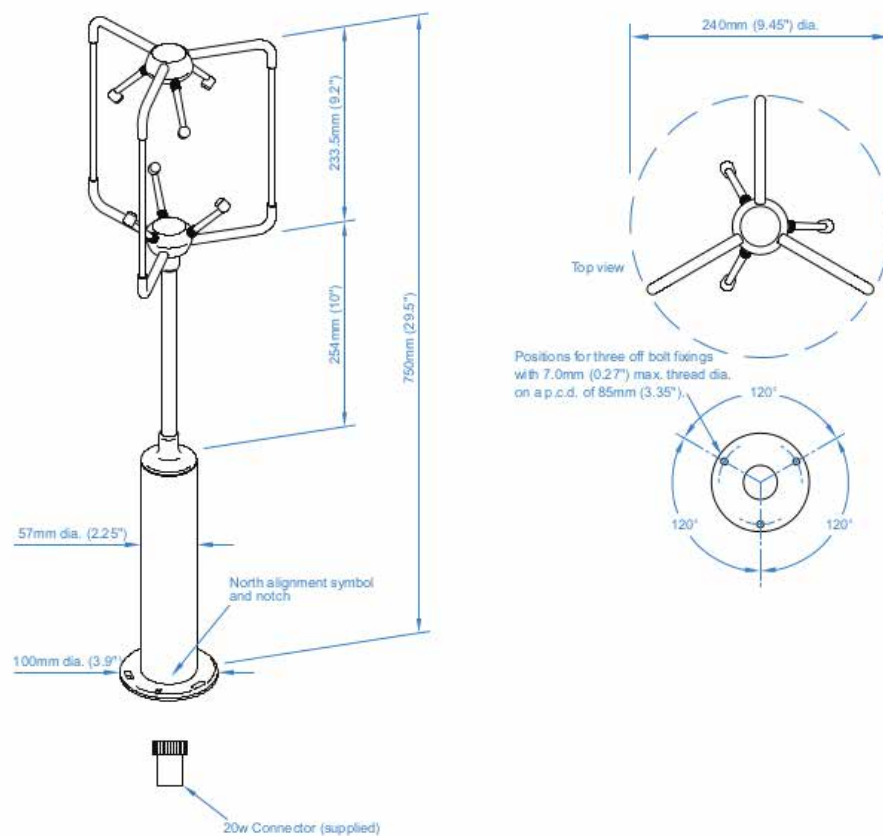


Figure 3.15: Gill Instrumentation R3-50 ultrasonic anemometer key elements and dimensions (Gill, 2013).

rubber tube which is fed away from the trackside to the north of the site, away from the influence of passing trains. Analogue signals from the pressure transducers were converted to a digital signal with a 16bit resolution by a Measurement Computing USB-1616FS analogue to digital converter (MCC, 2013). The converter was connected and operated via USB cables to a standard laptop computer.



Figure 3.16: The pressure probe and mounting used for the Uffington experiments.

The probes were positioned at either end of the test site, 39.5m apart, mounted to a 1.3m high safety fence, positioned 2m from the centre of track, giving probe positions P1 and P2 in table 3.3. The train speed was calculated by measuring the time difference between nose pressure transients observed at each transducer. A comparison between this method and a radar speed gun (section 3.3.2.2.3) generally found good agreement to within $\pm 0.5\text{m/s}$ (Baker and Quinn, 2012).

3.3.2.2.3 Radar speed gun Train speed was also measured manually using a Decatur RailMaster-VP radar speed gun. The radar gun, designed specifically for use with railway vehicles, monitors train speed by calculating the change in frequency, due to the Doppler effect, of an emitted signal reflected back off the vehicle (Decatur, 2013),

$$V_{train} = \frac{\Delta f}{f} \frac{c}{2} \quad (3.5)$$

where c is the speed of light and f is the frequency of the emitted signal. The radar gun features low and high speed ranges, outputting train speed in miles per hour which is converted to m/s when recorded in an Excel spreadsheet. The radar gun is accurate to within ± 0.25 m/s (Decatur, 2013; Baker and Quinn, 2012).

3.3.2.2.4 Ambient condition monitors Ambient wind conditions were monitored using an ultrasonic anemometer positioned 2.85m above ground level at a position 24m from the RRV MEWP, in open ground away from the influence of passing trains. TSI methodology states for full scale experiments ambient wind speeds should be below 2m/s (TSI, 2008). Recorded wind condition data acted as an additional data processing method to remove data recorded during ambient wind speeds above 2m/s. The air temperature during the tests was monitored using data from a local weather station.

3.3.3 Experiment Methodology

Data from measuring instrumentation was recorded continuously throughout the experiment using custom made data acquisition software on two laptop computers located in secure trackside boxes (Baker and Quinn, 2012). A total of 111 trains were recorded in a 51.5 hour experiment window, of which 23 were freight trains.

A sampling frequency of 50Hz was chosen for all measuring instrumentation in line with the ultrasonic anemometer maximum recording frequency. For a maximum freight train speed of 33.5m/s this provides a resolution of measurements every 0.67m; larger than the scaled up model scale experiment resolution but small in relation to an average freight train length (table 3.4).

During manned hours as a train approached on the track adjacent to the measuring equipment ambient conditions and time/date readings were recorded into an Excel spreadsheet. The radar gun was positioned to record the train speed, aiming the gun

at the train nose as the train passed through the experiment section, with readings recorded into an Excel spreadsheet. A video camera was set to record the train passage to enable train type and loading configuration to be referred to during data analysis. The camera videos were downloaded at the end of each manned shift. The site was unmanned during hours 5pm til 7am, thus no ambient condition data or videos were recorded, effectively negating any data recorded through these hours.

Freight train speeds were generally in the range 25-33m/s, close to the full UK freight line speed 33.5m/s. For a freight train travelling at 33.5m/s with a characteristic height of 3.9m the Reynolds number is defined as,

$$Re = \frac{V_{train} L_{ref}}{\nu} = \frac{33.5 * 3.9}{0.000015} = 8.7 \times 10^6 \quad (3.6)$$

3.3.4 Measured train types

Data was recorded at the test site continually from 11am on 31st July to 3pm on 2nd August 2012, during which 23 freight trains passed, made up of various locomotive and wagon configurations. Of these 23 trains, 9 were recorded at night and subsequently no record of train type was made, and for 6 trains either an error occurred during the data recording or no accurate record was taken of train type. The Uffington full scale data analysed therefore consists of 8 Class 66 hauled freight trains with differing wagon types and loading configurations. Table 3.4 shows the differing train types and lengths recorded, while figure 3.17 illustrates the different wagon types.



(a) Flatbed wagon



(b) Mineral wagon



(c) Maintenance wagon



(d) Coal wagon

Figure 3.17: A series of images to illustrate different wagon types recorded at Uffington, Oxfordshire (ITSV, 2013). The train formations are shown in table 3.4.

Train number	Locomotive type	Wagon type	Total train length (m)
1	Class 66	flatbed	450
2	Class 66	flatbed	420
3	Class 66	mineral	245
4	Class 66	flatbed	400
5	Class 66	mineral	300
6	Class 66		21.4
7	Class 66	maintenance	180
8	Class 66	coal	470

Table 3.4: Train types and lengths recorded at Uffington. All trains are hauled by a Class 66 locomotive, with differing wagon types including flatbed wagons with containers, mineral wagons, coal wagons and a maintenance train.

Chapter 4

Slipstream data processing methodology

4.1 Introduction

Chapter 4 introduces the methodology of processing full and model scale experimental data in preparation for analysing results in chapter 5. Through developing a series of computer scripts using Matlab, the data is converted from raw voltage data to meaningful physical data (sections 4.2.1 and 4.2.2). Section 4.3 discusses the process of normalising data to a non-dimensionalised coefficient to enable ease of comparison when analysing results. In section 4.4 the method and choice for aligning data with respect to the train nose is discussed. Section 4.5 calculates associated result uncertainties with respect to instrumentation and methods of collection. Finally section 4.6 presents an introduction to the development of wavelet analysis from Fourier transforms, an analysis technique utilised in chapter 5.

4.2 Data conversion

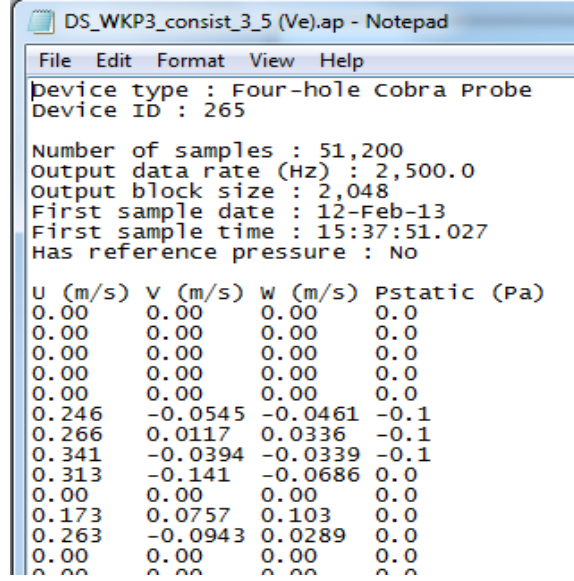
Experimental data is sampled for many cases in the rawest form as a series of voltages. Voltages can be converted to meaningful variables via conversion and calibration equations given by instrumentation manufacturers and calibration experiments. As different instrumentation is used for model and full scale experiments each will be discussed separately in sections 4.2.1 and 4.2.2.

4.2.1 Model scale data conversion

Model scale slipstream data collected by Cobra probes is outputted to the user in a converted form. The Cobra probe records data continuously in an analogue format which is digitally sampled at a data acquisition rate, set in these experiments at 5000Hz. Sampled data is converted from a series of voltage signals to meaningful variables by the TFI data logger and outputted at the sampling rate, set in these experiments at 2500Hz.

Each Cobra probe outputs a .TH* file (TFI time history file format) and a .as* file (a summary file of user inputted variables). * is a Cobra probe reference letter, for example if four Cobra probes are used then probe 1 would be A, probe 2 would be B and so on. .TH files are converted to .ap files through TFI software. As discussed, Cobra probes are individually calibrated before use, primarily by TFI when the probe is purchased. A comparison to assess calibration of all University of Birmingham Cobra probes is given in appendix A.

The .ap file consists of a series of lines giving the Cobra probe name and a summary of user inputted variables, followed by a series of columns for u , v , w and p . Further auxiliary inputs associated to light sensor position finders are outputted in separate .TH files which are again converted to .ap files. The .ap file can be imported directly into Matlab and processed as any standard data file (figure 4.1).



```

DS_WKP3_consist_3_5 (Ve).ap - Notepad
File Edit Format View Help
Device type : Four-hole Cobra Probe
Device ID : 265

Number of samples : 51,200
Output data rate (Hz) : 2,500.0
Output block size : 2,048
First sample date : 12-Feb-13
First sample time : 15:37:51.027
Has reference pressure : No

U (m/s) V (m/s) W (m/s) Pstatic (Pa)
0.00 0.00 0.00 0.0
0.00 0.00 0.00 0.0
0.00 0.00 0.00 0.0
0.00 0.00 0.00 0.0
0.00 0.00 0.00 0.0
0.00 0.00 0.00 0.0
0.246 -0.0545 -0.0461 -0.1
0.266 0.0117 0.0336 -0.1
0.341 -0.0394 -0.0339 -0.1
0.313 -0.141 -0.0686 0.0
0.00 0.00 0.00 0.0
0.173 0.0757 0.103 0.0
0.263 -0.0943 0.0289 0.0
0.00 0.00 0.00 0.0
0.00 0.00 0.00 0.0

```

Figure 4.1: TFI .ap file format. A series of summary lines are given at the top of the file, followed by a series of columns containing u , v , w , p and any auxiliary inputs.

4.2.2 Full scale data conversion

Full scale slipstream data is continuously recorded and saved into .CSV files automatically every hour by custom acquisition software (Baker and Quinn, 2012). A Matlab script was developed to isolate the train nose pressure transient, similar to the passenger train methodology carried out by Baker and Quinn (2012). Once isolated, the time at which the data was recorded is cross referenced against the experiment log and freight train data saved as a .dat file separately. Isolated train files included 60 seconds of data before the train nose and 90 seconds following the nose passage.

Each .dat file includes a sample number column followed by u , v , w data from anemometer V1, then P1 and P2 raw voltage pressure data. The anemometer outputs data in a converted form of three components of velocity, whereas the pressure probe data must be converted from voltage to pressure using equation 4.1,

$$\Delta P_i(t)|_r = P_{cf}(\text{Vol}_i(t)|_r - \text{Vol}_0|_r) \quad (4.1)$$

where r is an individual run, $\Delta P(t)$ is the converted differential pressure and P_{cf} is

the pressure transducer calibration factor; for the Honeywell 164PC01D37 differential pressure transducer $P_{cf} = \pm 441.5\text{Pa}$ per volt (Honeywell, 2013). Vol_i is the measured voltage for $i = 1, 2$ corresponding to pressure probes P1 and P2. Vol_0 is the zero offset voltage, calculated by averaging over the first 1000 samples (20 seconds) in each pressure trace, effectively calculating an average voltage in ambient conditions before the train influence.

Sections 3.3.2.2.1 and 3.3.2.2.2 discuss the ultrasonic anemometer and pressure transducer calibration methodology respectively. For this study full scale measuring equipment was calibrated at the University of Birmingham before the experiment was carried out.

4.3 Non-dimensionalised variables

Sampled data is given in terms of a sample number N_{samp} which is converted to time using,

$$t_{samp} = \frac{N_{samp} - 1}{f_{samp}}, \quad (4.2)$$

where $N_{samp}=1,2,\dots$ is the sample number and f_{samp} is the sampling frequency. For the model scale data $f_{samp}=2500\text{Hz}$ whereas for full scale data $f_{samp}= 50\text{Hz}$.

For analysis purposes the data is realigned (section 4.4) with the sample point at which the Class 66 nose passes the measuring position defined as $t = 0$. By the process of realigning the data, time is also realigned to measurements about the train nose, rather than measurement from the time series beginning. Therefore as the origin for time is shifted to be aligned by the train nose the ‘*samp*’ subscript is dropped.

Throughout this study slipstream velocity and pressure data is presented in terms of a non-dimensionalised coefficient, unless otherwise stated. The convention of non-dimensionalising data conforms with previous slipstream studies (Baker et al., 2001; Sterling et al., 2008). Data is normalised with respect to train speed for each individual

run, $V_{train}|_r$ (Deeg et al., 2008),

$$U(t)|_r = c_u(t)|_r = \frac{u(t)|_r}{V_{train}|_r} \quad (4.3)$$

$$V(t)|_r = c_v(t)|_r = \frac{v(t)|_r}{V_{train}|_r} \quad (4.4)$$

$$W(t)|_r = c_w(t)|_r = \frac{w(t)|_r}{V_{train}|_r} \quad (4.5)$$

$$C_p(t)|_r = c_p(t)|_r = \frac{P(t)|_r - P_{AMB}|_r}{\frac{1}{2}\rho_r V_{train}^2|_r} \quad (4.6)$$

where r is the individual run number and $u(t)$, $v(t)$, $w(t)$ are the instantaneous velocities at time t in the x , y and z directions respectively and $P(t)$ is the instantaneous pressure at time t . P_{AMB} denotes atmospheric pressure, measured by a GBP3300 Digital Barometer at model scale, whereas for the full scale experiment $(P(t) - P_{AMB}) = \Delta P(t)$, as in equation 4.1. Air density ρ is calculated by (TSI, 2008),

$$\rho = \frac{P_{AMB}}{RT_{room}}, \quad (4.7)$$

where the gas constant $R = 287\text{J}/(\text{kgK})$ and T_{room} is the temperature measured in Kelvin. An analysis using the partial pressure form of equation 4.7 found minimal differences of $\sim 1\%$ in the value of ρ (Picard et al., 2008).

As train speed differs for each run this creates small differences in measuring position along the train with respect to the sampling frequency. For example a train travelling at either end of a $V_{train} = 20 \pm 0.5\text{m/s}$ speed window covers a distance of 4.05m (model scale short train length) in 0.208s and 0.198s respectively, which for a sampling frequency of 2500Hz is a difference of 25 samples. Therefore to negate differences in train speed the data is resampled to a nominal train speed of $V_{train} = 20\text{m/s}$ for model scale and $V_{train} = 33.5\text{m/s}$ for full scale.

Firstly t is converted to a time for each run by,

$$t_r = \frac{t V_{train}|_r}{V_{train}}, \quad (4.8)$$

where r is the run number, e.g. for model scale experiments $r=1,2,\dots,25$. $V_{train}|_r$ is the train speed for each individual run and V_{train} is the nominal train speed. Equation 4.8 effectively alters the sampling frequency for each run to account for small changes in train speed. The normalised velocity and pressure data is then resampled using a linear interpolation method at the original sampling frequency, $f=2500\text{Hz}$ for model scale and $f=50\text{Hz}$ for full scale, thus giving a series of data for a nominal train speed V_{train} recorded at a sampling frequency f with a common time t .

For the purpose of this study, time is converted to distance travelled,

$$x = t V_{train}, \quad (4.9)$$

where V_{train} is the nominal train speed. The data is presented in terms of distance x , where $x = 0$ is the point at which the Class 66 nose passes the measuring position. For the model scale data x is multiplied by 25 to give results in terms of full scale distance for analysis purposes. Where direct comparisons are made, both model and full scale data are resampled with respect to the maximum UK freight line speed $V_{max} = 33.5\text{m/s}$.

4.4 Data alignment

Experimental data for velocities and pressure are aligned with respect to the train nose passing at the origin, indicated by the point at which pressure crosses the x-axis between the maximum positive and negative pressure peaks created about the train nose (figure 4.2).

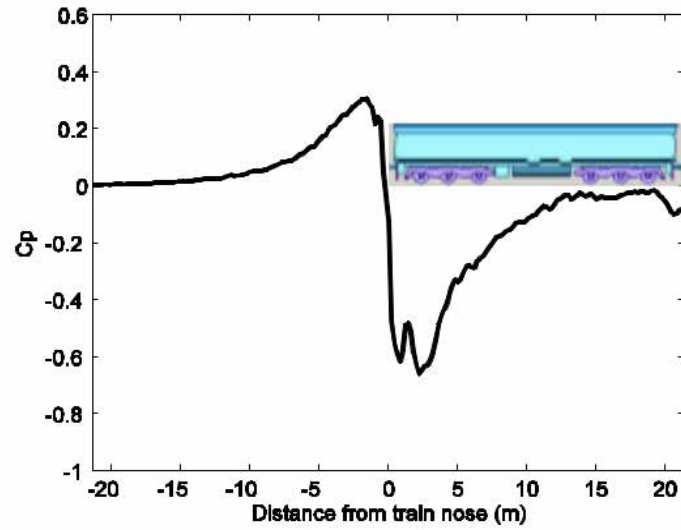


Figure 4.2: Illustration of how the data is aligned to the point at which pressure crosses the x-axis between the maximum positive and negative pressure peaks.

The choice of data alignment method was made in relation to a series of tests using a light sensor. As part of the TRAIN rig slipstream experiments a light source and detector were connected to an auxiliary channel in the Cobra probe data logger. The light source was positioned so that the light beam was in line with the measuring face of the Cobra probe head. This created an event finder for the train nose, outputting a time series recorded alongside Cobra probe data allowing velocity and pressure data to be aligned with respect to the auxiliary channel data. Results showed the zero crossing between the maximum positive and negative pressure peaks to be the point at which the train nose passes the Cobra probes.

4.5 Uncertainty analysis

An uncertainty analysis for the slipstream velocities and static pressure is presented in appendix B, the results of which are presented here. The true value of a physical or derived fluid property is in general an unknown quantity, estimated by recording a series of measurements. The difference between the measured and true value is defined as the

measurement error, quantified by calculating the measurement uncertainty (Tavoularis, 2005). Estimate values for the total error are calculated by a methodology developed by Taylor (1997) and Tavoularis (2005), taking into account the uncertainty associated with the equipment used to take the measurements through propagation of error theory (bias limit), as well as a quantification of the random uncertainty of results.

The uncertainties associated with the slipstream experiments are calculated in terms of maximum values for velocities and static pressure, in line with the TSI methodology and previous slipstream studies (Gil et al., 2010; Baker et al., 2012). The method of calculating uncertainties, adopted from the methodology presented for surface pressure coefficients in Dorigatti (2013), presented in terms of a bias limit and random uncertainty. The slipstream uncertainty analysis is presented for the 181.25m equivalent model train, for consists 1, 3 and 5, and also the full scale data.

The maximum and mean total uncertainties for the slipstream velocity and static pressure measurements are shown in table 4.1. Throughout this study experimental data is presented in terms of non-dimensional coefficients. The total uncertainties are expressed as a percentage error of the non-dimensional coefficient.

	Slipstream velocities		Static pressure	
	Mean	Maximum	Mean	Maximum
Consist 1	0.069	0.108	0.051	0.061
Consist 3	0.063	0.090	0.051	0.066
Consist 5	0.063	0.089	0.047	0.055
Full scale	0.098	×	0.045	×

Table 4.1: A table of mean and maximum total uncertainties for slipstream velocities and static pressure for each container loading configuration tested at model scale for the 181.25m train and mean values at full scale.

The values in table 4.1 provide an estimate to the uncertainties for slipstream velocity and static pressure measurements at model and full scale. The uncertainties are considered to be conservative estimations to the true error. Analysis in appendix B discusses the relative influence of the bias limit and random uncertainty in relation to the total uncertainty. Results show for all consists at both model and full scale the

bias limit values are relatively small in comparison to the random uncertainty. At full scale the lack of consistent freight types creates different flow development for each run measured. This creates a large standard deviation of maximum resultant velocity measuring position and magnitude, which is dependent on train type and loading configuration. At model scale the maximum resultant velocity is measured in the nose region, whereas at full scale values are either measured in the nose or boundary layer regions. The uncertainty in measuring position and magnitude increases the random uncertainty. However, for static pressure all measurements for the uncertainty analysis are taken in the nose region at both model and full scale, therefore similarity in results is observed; values are relatively small suggesting good agreement between maximum and minimum values of individual runs. In comparison to slipstream velocities the values for random uncertainty in static pressure are smaller. Results presented in table 4.1 for slipstream uncertainties exhibit similar values to previous studies (Baker et al., 2012; Dorigatti, 2013).

4.6 Wavelet analysis

In chapter 5 a discussion regarding the frequency content of slipstream velocities is carried out. For stationary flows Fourier transforms can be used to find frequency information for the infinite time domain. However for non-stationary flows, as frequencies are not present for all time, a method of transforming to a time-frequency domain is needed, this method is wavelet analysis (Torrence and Compo, 1998). To understand wavelet analysis it is important to introduce the developments from Fourier analysis which have led to wavelet analysis. Section 4.6.1 presents an introduction to the relevant theory needed to understand the wavelet analysis discussed in chapter 5.

4.6.1 From Fourier transforms to Wavelet analysis

Most signals are initially measured within the time domain, thus the signal is a function of time, usually plotted against amplitude or another dependent variable. In many cases to fully understand the information contained within a signal it is important to transform to a frequency domain and analyse the frequency spectrum, most commonly by a Fourier transform. A Fourier transform decomposes signals into complex exponential functions of different frequencies. The Fourier transform and inverse transform are defined as (Polikar, 2006),

$$W(f) = \int_{-\infty}^{\infty} w(t)e^{-2i\pi ft} dt, \quad (4.10)$$

$$w(t) = \int_{-\infty}^{\infty} W(f)e^{2i\pi ft} df, \quad (4.11)$$

where t is time, f is frequency, w is the signal in the time domain and W the signal in the frequency domain. It is possible to use Fourier transforms for non-stationary signals to find the spectral components but not the time at which these components occur.

As discussed, the problem associated with Fourier transforms is the lack of knowledge of which frequencies occur at which times for non-stationary flows. It is however possible to alter the Fourier transform process to solve this problem. The short time Fourier transform assumes parts of a non-stationary signal are stationary by using narrow windows to portion the signal into stationary windows. The window function ω is chosen with window width equal to the size of the stationary segment needed within the signal. The short time Fourier transform is defined as the Fourier transform

multiplied by a window function $\omega(t)$ (Polikar, 2006),

$$STFT_W^{(\omega)}(t, f) = \int_t [w(t)\omega^*(t - t')] e^{-2i\pi ft} dt, \quad (4.12)$$

where $w(t)$ is the signal, $\omega(t)$ is the window function, t' is the window position and $*$ is the complex conjugate. The solution of equation 4.12 results in a transformation from the time domain to a time-frequency domain.

There are however problems associated with the short time Fourier transform stemming from the ‘Heisenberg Uncertainty Principle’. The principle states that an exact time-frequency representation of a signal is not possible, but a representation in regards to time intervals for certain frequencies is possible (Polikar, 2006). This creates a resolution problem in relation to the selected window function width. As the window is of finite length it only covers a certain section of the signal, allowing a time-frequency representation but creating poor frequency resolution. This allows bands of frequencies to be observed, not exact spectral components, leading to the paradox of window width; an infinite width window allows perfect frequency resolution but no time information, however a smaller width window allows for time information but reduced frequency resolution (Polikar, 2006).

A partial solution to this paradox is to use Wavelet analysis which uses multi-resolution analysis to analyse the signal at different frequencies with different resolutions, differing from short time Fourier analysis as every spectral component is not resolved equally (Polikar, 2006). The method of multi-resolution is designed such that for high frequencies the transform gives good time resolution but poor frequency resolution, and for low frequencies gives good frequency but poor time resolution (Polikar, 2006).

The continuous wavelet transform is defined as the inner product of the signal $w(t)$ and an analysing wavelet (Polikar, 2006),

$$CWT_w^\psi(\tau, s) = \Psi_w^\psi(\tau, s) = \frac{1}{\sqrt{|s|}} \int w(t)\psi^*\left(\frac{t - \tau}{s}\right) dt, \quad (4.13)$$

where τ is the translation parameter, s is the scale parameter and $\psi(t)$ is the mother wavelet transforming function. The wavelet is a small wave with a characterised finite length set by the function. The scale parameter s is the inverse of frequency $\frac{1}{frequency}$ and has the effect of compression or dilation on a transform. Thus for high scales where $s > 1$ the transform is a dilated view, however for low scales $s < 1$ the transform is more detailed compressed view.

The mother wavelet is the function from which all the wavelet functions in the transformation are defined. The mother wavelet is dilated, compressed and translated throughout the wavelet analysis. There are many different mother wavelets including the Morlet wavelet and DOG wavelet, the choice of these depends on the signal $w(t)$. For this study a series of mother wavelets were tested, however in line with previous studies the Morlet wavelet is shown to be most appropriate (Torrence and Compo, 1998; Baker et al., 2001; Gil et al., 2008).

Once the mother wavelet is chosen a starting scale is defined and substituted into equation 4.13, multiplied by the signal $w(t)$. The integration in equation 4.13 is multiplied by $\frac{1}{\sqrt{|s|}}$, to normalise the energy so that the transform will have the same energy at every scale (Polikar, 2006). If the signal has a frequency corresponding to the current scale of mother wavelet then a relatively large number is calculated for the time at which the frequency occurs, and visa versa (Polikar, 2006). The process is repeated until the wavelet reaches the end of the signal for all measured scales for all time. The resulting set of data is a time-scale representation of the signal, which can be converted to a time-frequency representation as $s = \frac{1}{frequency}$.

Chapter 5

Slipstream data analysis, results and discussion

5.1 Introduction

In this section the analysis and results from the freight slipstream experiments will be discussed. Throughout the analysis model scale results are presented in terms of a series of container loading configurations defined as consists 1 to 5, in figure 3.8, measured at a series of probe positions defined in table 3.1. Results will be presented in terms of the equivalent full scale distances in various flow regions at train side and above train roof (sections 5.3-5.4). Firstly a comparison of flow development for different loading efficiencies is undertaken. By expanding this comparison and focusing on key flow regions (section 5.6), conducting a series of analyses including displacement thickness, turbulence intensity and autocorrelation calculations, a thorough view of slipstream development for a Class 66 hauled container freight train and the influencing factors on slipstream development is possible. Section 5.7 discusses the influence of train speed on slipstream development at model scale. Finally comparisons are made between full and model scale data with conclusions drawn on the suitability of using model scale experiments to understand freight slipstream development (section 5.8).

5.2 Ensemble averaging

European TSI standards state an experiment should be conducted at least 20 times to validate results and create ensemble averages (Gil et al., 2008). Ensemble averaging is a method based on the assumption of the existence of independent statistical events (George, 2004). Experimental data may have considerable test to test differences, inhibiting averages to be taken by a normal method. The results gained from experiments can be non-dimensionalised and averages constructed using non-dimensional coefficients (Temple and Dalley, 2001; Deeg et al., 2008).

To non-dimensionalise velocity and pressure a standard reference speed can be used to normalise in relation to the varying local train speed, as in equations 4.3–4.6 (Baker et al., 2001). It is assumed that a signal $c(x)$ is measured n times with respect to an axial coordinate position x , relating to a defined position along the train. The ensemble average $\bar{c}(x)$, variance $var(x)$ and standard deviation $\sigma(x)$ are then defined as (Deeg et al., 2008),

$$\bar{c}(x) = \frac{1}{n} \sum_{r=1}^n c_r(x), \quad \overline{c^2} = \frac{1}{n} \sum_{r=1}^n c_r^2(x), \quad var(x) = \overline{c^2} - \bar{c}^2 \quad \sigma(x) = \sqrt{\overline{c^2} - \bar{c}^2}, \quad (5.1)$$

where r is the r^{th} passage of a train and n denotes the number of independent measurements, or the ensemble size.

To understand the effect of ensemble averaging consider figure 5.1. Figure 5.1 shows the normalised longitudinal component of velocity U , for all 25 runs undertaken for the full scale equivalent 101.25m freight consist 5 measured at probe position 2 for train speed 20m/s. It is clear to see the run to run differences, especially in the boundary layer region.

Figure 5.2 and 5.3 illustrate a series of images with increasing number of runs added to the ensemble for consist 5 at probe 2 for train speed 20m/s. Figure 5.2(a) shows a single run for consist 5. In figure 5.2(b) two individual runs of data and the ensemble

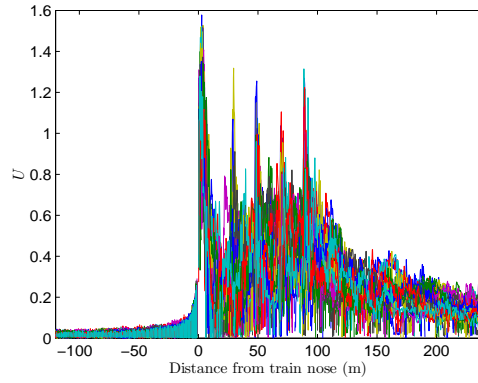


Figure 5.1: Run to run variability in 25 runs of data for consist 5 for the 101.25m train recorded at probe position 2 at train speed 20m/s.

average for the two runs are plotted. This method continues, including a five run (figure 5.2(c)), ten run (figure 5.2(d)), fifteen run (figure 5.2(e)) and finally the twenty five run ensemble (figure 5.2(f)).

It is clear to see in figure 5.3 as the number of runs contained in the ensemble increases the variability of the mean decreases. By creating an ensemble average it is possible to pick out key statistical events in the flow, such as the nose/tail regions and the influence of container loading positions on coefficient of pressure and normalised velocities.

An issue associated with the ensemble averaging process and Cobra probe results is the $\pm 45^\circ$ cone of influence, which if exceeded creates a zero in the outputted time series. In figure 5.2 it is possible to observe a region of no data about the train nose. As flow separates from the leading edge of the train nose (section 5.6.1) there is a flow reversal which cannot be recorded by the Cobra probe, due to the $\pm 45^\circ$ cone of influence. There are also sections of zeroes recorded in the boundary layer region associated with the highly turbulent nature of this region.

To eliminate the Cobra probe cone of influence issue in relation to the ensemble average, the zero data is disregarded in the ensemble calculation. For example consider a time step within the matrix of time series recorded for the 25 runs. At this time step, due to the 3-dimensional complexities of the flow, the time step has 16 runs of non-zero data and 9 runs with a zero recorded. If the zeroes are included in the ensemble size

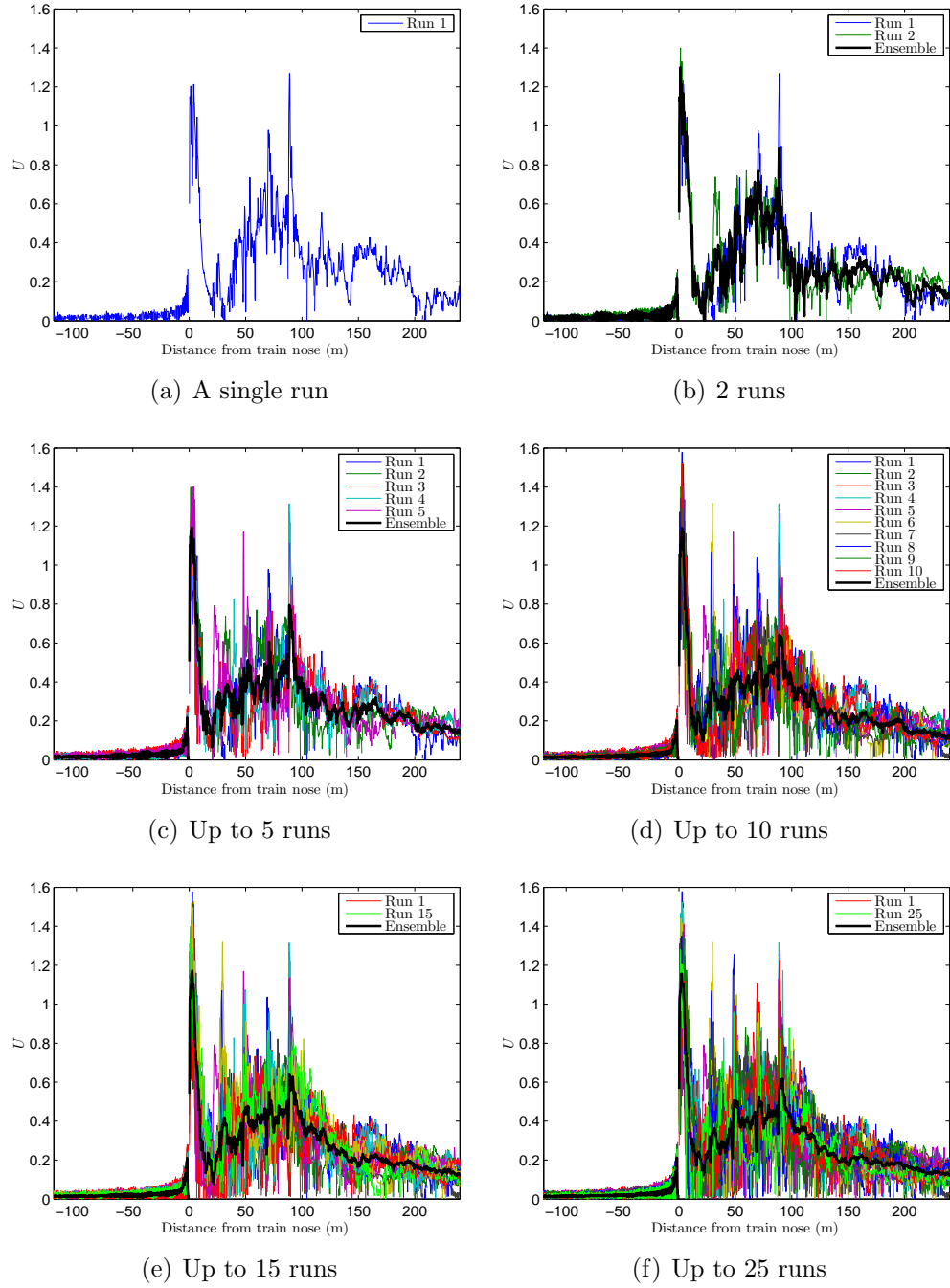


Figure 5.2: A series of figures to illustrate the process of ensemble averaging using normalised longitudinal velocity U data from probe 2 for consist 5 for the 101.25m train. In each plot the individual data for each run is plotted with the ensemble average of all the data (thick black line).

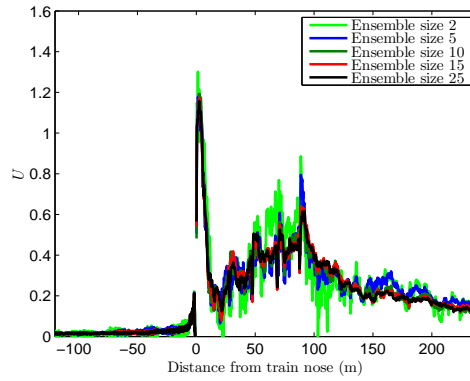


Figure 5.3: An illustration of the effect of increasing ensemble size on the ensemble average for the normalised longitudinal velocity U data from probe 2 for consist 5 for the 101.25m train.

to create the average at this time step it will intuitively give a false answer. Therefore a moving ensemble size at each time step is employed to the ensemble average, thus in the example above the ensemble size at this time step would be 16 not 25. If a zero is recorded for every run at a time step, the measured region is considered individually; either the region is in still air before the train, or the region is highly turbulent and a possible flow reversal has occurred.

It is important to understand the differences created by employing a moving ensemble size in relation to a fixed ensemble size on the magnitude of normalised velocities and the coefficient of pressure. By calculating the percentage difference at each time step between the normalised ensemble velocities and coefficient of pressure for consist 5 for a moving ensemble size and a fixed ensemble of 25 it will be possible to analyse differences created. Consist 5 was chosen for this analysis as the largest variations in normalised velocities and coefficient of pressure are witnessed for this loading configuration. In the region of the train (i.e. from 0m to 101.25m) an average percentage difference of 10% is observed, with a minimum to maximum difference range of 50%. Therefore by including the zero data with an ensemble size of 25 the ensemble average magnitude is significantly smaller than when calculated with a moving ensemble size. For consists with higher loading efficiency the average percentage difference value decreases.

The moving ensemble size method in turn has a series of issues for analysis of data.

European TSI standards state an experiment should be conducted at least 20 times to create an ensemble average without the influence of run to run variability (TSI, 2008; Gil et al., 2008). To analyse this in respect to the results from the TRAIN rig experiment, the mean, maximum and minimum ensemble sizes and the percentage of time steps with ensemble size greater than or equal to 20 are shown in table 5.1 for consists 1 and 5 on the 101.25m freight model measured at probe positions 1 to 4 (table 3.1) for various flow regions. Consist 1 and 5 have been chosen to represent the extremes of loading efficiency for this analysis.

It is clear from table 5.1 that the ensemble size varies dramatically with position. The average ensemble size is much smaller in the upstream region in comparison to the train and wake regions. Intuitively this is expected as in the upstream region velocities and pressure should be zero, therefore any readings taken are very small and relate to ambient fluctuations within the TRAIN rig. As the distance along the train is increased the ensemble size increases. In the nose region, as discussed, there is a flow reversal following separation from the leading edge of the train nose, accounting for the small minimum ensemble size of 1 for many of the probes. If the nose region is taken out of the train flow (i.e. boundary layer region) the minimum ensemble size increases to 10 samples.

The ensemble size is also affected by probe position. Probe 2 has the highest ensemble size for both consists, suggesting that as distance from train side is increased the disturbance to the air is lower and towards the cut-off range of the Cobra probe. The mean ensemble size is not affected by consist type; this remains true if all consist types are included.

By calculating the percentage of time steps with ensemble size greater than or equal to 20 it is possible to analyse the effect of the moving ensemble size in relation to the ensemble average. For all regions the percentage of time steps greater than or equal to 20 is 53.5%, however if the upstream region is removed this increases to 75%. By altering the ensemble size criteria it is possible to see that over 80% of time steps in

		Consist 1				Consist 5			
		1	2	3	4	1	2	3	4
All regions	Mean	17.527	19.293	18.361	17.259	17.649	19.834	19.334	18.980
	Maximum	25	25	25	25	25	25	25	25
	Minimum	1	1	2	1	1	2	1	1
	Percentage ≥ 20	41.420	66.272	55.356	36.292	48.323	64.103	61.473	54.898
Upstream	Mean	12.832	12.588	12.947	13.406	12.580	12.903	13.039	13.718
	Maximum	25	25	25	25	25	25	25	25
	Minimum	3	3	2	4	1	4	3	5
	Percentage ≥ 20	7.101	12.821	18.146	5.917	9.467	5.523	9.073	7.298
Train Region	Mean	18.041	22.167	19.803	17.030	19.478	22.486	21.250	20.010
	Maximum	25	25	25	25	25	25	25	25
	Minimum	1	1	4	1	2	2	1	1
	Percentage ≥ 20	30.512	88.780	55.118	18.110	54.331	86.811	75.394	59.056
Boundary layer	Mean	17.395	22.042	19.501	17.019	19.133	22.654	21.547	20.416
	Maximum	23	25	25	23	25	25	25	25
	Minimum	10	14	11	9	9	12	11	10
	Percentage ≥ 20	19.613	88.862	50.363	16.223	49.395	88.862	78.208	63.196
Tail Region	Mean	21.709	23.130	22.337	21.348	20.906	24.116	23.720	23.226
	Maximum	25	25	25	25	25	25	25	25
	Minimum	12	17	17	14	14	20	20	18
	Percentage ≥ 20	86.614	97.244	92.717	84.843	81.299	100	100	98.425
									92.643

Table 5.1: Mean, maximum and minimum ensemble sizes, as well as the percentage of time steps with a ensemble size greater or equal to 20 for consist 1 and 5 at probe positions 1 to 4 at train speed 20m/s. The analysis is broken into a series of flow regions; upstream -120 to 0m, train region 0m to 101.25m, boundary layer region 18.75m to 101.25m and tail region 101.25m to 240m.

the train region have an ensemble size of 17 or greater. If the percentage difference is calculated between the ensemble average for an ensemble size of 17 and 20 a maximal difference of less than $\pm 2\%$ is found; similar to the error range of the Cobra probe. It is therefore concluded that the method of a moving ensemble size for the process of ensemble averaging is suitable for TRAIN rig data collected using the Cobra probe. The discussion of ensemble stability is discussed further in appendix D.

5.3 Coefficient of pressure

5.3.1 Train side

Figure 5.4 shows the ensemble coefficient of pressure for the 101.25m train with consists 1 to 5 measured at probe positions 2 to 4. As in previous slipstream studies the flow can be split into a number of key regions; upstream, the nose, boundary layer, tail and wake (Baker et al., 2001). As the leading vehicle of the train is always the same (Class 66 locomotive) the upstream and nose regions are essentially the same for each consist, with small differences due to statistical run to run variability as discussed in section 5.2.

Upstream of the train the coefficient of pressure is zero, as would be expected. Ahead of the train nose there is a positive peak in coefficient of pressure, to a maximum of 0.4 close to the train side. This is followed by a negative peak in coefficient of pressure, on average to a minimum of nearly twice the magnitude at -0.7, following the passage of the train nose.

It should be noted that between the positive and negative coefficient of pressure peaks there is a section of no data. In the nose region the highly three-dimensional flow is beyond the ± 45 degree cone of influence capability of the Cobra probe. In the raw data this is seen as a series of zeroes, which throughout this study are disregarded (section 5.2).

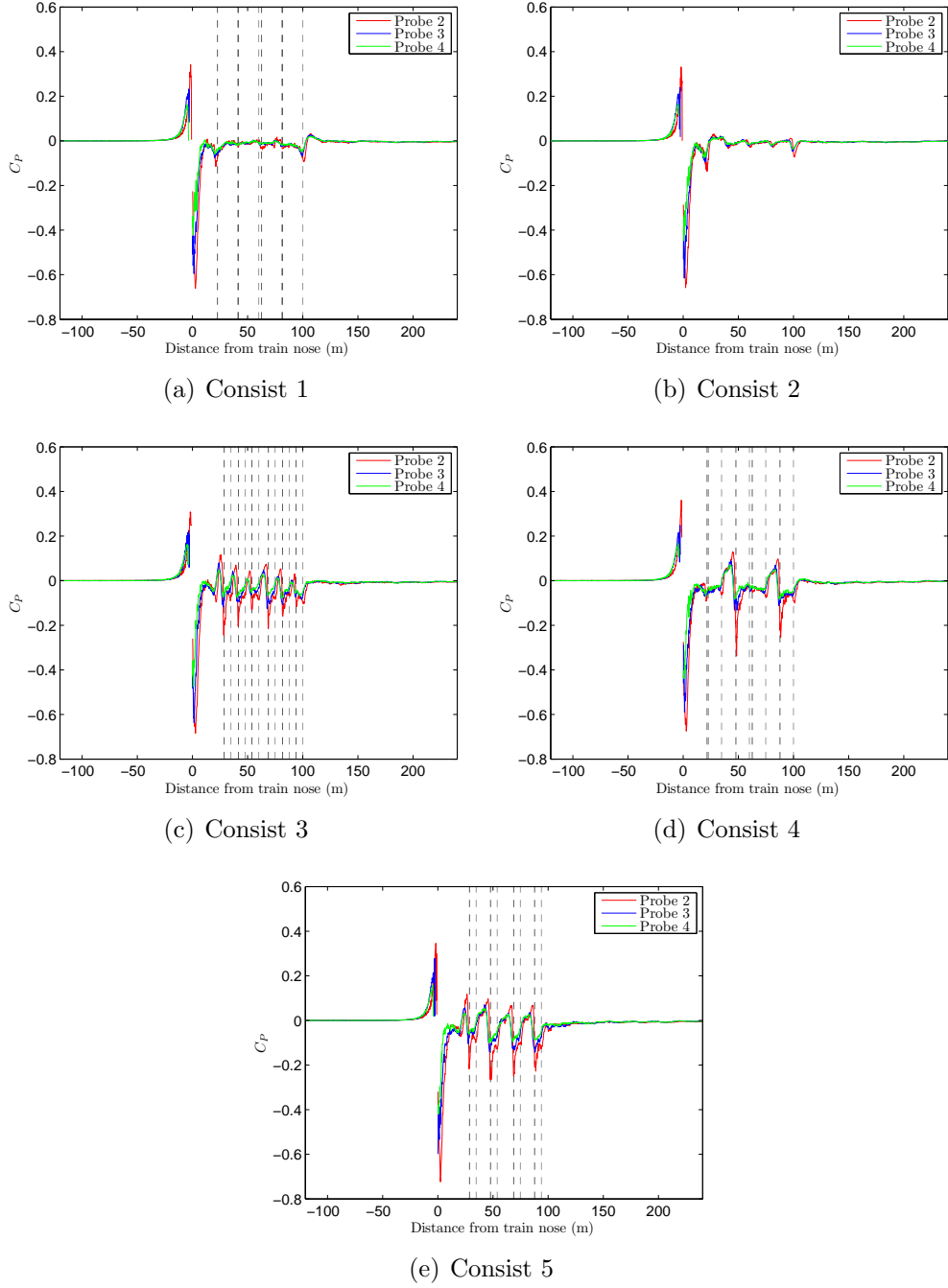


Figure 5.4: Coefficient of pressure for freight consists 1 to 5 for train lengths 101.25m, measured at train speed 20m/s for probes 2 (red), 3 (blue) and 4 (green) at the side of the train. The vertical dashed lines indicate the front (black) and rear (grey) faces of the containers.

The train nose is seen to pass the measuring point when the coefficient of pressure passes through zero between the positive and negative peaks. The nose region extends from $\pm 18.75\text{m}$ at full scale, nearly the total length of the Class 66 locomotive. The magnitude of peaks in this region are unlike those seen previously in passenger studies (Baker et al., 2001; Hemida et al., 2010), however it was shown in Baker et al. (2012) that the Class 66 created much greater nose peak magnitudes than either a Class 390 or Class 158 passenger train on trackside structures. For example the nose pressure coefficient magnitudes measured on a trackside hoarding 1.4m from the centre of track at a height of 0.25m from the top of the rail for a Class 390, Class 158 and Class 66 are shown in table 5.2 (Baker et al., 2012). Similar pressure coefficient magnitudes are observed for the Class 66 data in table 5.2 and figure 5.4. It is suggest that the magnitude of coefficient of pressure in this region is closely related to the shape of the train nose, which for the Class 66 is highly bluff.

Train type	Coefficient of pressure	
	Positive peak	Negative peak
Class 390	0.28	-0.18
Class 158	0.35	-0.25
Class 66	0.52	-0.6

Table 5.2: Nose coefficient of pressure peaks measured on a trackside hoarding placed 1.4m from the centre of track and 0.25m above the top of the rail for a Class 390, Class 158 and Class 66 (Baker et al., 2012).

In the boundary layer region differences in container loading efficiency can clearly be seen. For consist 1 the coefficient of pressure stabilises to zero following the nose region, with disturbances due to the small gaps between the loaded containers. The fully loaded configuration acts similarly to a passenger train with inter-carriage gaps (Hemida et al., 2010). Similarly for consist 2 following the Class 66 the coefficient of pressure stabilises to zero, however small disturbances are larger than those seen for consist 1. It is thought that these small disturbances are created due to a modelling issue regarding the attachment of trailing wheels, creating a series of 15mm high displacements from the aluminium plate.

For consists 3, 4 and 5 the influence of larger spaces between loaded containers creates a series of positive and negative peaks, similar to the nose region, about the lead face of each container. At the rear face of the container a smaller negative peak is observed. Between loaded containers the coefficient of pressure increases to the positive peak seen before the face of the following container.

The magnitude of pressure coefficient peaks associated with the lead face of loaded containers are affected by space size between containers. Consist 3 and 5 loading configurations are formed of a series of 6.096m containers, however the space between containers is much larger for consist 5 than 3. A similar flow pattern to the nose region is observed at the lead face of each container. For consist 5 (figure 5.4(e)) larger spaces between containers creates peaks with larger magnitudes than consist 3 (figure 5.4(c)). This is also observed for consist 4, loaded with containers with both large and small spaces between. For closely loaded containers the influence of small spaces on the coefficient of pressure is similar to the fully loaded configuration; however following a larger space the characteristic flow pattern about the leading face of a container is observed.

The influence of wagon design in relation to the coefficient of pressure is apparent for consist 3. The FEA-B wagon is designed as a twin set wagon, i.e. two wagons constantly joined together. FEA-B wagons are designed with the braking mechanisms situated at the outer end of each twin wagon set, thus the space between two wagons in a twin is smaller than the space between two twin sets. For consist 3 the influence of the larger space between two wagon sets creates a larger disturbance in coefficient of pressure within the boundary layer in comparison to the space between wagons in a twin set (figure 5.4(c)).

In the tail region a reversal of the nose region is witnessed, with a negative peak followed by a positive peak, however much smaller in magnitude. The characteristic tail region flow pattern has previously been observed in passenger train studies with a much greater magnitude, of order similar to passenger nose region peaks. It is suggested

that the difference between passenger and freight tail regions are due to tail shape. The tail feature is also affected by container loading. For consists 1, 3 and 4, with a loaded container close to the train tail, the tail feature is more defined than for consists 2 and 5 without.

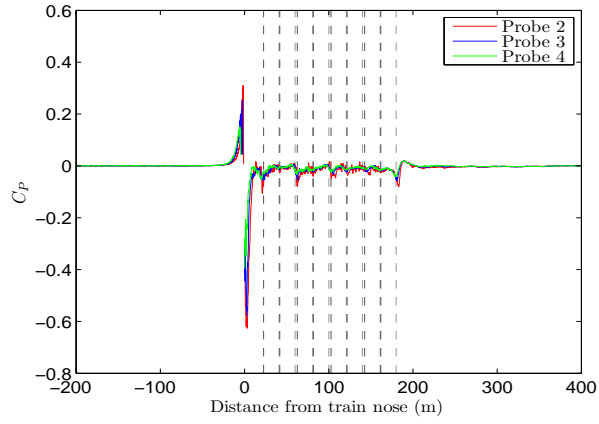
In the wake region the coefficient of pressure stabilises to zero within 20m of the train tail for all consists. As the measuring distance from centre of track is increased the magnitude of coefficient of pressure decreases for all loading configurations.

Figure 5.5 illustrates the coefficient of pressure for consists 1, 3 and 5 with train length 181.25m, measured at probe positions 2 to 4. It is clear to see the characteristic flow pattern is extended for the lengthened train in comparison to results seen in figure 5.4. For consists 3 and 5 the pressure gradient between peak magnitudes at container lead faces is much larger than at container rear faces, suggesting a much larger deformation in the air at the lead face in comparison to the rear face. For the longer train peak magnitudes witnessed at container lead faces decrease slightly after 100m (wagon 5 in the consist), suggesting a possible transition between boundary layer growth and stability.

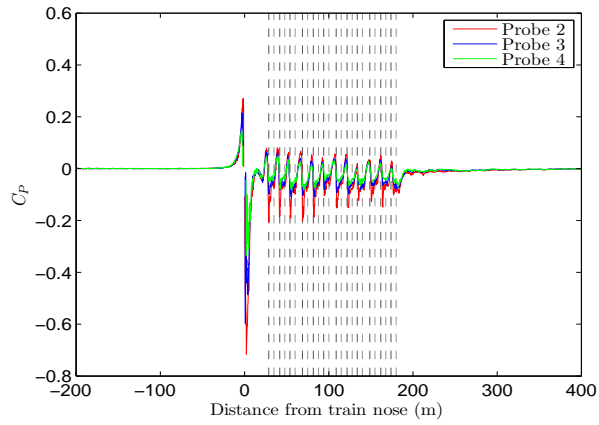
5.3.2 Train roof

Figure 5.6 shows the coefficient of pressure for train length 101.25m for consists 1 to 5 measured at probe position 1 above the train roof. A similar series of flow regions to the train side are witnessed above the train roof.

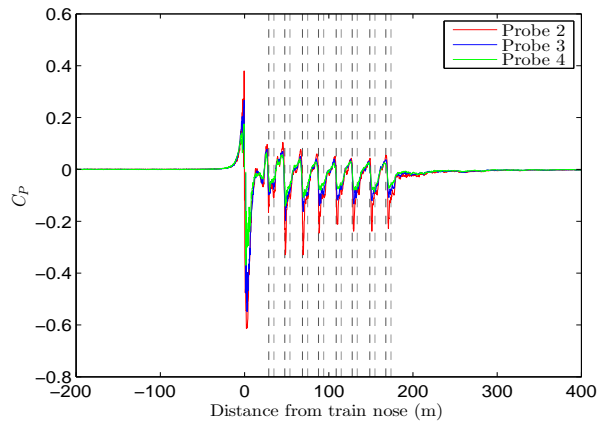
Upstream of the train coefficient of pressure is zero, again as would be expected. The characteristic nose flow pattern is observed, however with different maxima to those at a similar distance from train side. The positive peak magnitude is similar to probes 3 and 4, but much lower than probe 2, whereas the negative peak magnitude is similar to probe 2. It is hypothesised that differences between positive coefficient of pressure



(a) Consist 1



(b) Consist 3



(c) Consist 5

Figure 5.5: Coefficient of pressure for freight consists 1, 3 and 5 for train lengths 181.25m, measured at train speed 20m/s for probes 2 (red), 3 (blue) and 4 (green) at the side of the train. The vertical dashed lines indicate the front (black) and rear (grey) faces of the containers.

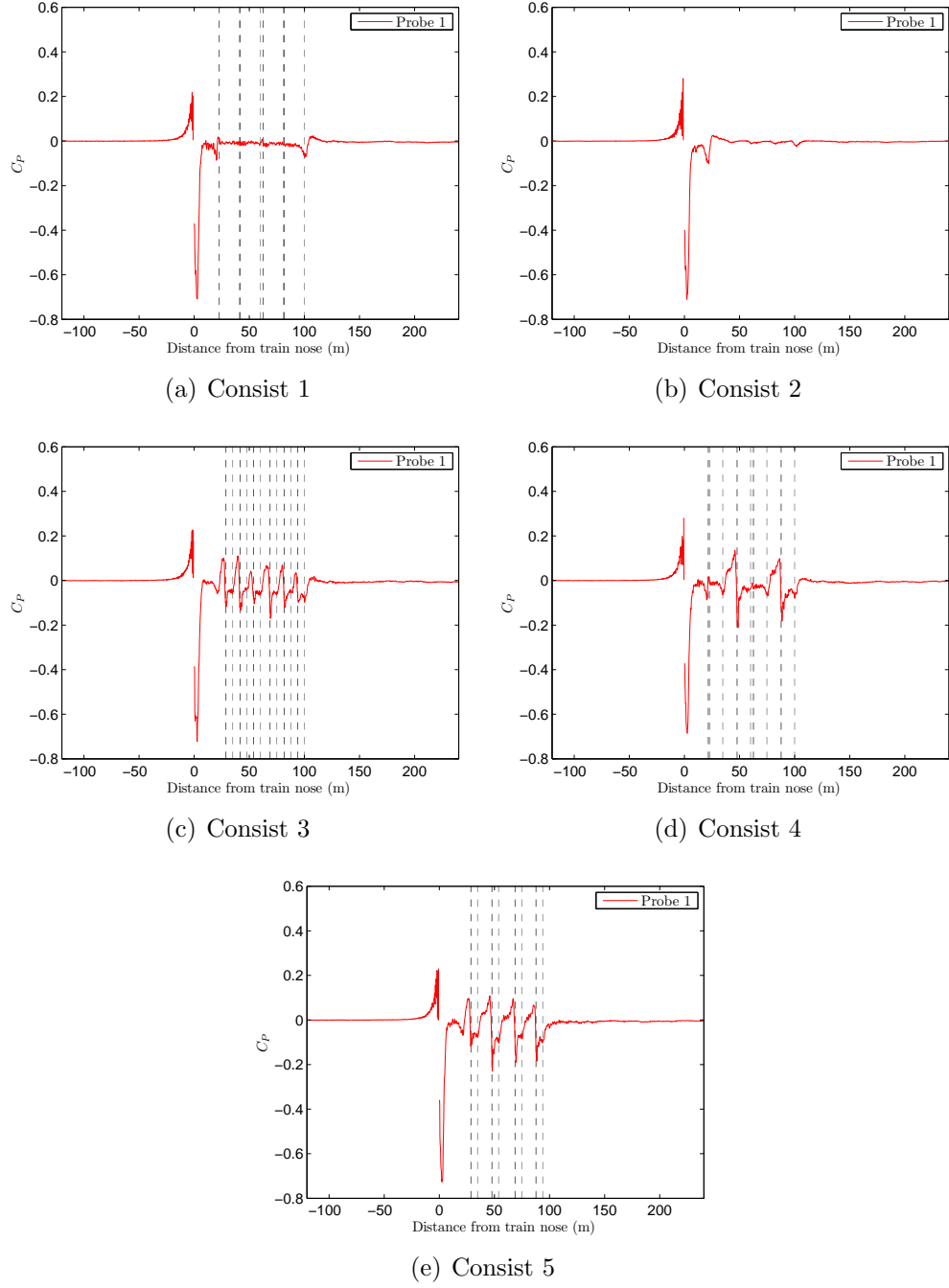


Figure 5.6: Coefficient of pressure for freight consists 1 to 5 measured at train speed 20m/s for probe 1 (red) above the train roof. The vertical dashed lines indicate the front (black) and rear (grey) faces of the containers.

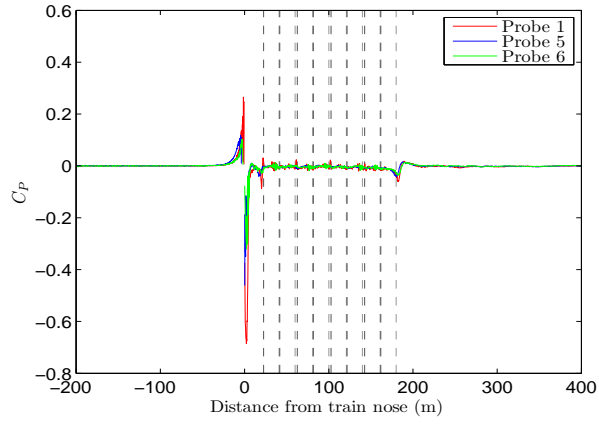
peak magnitudes above the train roof and train side are due to the concave Class 66 nose shape and hooded section. The nose region extends from $\pm 18.75\text{m}$ at full scale.

In the boundary layer region differences between container loading configurations are observed again. Characteristic flow patterns at container lead faces observed at train side are seen above the train roof, with similar magnitudes to probe 3. Probe 1 is 600mm from the train surface, whereas probe 3 is 1150mm, indicating the magnitude of coefficient of pressure is lower above the train roof than at train side.

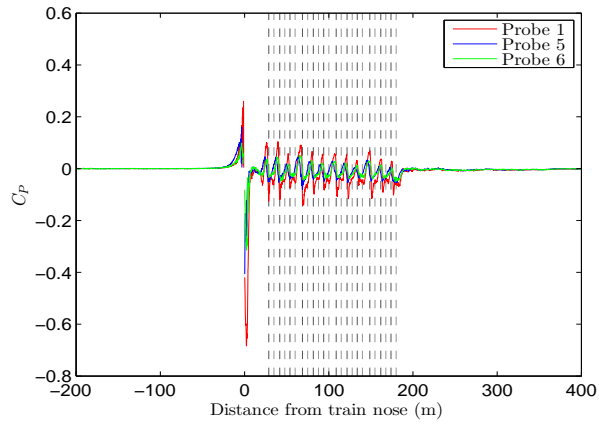
In the tail region a reversal to the nose region is observed; a negative peak followed by a positive peak, with similar magnitudes to the train side. The influence of containers loaded close to the train tail is also seen above the train roof as at train side. In the wake region the coefficient of pressure stabilises to zero within 20m of the train tail for all consists.

Figure 5.7 illustrates coefficient of pressure for probes 1, 5 and 6 above the train roof for consists 1, 3 and 5 with train length 181.25m. The characteristic flow pattern in the nose region is observed for all distances above the train roof, extending from $\pm 18.75\text{m}$ at full scale. In the boundary layer region the influence of spaces between containers creates a series of positive and negative peaks about the lead face of each container, with a smaller negative peak at the rear container face. Between loaded containers the coefficient of pressure increases to the positive peak seen before the face of the following container.

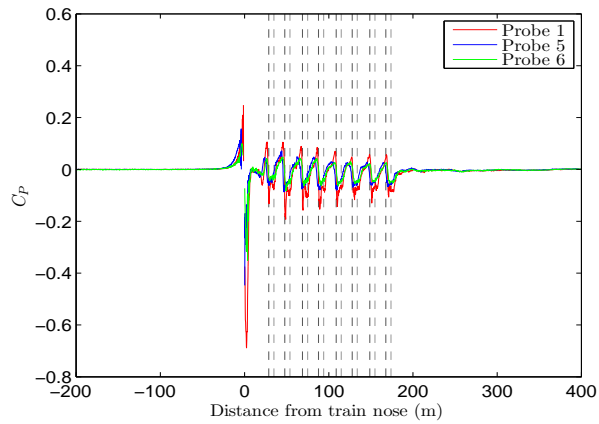
In the tail region, as seen previously for consist 5, the container loading configuration negates the tail feature seen for consists with a container loaded close to the train tail, for example consist 1. The coefficient of pressure stabilises to zero within 20m of the train tail for all consists at all measuring positions. As the measuring height is increased the magnitude of coefficient of pressure decreases for all loading configurations.



(a) Consist 1



(b) Consist 3



(c) Consist 5

Figure 5.7: Coefficient of pressure for freight consists 1, 3 and 5 for train lengths 181.25m, measured at train speed 20m/s for probes 1 (red), 5 (blue) and 6 (green) above the train roof. The vertical dashed lines indicate the front (black) and rear (grey) faces of the containers.

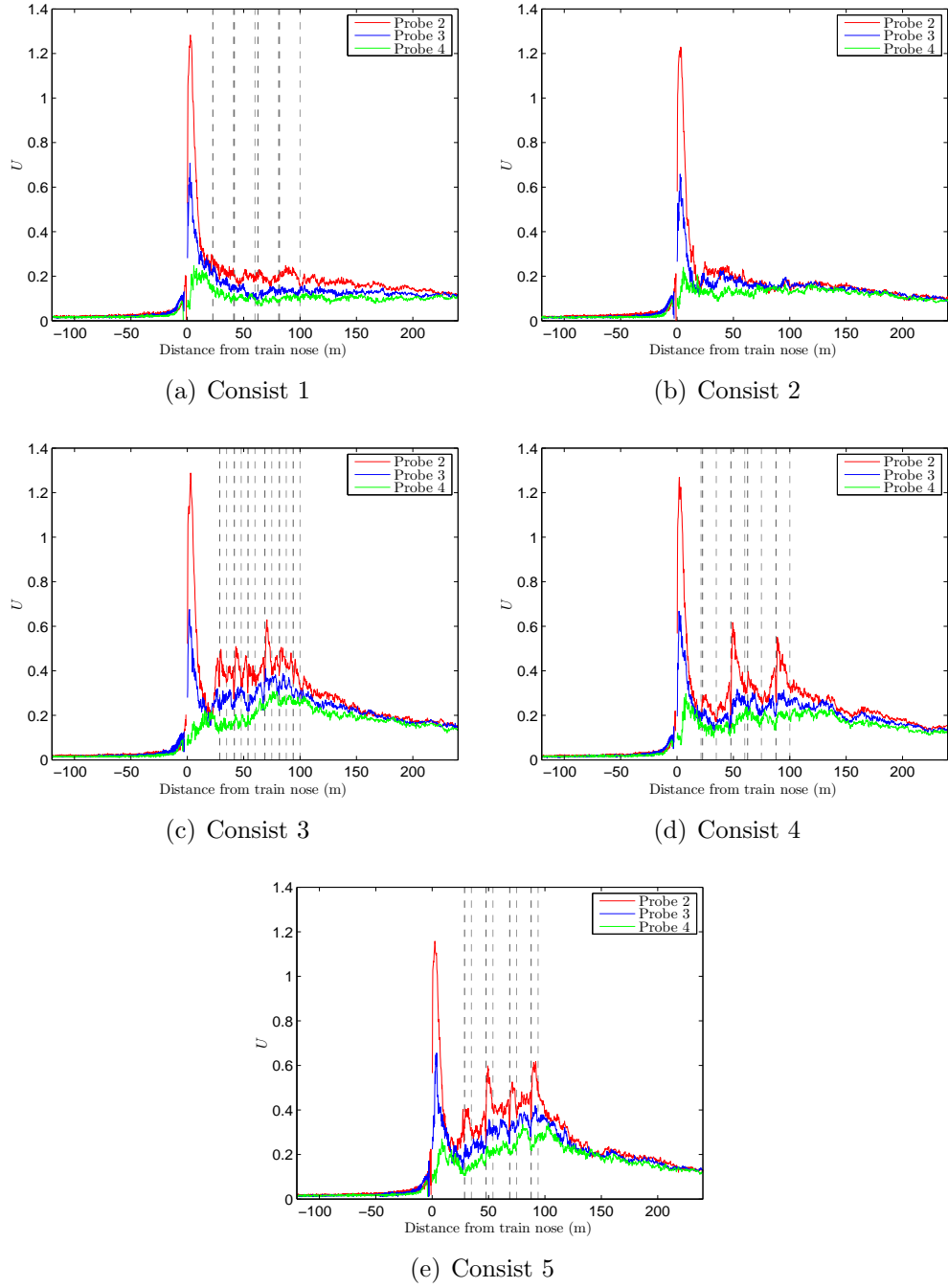


Figure 5.8: Normalised ensemble longitudinal component of velocity U for freight consists 1 to 5 for train lengths 101.25m, measured at train speed 20m/s for probes 2 (red), 3 (blue) and 4 (green) at the side of the train. The vertical dashed lines indicate the front (black) and rear (grey) faces of the containers.

5.4 Normalised ensemble longitudinal component of velocity U

5.4.1 Train side

Figure 5.8 illustrates the normalised ensemble longitudinal component of velocity U , i.e. the normalised with respect to train speed ensemble velocity in the x-direction; for a train length of 101.25m with consists 1 to 5 measured at probe positions 2 to 4. As discussed previously in section 5.3.1 it is clear to see that the flow can be split into a number of key regions; upstream, the nose, boundary layer, tail and wake.

Upstream of the train U is not zero as would be expected, instead there is a very small velocity close to 1% of train speed. Further analysis of raw data files highlighted a half oscillation about zero with the negative components removed, due to the Cobra probe method of sampling. When the ensemble average is calculated these oscillations create a positive shift in velocity from what should be zero. The influence of the transient flow in the train slipstream creates velocities above zero, negating the oscillating sampling issue observed in the upstream region for all other flow regions.

In the nose region there is a peak in U corresponding to the difference between positive and negative coefficient of pressure peaks. The velocity in this region reaches 120% of train speed at 1.75m from centre of track (probe 2), much higher than previously witnessed in passenger studies. As with the coefficient of pressure this is hypothesised to be related to the Class 66 nose shape. The nose peak magnitude is dramatically affected by distance from train side. Due to flow shearing/separation (see section 5.5) at the Class 66 nose side edge there is a flow acceleration close to train side in the region containing probe 2. As the distance from train side is increased the influence of the shearing/separation is reduced and so U is much lower and slipstream development rapidly forms into boundary layer growth. The nose region extends from $\pm 18.75\text{m}$ at full scale.

In the boundary layer region, as with coefficient of pressure, the difference in container loading configuration can clearly be seen. For consist 1 the boundary layer stabilises rapidly after the train nose due to relatively smooth train sides, exhibiting similar flow development to a passenger train with inter-carriage gaps (Hemida et al., 2010). For probes 3 and 4, U is lower than for probe 2, suggesting a thin boundary layer in this region due to relatively smooth train sides (section 5.6.2.2). Similarly for consist 2, U falls away rapidly following the Class 66.

For consists 3, 4 and 5 the influence of larger spaces between loaded containers creates increasing velocities along the train length, indicating a thickening boundary layer along the train side. The influence of spaces between containers causes pulse peaks in U within the boundary layer following container leading faces; related to the difference between positive and negative peaks in coefficient of pressure. As with coefficient of pressure the space size between loaded containers affects pulse peak magnitudes. Comparing consists 3 and 5, as in section 5.3.1, the influence of larger spaces between loaded containers in consist 5 creates pulse peaks with a higher magnitude than consist 3. Similarly for consist 4 the smaller gaps between closely loaded containers act similar to a passenger train inter-carriage gap, whereas the larger gaps create pulse peaks of magnitude 60% of train speed. The influence of spaces between loaded containers leads to a greater magnitude of U within the boundary layer region, thus a thicker boundary layer developing quicker than for a loading configuration with less spaces between loaded containers.

In the tail region boundary layer growth ceases and U falls away into the wake. This differs to the tail region of a passenger train, where a large tail velocity peak is observed due to shedding vortices (Sterling et al., 2008). The lack of velocity peak at the tail of a freight train has been observed previously by Sterling et al. (2008). It was also noted that the tail peak for a passenger train was only visible when the vortex shedding was in phase with the side on which the measuring equipment was situated. Therefore an additional piece of analysis was undertaken to identify if a tail peak existed for

each individual run. As with previous research this tail peak was non-existent for the TRAIN rig model freight train. It is suggested that differences between slipstream development in passenger and freight tail regions are due to tail shape.

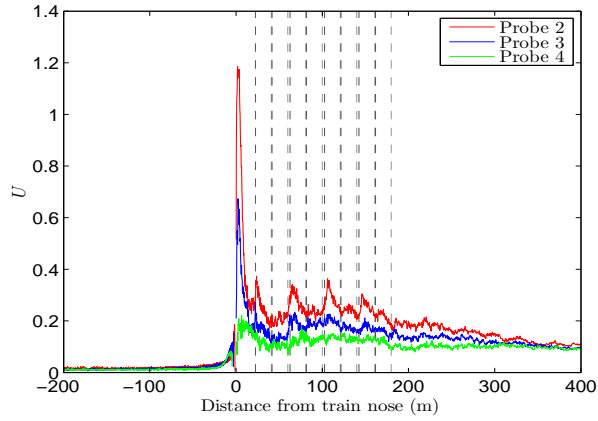
In the wake region U falls away at a similar rate for all probes. The influence of the train is still visible into the far wake at a distance of over twice the train length from the train nose. As measuring distance from the centre of track is increased the magnitude of U decreases for all loading configurations.

It is possible to assess the influence of train length on U by comparing figures 5.8 and 5.9. Figure 5.9 illustrates the normalised ensemble longitudinal component of velocity U for consists 1, 3 and 5 with train length 181.25m, measured at probe positions 2 to 4. As is expected the flow can be split into a number of key flow regions with an extended boundary layer region in comparison with the shorter train length of 101.25m.

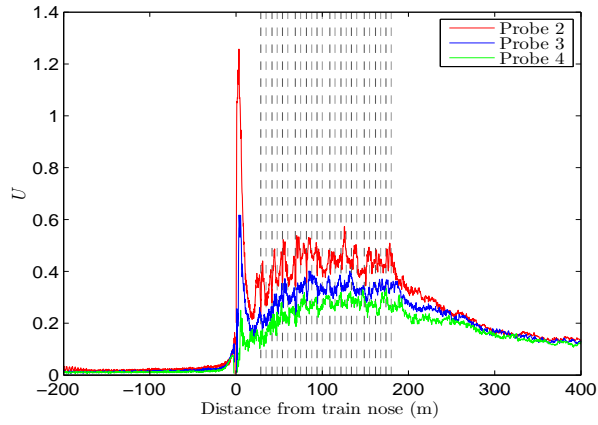
In section 5.3.1 a decrease in peak magnitudes witnessed at container lead faces was hypothesised to be a possible transition between boundary layer growth and stability. Figures 5.9(b) and 5.9(c) clearly show the transition between boundary layer growth and stability in U for consists 3 and 5. For partially loaded consists on the shorter freight train (figure 5.8) following the nose region the boundary layer is seen to continually grow, punctuated with pulse peaks relating to the change in coefficient of pressure at container lead faces. The longer train witnesses similar boundary layer growth to a distance of 100m after which boundary layer stability is observed, whereby although pulse peaks in U are witnessed at container lead faces the mean boundary layer velocity U is relatively constant.

5.4.2 Train roof

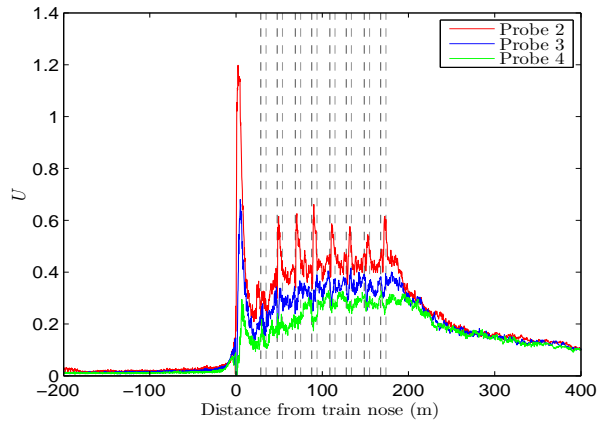
Figure 5.10 shows the normalised ensemble longitudinal component of velocity U for train consists 1 to 5 measured at probe position 1 above the train roof. In the upstream



(a) Consist 1



(b) Consist 3



(c) Consist 5

Figure 5.9: Normalised ensemble longitudinal component of velocity U for freight consists 1, 3 and 5 for train lengths 181.25m, measured at train speed 20m/s for probes 2 (red), 3 (blue) and 4 (green) at the side of the train. The vertical dashed lines indicate the front (black) and rear (grey) faces of the containers.

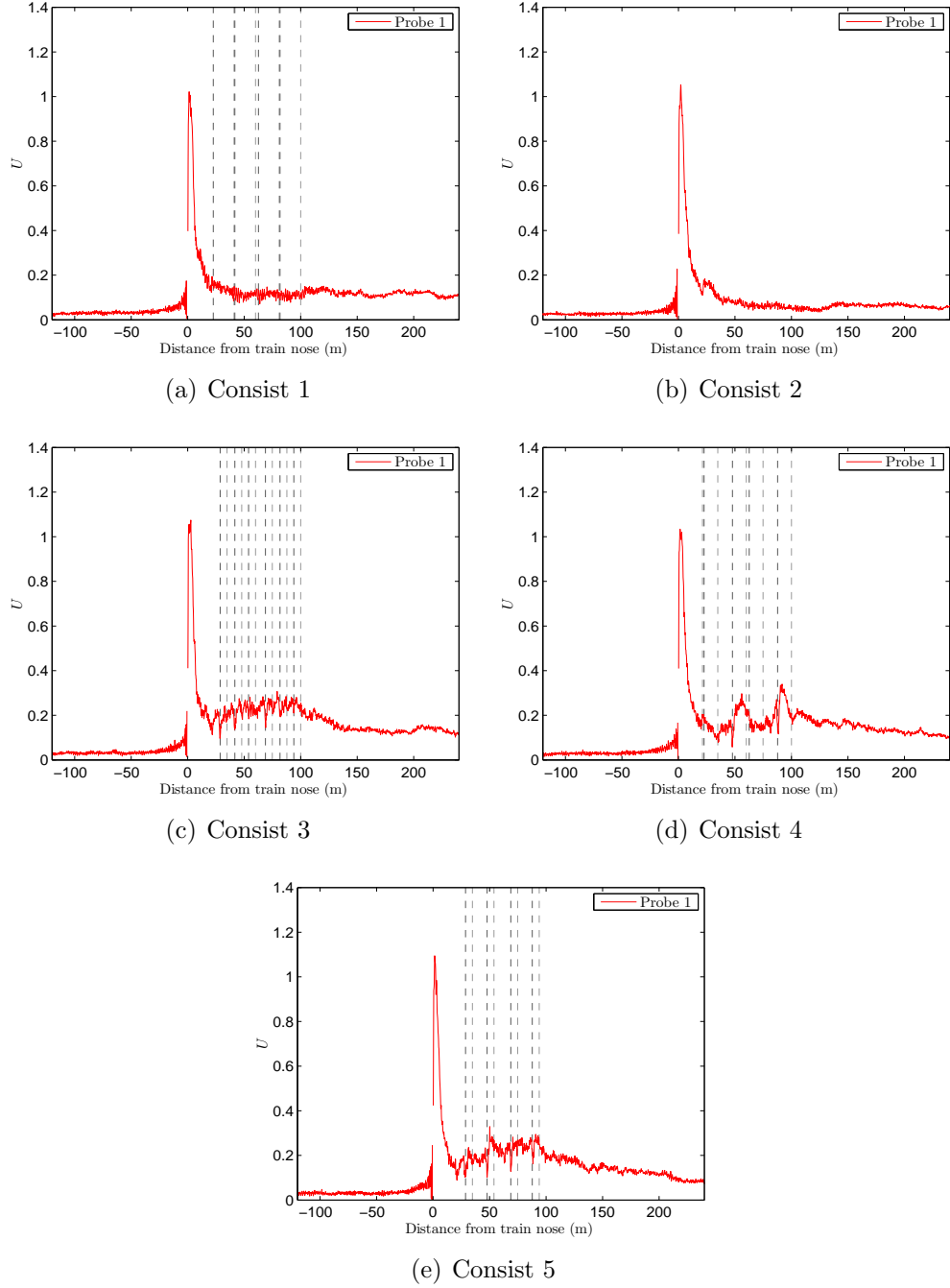


Figure 5.10: Normalised ensemble longitudinal component of velocity U for freight consists 1 to 5 measured at train speed 20m/s for probe 1 (red) above the train roof. The vertical dashed lines indicate the front (black) and rear (grey) faces of the containers.

region, as for U at train side, a velocity in the region of 1% of train speed is recorded due to the probe sampling method and ensemble averaging.

In the nose region the peak in U corresponds to the difference between positive and negative coefficient of pressure peaks. The velocity above the train roof reaches 100% of train speed. This velocity peak is lower than those recorded at train side and higher than previous passenger results (Baker et al., 2001). Differences are hypothesised to be related to the hooded section at the Class 66 nose roof.

In the boundary layer region the effect of container loading configuration can be observed, however the effect is suppressed in comparison to train side. As seen previously, for consist 1 the boundary layer stabilises rapidly following the train nose due to the relatively smooth roof. In previous passenger studies (Baker et al., 2001; Gil et al., 2008), measurements taken above the train roof exhibit lower U than those recorded at train side. Once again consist 1 can be compared to a passenger train with inter-carriage gaps.

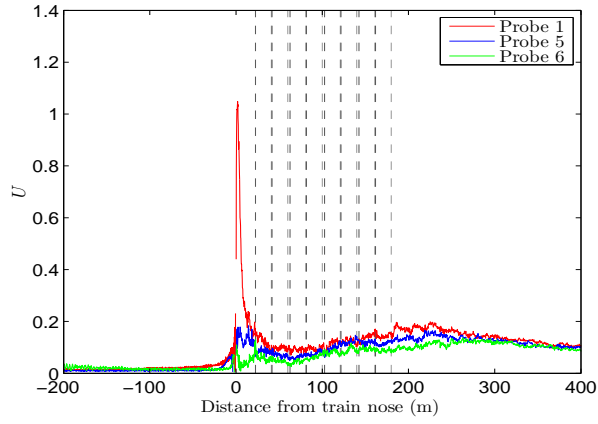
In the boundary layer region of consist 2, above the train roof U is much lower than at train side. It is suggested that the placement of trailing wheels, creating a series of 15mm high blocks along the flat plate, affects boundary layer development. At train side this influence is recorded by the probes, however above the train roof the probe is positioned far enough from these blocks that any effects are not measured.

For consists 3, 4 and 5 the influence of larger spaces between loaded containers creates increasing U along the train length, indicating a thickening boundary layer along the train roof. The rate at which U increases is lower above the train roof than at train side for all consists. Once again the influence of larger spaces between containers creates pulse peaks in velocity within the boundary layer, relating to the change between peaks in coefficient of pressure at a container leading face. However, for smaller spaces these peaks are much less defined than corresponding peaks at train side. Maximum peaks of 30% of train speed are recorded for consist 4. In the tail region boundary layer growth

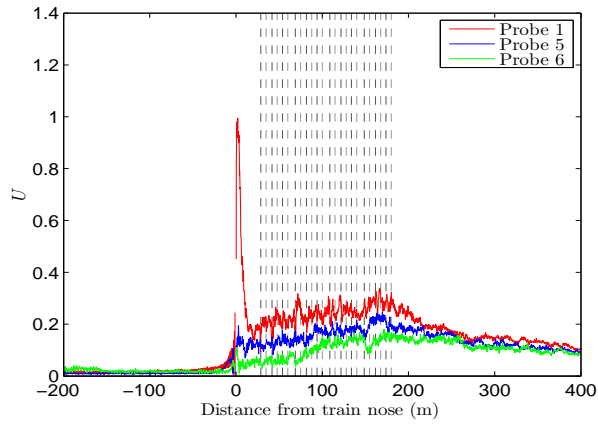
ceases and U falls away after the train tail into the wake region at a similar rate as recorded at train side.

Figure 5.11 illustrates the normalised ensemble longitudinal component of velocity U for probes 1, 5 and 6 above the train roof for the 181.25m train with consists 1, 3 and 5. In the nose region a peak in U corresponds to the difference in coefficient of pressure, reaching 100% of train speed close to the train roof. However, the nose peak magnitude dramatically decreases as measuring height is increased, suggesting flow remains relatively close to the train roof with a smaller boundary layer thickness than witnessed at train side.

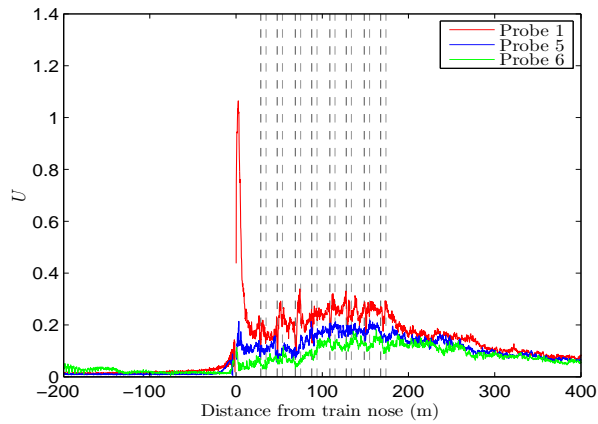
In the boundary layer region the effect of container loading for consists 3 and 5 create pulse peaks within an increasing U along the train length, however as discussed, these peaks are somewhat negated as the height above train roof is increased. In comparison to train side, the boundary layer development above the roof is much slower and appears to be continually increasing, unlike the transition from boundary layer growth to stability witnessed at train side with the 181.25m train. In the tail region boundary layer growth ceases and U falls away into the wake at a similar rate for all probes.



(a) Consist 1



(b) Consist 3



(c) Consist 5

Figure 5.11: Normalised ensemble longitudinal component of velocity U for freight consists 1, 3 and 5 for train length 181.25m, measured at train speed 20m/s for probes 1 (red), 5 (blue) and 6 (green) above the train roof. The vertical dashed lines indicate the front (black) and rear (grey) faces of the containers.

5.5 Normalised ensemble components of velocity V and W

This study has, so far, focused on the normalised ensemble longitudinal component of velocity U . The choice of U for analysis reflects the relative magnitude in relation to V and W and the methods of analysis in previous full scale freight studies (Temple and Johnson, 2008; Sterling et al., 2008), to which comparisons are drawn. It will however be shown that for a container freight train it must be acknowledged that components V and W are not negligible as in passenger studies (Baker et al., 2001; Sterling et al., 2008; Gil et al., 2008). Figures 5.12 and 5.13 illustrate the normalised ensemble components of velocity V and W for the 181.25m train with consists 1 and 5 at train side probe positions 2 to 4 and train roof positions 1, 5 and 6.

Previous passenger studies noted that except around the train nose and tail regions the overall magnitude is within 2% of the longitudinal velocity component U ; suggesting lateral and vertical components of velocity are significantly small and below the performing range of the Cobra probe (Gil et al., 2008; Sterling et al., 2008). As discussed, consist 1 exhibits the closest relation to a passenger train. At train side and above train roof both V and W remain relatively constant below the Cobra probe performing range except for the nose region where a positive then negative peak in velocity are observed, of magnitude to 25% of train speed close to train side. The nose region peaks are highly repeatable, as seen for U .

V and W magnitudes are higher at train side than above train roof, as with U . At train side, in general, the lateral component V has greater magnitude than the vertical component W , especially at the train nose and leading container faces, suggesting the bluff shape creates high U and V components and with little influence on W . However, above the train roof the opposite occurs with a larger component of W than V . At the train nose or a container leading face a positive then negative peak is observed, i.e. flow away from the vehicle followed by flow towards the vehicle. This pattern is

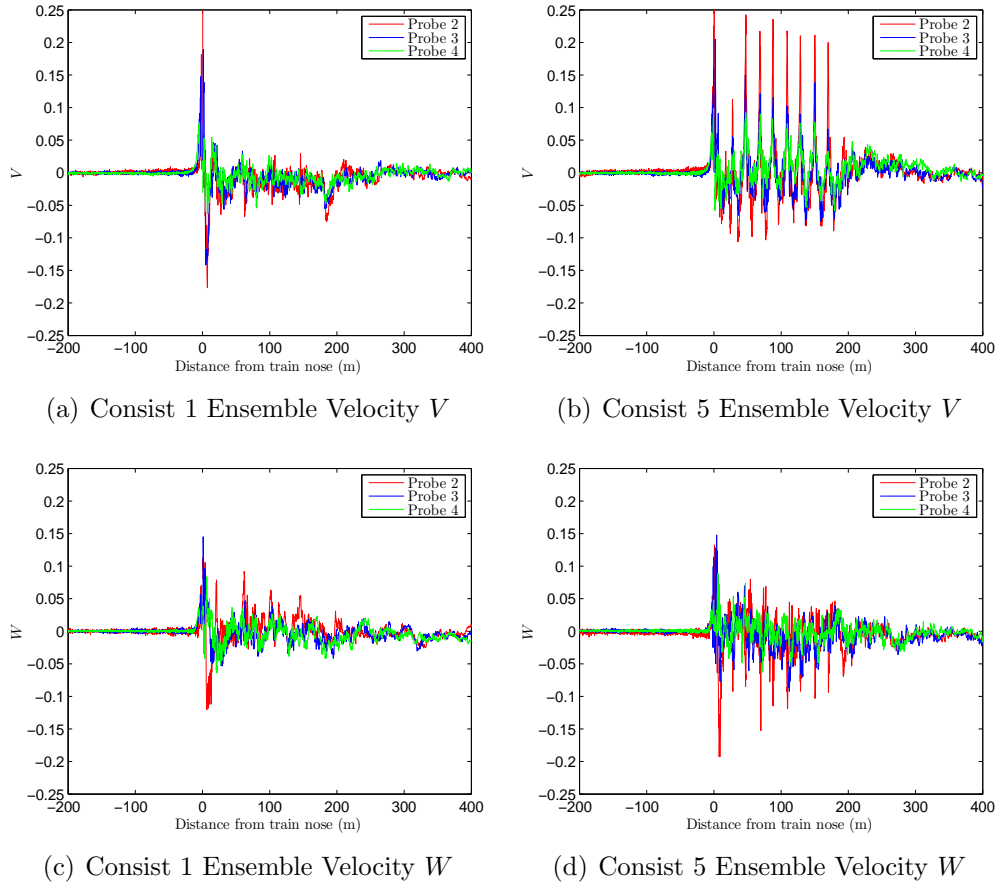


Figure 5.12: Normalised ensemble longitudinal components of velocity V and W for the 181.25m train with freight consists 1 and 5 measured at train speed 20m/s for probes 2 (red), 3 (blue) and 4 (green) at the side of the train.

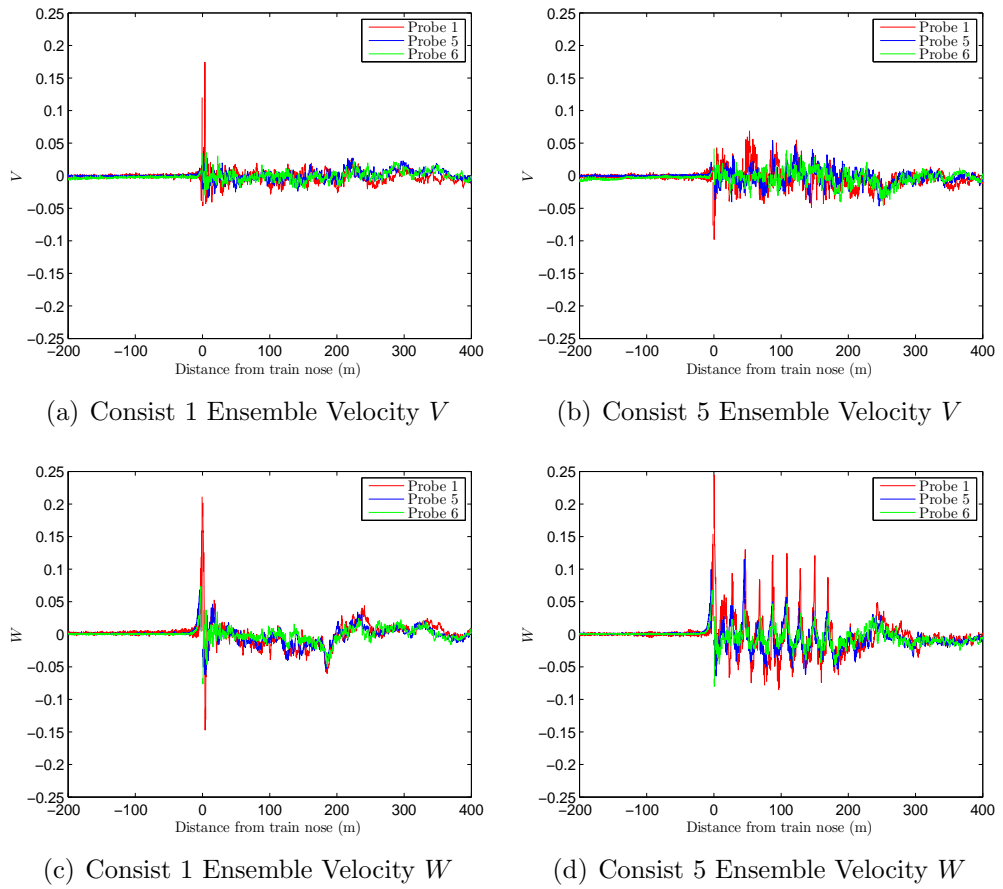


Figure 5.13: Normalised ensemble longitudinal components of velocity V and W for the 181.25m train with freight consists 1 and 5 measured at train speed 20m/s for probe 1 (red), 5 (blue) and 6 (red) above the train roof.

characteristic of flow separation into a recirculation (Hemida and Baker, 2010). At train side this occurs in the lateral plane, creating greater increases in V than W , however above the train roof this process is dominated in the vertical plane, creating greater increases in W .

As the loading efficiency is reduced it is possible to see similar pulse peaks at container faces in V and W as with U . At train side these peaks have a larger magnitude in V , to nearly 20% of train speed, whereas above train roof a larger magnitude in W , to nearly 10% of train speed. Pulse peaks create velocities in the boundary layer above the Cobra probe lower range, increasing the overall magnitude to above 2% of the longitudinal velocity component.

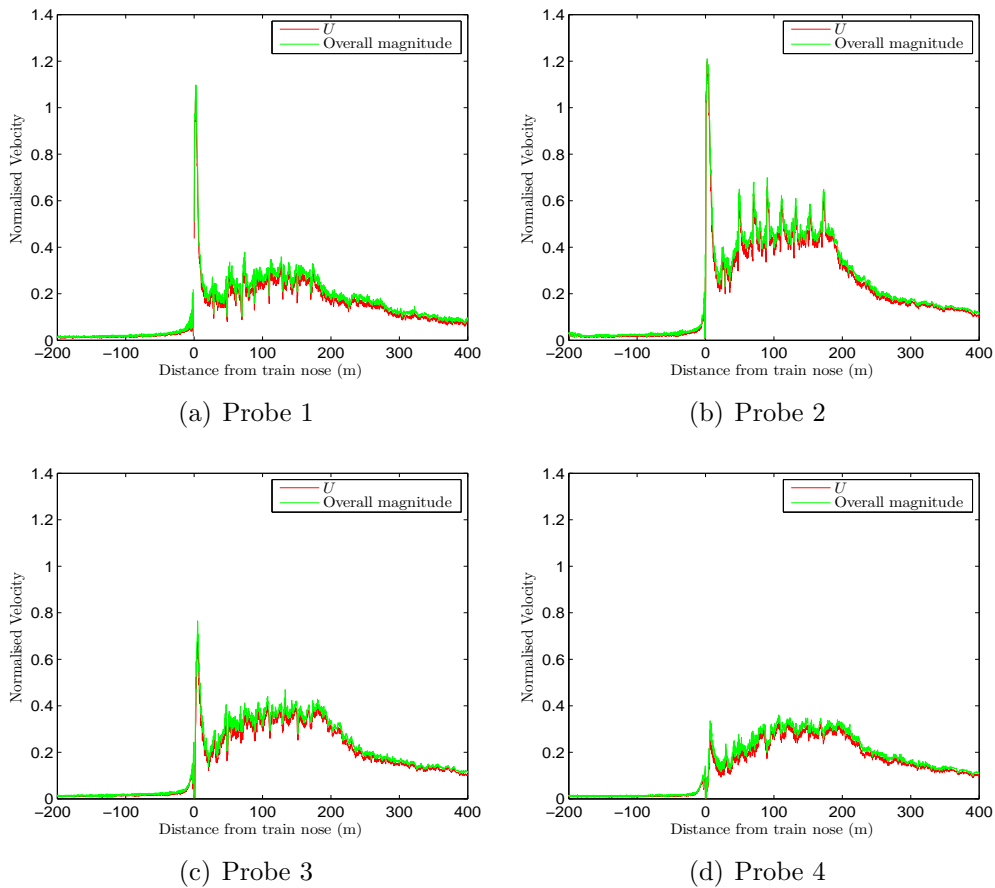


Figure 5.14: A series of figures illustrating the overall magnitude (green) in relation to the normalised ensemble longitudinal components of velocity U (red) for freight consist 5 measured at train speed 20m/s for probes 1 to 4.

Figure 5.14 illustrates the overall magnitude calculated with all three components of

velocity plotted in relation to the longitudinal velocity component U for consist 5 at probe positions 1 to 4 to understand the influence of V and W on the overall velocity magnitude. Consist 5 was chosen for this comparison as the largest peaks in V and W occur for this loading configuration.

For all probes the overall magnitude is higher than U with a very similar flow pattern. This is expected as the flow is dominated by U and key flow events (nose/loading containers) also appear in V and W . To understand the increase in magnitude the percentage difference between U and the overall magnitude has been calculated. On average for each probe the difference between the overall magnitude and U is an increase of 11%, much higher than 2% witnessed in previous passenger studies. If all loading configurations are included an average increase of 10% is observed. These figures highlight for container freight trains the significant influence of V and W on the overall flow in relation to U . The largest differences occur in the nose region and at leading container faces, where high magnitudes of V and W added to U create a greater overall magnitude.

5.6 Detailed consideration of the flow within specific flow regions

In sections 5.3-5.4 it was possible to analyse results by splitting the flow into a number of key flow regions (upstream, nose, boundary layer, tail and wake), each with different flow characteristics. In this section a more detailed analysis of the normalised ensemble longitudinal velocity U within these specific regions is undertaken using a variety of analysis techniques to understand the varying flow nature.

5.6.1 Nose region

Previous model and full scale studies (Baker et al., 2001; Sterling et al., 2008) suggest the nose velocity peak is highly reproducible, with only small differences between experimental runs. In section 5.4 the reproducibility of the nose peak has again been highlighted. In figure 5.15 the normalised ensemble longitudinal component of velocity U and normalised ensemble standard deviations, as defined by equation 5.1, are plotted for all loading configurations at probe positions 1 to 4 in the nose region, extending from $\pm 18.75\text{m}$.

As the distance from train side is increased the velocity peak magnitude in the nose region decreases, however magnitude at train side is greater than above the train roof at comparable positions. As in Sterling et al. (2008), normalised ensemble standard deviations of freight data are higher than observed in passenger studies, hypothesised to be related to the nose shape of the Class 66 locomotive. For probe 4 the nose region velocity peak is poorly defined and merges rapidly into the developing boundary layer.

Upstream ahead of the train nose, for all probes, there is a small increase in U to a peak of $\sim 0.1-0.2$. The normalised ensemble standard deviation remains fairly constant, implying the high reproducibility of this feature. It is suggested the concave shape of

the Class 66 nose has an effect on air in the region extending to 5m ahead of the train. The magnitude of this feature is greater at train side than roof.

Following the front of the Class 66 passage, as velocity increases to the peak, the highest normalised ensemble standard deviation values, ~ 0.4 , are observed. By inspecting individual runs the variation in this region is seen to be related to the Cobra probe cone of acceptance. For probes 1 and 2 there are small sections of data outside the cone of acceptance, however for probes 3 and 4 these sections of zero data are much larger. The zero data section size varies between each experimental run, as does the position of the velocity peak. Therefore, when calculating standard deviation for each run in respect to the ensemble average, if the section of zero data for the individual run differs in size to the ensemble a high standard deviation is created. This effect is magnified for probes 3 and 4, with large regions of data outside the Cobra probe cone of acceptance.

Unlike previous studies (Baker et al., 2001; Sterling et al., 2008) the nose peak magnitude is much higher than peaks observed in the boundary layer region. As discussed, it is hypothesised that the magnitude of 120% of train speed close to the train side is related to the nose shape of the Class 66 locomotive. In Sterling et al. (2008), full scale RAPIDE project container freight data hauled by a Class 92 locomotive was analysed and a nose peak magnitude in U of 25% of train speed, extending 7m was found. It was suggested the time scale of this peak, 0.2s based on train speed 33m/s, could potentially cause passenger instability; however it was concluded that the relatively small magnitude was unlikely to create this problem (Sterling et al., 2008). In this study, close to the train side (probe 2) a nose peak of magnitude 120% in U extending 10m has been found. At train speed 20m/s this relates to a time scale of 0.5s, beyond the range of creating passenger instability (Sterling et al., 2008; Jordan et al., 2009). However, it will be shown in section 5.7 that the nose peak extents and normalised magnitudes remain relatively constant as train speed is increased, highlighting Reynolds number independence. Therefore, at full UK freight speed of 33.3m/s this relates to a nose

peak time scale of 0.3s which, coupled with a peak magnitude of 120% of train speed, could potentially cause passenger instability.

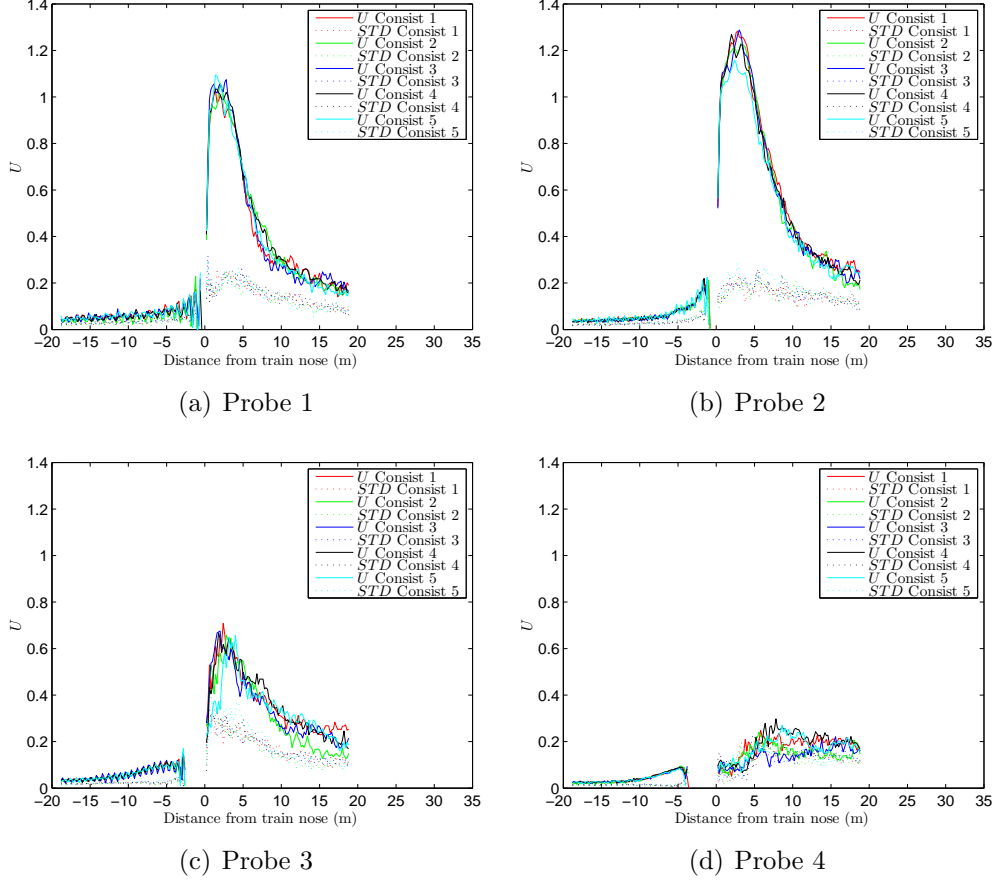


Figure 5.15: Normalised ensemble longitudinal component of velocity U and normalised ensemble deviations for train consists 1 (red), 2 (green), 3 (blue), 4 (black), 5 (cyan) in the nose region for probes 1, 2, 3 and 4.

5.6.2 Boundary layer region

5.6.2.1 Velocity profiles

Figure 5.16 shows a series of developing velocity U profiles for probes 2, 3 and 4 at distances 25m, 50m, 75m and 100m from the train nose for consists 2 and 4 and distances 25m, 50m, 75m, 100m, 125m, 150m and 175m for consists 1, 3 and 5. Although there are only three measuring points, it is felt that figure 5.16 is a useful indicator of boundary layer development. All consists, apart from consist 2, exhibit the classic boundary

layer development profile. Consist 2 results remain relatively stable, as discussed in section 5.4.1, due to the lack of loaded containers. At position 50m for consists 3 and 5 and 75m for consist 4, the velocity profile exhibits a much higher value close to the train side. If these positions are compared to figure 5.8 it is possible to see that these values relate to the pulse peaks seen at the lead face of a loaded container.

Figure 5.16 illustrates the effect of container loading configuration in relation to boundary layer development. For consist 1 the relatively smooth train side creates little boundary growth and velocities remain relatively stable along the train length. However, as the loading efficiency is reduced the boundary layer increases rapidly along the train length with greater U . For consists 3 and 5, plotted for the 181.25m train it is possible to see the transition between boundary layer growth and stabilisation as discussed in section 5.4.1. In general the velocity profiles to 100m exhibit continual growth for each probe position, however from 125m to 175m the velocity profiles remain relatively constant in value at each probe position, unless influenced by a container leading face effect.

The velocity profiles shown in figure 5.17 for probes 1, 5 and 6 above the train roof of consists 1, 3 and 5 all exhibit classic boundary layer development profiles. Velocities are highest closest to the train roof and velocities decrease with increased distance from the roof. In comparison to figure 5.16, velocity profiles above the train roof are much smaller than at train side, indicating smaller boundary layer development over the train roof. Baker (2010) cited that increased flow development at the train side in comparison to above the train roof was due to the influence of the rough bogie region at train side.

5.6.2.2 Displacement thickness

The displacement thickness or mass deficit thickness measures the amount by which the mass carried in the boundary layer lies below the uniform flow (Durbin and Medic,

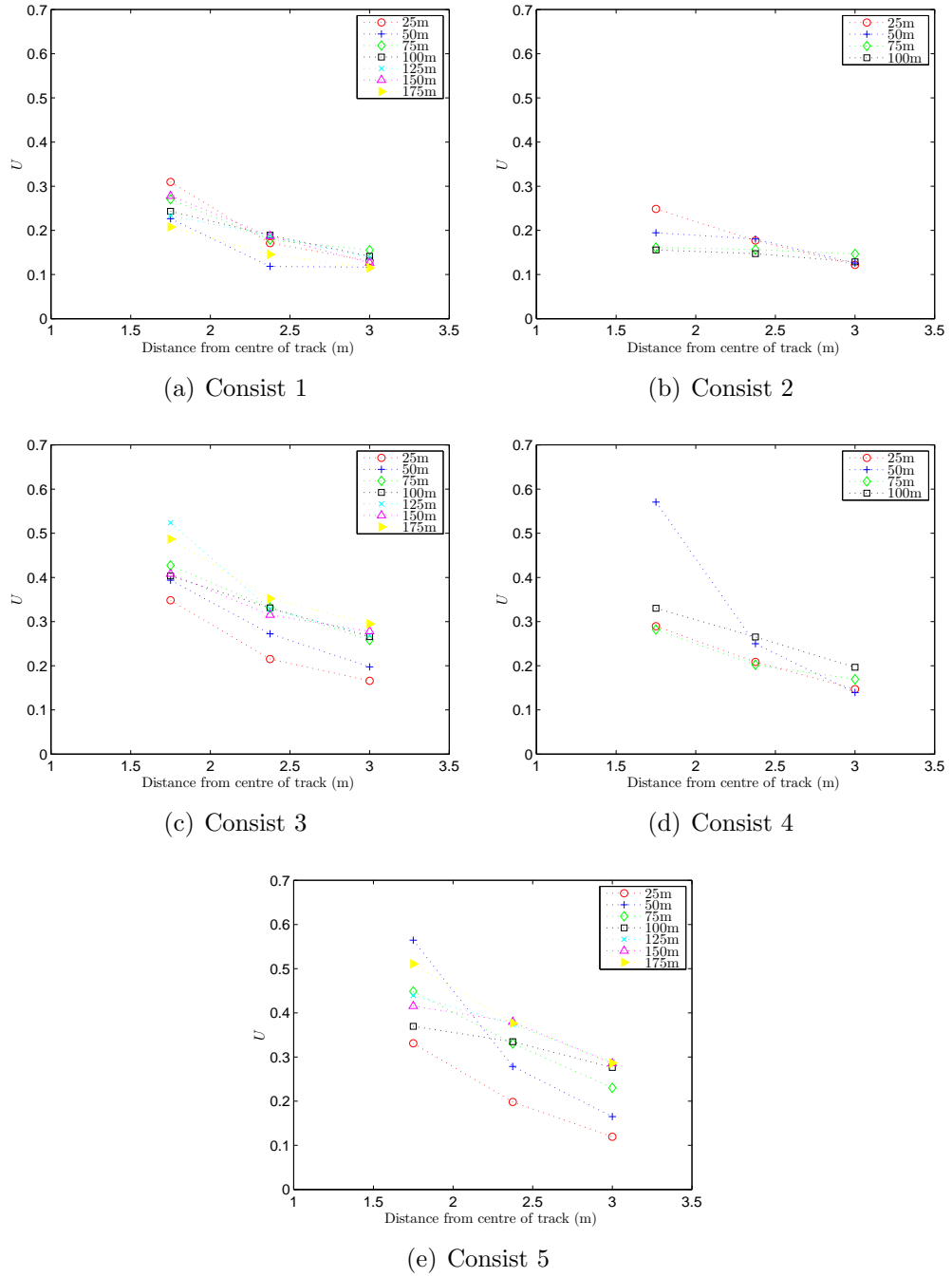


Figure 5.16: The development of velocity U profiles along the train side in the boundary layer. Measurements are taken using probes 2, 3 and 4 at distances 25m (red circles), 50m (blue crosses), 75m (green diamonds), 100m (black squares), 125m (cyan crosses), 150m (magenta upward pointing triangles) and 175m (yellow filled triangles) from the train nose.

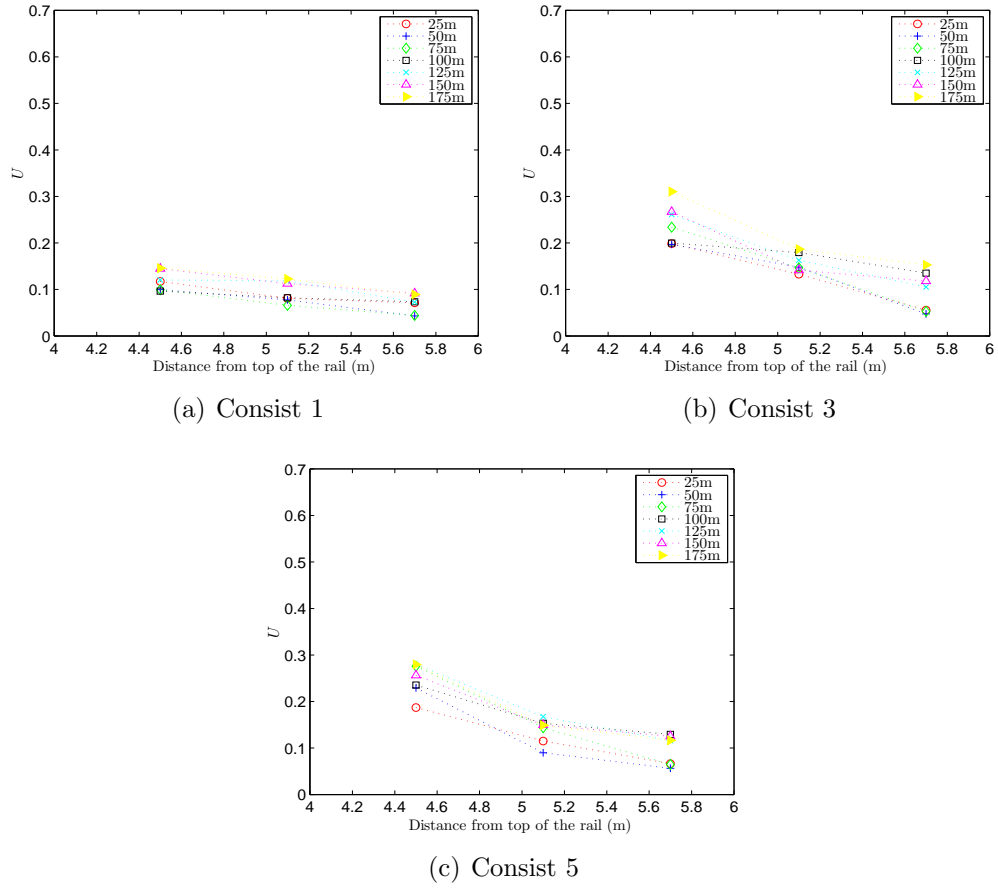


Figure 5.17: The development of velocity U profiles above the train roof of consists 1, 3 and 5 in the boundary layer. Measurements are taken using probes 1, 5 and 6 at distances 25m (red circles), 50m (blue crosses), 75m (green diamonds), 100m (black squares), 125m (cyan crosses), 150m (magenta upward pointing triangles) and 175m (yellow filled triangles) from the train nose.

2007). It measures the deficit in volume flow within the boundary layer. If the displacement thickness grows along the train length it can be inferred that fluid flows out of the top of the boundary layer. Therefore by mass conservation, a flow out of the boundary layer is equal to the decrease in flow carried inside the boundary layer, the displacement effect (Durbin and Medic, 2007).

Alternatively the displacement thickness is the distance by which a wall would have to be displaced in a hypothetical frictionless flow to maintain the same mass flux as that in the actual flow, i.e. the distance by which streamlines outside of the boundary layer are displaced due to the boundary layer presence (Kundu and Cohen, 2010).

The displacement thickness is defined as the thickness of a layer of zero-velocity fluid that has the same velocity deficit as the actual boundary layer. The velocity deficit in a boundary layer is measured as $U_\infty - U$, thus (Durbin and Medic, 2007),

$$\begin{aligned} \int_{y=0}^h (U_\infty - U) dy &= \int_{y=0}^{\delta^*} (U_\infty - 0) dy = U_\infty \delta^* \\ \Rightarrow \delta^* &= \int_{y=0}^{\infty} \left(1 - \frac{U}{U_\infty} \right) dy \end{aligned} \quad (5.2)$$

where h is a surface-normal distance that lies outside of the boundary layer, so $h \rightarrow \infty$ as $U_\infty - U \rightarrow 0$ as $y \rightarrow \infty$. For this moving model study the displacement thickness definition is altered to account for the different frame of reference (Baker et al., 2001). Essentially the displacement thickness is calculated by integrating U across the boundary layer,

$$\delta^* = \int_{y=0}^{\infty} U dy \quad (5.3)$$

where the boundary layer region is defined from 18.75m to 101.25m for the shorter train and 18.75m to 181.25m for the longer train. Equation 5.3 is the two-dimensional definition of displacement thickness, which for the highly three-dimensional flow within

the boundary layer of a freight train is only slightly appropriate, however it is felt to be a useful indicator of boundary layer development.

To calculate the displacement thickness, equation 5.3 is firstly discretised using the trapezium rule for values of $y'=0\text{m}$ to $y'=5\text{m}$ from train side, i.e. for probes 2, 3 and 4 and assuming the boundary layer edge lies at 6.225m from centre of track. The assumed boundary layer edge position is estimated by curve fitting the velocity profiles and calculating the distance from centre of track at which boundary layer velocities are zero. It is important to note that the number of points in this integral is five, potentially leading to an error in actual displacement thickness; however again it is felt this calculation is a useful indicator of boundary layer development.

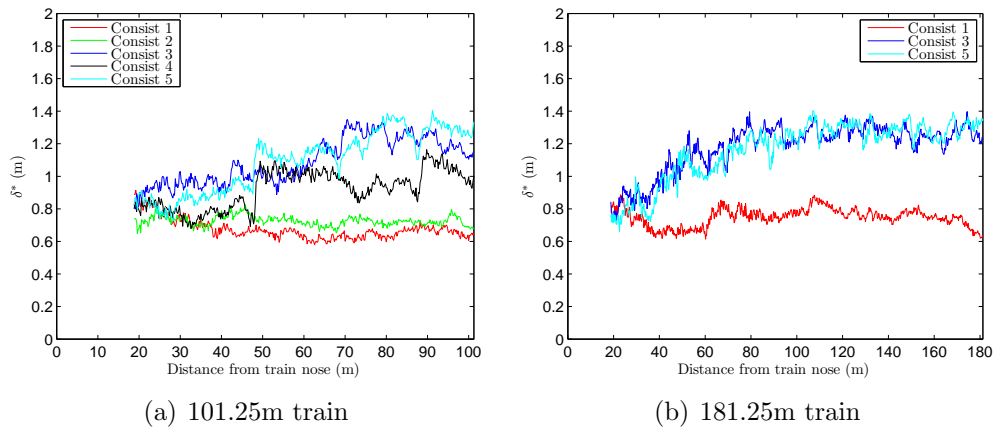


Figure 5.18: Displacement thickness (m) along the train length for freight consists 1 (red), 2 (green), 3 (blue), 4 (black), 5 (cyan).

Figure 5.18 illustrates a comparison of displacement thicknesses for all freight loading configurations for the 101.25m and 181.25m trains, shown in full scale dimensions. It is clear to see that the existence of spaces between loaded containers creates an increased displacement thickness along the train side. The displacement thicknesses seen for the freight train are larger than those seen previously in passenger studies; maximum values of displacement thicknesses for passenger trains in previous studies were $\sim 0.4\text{m}$ (Baker et al., 2001; Sterling et al., 2008). As expected, consist 1 exhibits the closest comparison of displacement thickness to a passenger train.

For consists 1 and 2 the displacement thickness remains relatively constant for the entire train length. The relatively smooth sides of consist 1 create an almost constant displacement thickness, increasing only very slowly, indicating slow growth within the boundary layer, as seen in figure 5.18(a). For consist 2 following the Class 66 locomotive there is a sharp increase in displacement thickness. It is thought this increase occurs because of an interaction creating a recirculation zone at the trailing edge of the Class 66. This feature is also seen for consists 3 and 5 with a space between the Class 66 and the first loaded container.

As container loading efficiency is reduced this creates increased boundary layer growth and thus an increasing displacement thickness. For Consist 4 smaller spaces between containers create a similar displacement thickness profile to consist 1, with a slight continual growth. A larger space before a loaded container creates a pulse peak in U at the container leading face, creating a well-defined peak in displacement thickness, increasing the displacement thickness rapidly.

The displacement thickness profiles for consists 3 and 5 are similar although the loading configurations are different. As discussed, the influence of large spaces between containers in consist 5 creates pulse peaks in U , creating a peak in the displacement thickness. Along the train length this has the effect of rapidly increasing displacement thickness. Consist 3 however has smaller spaces between containers but the influence of more loaded containers creates lots of smaller peaks in U , increasing boundary layer growth. This initially creates a larger displacement thickness for consist 3 than consist 5 (figures 5.18(a) and 5.18(b)). Therefore, although the displacement thickness grows slower for consist 3, the initial rapid growth in displacement thickness for consist 3 creates a similar overall profile to consist 5.

The transition between boundary layer growth and stability hypothesised in section 5.4.1 is visible to understand in figure 5.18(b). At 100m from the train nose there is a transition from an increasing displacement thickness to a relatively constant displacement thickness, indicating a transition from boundary layer growth to stability.

Analysing previous full scale partially loaded container freight research the boundary layer transition is observed again at 100m i.e. a length of the lead locomotive and four flatbed wagons (Sterling et al., 2008; Temple and Johnson, 2008). This implies that for model scale research on partially loaded container freight trains, a total full scale equivalent train length of over 100m is needed to take measurements within a fully developed boundary layer.

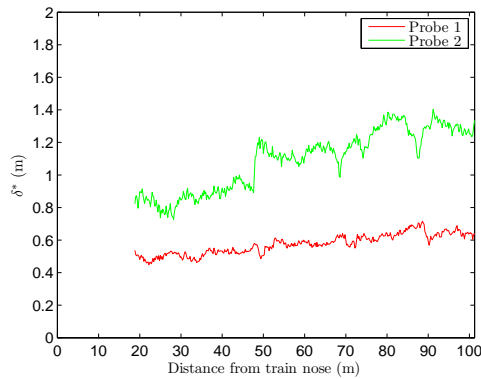


Figure 5.19: A comparison of displacement thickness (m) for consist 5 above the train roof (red) and at the train side (green).

The velocity profiles in figure 5.17 indicate smaller boundary layer growth above the train roof than at train side. This can be developed by calculating the displacement thickness above the train roof by discretising the integral in equation 5.3 for probes 1, 5 and 6 above the train roof. It is important to note again there are only five points in this integral, therefore potentially errors in this calculation, however it is felt to be a useful indicator of boundary layer development.

Figure 5.19 illustrates a comparison of displacement thickness above the train roof and at the train side in the boundary layer region for consist 5. It is clear that the boundary layer displacement thickness above the train roof, at maximum 0.5m, is much smaller than at train side. The displacement thickness at train side also increases more rapidly than above the train roof. Baker et al. (2001) published results for passenger trains with similar findings when comparing train side to the roof; however velocity magnitudes and subsequent analysis technique values are much lower for the passenger

train in comparison to container freight train results.

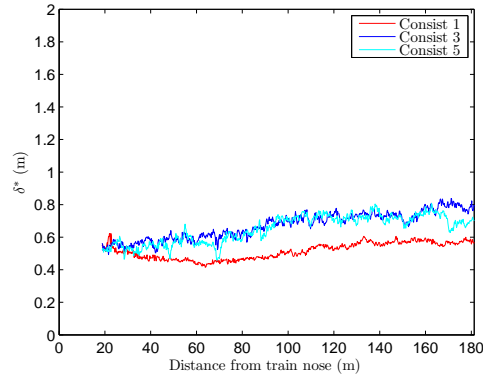


Figure 5.20: Displacement thickness (m) for consist 1 (red), 3 (blue) and 5 (cyan) above the train roof.

Contrary to the transition between boundary layer growth and stability witnessed at train side, above the train roof figure 5.20 illustrates continued growth in displacement thickness along the train roof. For consist 1 there is initial fall in displacement thickness in the region $x < 60\text{m}$ before growth is observed again. It is thought the reduction in displacement thickness is due to the stabilisation of velocities in the boundary layer following the large nose peak. The sharp increase in displacement thickness observed for consists with a space following the Class 66 at train side is not seen above the train roof for consist 3 and 5, although smaller pulse increases in displacement thickness are observed at container leading faces.

5.6.2.3 Turbulence intensity

In a boundary layer region the spatial variation between the moving body and the air surrounding that body is called shear; shear produces turbulence (Davidson, 2004). In a turbulent region the velocity can be thought of as composed of two parts; an average velocity component and a component representing fluctuations about the mean (Davidson, 2004). Turbulence intensity is a measure of the strength of the turbulent fluctuations about the mean, expressed as a percentage by dividing by the ensemble mean, $\bar{c}(x)$. For the TRAIN rig study as the train is moving in relation to the measuring

equipment, so to ensure the right frame of reference is considered, the turbulence intensity is normalised by $1 - (\bar{c}(x))$, a moving frame of reference format.

The turbulence intensity is calculated in this case for the boundary layer region measured from 18.75m to 101.25m for the shorter train and 18.75m to 181.25m for the longer train. The turbulence intensity is defined as the ratio of the standard deviation of the ensemble velocity to one minus the ensemble mean, therefore the turbulence intensity for a moving frame of reference format, for each normalised time step is (Baker et al., 2001; Sterling et al., 2008),

$$I = \frac{\sigma_u(x)}{(1 - (U(x)))} \quad (5.4)$$

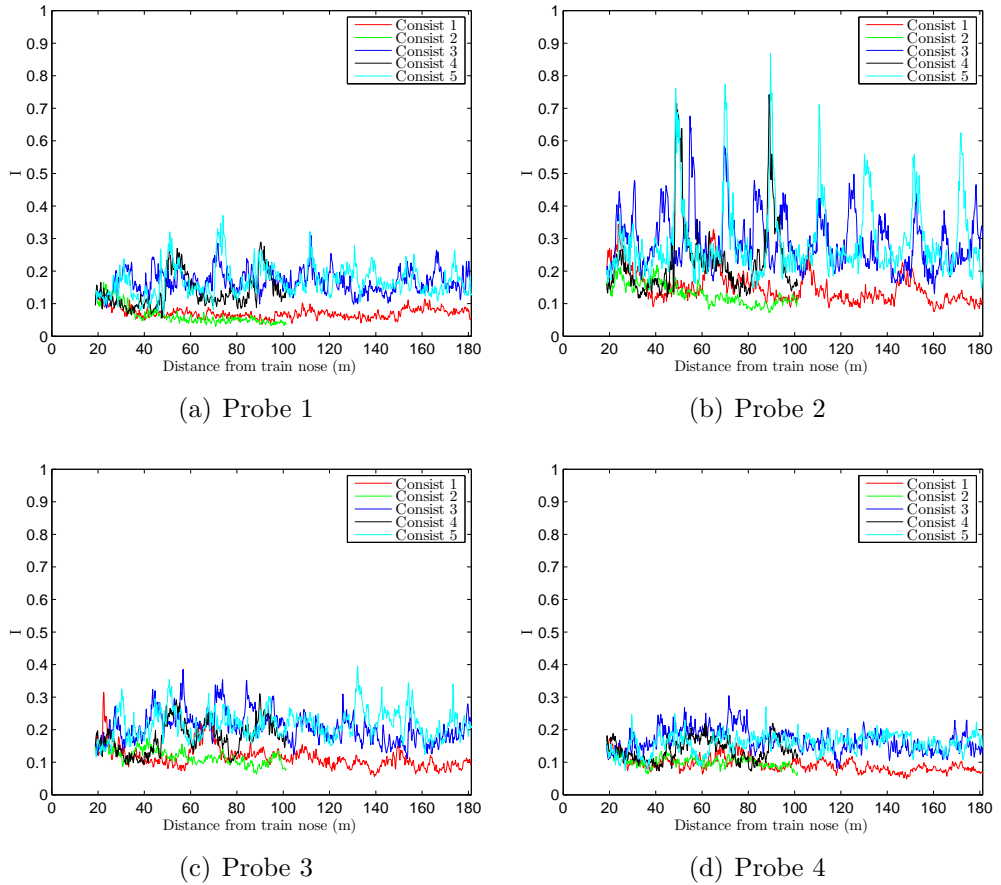


Figure 5.21: Turbulence intensity for the normalised ensemble longitudinal component of velocity U for train consists 1 (red), 2 (green), 3 (blue), 4 (black), 5 (cyan) in the boundary layer region for probes 1, 2, 3 and 4.

Figure 5.21 illustrates turbulence intensity for the normalised ensemble longitudinal component of velocity U for different train consists in the boundary layer region for probes 1, 2, 3 and 4. It should be noted that for consists 1, 3 and 5 data for the 181.25m train is presented. It is clear that turbulence intensity is higher at train side than above the train roof. Values recorded above the train roof are similar to those for probe 4 at train side, highlighting a less turbulent boundary layer development above the roof. For consist 2 above the train roof the turbulence intensity is very low due to the large distance between the wagon bed and the measuring position. It is hypothesised at train side the influence of bogies and undercarriage equipment increases vehicle surface roughness thus increasing turbulence intensities in comparison to the train roof. As discussed in section 5.6.2.2, the rough bogie and undercarriage region also increases displacement thickness at the train side in comparison to above the train roof.

Turbulence intensity increases as container loading efficiency decreases, with consist 1 exhibiting a similar level of turbulence intensity to that seen previously in passenger studies (Sterling et al., 2008). Both consist 1 and 2 have relatively constant turbulence intensities, with only a small peak following the end of the Class 66. The constant turbulence intensities reflect rapid boundary layer development which stabilises with little growth, as seen in section 5.6.2.2 (Sterling et al., 2008).

As container loading efficiency is decreased the variation in turbulence intensity increases along the train length, with clear peaks in intensity close to train side (probe 2) due to container leading faces. The intensity values for consists 3, 4 and 5 are similar to those seen in full scale container freight data, with peaks to around 40% intensity (Sterling et al., 2008). By comparing figures 5.18 and 5.21 it is possible see that rapid increases in the boundary layer displacement thickness align with high turbulence intensities corresponding to the container leading face following a space between two loaded containers. By reducing container loading efficiency and introducing spaces between containers a thicker boundary layer develops, with large pulse increases and fluctuations in relation to loading configurations, which in turn cause regions with

higher turbulence intensity.

As the distance from train side is increased turbulence intensity reduces. For partially loaded consists as the distance from train side is increased turbulence intensity decreases and the influence of container lead faces reduces, creating only small peaks in intensity. As witnessed previously, loading configurations with larger space between containers create larger pulses in slipstream velocities, causing higher turbulence intensities than consists with smaller spaces between loaded containers.

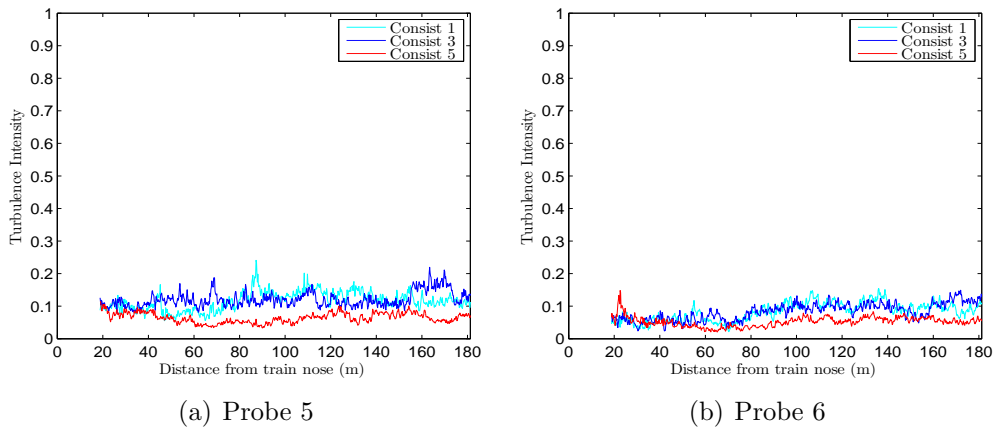


Figure 5.22: Turbulence intensity for the normalised ensemble longitudinal component of velocity U for train consists 1 (red), 3 (blue) and 5 (cyan) at probe positions 5, and 6 above the train roof.

The turbulence intensities for probes 5 and 6 above the train roof of consists 1, 3 and 5 are illustrated in figure 5.22. It is clear by comparing with figure 5.21 that turbulence intensity is higher at train side than above train roof. The maximum values recorded above the train roof are similar to values recorded at the furthest distance from the train side, indicating a much smaller boundary layer development above the roof. As the measuring height increases turbulence intensities decrease to less than 5%.

5.6.2.4 Autocorrelation

The cross correlation function is a measure of dependence of values in one signal to those in another signal (Taghizadeh, 2000). The autocorrelation function is a special

case of cross correlation in which the measure of dependence is calculated for a signal with itself by measuring the dependence of values of the signal at one time with values of the signal at another time (Taghizadeh, 2000). For a continuous time series the autocorrelation function is defined as (Taghizadeh, 2000),

$$R_{xx}(\tau) = \lim_{T \rightarrow \infty} \frac{1}{2T} \int_{-T}^T U_r(t) U_r(t + \tau) dt, \quad (5.5)$$

where T is the period of observation and the autocorrelation function R_{xx} is always real-valued and an even function with a maximum value at $t = 0$. Autocorrelation can be used to detect non randomness in data and identify appropriate time series models if data is not random (Box and Jenkins, 1970).

For a time series with constant time step the lag is number of time steps between the signal and itself in the autocorrelation function. Therefore for a sampled time series with a constant time step the normalised discretised form of the autocorrelation function is (Box and Jenkins, 1970),

$$corr_{\tau} = \frac{\sum_{t=1}^{N-k} (U_r(t) - U(t))(U_r(t + \tau) - U(t))}{\sum_{t=1}^k (U_r(t) - U(t))^2} \quad (5.6)$$

where $U_r(t)$ is a normalised individual run at time step t , $U(t)$ is the normalised ensemble average at time step t and $corr_{\tau}$ is the autocorrelation coefficient at lag τ . A correlogram is the plot of the autocorrelation as a function of the lags (Box and Jenkins, 1970).

The autocorrelation function can be applied to the boundary layer region to calculate the correlation of turbulent fluctuations and provide information about the duration of gusts in this region. The autocorrelation is calculated with respect to each raw non-resampled individual run by resampling other run data to create an ensemble average in relation to the individual run train speed. The autocorrelation is then calculated for each run in relation to the ensemble average for that train speed. Autocorrelation data

is then resampled for the nominal train speed V_{train} and an average autocorrelation calculated, in which high values indicate high correlations and vice versa.

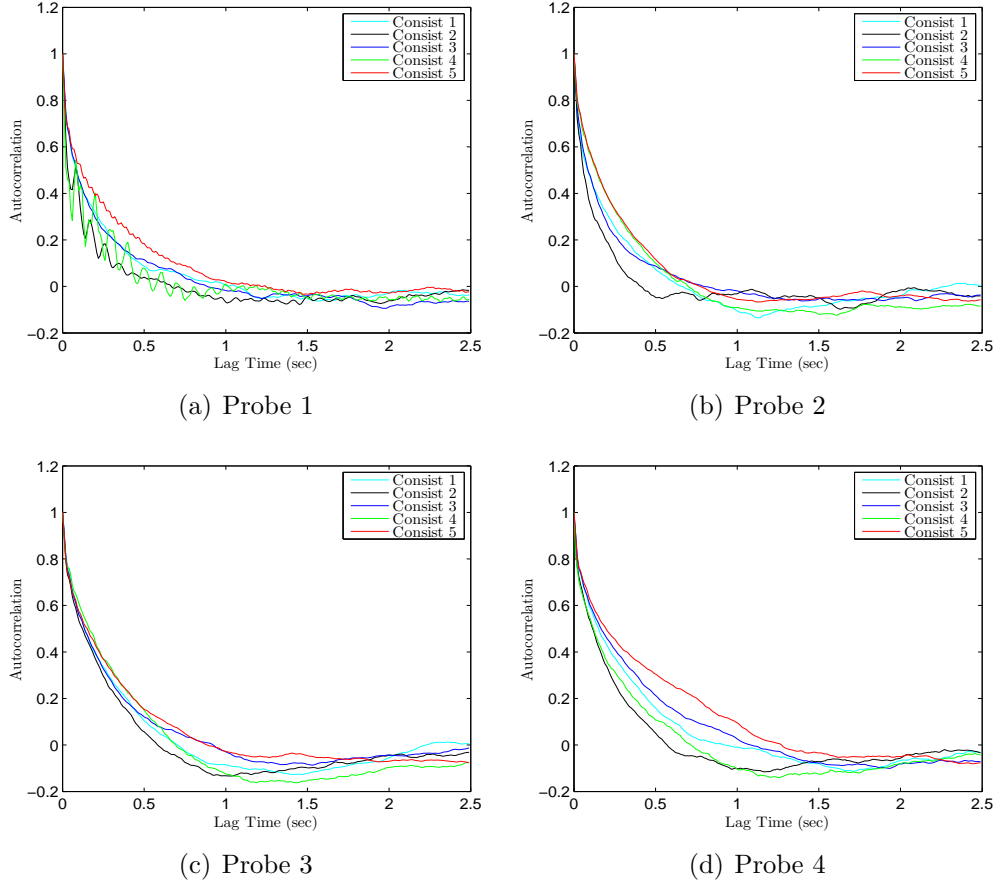


Figure 5.23: Autocorrelation for the normalised ensemble longitudinal component of velocity U for train consists 1 (red), 2 (green), 3 (blue), 4 (black), 5 (cyan) in the boundary layer region for probes 1, 2, 3 and 4.

In figure 5.23 correlograms for consists 1, 3 and 5 with train length 181.25m and consists 2 and 4 with train length 101.25m at probe positions 1 to 4 are illustrated. In all cases the correlations fall away rapidly over the first 0.5 seconds. This indicates that much of the energy in the boundary layer region is at time scales below 0.5 seconds, as witnessed in full scale container freight data analysed by Sterling et al. (2008).

Sterling et al. (2008) hypothesised that small peaks at higher lag time were due to larger scale turbulence, possibly due to spaces between containers. It is possible to see in figure 5.23 that configurations with low loading efficiency have more peaks after 0.5 seconds than consist 1 and 2, indicating the possible observation of larger turbulent time scales due to spaces in container loading. For consists with lower loading efficiency correlations fall away more rapidly than consist 1, suggesting that spaces between containers creates higher levels of small scale turbulence.

As the distance from train side is increased the correlations fall away less rapidly, indicating that smaller scale turbulence which existed close to the train side dissipates as the distance from train side is increased. Figure 5.23(c) shows very similar correlations for consists 1, 3, 4 and 5 suggesting higher levels of small scale turbulence created by consists 3, 4 and 5 has dissipated at this distance from train side and only larger scale turbulence, similar to that created by consist 1 exists.

The autocorrelation above the train roof for all consists, shown in figure 5.23(a), indicate towards a periodic oscillation. A property of autocorrelation is that the autocorrelation of a periodic signal is also periodic, therefore the autocorrelations above the train roof have detected a non-random part of the time series. By calculating a Fast Fourier Transform (FFT) it is possible to see that the frequency of this oscillation is between 10-20Hz with a higher frequency oscillation of 270-300Hz as well. The FFT transforms between the time domain and the frequency domain, therefore when the time series is transformed to the frequency domain information about at which time such frequencies occur is lost. The method of Wavelet analysis allows a time series to be transformed from the time domain to a time-frequency domain, providing a series of

powers for each frequency present at each time step. This method will be described in further detail in section 5.6.4, where it will be possible to explore the higher frequency periodic oscillation further. It is hypothesised the lower 10-20Hz oscillation witnessed could be caused by periodic flow separation from the leading edge of the train roof at the nose. Leading edge periodic flow separations similar to the hypothesised case have been observed in previous CFD bluff vehicle studies (Hemida and Baker, 2010; Hemida et al., 2010).

A useful property of the correlogram is the integral under the curve represents the integral time scale (Kundu and Cohen, 2010). By taking the integral under the average autocorrelation from the zero lag to the first zero crossing it is possible to find the integral time scale for each consist, and thus multiplying by train speed an integral length scale. The results are shown in table 5.3, note all integral time and length scales are given as the full scale equivalent.

		Consist Number				
Probe Number		1	2	3	4	5
1	time scale (s)	0.19	0.10	0.14	0.09	0.14
	length scale (m)	4.83	2.52	3.57	2.25	3.60
2	time scale (s)	0.16	0.16	0.13	0.08	0.13
	length scale (m)	4.10	3.94	3.19	2.02	3.21
3	time scale (s)	0.17	0.18	0.17	0.14	0.16
	length scale (m)	4.67	4.49	4.23	3.52	4.05
4	time scale (s)	0.28	0.15	0.22	0.13	0.19
	length scale (m)	7.09	3.85	5.57	3.28	4.67

Table 5.3: Autocorrelation integral time and length scales for freight consists 1 to 5 at probe positions 1 to 4.

For all consists the integral time scales are shorter than 0.3 seconds. The shortest time scales exist close to the train side for consists with lower loading efficiency. As the distance from train side is increased the time scales increase suggesting dissipation of energy within the boundary layer further away from the train side, as smaller turbulent scales decay. The integral length scale ranges from 2m to 5m for consists with containers.

The influence of spaces between containers not only creates larger turbulent scales

during processes such as flow separation at container lead faces but this also creates higher levels of small turbulent scales within the boundary layer. This is reflected by shorter integral time and length scales for poorly loaded consists 3, 4 and 5 in relation to consist 1. Sterling et al. (2008) stated that time scales less than 0.1 seconds with a length scale between 3-5m are too rapid for the human body to react and are unlikely to cause human instability. However for a partially loaded consist with a repeated loading configuration there are repeating gusts within a timescale that could lead to human instability. If the results are scaled to full UK freight line speed of 33.5m/s this creates an average time scale of 0.2 seconds with a length scale between 5-8.5m, within the suggested range likely to cause human instability (Sterling et al., 2008; Jordan et al., 2009).

In comparison to full scale results published in Sterling et al. (2008), trackside measuring positions give comparable results to model scale, however model scale integral time scales are smaller than those measured at a similar position to the full scale platform position. It is suggested differences in results at this position are due to platform interaction, negating the influence of bogies and undercarriage equipment in the full scale results. In comparison of model and full scale results it is hypothesised that due to Reynolds number effects the boundary layer development at smaller turbulent scales is different between full and model scale experiments (section 5.9.1).

5.6.3 Tail and wake region

In the tail region boundary layer growth ceases and U falls away into the wake. In previous passenger studies a large tail velocity peak is witnessed due to shedding vortices, however visualisation of this peak depends on whether the vortex shedding is in phase with the side on which the measurements are made (Sterling et al., 2008). In section 5.4, an additional piece of analysis was undertaken to identify if a tail peak existed for each individual run. This analysis showed no tail peak existed for the TRAIN rig

model freight train for any loading configuration. Differences between flow in passenger and freight tail regions are due to train tail shape. Intuitively it is suggested that research into flow around surface mounted cuboids in a line should provide the closest comparison for a container freight train.

At the rear face of a surface mounted cuboid a recirculation zone is observed for flows with a similar Reynolds number to the model freight train at the TRAIN rig, however the zone extents remain relatively bounded by the cuboid rear face edges (Stoesser et al., 2003). It is hypothesised that contrary to a passenger train with shedding vortices, a container freight train is more likely to have a recirculation zone in the tail region. Analysis in section 5.5 highlighted peaks in V and W observed at the train nose and container lead faces were a characteristic pattern of flow separation into a recirculation zones. At the train tail there is a negative peak in V at train side and a negative peak in W above the train roof at 10m beyond the train end, suggesting a recirculation bubble closely bounded to the rear of the last container. However due to Cobra probe positioning and sampling capability it is suggested that it will not be possible to fully observe this recirculation at the TRAIN rig. A numerical simulation through the application of CFD focusing on the rear of a container freight train is most likely to highlight characteristic flow patterns in this region.

Figure 5.24 shows the normalised ensemble longitudinal component of velocity U in the near and far wake regions measured from 101.25m (end of short train) to 1500m from the train nose for all consists at probe positions 1 to 4. In the wake region U decays at a similar rate for all probes. For probes 3 and 4 there is initially an increase in U before the decay into the far wake. This effect is caused by lateral spread of the wake (Baker, 2010). Baker et al. (2013a) discusses similarity of velocity decay in the far wake region between different passenger train types. By modelling velocity decay using a power law type equation,

$$U = a(x)^q \quad (5.7)$$

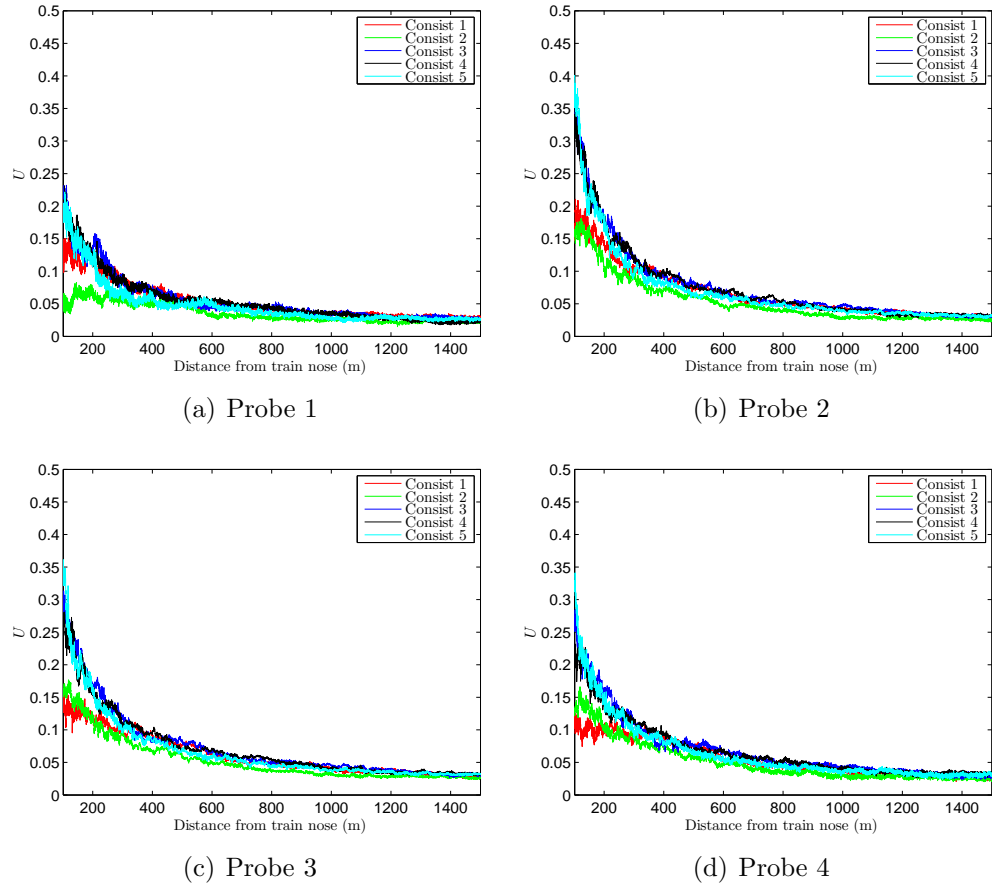


Figure 5.24: The wake region for the normalised ensemble longitudinal component of velocity U for train consists 1 (red), 2 (green), 3 (blue), 4 (black), 5 (cyan) in the boundary layer region for probes 1, 2, 3 and 4.

where x is the longitudinal position of the train, Baker et al. (2013a) found for passenger trains a common power of $q = -0.5$ could be applied. Using equation 5.7 and the definition from Baker et al. (2013a) that the far wake is taken to occur at distances greater than 100m from the end of the train, a common power of $q = -0.85$ has been calculated for the freight train. Figure 5.25 shows the decay of U in the far wake for consists 1 and 5 for the 181.25m train plotted with the fitted power law curve. The curve fit generally exhibits good agreement with the far wake data for all consists. It is expected that differences between passenger and freight train common powers occur because of differences in shape between train tails, with freight trains lacking any aerodynamic features found on passenger trains. Passenger trains are generally self-contained vehicles which can be driven from both ends, thus the nose and tail features are in most cases the same, unlike a freight train hauled by a locomotive at the front.

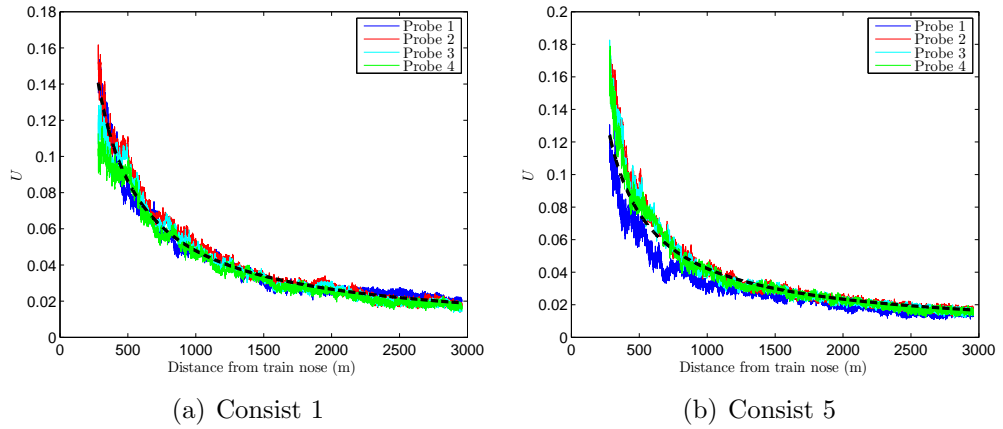


Figure 5.25: The far wake region (100m from the train end) for the normalised ensemble longitudinal component of velocity U for train consists 1 and 5 for probe 1, 2, 3 and 4. The dashed black line indicates the fitted curve by the power law equation 5.7 with q set to -0.85.

As discussed in previous studies, the influence of the train is still visible into the far wake (Baker, 2010; Baker et al., 2013a). It is striking to note that following an initially rapid reduction in slipstream velocities following the train passage, dissipation of slipstream velocities reduces and velocities are seen to extend into the far wake. This

suggests large scale flow structures decay rapidly in the near wake and therefore the far wake exhibits a gradual decrease in remaining velocities (Baker, 2010). Slipstream velocity magnitudes above 10% of train speed are present to over three times train length following the train tail passage (two times train length for slipstream velocities above the train roof).

5.6.4 Wavelet analysis

In section 4.6 and 5.6.2.4 a brief introduction was given to wavelet analysis and the advantages over Fourier transforms. For stationary flows Fourier transforms can be used to find frequency information for the infinite time domain. However for non-stationary flows, as frequencies are not present for all time, a method of transforming to a time-frequency domain is needed, this method is wavelet analysis (Torrence and Compo, 1998). By calculating wavelet plots for individual runs it is possible to analyse the frequency content of slipstream velocities and develop an understanding of any key flow characteristics.

5.6.4.1 Wavelet analysis of TRAIN rig data

Figures 5.26 - 5.29 illustrate wavelet plots for the normalised longitudinal velocity component U for specifically chosen individual non-resampled runs for the 181.25m train with consists 1, 3 and 5 at probe positions 1 to 4. Analysis of individual runs is used to assess all frequencies present in the flow, thus representative runs are chosen with train speed closest to the nominal train speed $V_{train}=20\text{m/s}$. Analysing ensemble averages is not appropriate as through the averaging process many frequencies are suppressed. The wavelet plots give a visual representation of the dimensionless power of frequencies present at each time step, which for these plots has been converted to full scale distance. In these figures the y-axis has been converted to a Log axis for ease of analysis.

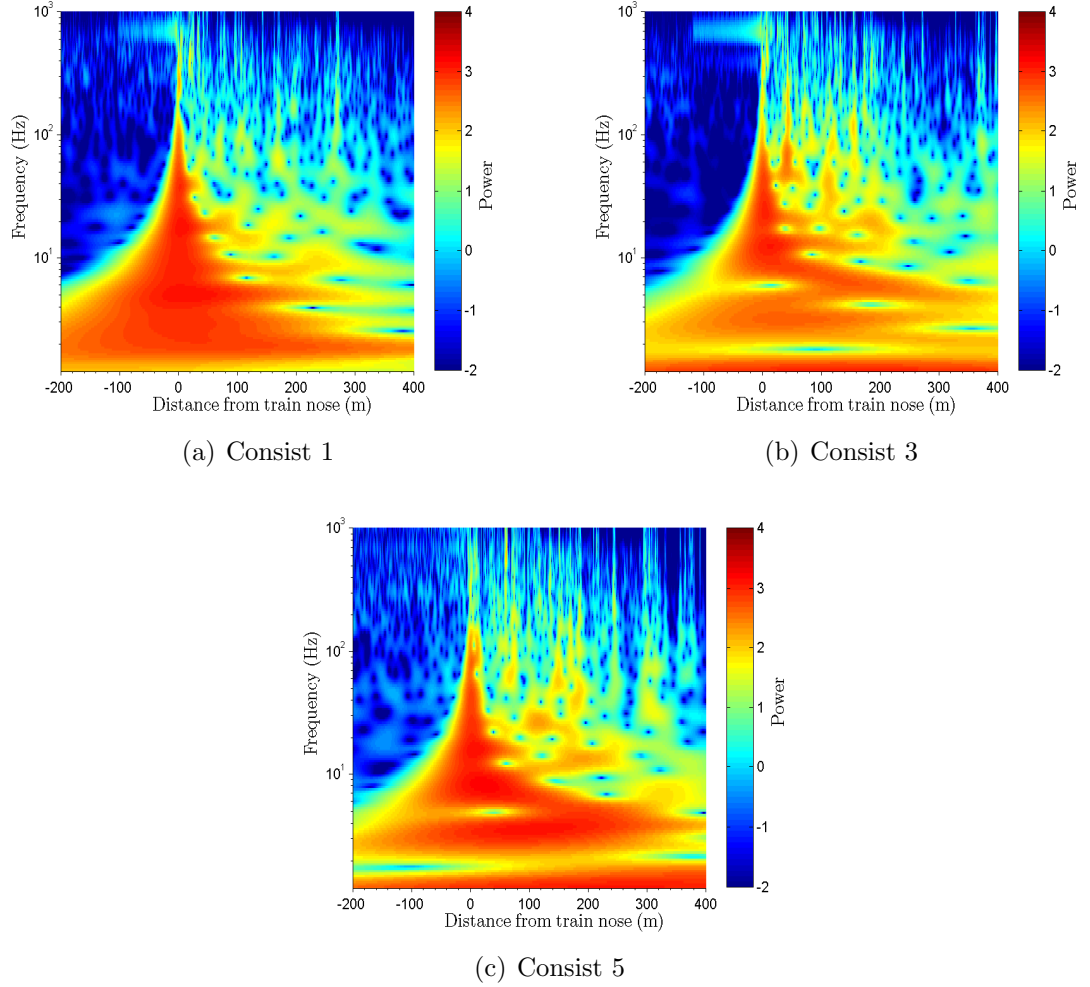


Figure 5.26: A series of wavelet plots for normalised longitudinal component of velocity U for consists 1, 3 and 5 at probe position 1.

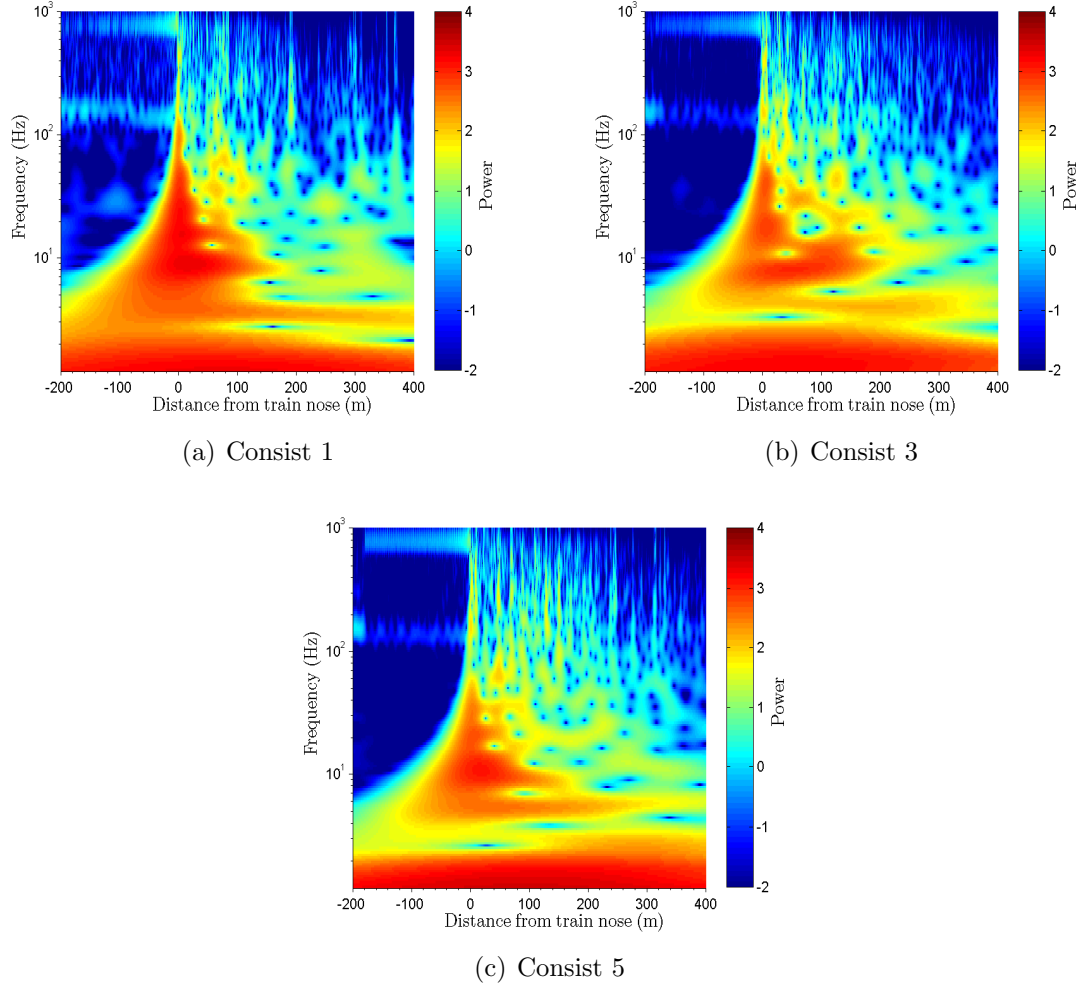


Figure 5.27: A series of wavelet plots for normalised longitudinal component of velocity U for consists 1, 3 and 5 at probe position 2.

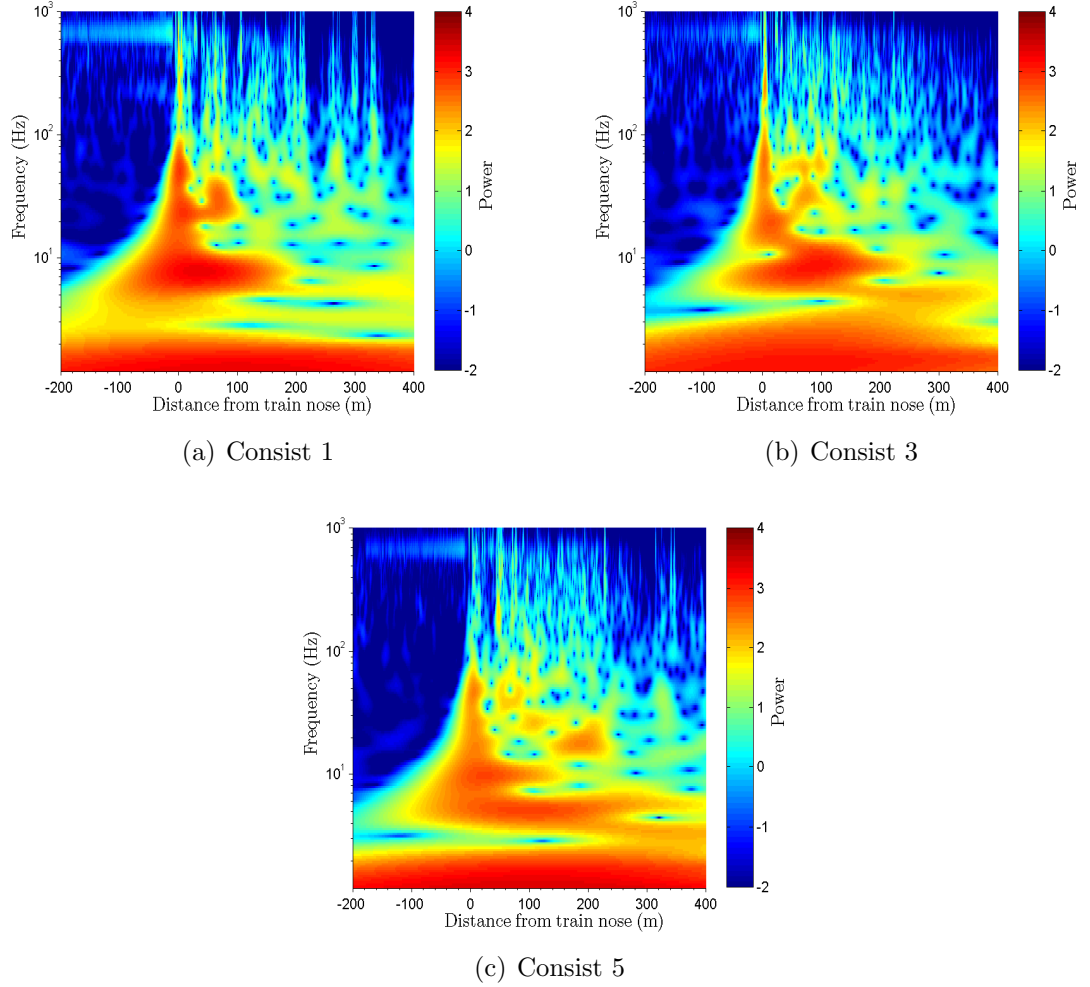


Figure 5.28: A series of wavelet plots for normalised longitudinal component of velocity U for consists 1, 3 and 5 at probe position 3.

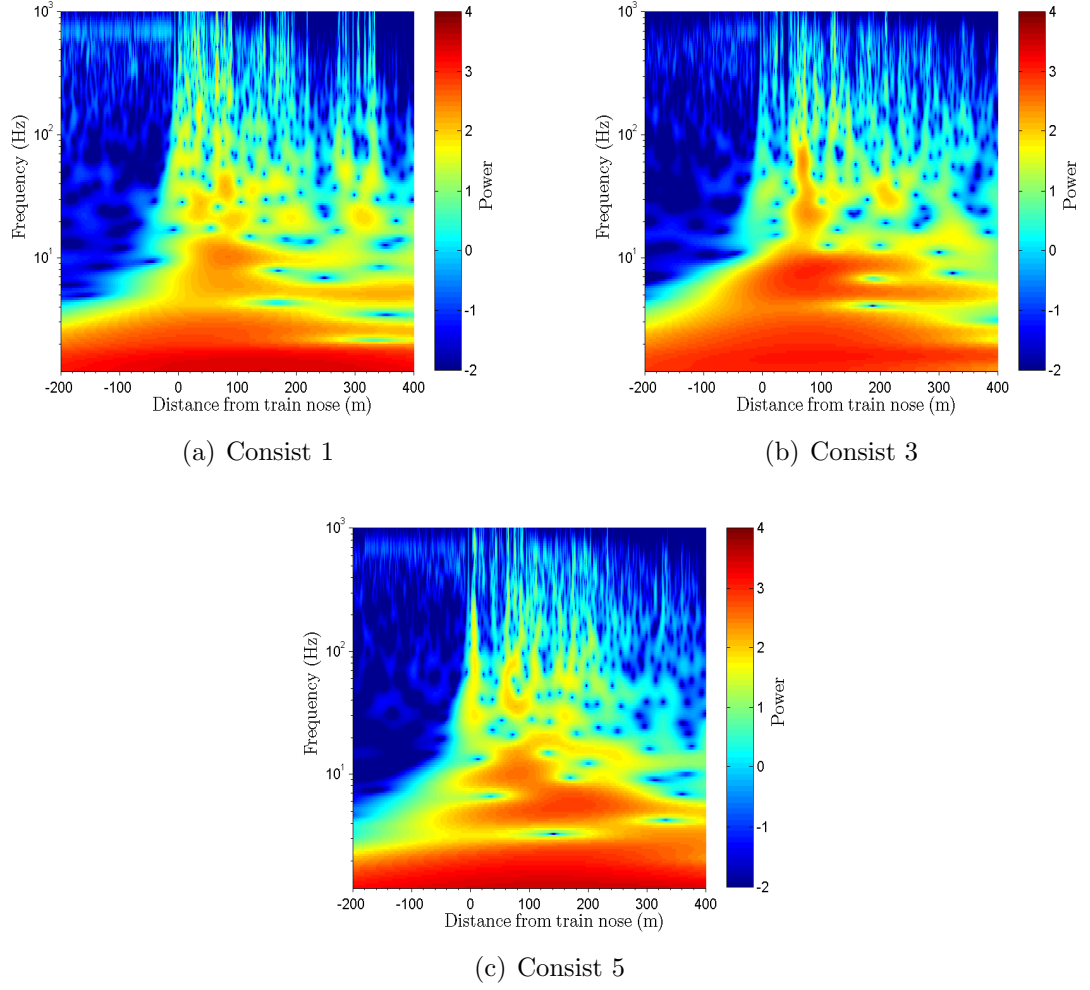


Figure 5.29: A series of wavelet plots for normalised longitudinal component of velocity U for consists 1, 3 and 5 at probe position 4.

The highest powers in all figures occur at lower frequencies (less than 10Hz), reflecting variations in the overall flow field. By extending the x-axis to include the whole 20 seconds of recorded Cobra probe data it is possible to see the extents of the high power region for low frequencies. Upstream the power at low frequencies builds around 500m ahead of the train nose, corresponding to 20m at model scale (figure 5.30), hypothesised to be related to the firing process. As the firing carriage is released an audibly loud noise occurs, which is registered by the Cobra probes. In the wavelet plot (figure 5.30) the peak in the velocity creates a high power peak across all frequencies 500m upstream (the position from which the train is fired); seen to be the root of the high frequencies oscillations witnessed for probe 1 (section 5.6.2.4). It should be noted that changes in velocity due to the firing process fall below the Cobra probe range of accuracy of $\pm 0.5\text{m/s}$.

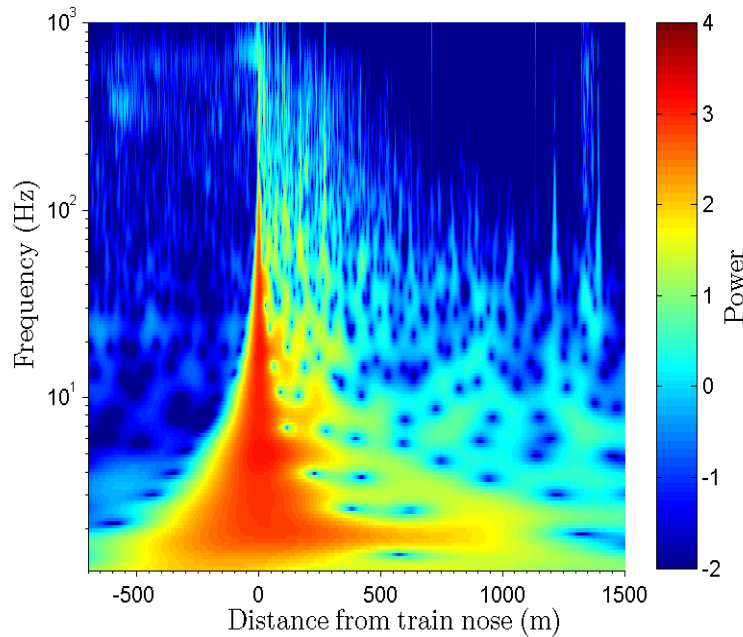


Figure 5.30: A wavelet plot for normalised longitudinal component of velocity U for consist 1 at probe position 1 with extended x-axis.

In the wake region the high power at low frequencies is seen to extend into the far wake to nearly 800m, however the power gradually decreases after 400m. As discussed in section 5.6.3, velocities in the near wake decay rapidly to 10% of train speed at a

distance 400m from the train nose, related to the decay of large scale flow structures; however in the far wake remaining velocities decrease gradually. The high power of low frequencies relate to larger flow structures present until 400m, then the power gradual decreases relating to the decreasing velocities remaining. Above the train roof high frequency oscillations decay rapidly in the wake region.

As the train passes the measuring position the power is increased for both high and low frequencies, reflecting the large and small scale turbulence within slipstream velocities. The high frequencies decay rapidly after key features, such as the train nose and into the wake following train passage.

In the nose region high power at all frequencies reflect the large velocity magnitude created due to the bluff shape of the Class 66 nose. Following the train nose into the boundary layer region high frequencies decay, however for consist 3 and 5 pulses in power at higher frequencies are witnessed at container lead faces. As discussed, the influence of spaces between containers creates pulse peaks in U within the boundary layer, which increase displacement thickness and turbulence intensity. The wavelet plots highlight that these pulses create increases in both high and low frequencies, related to both large and smaller scale turbulence, as predicted in section 5.6.2.4. The influence of wagon design creating larger spaces between containers at the wagon brake end creates pulse peaks with high power across higher frequencies.

As the distance from train side is increased the power across all frequencies and the power of pulse peaks created at container leading faces following a space in the loading configuration reduces. Power above the train roof is lower than results recorded at a similar position at train side, suggesting smaller boundary layer growth above the train roof.

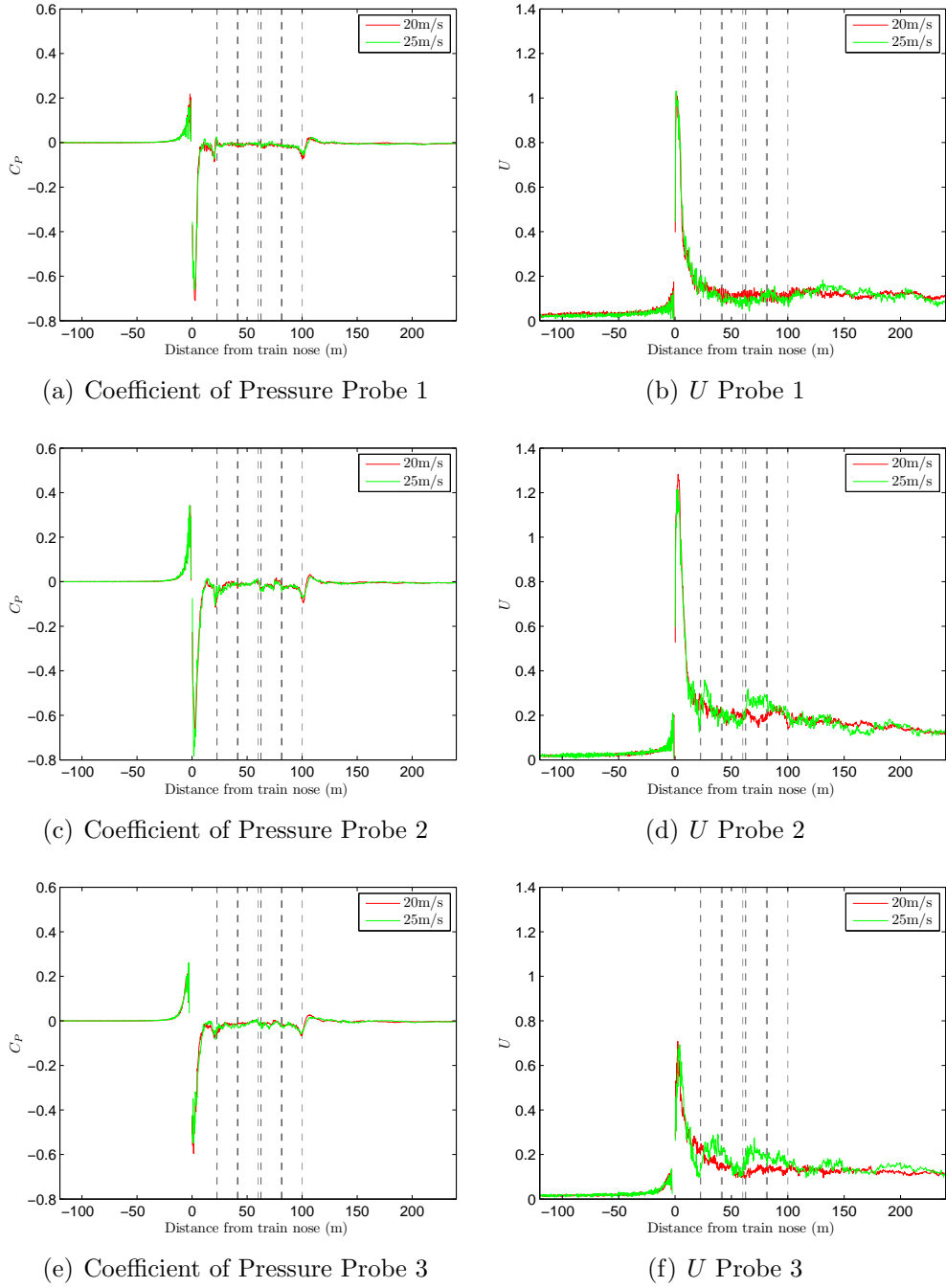


Figure 5.31: Coefficient of pressure and normalised ensemble longitudinal component of velocity U for freight consist 1 measured at train speeds 25m/s (green) and 20m/s (red) for probes 1, 2 and 3. The vertical dashed lines indicate the front (black) and rear (grey) faces of the containers.

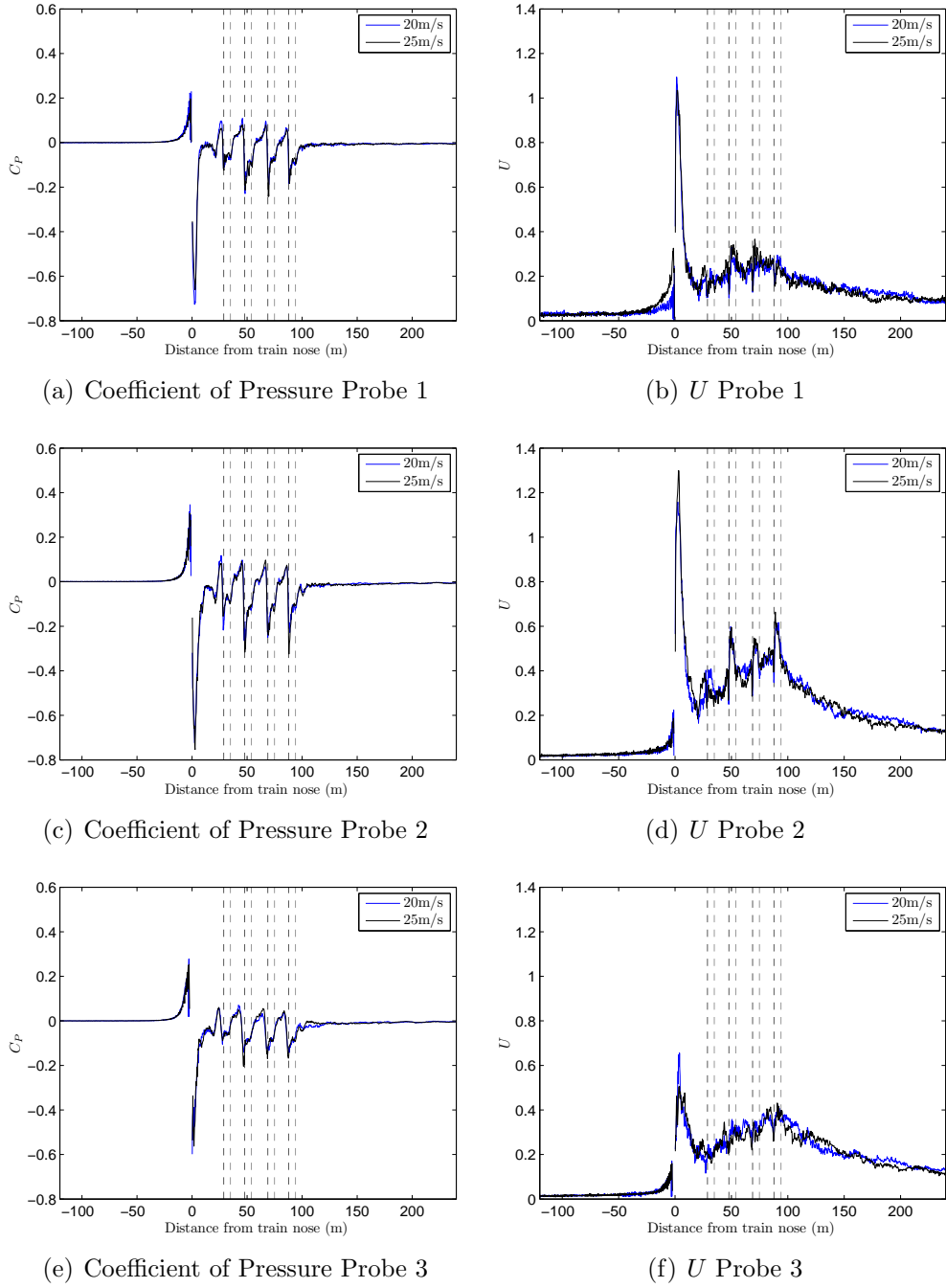


Figure 5.32: Coefficient of pressure and normalised ensemble longitudinal component of velocity U for freight consist 5 measured at train speeds 25m/s (black) and 20m/s (blue) for probes 1, 2 and 3. The vertical dashed lines indicate the front (black) and rear (grey) faces of the containers.

5.7 Assessing the effect of train speed

In appendix C the results from a series of preliminary experiments using the 101.25m train with consist 1 and 5 at train speed 25m/s are discussed. By comparing the preliminary experiment results with those discussed in sections 5.3 and 5.4 an analysis to assess the effect of train speed on slipstream development can be undertaken. In the preliminary experiments the ensemble size (nine runs for consist 1 and nineteen runs for consist 5) is lower than TSI standards. For consist 1, an analysis of individual runs was undertaken, which found run to run variability in comparison to consist 5 was much lower, due to relatively smooth train sides and roof. Therefore it is felt this comparison can be used as an indicator to the effect of train speed on slipstream development.

Figures 5.31 and 5.32 illustrate the coefficient of pressure and normalised ensemble longitudinal component of velocity U for consists 1 and 5 measured at train speed 25m/s and 20 m/s for probes 1, 2 and 3. For all plots the characteristic flow regions and magnitudes created within these regions match closely for both train speeds, indicating a linear relation between slipstream velocity magnitudes and train speed.

The coefficient of pressure remains closely linked in all flow regions for both train speeds, whereas U exhibits more variation. The largest variations occur for consist 1 in the boundary layer region, due to the relatively small number of runs undertaken creating a small ensemble size of nine runs for train speed 25m/s. As discussed in section 5.2, the ensemble becomes more stable as the ensemble size is increased, hence the TSI requirement of at least 20 repeats. For consist 1 the nose peaks exhibit close relation, indicating the reproducibility of the nose peak. In the boundary layer region, for train speed 25m/s the ensemble varies around the ensemble for 20m/s, indicating the turbulent nature of the boundary layer region, and thus the need to increase the ensemble size. There is more variation at train side than above the train roof, reflecting a more turbulent development at train side than over the train roof, as seen in section

5.6.2.3.

In section 5.6 a detailed analysis of slipstream development for different flow regions was undertaken comparing various container loading efficiencies. Similar analysis has been completed comparing results for differing train speeds; in all cases good agreement is found. This is expected as analysis methods in section 5.6 are based on U , which has been shown in figures 5.31 and 5.32 to be closely related for different train speeds.

In section 5.6.2.4 a discussion regarding slipstream development in relation to Reynolds number independence suggested although key statistical regions developed with comparable boundary layer growth and similar velocity and pressure magnitudes, finer small turbulent scale development would be different. Figures 5.31 and 5.32 highlight the comparable growth between normalised results, indicating a linear relationship between velocity magnitudes and a squared relationship in pressure. This relationship indicates Reynolds number independence for key statistical events in the boundary layer growth within the range of Reynolds number tested. The range of Reynolds numbers created by varying the train speed from 20m/s to 25m/s for the model train is relatively small in comparison to a full scale train. The discussion of the Reynolds number independence is developed further in sections 5.8 and 5.9.1 by analysing comparisons of model and full scale data over a large range in Reynolds number.

5.8 Full scale results

In general full scale slipstream experiments are expensive and difficult to complete, with results highly susceptible to changes in ambient conditions. Model scale experiments offer a cheaper, easier option to understanding slipstream development, but results need validation. Section 5.8.1 compares model and full scale results for U and coefficient of pressure, drawing conclusions on the suitability of using model scale experiments to understand slipstream development of a freight train. The comparison is further explored by carrying out TSI and UK safety position calculations, comparing results

to previous high speed passenger studies and assessing the suitability of standardised codes in relation to freight trains.

5.8.1 Validation of model scale results

In sections 5.3 and 5.4 key flow regions and slipstream development was discussed in terms of U and coefficient of pressure. Full scale data from Uffington can provide validation for model scale TRAIN rig data, however a series of assumptions must be made.

Recorded train types at Uffington (table 3.4) are all hauled by a Class 66 locomotive but with different consists, wagon types and train lengths. Therefore it is not possible to create an ensemble average for all trains. It is however possible to focus on the Class 66 locomotive and create an ensemble of all data in the nose region for comparison to model scale data. Furthermore Uffington train 4 is hauled by a Class 66 locomotive followed initially by 12 fully loaded flatbed wagons, thus a comparison can be made with consist 1 at model scale.

As discussed in section 3.3.2.1, although not modelled at the TRAIN rig, it is felt the influence of the relatively shallow 0.3m ballast shoulder on slipstream velocities would be negligible in relation to the probe positions tested in this study (Sterling et al., 2008). Pressure probes P1 and P2 at Uffington match probe position 8 at model scale, thus comparison is restricted to the 181.25m train. Anemometer position V1 is closest to probe position 7 at model scale, however differences in measuring height may account for any small differences in slipstream development.

5.8.1.1 Coefficient of pressure

Figure 5.33 illustrates a comparison of the ensemble coefficient of pressure for model and full scale data in the nose region. Data for pressure probes P1 and P2 is ensemble

averaged in the nose region to give an ensemble size of 16. Similarly model scale data for probe 8 for all consists has been ensemble averaged creating an ensemble size of 75 runs.

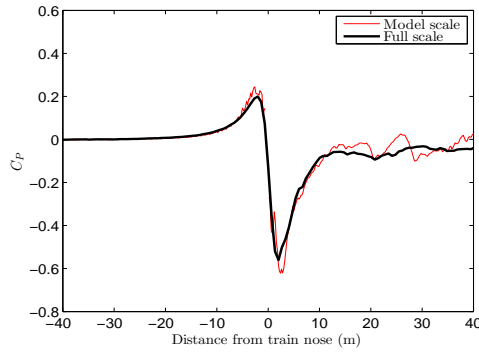


Figure 5.33: A comparison of coefficient of pressure for model (red) and full scale (black) data.

Good agreement is seen throughout the nose region in coefficient of pressure development and peak magnitudes between model and full scale data. Upstream the coefficient of pressure is zero, rising to a positive peak ahead of the train nose, falling away to a negative peak following the nose passage. The positive peak magnitude is very similar, with close relation seen between growth and decay of this feature. The negative peak magnitudes are slightly different, of the order 0.05, but general growth and decay follow similar patterns. It is hypothesised that the small difference between negative peak magnitudes may be due to the shallow ballast shoulder influence.

5.8.1.2 Normalised ensemble longitudinal component of velocity U

Figure 5.34 illustrates a comparison of the normalised ensemble longitudinal component of velocity U for model and full scale data in the nose region. Data for anemometer V1 is ensemble averaged in the nose region to give an ensemble size of 8. Similarly model scale data for probe 7 for all consists has been ensemble averaged creating an ensemble size of 75 runs.

The general development of U through the nose region shows good agreement in flow

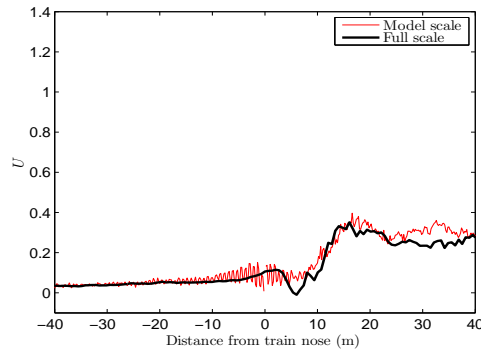


Figure 5.34: A comparison of normalised ensemble longitudinal component of velocity U for model (red) and full scale (black) data.

development and peak magnitudes between model and full scale data. Upstream velocity is zero, rising to a small peak in U at the front of the Class 66 nose. This is followed by a fall in U before rising to the nose peak, which rapidly forms into boundary layer growth. Nose peak development follows a similar pattern for both model and full scale, with peak magnitudes showing good agreement. It is hypothesised small differences in peak magnitudes are created by the difference in measuring height between probe 7 and V1 and the interaction influence with the shallow ballast shoulder.

Figure 5.35 shows the individual runs for U of consist 1 at probe 7, plus the ensemble average for the 25 runs. The full scale data for train 4, a 400m long fully loaded container freight train, is also plotted to compare boundary layer development for the fully loaded configuration. As only one run is available for a fully loaded train at full scale it is important to compare the fluctuating boundaries of the individual data and how this compares to the ensemble (section 5.2).

In general the full scale data follows the flow development seen at model scale. The nose region, as discussed exhibits good agreement with the ensemble. As flow develops into the boundary layer region it remains bounded by the limits created by individual model scale runs, oscillating about the ensemble for the entire model scale train length of 181.25m. Following the end of the model train the full scale data continues to remain bounded within the limits set by the model scale boundary layer, until the train tail where velocities fall away into the wake. As with the model scale data there is no peak

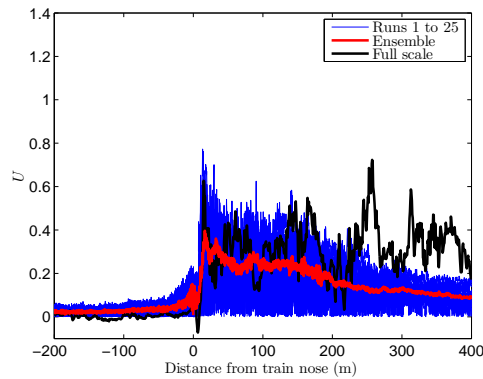


Figure 5.35: A comparison of normalised longitudinal component of velocity U for individual runs (blue) and the ensemble (red) at model scale and the equivalent full scale (black) data.

at the train tail of any full scale velocity time history. It is hypothesised that if a series of full scale runs were undertaken with the fully loaded train 4 configuration to create an ensemble size ~ 25 , the ensemble average would exhibit similar growth to the model scale ensemble.

Unlike the fully loaded consist (figure 5.35), no direct comparisons can be made for partially loaded configurations between full and model scale. Figure 5.36 illustrates a comparison of U for all train types at model and full scale. Essentially the upstream and nose regions are the same for each train, but boundary layer growth differs greatly depending on wagon type and loading configuration. Velocity magnitudes in the boundary layer region reach maximum values of 0.6-0.7 of train speed, similar to individual runs for the partially loaded consists at model scale. Although it would be wrong to draw solid conclusions to the suitability of modelling partially loaded container freight trains, figure 5.36 illustrates that peak magnitudes for individual runs are of similar order to model scale, with a very similar flow development.

5.8.2 TSI analysis

In figure 5.36 velocity magnitudes for individual runs in the boundary layer region reach maximum values of 0.6-0.7 of train speed for both model and full scale. European

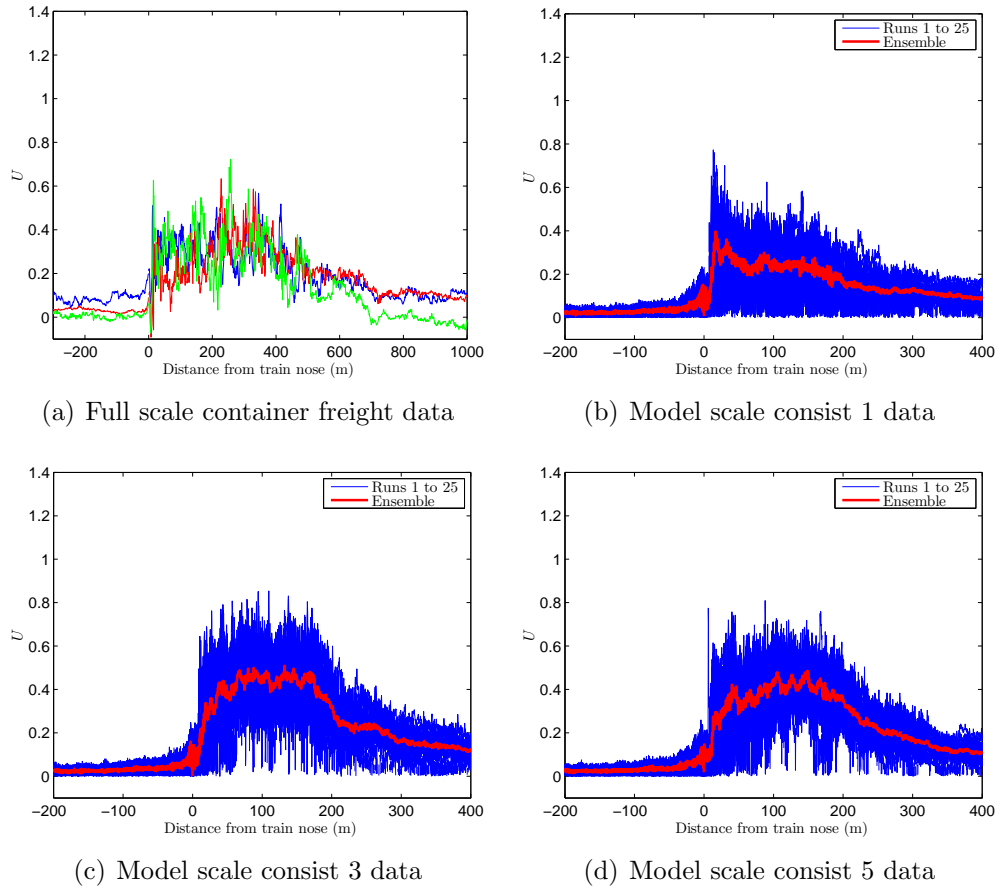


Figure 5.36: A comparison of normalised longitudinal velocity U for all train types at full scale. Consists 1, 3 and 5 data and ensemble averages at model scale are also plotted to provide a comparison for flow development.

standards state for open track a train running at 50-70 m/s should not cause velocities exceeding 20.0 m/s at 0.2 m above top of rail and 3.0 m from the centre of the track (TSI, 2008).

TSI methodology aims to provide a standardised set of regulations to allow interoperability throughout the European rail network. For straight open ballasted track the limit velocity is calculated as (TSI, 2008),

$$u_{2\sigma} = \bar{u} + 2\sigma \quad (5.8)$$

where \bar{u} is the mean value of all maximum resultant air speed measurements in the x-y plane, and σ is the standard deviation. The TSI states tests should be carried out on track where the distance from the top of rail to the cess is 0.75 ± 0.25 m and at least 20 independent measurements taken in ambient wind speeds of less than 2 m/s at least 15 seconds before the train passes (TSI, 2008). In general measurements should be taken close to maximum operational line speed V_{train} with a least 50% of measurements within $\pm 5\%$ of V_{train} and 100% within $\pm 10\%$ of V_{train} . For Uffington tests all 8 freight runs fall within these limits and have therefore been resampled for $V_{train} = 33.5$ m/s, the full UK maximum operational freight line speed.

To calculate the TSI limit velocity for each independent run the resultant velocity of U and V is calculated then realigned and cropped to include the whole train passing event, starting 1 second before the train nose and 10 seconds following the train tail (TSI, 2008). Data is filtered using a 1 second moving average filter before calculating the mean \bar{u} and standard deviation σ .

Before discussing TSI analysis results it is important to understand the limitations of the model and full scale data in regards to this analysis. The TSI open track measuring position is recorded at a height of 0.2 m above the top of rail; the bogie region of the train. At model scale the bogie region is highly simplified for modelling purposes, thus it is accepted flow development in this region may be different to full scale (figure

3.4). The model scale open track measurements are taken for a non-ballast shoulder simulation, falling beyond the 0.75 ± 0.25 m top of rail to cess limit.

In regards to full scale data the lack of train passes and consistent train types will influence the TSI value. The analysis should be carried out with the same train at least 20 times, not a mixture of wagon and consist types. The lack of consistent data is expected to increase variability of measured velocities, altering the standard deviation, leading to an overestimate in value. Similarly the influence of meteorological conditions is also expected to increase variation in data, leading to an overestimate in TSI values (Baker and Quinn, 2012). Finally the trackside measuring position V1 was at a height of 0.7m above top of rail, which although still in the bogie region may give different results to a height of 0.2m.

Table 5.4 shows the TSI calculation results for the resampled 181.25m model freight train with consists 1, 3 and 5 and the full scale train at maximum UK freight line speed $V_{train} = 33.5$ m/s. Firstly all values lie below the 20m/s TSI limit, except the combined value for consists 1, 3 and 5 at model scale. Analysis for individual freight consists at model scale gives a standard deviation value of $\sigma \simeq 0.9$ m/s, however for the mixed consists at both model and full scale this value increases to $\sigma \simeq 2.5$ m/s. The difference in σ for the mixed calculation quantifies the effect of calculating TSI limit velocities for different freight types, exhibiting increased variability in maximum velocities created within the slipstream of different train types.

The values in table 5.4 are calculated for maximum UK freight line speed $V_{train} = 33.5$ m/s, however this speed lies below the lower train speed boundary for the TSI calculation (TSI, 2008). Similarly proposed increases in UK freight line speed to 40m/s would still leave freight train speeds below levels tested in the TSI, but values calculated using TSI methodology would, as shown in table 5.4, break TSI limit values not only for the 50-70m/s speed range but also the 70-83.5m/s range. The results highlight differences between maximum values created by passenger and freight slipstreams and the need to understand freight slipstream development. The TSI methodology is set

out in terms of passenger train design in line with increasing train speeds, however table 5.4 clearly shows for freight trains travelling at speeds below the lower bounds of TSI calculation the values calculated break current prescribed safety limits.

Consist type	Dimensional TSI value $u_{2\sigma}$			
	Train speed $V_{train}=33.5\text{m/s}$		Train speed $V_{train}=40\text{m/s}$	
	Model scale	Full scale	Model scale	Full scale
1	13.40	×	15.99	×
3	19.59	×	23.37	×
5	18.11	×	21.60	×
Mixed	20.63	17.02	24.62	20.31

Table 5.4: A table showing TSI calculation results for both model and full scale freight trains at train speeds $V_{train}=33.5\text{m/s}$ and $V_{train}=40\text{m/s}$.

Figure 5.37 illustrates maximum TSI velocities and the positions where values are recorded for a train speed $V_{train}=33.5\text{m/s}$. As discussed in section 5.4, higher slipstream velocities are witnessed for partially loaded consists. Maximum velocities are generally recorded in the boundary layer region for partially loaded consists and the nose region for fully loaded consists. This result differs from previous passenger studies, where in general the largest velocities are recorded in the near wake region (Sterling et al., 2008; Baker and Quinn, 2012). The spread in full scale values reflect the differences between train types and consist within the full scale data. In general, maximum velocities for full scale trains lie within the bounds of model scale data, exhibiting good agreement between full and model scale data.

Sterling et al. (2008) discusses the merits of 1 second moving averages in relation to passenger/trackside worker stability, concluding a 0.2-0.5 second moving average would provide a more realistic method of filtering for safety limits. The TSI methodology is repeated but with a 0.35 second moving average filter for the model and full scale data, results are shown in table 5.5.

As the filter size is reduced the smoothing effect is decreased and thus TSI values $u_{2\sigma}$ increase, as standard deviation values also increase. Reducing the filter size to a value similar to the time scale at which human instability may occur has increased

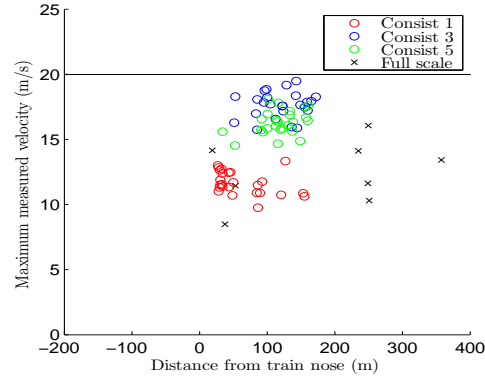


Figure 5.37: Maximum 1 second moving average velocities and the position where the value was recorded for train speed $V_{train}=33.5\text{m/s}$. The values show a comparison of model scale consist 1 (red circles), 3 (blue circles) and 5 (green circles) and full scale data (black crosses). An additional line has been plotted to show the TSI limit value of 20m/s .

	Dimensional TSI value $u_{2\sigma}$	
	Train speed $V_{train}=33.5\text{m/s}$	
Consist type	Model scale	Full scale
1	16.98	×
3	22.11	×
5	20.48	×
Mixed	22.79	22.33

Table 5.5: TSI calculation results for a 0.35 second moving average filter for both model and full scale freight trains at train speeds $V_{train}=33.5\text{m/s}$.

TSI calculated values beyond the 20m/s safety limit. This analysis implies the TSI methodology, when relating to passenger/trackside worker instability should possibly include an additional test with a filter size similar to human instability, as well as providing safe operational limits at prescribed safety positions.

5.8.3 UK safety position analysis

A similar analysis comparing data measured at the UK trackside safety position is carried out using results of full scale data presented by Temple and Johnson (2008) and Sterling et al. (2008) and the equivalent loading configuration, consist 3, at model scale for a 1 second and 0.35 second moving average filter. The trackside worker safety condition is defined as a distance of 2m from the centre of track for a train speed of less than 45m/s. Temple and Johnson (2008) found at this position passenger trains created a maximum 1 second moving average slipstream velocity of 17m/s measured 1m above the top of rail.

In general model scale data gives comparable results to the full scale data for the 1 second moving average, however as the filter size is reduced the model scale results give higher maximum values in comparison to full scale. Comparing ensemble averages recorded at the UK trackside safety position the Class 66 nose peak reaches a maximum of 100% of train speed, in comparison to the Class 92 nose peak reaching 30% of train speed, hypothesised to be related to the train nose shape. The time scale for the Class 66 nose peak for a train speed of 33.5m/s is 0.5 seconds, therefore as the filter size is reduced to 0.35 seconds the flow smoothing effect also reduces, and thus maximum velocity values move from being measured in the boundary layer region to the nose region (figure 5.38), accounting for differences created between full and model scale data.

For both filters all model scale maximum slipstream velocities exceed values recorded at the trackside safety position previously. A scaling is created with respect to the pre-

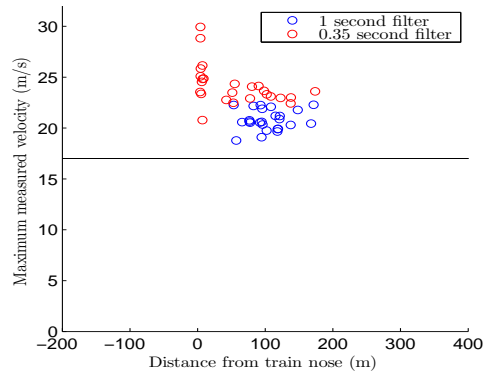


Figure 5.38: Maximum velocities and the position where the value was recorded within the train slipstream, for a train speed of $V_{train}=33.5\text{m/s}$ for consist 3 at the UK trackside safety position. Values show a comparison of a 1 second moving average filter (blue circles) and a 0.35 second moving average filter (red circles). An additional line has been plotted to show the maximum values recorded for a high speed passenger train of 17m/s .

vious maximum trackside slipstream velocity, 17m/s , to analyse the effect of increased slipstream velocities created by freight trains travelling at much lower train speeds in comparison to passenger trains (table 5.6).

Filter size	Changes to UK trackside safety position			
	Train speed (m/s)		Distance from centre of track (m)	
	Model scale	Full scale	Model scale	Full scale
1 second	27.39	24.89	2.45	2.40
0.35 second	23.57	23.16	2.84	2.54
none	15.07	16.31	4.45	3.29

Table 5.6: A table showing changes to the UK trackside safety position and train speed in relation to the suggested trackside safety limit of 17m/s calculated for a freight train passage at $V_{train} = 33.5\text{m/s}$. The table shows a comparison of different filter sizes.

The results in table 5.6 clearly indicate to create maximum slipstream velocities similar to passenger trains the distance from centre of track must be increased or train speed decreased for freight passage. Comparing maximum velocities for unfiltered and 1 second moving average data there is a difference of 45%, highlighting whether the use of a 1 second moving average filter as a measure for safety is appropriate. A more suitable length scale of 0.35 seconds suggests a reduced train speed below 24m/s to create similar maximum slipstream velocities to those presented in Temple and Johnson (2008).

A similar analysis of the UK ‘yellow line’ platform safety position is carried out comparing full and model scale data (Temple and Johnson, 2008). The yellow safety line was introduced as a passenger safety measure following slipstream incidents (chapter 2). The platform yellow line safety position is specified as 1.5m from the platform edge (2.95m from centre of track) for a passenger train passing at speeds up to 55m/s. Temple and Johnson (2008) found passenger trains recorded at this position created a maximum 1 second moving average slipstream velocity of 11m/s measured 1m above the platform. Although no platform is modelled in the model scale experiment, it is felt the results provide a useful indication to how freight trains differ from passenger trains at this prescribed safety position.

	Changes to UK platform safety position			
	Train speed (m/s)		Distance from centre of track (m)	
	Model scale	Full scale	Model scale	Full scale
Filter size				
1 second	29.01	25.77	3.41	4.12
0.35 second	24.28	23.04	4.07	4.40
none	16.51	19.10	5.99	4.80

Table 5.7: A table showing changes to the UK platform safety position and train speed in relation to the suggested platform safety limit of 11m/s calculated for a freight train passage at $V_{train} = 33.5\text{m/s}$. The table shows a comparison of different filter sizes.

The maximum 1 second moving average results imply that in relation to the passenger train value of 11m/s, the freight train speed should be reduced to below 25m/s. Similarly to trackside results the 0.35 second filter further increases the measuring distance away from current positions and differences between 1 second moving averages and none filtered data are around 45%.

5.9 Discussion

5.9.1 Reynolds number effect

In general good agreement is observed for velocity and coefficient of pressure magnitudes for differing train speeds (section 5.7) and between full and model scale (sec-

tion 5.8). This agreement suggests Reynolds number independence over the range of Reynolds numbers tested in the data presented; indicating the TRAIN rig facility is a viable option for carrying out experiments to understand slipstream development for a container freight train.

However, as the Reynolds number differs for the full and model scale experiments (5×10^6 vs 2×10^5) there is a difference in the range of turbulent length scales. As the Reynolds number increases the dissipation of energy by viscous forces increases in dependence on small scales. The differing Reynolds numbers imply different scales at which dissipation occurs, highlighted through the autocorrelation calculations (section 5.6.2.4). Therefore although key statistical regions, with comparable boundary layer growth and similar velocity/pressure magnitudes are observed at both full and model scale, the finer small turbulent scales development within the boundary layer are different.

Validation of model scale data to compare turbulent scale development within the slipstream relies on a comprehensive series of full scale experiments, including a number of measuring positions and runs undertaken with the same loading configuration. However, as discussed, full scale experiments are expensive and difficult to carry out. Therefore, based on the data available it is not possible to fully explore differences in turbulent scale development between model and full scale. This implies that model scale experiments can be used to offer an insight into key flow characteristics and the overall magnitude of velocities and pressures created but smaller turbulent scales cannot be accurately modelled, and so analysis of these must be compared further with full scale data.

5.9.2 Safety limits and positions

The results presented in section 5.8.3 highlight the magnitude of freight slipstream velocities created at much lower line speeds than passenger trains. Currently a train

is assumed safe for passengers and trackside workers if it passes the TSI methodology (section 5.8.2), however the UK trackside and platform safety positions are different to the TSI methodology positions. At UK safety positions there is no prescribed maximum slipstream velocity limit in relation to safety.

Jordan et al. (2009) and Sterling et al. (2008) concluded many factors are involved in understanding human stability in relation to slipstream velocities, therefore defining a safety limit at these positions would be difficult. The number of slipstream incidents is relatively low considering the magnitude of slipstream velocities created by freight train passage, highlighting whether current safety limits need reassessing or not. However results in section 5.8.2 indicate that TSI values calculated in line with proposed increases in freight train speed to 40m/s break TSI limits, potentially creating slipstream velocity magnitudes capable of causing instability in trackside workers or passengers at UK safety positions. Slipstream velocity magnitudes are however affected by loading efficiency and freight type, and as such the results in tables 5.6 and 5.7 should only be treated as an indicator to possible maximum slipstream velocities.

5.9.3 General concluding remarks

A series of conclusions can be drawn from the results and analysis presented in this chapter:

1. It is possible to present slipstream results as a series of flow regions as in previous passenger studies, albeit with differing flow development within these specific regions. Results are compared with typical passenger train magnitudes and large differences are found in the nose and tail regions, hypothesised to be related to vehicle shape. Velocity and pressure magnitudes in the nose region are much larger than any values observed in train slipstream studies previously, recorded at equivalent measuring positions.
2. Clear differences in slipstream development are observed for differing container

loading configurations.

- (a) For the coefficient of pressure, as loading efficiencies are decreased, a series of positive then negative peaks are observed about the lead face of loaded containers, the magnitude of which are dependent on space size between loaded containers.
 - (b) As loading efficiencies are decreased the magnitude of velocities within the boundary layer are increased, with a series of pulse peaks relating to the change in pressure at the lead face of loaded containers.
 - (c) For loading efficiencies of more than 50% boundary layer growth stabilises rapidly within the first four wagon lengths. However, for loading efficiencies of less than 50% continual boundary layer growth is observed until after five wagon lengths when boundary layer stabilisation occurs.
 - (d) Velocities in the lateral and vertical directions have magnitudes much larger than previously observed in passenger studies; increasing the overall magnitude by $\sim 10\%$. A series of pulse peaks are observed in V and W at the lead face of containers as loading efficiencies are decreased. Flow directions in the nose region suggest a flow reversal emanating from the leading edges of the Class 66 nose. Similarly flow directions in the tail region suggest a recirculation zone following the final loaded container.
 - (e) Magnitudes of velocities and pressure above the train roof are smaller than magnitudes recorded at a similar distance from the train surface at the train side. For all cases as the distance from the train surface is increased velocity and pressure magnitudes decrease.
3. A series of in depth analysis has been undertaken in each of the flow regions identified. Analysis has highlighted differences created through decreased loading efficiencies, creating increased boundary layer growth with a larger displacement thickness with higher turbulence intensities. Autocorrelation analysis highlighted

a possible vortex shedding emanating from the leading edge of the Class 66 nose above the roof. Integral time and length scales calculated through autocorrelation highlighted that limits of human instability hypothesised by Sterling et al. (2008) are exceeded for the container freight train with a lower loading efficiency.

4. A comparison of different train speeds and with full scale data is undertaken to validate model scale results and analyse Reynolds number independence. Results show good agreement for velocity and pressure magnitudes for both cases, indicating the validity of model scale experiments and Reynolds number independence for magnitudes. As discussed, it is hypothesised that although key flow characteristics and the overall magnitude of velocities and pressures created are similar, smaller turbulent scales cannot be accurately modelled.
5. An analysis of TSI and UK safety limits found results lie close to, but do not break, existing limits; however proposed increases to train speeds would create slipstream velocities which do exceed TSI limits. The TSI methodology in relation to freight was questioned as to how differing freight types should be measured and whether large standard deviations created by including differing freight configurations are appropriate for this method of calculation. Velocity magnitudes recorded at UK safety positions are much larger than previously recorded values for passenger trains.

Chapter 6

Aerodynamic load experiment setup

6.1 Introduction

Chapter 6 introduces a series of model scale experiments undertaken at the TRAIN rig facility to assess aerodynamic forces subjected on an ISO container loaded onto a Class 66 hauled moving model container freight train in an open air and crosswind simulation. The TRAIN rig facility and crosswind generator, previously introduced in section 3.2.1, are discussed in further detail in section 6.2. Section 6.3 discusses adaptations to the moving model to include an on-board pressure monitoring system and data logger. Section 6.4 defines the coordinate system adopted for the aerodynamic load experiments and details of measuring positions. Trackside instrumentation, including measuring probes, position finders and ambient condition monitors are described in section 6.4.2. The experiment methodology for the open air and crosswind sections, bringing together the experiment setup and instrumentation, is discussed in section 6.5.

6.2 TRAIN rig crosswind generator

The University of Birmingham TRAIN rig facility was introduced in detail in section 3.2.1. Since the facility was acquired by the University of Birmingham Centre for Railway Research and Education (BCRRE) in 2009 a specifically designed, built in crosswind generator has been installed, seen in figure 6.1 (Dorigatti, 2013). The TRAIN rig propulsion system is ideal for use in crosswind experiments as it minimises flow interferences around the vehicle in relation to previous moving model crosswind experiments (Baker, 1986).



Figure 6.1: The TRAIN rig crosswind generator with the Class 66 haulied container freight train. The 16 axial flow fans are situated to the left of the photograph. Simulated crosswind flows from the right to the left in the photograph.

The crosswind generator consists of a series of 16 axial flow fans (Ziehl-Abegg, 2010) arranged in two rows of eight units positioned at the trackside. The fans are attached to a steel supporting structure built into an enclosed unit to ensure flow is entrained within a 6.35m test section, through which the TRAIN rig tracks pass (figures 6.1-6.3). Due to constraints associated with the TRAIN rig location, the crosswind generator is constructed completely within the building envelope (Dorigatti, 2013). The fans operate as an open circuit design by which air is sucked through an enclosed duct,

generating flow directed perpendicular to the tracks. Exhausted air is recirculated inside the building.

The crosswind generator test section extends 1.685m in the mean flow direction, 1m in height above the top of the rail, over 6.35m of track (figures 6.2 and 6.3). For this study a flat ground simulation is modelled to replicate the open air test section (figures 6.1 and 6.2). Additional ground simulations include ballast shoulder and embankment setups.

The crosswind generator can also be used for static model wind tunnel tests (Dorigatti, 2013). A 24mm high static track bed, replicating the TRAIN rig track layout, can be installed on top of the TRAIN rig tracks. The static bed setup includes a turntable to enable model rotation with respect to the onset wind. Static experiments are not carried out in this study, due to the limited size of the crosswind generator in relation to model length. A detailed discussion of the crosswind generator development and a comparison of static and moving model experiments for a Class 390 high speed passenger train can be found in Dorigatti (2013).

6.2.1 Flow characterisation

An in-depth flow characterisation of the crosswind generator creating horizontal and vertical wind profiles was carried out by Dorigatti (2013). By characterising the flow it is possible to discuss the simulated crosswind in terms of a mean wind speed, turbulence intensity and static pressure. Measurements made by Dorigatti (2013) were retested to ensure the previous flow characterisation was valid for this study.

Dorigatti (2013) created a horizontal wind profile by measuring sixty four spanwise positions distributed parallel to the track at a distance 0.2m upstream of track 1 (figure 6.2) at height of 0.12m. The height 0.12m, equivalent to 3m at full scale, is adopted as a reference height for this study in line with the TSI methodology (TSI, 2008). Dorigatti (2013) highlighted an influence on crosswind flow from the model entrance

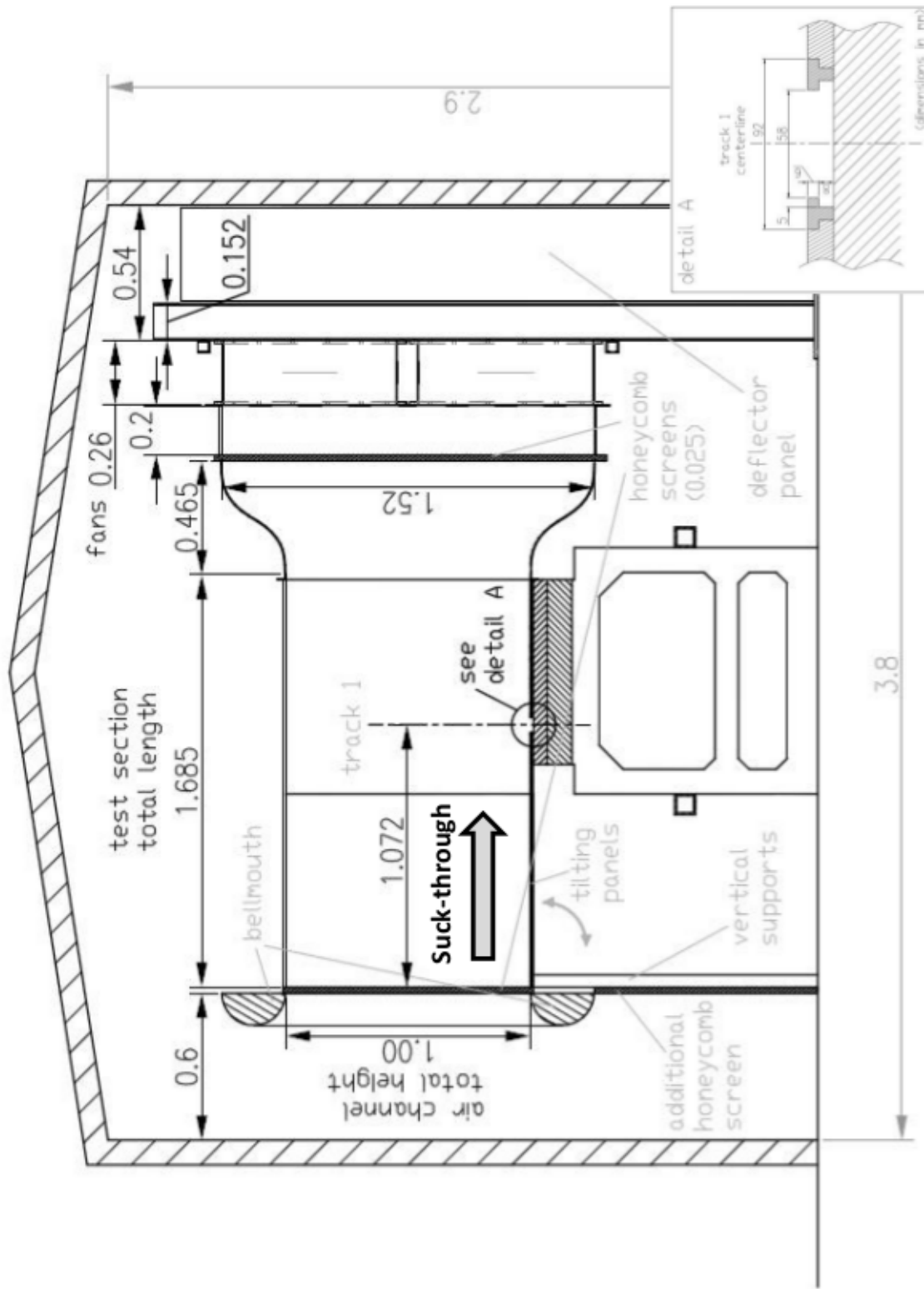


Figure 6.2: A schematic of the TRAIN rig crosswind generator orientated in the direction of model vehicle travel i.e. the model travels into the page. The 16 axial flows fans are located to the right of the schematic and simulated crosswind flow goes from left to right (Dorigatti, 2013). This schematic shows the flat ground simulation layout as used in the experiments.

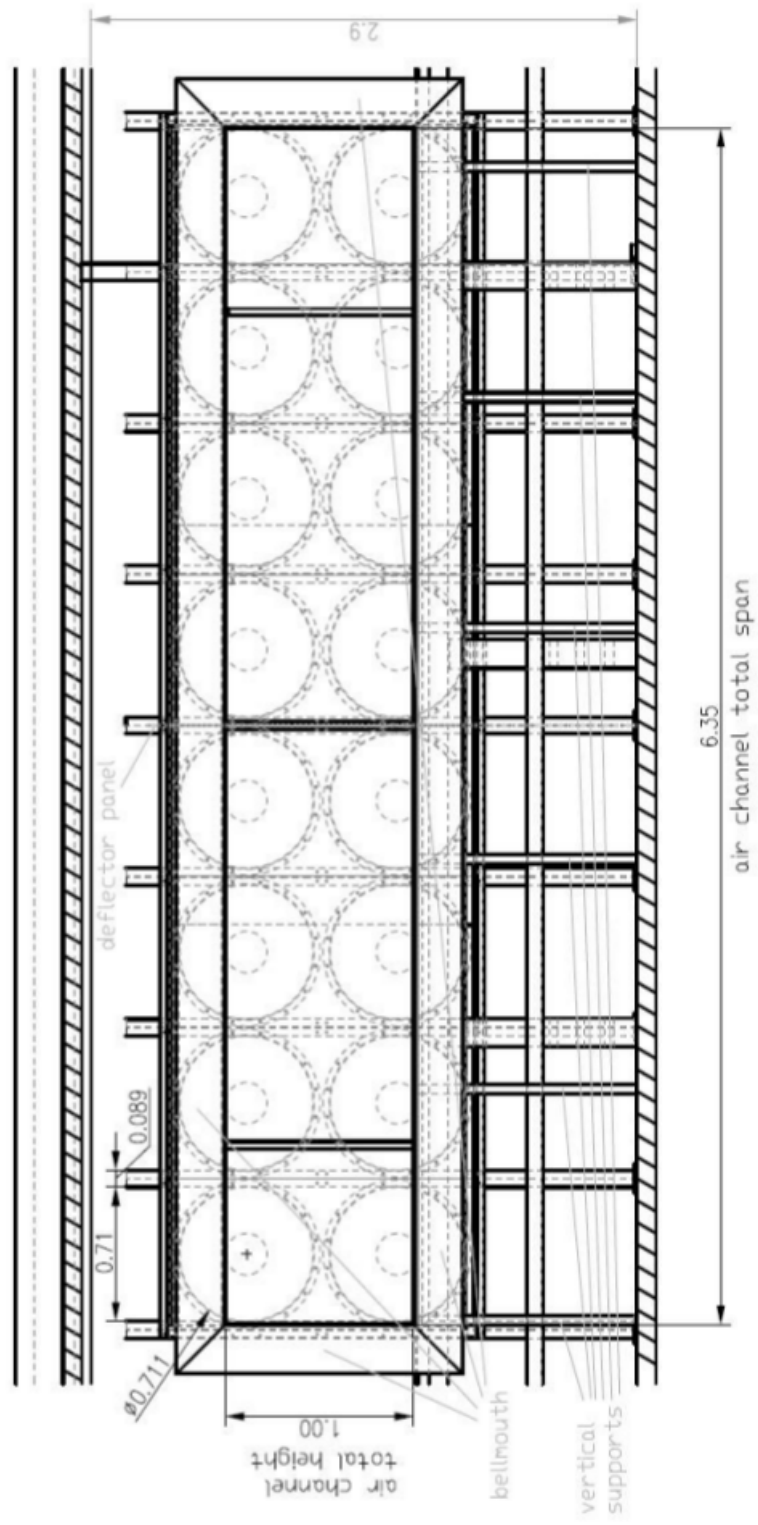


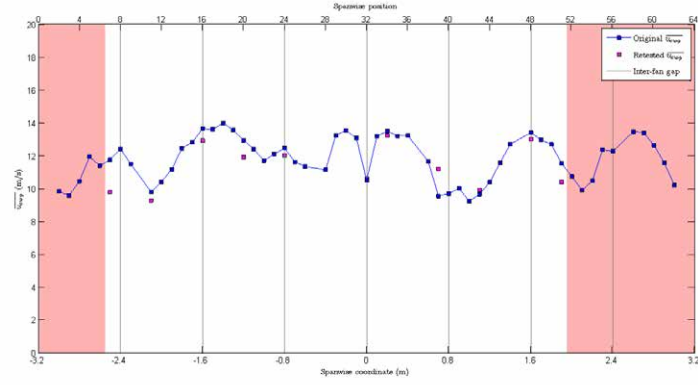
Figure 6.3: A schematic of the TRAIN rig crosswind generator orientated so the direction of model vehicle travel is from right to left (Dorigatti, 2013). The crosswind flow is perpendicular to the model movement i.e. flow into the page.

portals in the crosswind generator side walls; concluding that measurements should be disregarded for the initial 1.27m and final 0.635m of the crosswind generator, measured in the direction of model travel (figures 6.3 and 6.4).

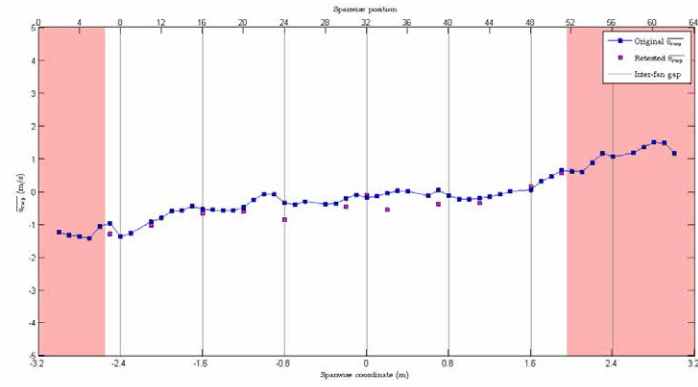
The flow characterisation carried out in this study retested twelve of the central forty five points tested previously, following the flow characterisation methodology presented in Dorigatti (2013). Series 100 Cobra probes (section 3.2.3.2.1) were used to measure three components of velocity and the static pressure of the crosswind flow. The probes were mounted to clamp stands, positioned at the measuring point to be retested, according to the method in section 3.2.3.2.1. The reference pressure tubing was vented 8m from the crosswind generator underneath the TRAIN rig deck (figure 3.11(b)). For each measurement the Cobra probe was ‘zeroed’, using the TFI software, before the crosswind generator was turned on, to ensure measurements were made in relation to a still air situation. The crosswind generator was then turned on and allowed to power up to full running capacity. At each characterisation position ten 60 second measurements were recorded at a sampling frequency of 1000Hz, to enable ensemble and time averages to be calculated for three components of velocity and static pressure over the entire time history length.

Figure 6.4 illustrates the horizontal wind profiles for three mean components of crosswind velocity, $\overline{u_{\text{cwg}}}$, $\overline{v_{\text{cwg}}}$, $\overline{w_{\text{cwg}}}$, and figure 6.5 the mean differential static pressure $\overline{\Delta P_{\text{ST}}}$, for the original flow characterisation and retested points. Figure 6.6 shows the corresponding streamwise $I_{u_{\text{cwg}}}$, lateral $I_{v_{\text{cwg}}}$ and vertical $I_{w_{\text{cwg}}}$ turbulence intensities. The shaded areas on each figure represent the areas significantly influenced by air sucked through the model entrance and exit portals; subsequently disregarded in this study.

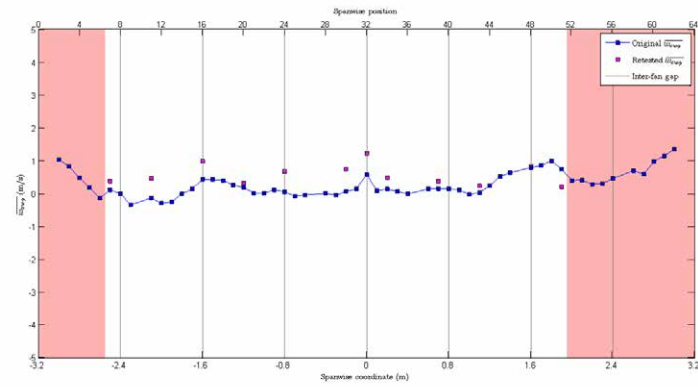
The flow characterisation exhibits limited spanwise uniformity for the mean streamwise component of velocity $\overline{u_{\text{cwg}}}$ (Dorigatti, 2013). Lateral mean velocities $\overline{v_{\text{cwg}}}$ show negative then positive values across the horizontal profile, consistent with air not only drawn in through the inlet section but also sucked through the model entrance portals



(a)



(b)



(c)

Figure 6.4: A comparison of horizontal wind profiles for a) the streamwise mean velocity \overline{u}_{cwg} , b) the lateral mean velocity \overline{v}_{cwg} and c) the vertical mean velocity \overline{w}_{cwg} for the original crosswind generator flow characterisation (blue) and the retested points (magenta) (Dorigatti, 2013). Vertical grey lines indicate the inter-fan gap. Shaded red areas indicate sections of the crosswind generator effected by high lateral and vertical velocities, subsequently left out from this study.

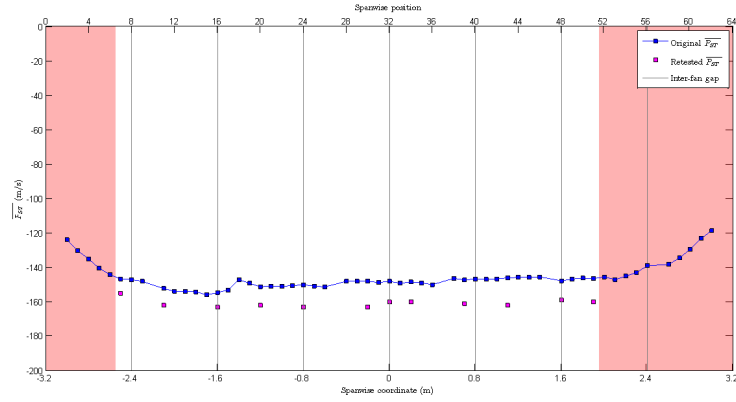


Figure 6.5: A comparison of horizontal wind profiles for the mean differential static pressure $\overline{\Delta P_{ST}}$ for the original crosswind generator flow characterisation (blue) and the retested points (magenta) (Dorigatti, 2013). Vertical grey lines indicate the inter-fan gap. Shaded red areas indicate sections of the crosswind generator effected by high lateral and vertical velocities, subsequently left out from this study.

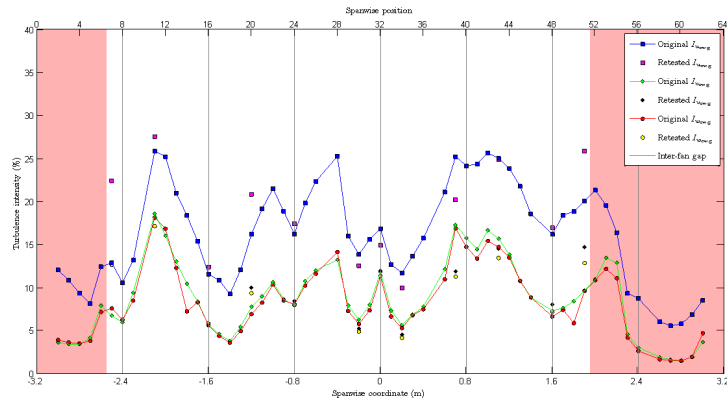


Figure 6.6: A comparison of horizontal wind profiles for the streamwise $I_{u_{cwg}}$, lateral $I_{v_{cwg}}$ and vertical $I_{w_{cwg}}$ turbulence intensities (Dorigatti, 2013). Vertical grey lines indicate the inter-fan gap. Shaded red areas indicate sections of the crosswind generator effected by high lateral and vertical velocities, subsequently left out from this study.

at each side of the crosswind generator (Dorigatti, 2013). The entrance portal influence is also observed for $\overline{\Delta P_{ST}}$, which exhibits relatively stable values across the central portion of the crosswind generator but large differences in the areas disregarded near the model vehicle entrance portals. Dorigatti (2013) found limited spanwise uniformity for turbulence intensities, related to a series of windholes associated with $\overline{u_{cwg}}$ and the relative position in relation to the fans.

In general the results of retested positions exhibit good agreement with the original flow characterisation (within $\sim 4\%$). $\overline{\Delta P_{ST}}$ is consistently lower than the original characterisation, albeit within $\sim 4\%$ of original values. It is suggested that differences in turbulence intensities between the original flow characterisation and the retest are thought to be caused by differences in ambient conditions and possible differences in probe orientation. It is assumed the values from the original characterisation are valid for this study. Adopting the original full crosswind flow characterisation allows spanwise averages to be calculated, shown in table 6.1.

Spanwise average	$\overline{u_{cwg}}$ (m/s)	$\overline{v_{cwg}}$ (m/s)	$\overline{w_{cwg}}$ (m/s)	$\overline{\Delta P_{ST}}$ (Pa)	$I_{u_{cwg}}$ (%)	$I_{v_{cwg}}$ (%)	$I_{w_{cwg}}$ (%)
Central span (-2.55m to 1.95m)	12	-0.3	0.2	-150	18	10	9

Table 6.1: Spanwise averages for the horizontal wind profile calculated from the Dorigatti (2013) crosswind flow characterisation at reference height 0.12m.

6.3 TRAIN rig model

The 1/25th scale Class 66 hauled four wagon 101.25m container freight train was adapted for measuring surface pressures in the open air and crosswind sections. The specifics of the moving model are introduced in section 3.2.2. Container freight was chosen for this crosswind study to reflect a series of incidents in the UK and abroad in which containers have become detached from a train under the influence of a crosswind, discussed in chapter 2. The ISO freight container when unloaded is a relatively light weight object with a large bluff surface area, therefore highly susceptible to possible overturning. Modification of the model Class 66 hauled container freight train allowed for continuity with the slipstream experiments; creating a study not only providing results for the aerodynamic influence on trackside objects but also developing an understanding of vehicle dynamics while travelling through an open air or crosswind situation.

6.3.1 On-board pressure measuring system

The existing freight model was modified to include an on-board pressure monitoring system with a stand-alone data logger in one 12.192m x 2.438m x 2.590m (40 foot) container. An on-board stand-alone measuring system is essential for moving model experiments, in contrast to wind tunnel experiments which tend to use a force balance (Dorigatti, 2013). Previous moving model crosswind experiments have used wires connecting the rear of the model to an external data logging system, however, this applies additional constraints to the experiment in terms of train speed and inaccurate modelling (Baker, 1986). An on-board system enables the local surface pressure distribution to be monitored rather than the overall aerodynamic loads on the vehicle. Overall forces and moments can be estimated by discrete integration of mean surface pressure values over the entire container.

Designed and built by the BCRRE at the University of Birmingham, the purpose

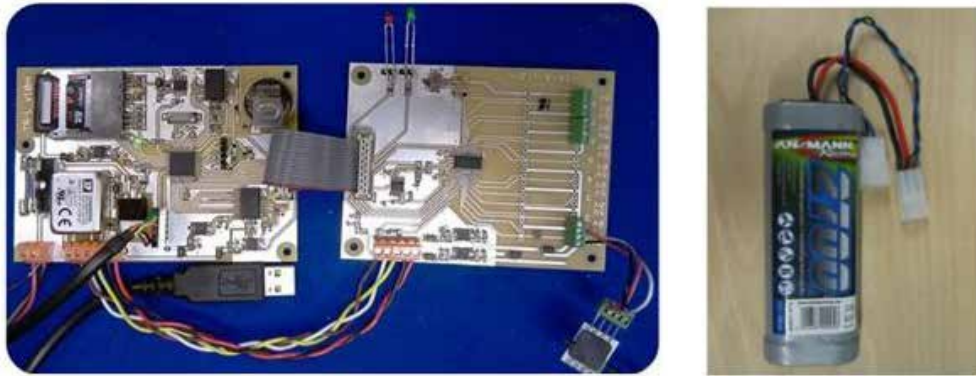
built on-board measuring system consists of a stand-alone data logger powered by a rechargeable battery, connected via three-core shielded cables to fifteen miniaturised differential pressure transducers and a light detector. The pressure transducer measuring ports are connected via silicon tubing to metal tubing adapters glued into the container side walls, acting as pressure taps. The pressure transducer reference ports are connected via silicon tubing to a manifold which in turn is connected to a sealed reservoir, acting as an on-board reference pressure system. The following sections will introduce each component in greater detail.

6.3.1.1 Data logger

The purpose built stand-alone data logger is capable of monitoring 16 channels at a maximum sampling rate of 4000Hz. The data logger was designed for, and has previously been utilised as part of, the AeroTRAIN project and a PhD study assessing surface pressures and aerodynamic forces on a Class 390 model (Dorigatti, 2013). The Class 390 studies found it necessary to employ a custom built data logger to ensure the system was compact enough to fit inside the model and withstand forces subjected to the model under the firing and braking phases of an individual run (estimated to be in the range of $\sim 3g$) (Dorigatti, 2013).

The data logger design and construction was undertaken by Mr. Mani Entezami at the BCRRE. Comprising of two dual side printed circuit boards and a rechargeable battery (figure 6.7), the logger has 16 analogue channels with a 16-bit resolution capable of a 4000Hz maximum sampling rate. The circuit board integrates a 4GB SD memory card for data storage and provides a 5 Volt power supply and ground reference to all 15 pressure transducers and the light detector (Dorigatti, 2013).

Bespoke control software allows user control and real time onscreen monitoring when connected to the on-board measuring system (figure 6.8). The software is used on a standard laptop computer, connected to the model via a USB cable and coaxial adapter.



(a) Data logger circuit boards

(b) Data logger rechargeable battery

Figure 6.7: The data logger circuit boards and rechargeable battery (Dorigatti, 2013).

The software provides the facility to start and stop data sampling, while also providing a self-trigger option set either when a selected channel exceeds a predetermined threshold, or as a countdown. The software enables saved data on the SD card to be downloaded in a .TSV file format.

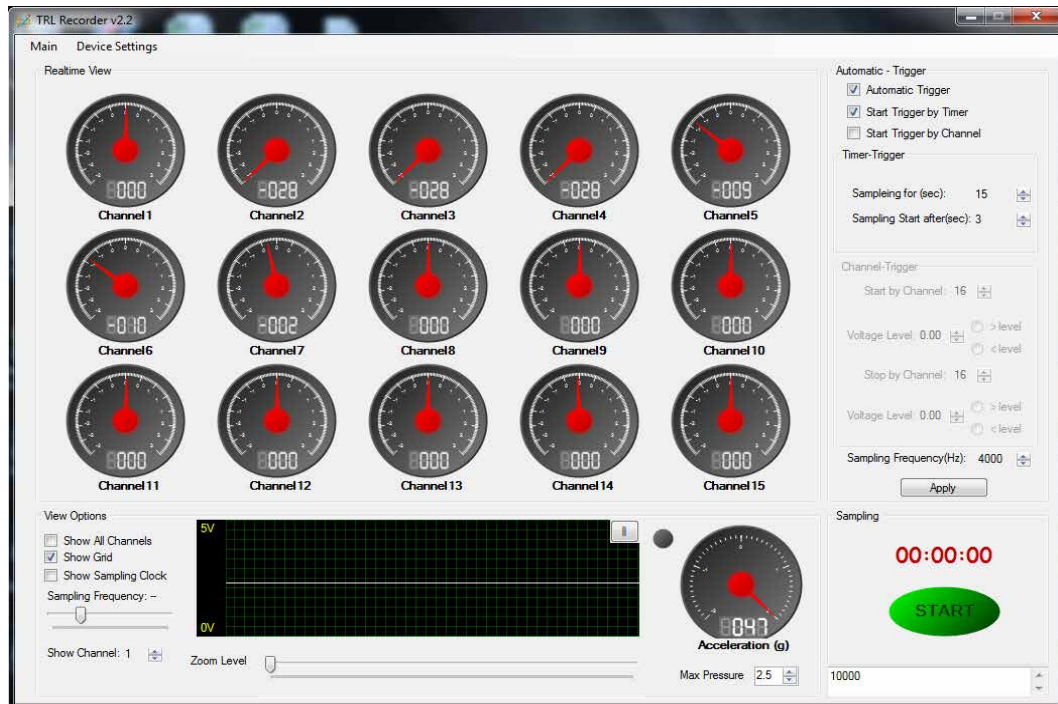
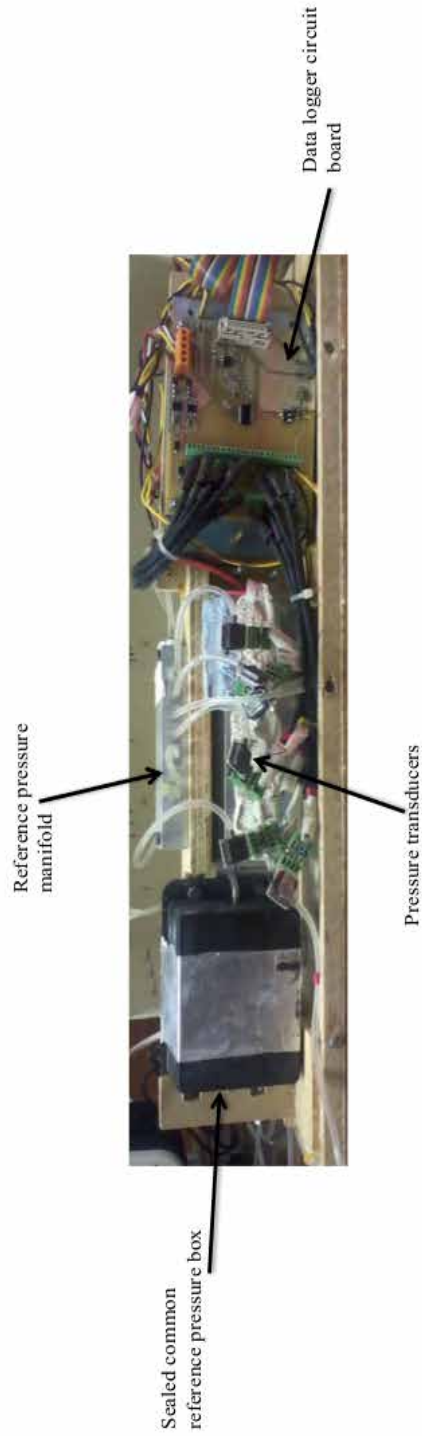


Figure 6.8: The data logger control software.

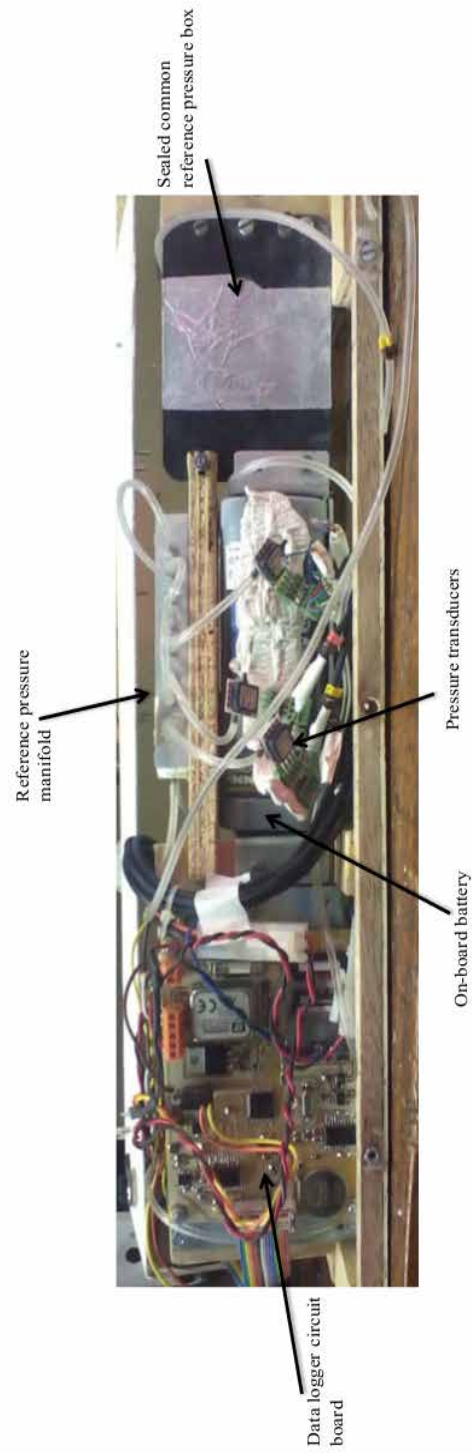
In previous studies the logger was mounted inside a 1/25th scale Class 390 half carriage, with the remaining on-board equipment mounted inside the Class 390 power car. The

Class 390 half carriage has similar dimensions to a 12.192m container; however, for these experiments all the on-board equipment is mounted in this space. Figure 6.9 shows a photograph of the internal setup of equipment.

To ensure usability of the logger, key controls are mounted to the container walls, thus externally accessible. A multi-pin circular socket for computer connection and battery recharging is mounted to the non-pressure tap end of the container. For the fully loaded consist a 6.096m container, mounted flush to the measuring container on the FEA-B wagon, was adapted to include the USB and charging cable required to attach the data logger to the laptop computer. An on/off switch is mounted to the container wall to control the data logger and preserve battery life. Finally two LED lights mounted to the container wall allowed easy monitoring of the data logger state without removing the container walls (figure 6.10).



(a) Internal data logger setup



(b) Internal data logger setup

Figure 6.9: Images to show how the data logger and on-board equipment is positioned and setup within the measuring container.

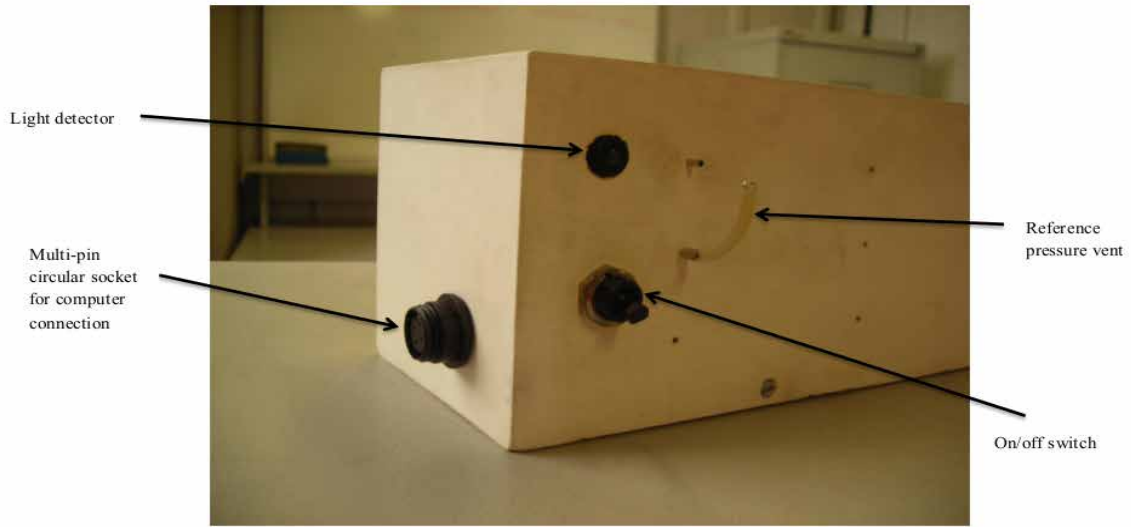


Figure 6.10: The measuring container external features.

6.3.1.2 Pressure transducers

The on-board measuring system uses fifteen channels of the data logger for measuring surface pressures with fifteen HCLA12X5PB miniaturised differential pressure transducers by Sensortechncs GmbH (Sensortechncs, 2013). The piezoresistive miniaturised amplified differential low pressure sensors have a $\pm 1250\text{Pa}$ range and an analogue signal range 0-5Volts, compatible with the 5Volt power supply from the data logger (Dorigatti, 2013). The HCLA12X5PB pressure transducers have a typical non-linearity and hysteresis error of 0.05% in the full span of 2500Pa (Sensortechncs, 2013). This manufacturer specification was however retested during a series of calibration experiments using a Betz-micro manometer (appendix A).

The pressure transducer is fitted with two pressure ports (figure 6.3.1.2). The transducer measuring pressure port (HPP in figure 6.3.1.2) is connected via silicon tubing (3.2mm outside diameter OD and 1.6mm internal diameter ID) to 12mm x 2.00mm x 1.5mm cylindrical metal tubing adapters. The metal adapters are glued into holes through the container wall acting as pressure taps, shown in figure 6.12. The transducer reference pressure port (LPP in figure 6.3.1.2) is connected via silicon tubing to

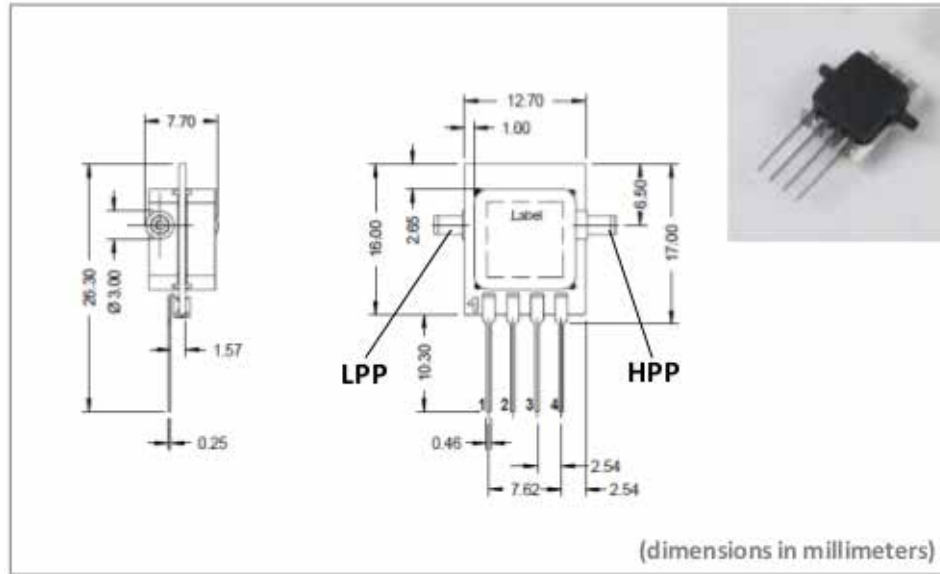


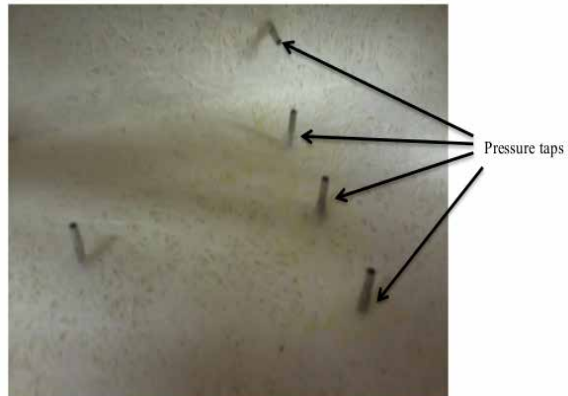
Figure 6.11: An image and schematic of a miniaturised differential pressure transducer (Sensortech, 2013). HPP is the measuring port, whereas LPP is the reference port (Dorigatti, 2013)

a manifold which in turn is connected to a sealed container (figure 6.9).

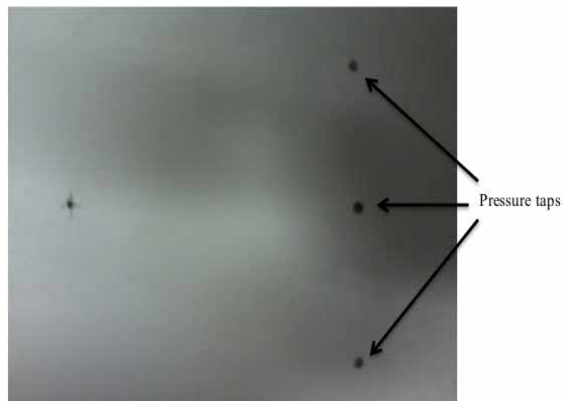
6.3.1.3 Pressure taps and loading consists

The measuring container is fitted with thirty one pressure taps arranged in a series of loops. Pressure taps are created by inserting 12mm x 2.00mm x 1.5mm cylindrical metal tubing adapters through holes in the container wall, fitting flush with the exterior of the container wall (figure 6.12(b)). The adapters are glued in place using an epoxy structural adhesive on the inside surface of the container wall.

An array of nine taps are positioned at the container end face and loops of nine taps are positioned at 25% and 50% of the container length (figure 6.12(a)). In addition to these loops, pressure taps are placed at container mid-height at 12.5% and 32.5% of container length on each side (figure 6.12(a)), creating a ring of pressure taps at mid-height around the container. It should be noted that no pressure taps are placed in the container base. Due to the method of container attachment the flatbed wagon was modelled as a solid loading base, therefore as the experiment assesses forces on



(a) Pressure taps inside view



(b) Pressure taps outside view

Figure 6.12: The pressure tapping shown from inside and outside the measuring container.

the container, not the container and wagon, no taps were needed in the container base. If a spine loading system was adopted for the flatbed wagon, pressure taps would be needed in the container base. This issue will be discussed later in chapter 8 when a comparison to previous freight aerodynamic load studies is carried out.

The measuring container is detachable from the wagon, enabling free movement of measuring equipment about the train. In chapter 5 a discussion of model length in relation to slipstream development found for consists with poor loading efficiency (generally below 50%) an eight wagon train was needed to observe the transition from boundary layer growth to stability. As the data logger is built into a 12.192m container, due to size restrictions, to allow continuity with slipstream experiments (section 3.2.2.4) the minimum loading efficiency tested was 66%. Therefore, as boundary layer stability is observed for the four wagon 101.25m train with loading efficiencies above 50% and due to the additional weight associated with the on-board data logger (1.5kg), the four wagon model is chosen for these experiments.

Container loading configurations were chosen to represent a series of loading efficiencies while providing continuity with slipstream experiments. Three consists were tested with loading efficiencies of 100% and 66%, illustrated in figure 6.13. Consist 1 and 4 were previously analysed in chapter 5 and consist 6 was chosen to analyse the influence of individual container positioning in relation to consist 4.

Previous container freight wind tunnel studies found 1.5 wagons before and 0.5 wagons following the measuring wagon were required to observe the wagon consist influence (Saunders et al., 1993). Therefore, the third wagon behind the Class 66 locomotive was chosen as the measuring wagon onto which the container with built in data logger is mounted. As the measuring container is detachable it was possible to rotate the container by 180 degrees, thus creating in effect five loops with a total of 53 pressure taps for consist 4 and 6 and seven loops with a total of 75 pressure taps for consist 1. The pressure tap positions on all measured loops are shown in figures 6.14-6.17 for consists 1, 4 and 6. In addition to the vertical pressure tapping loops, a series of

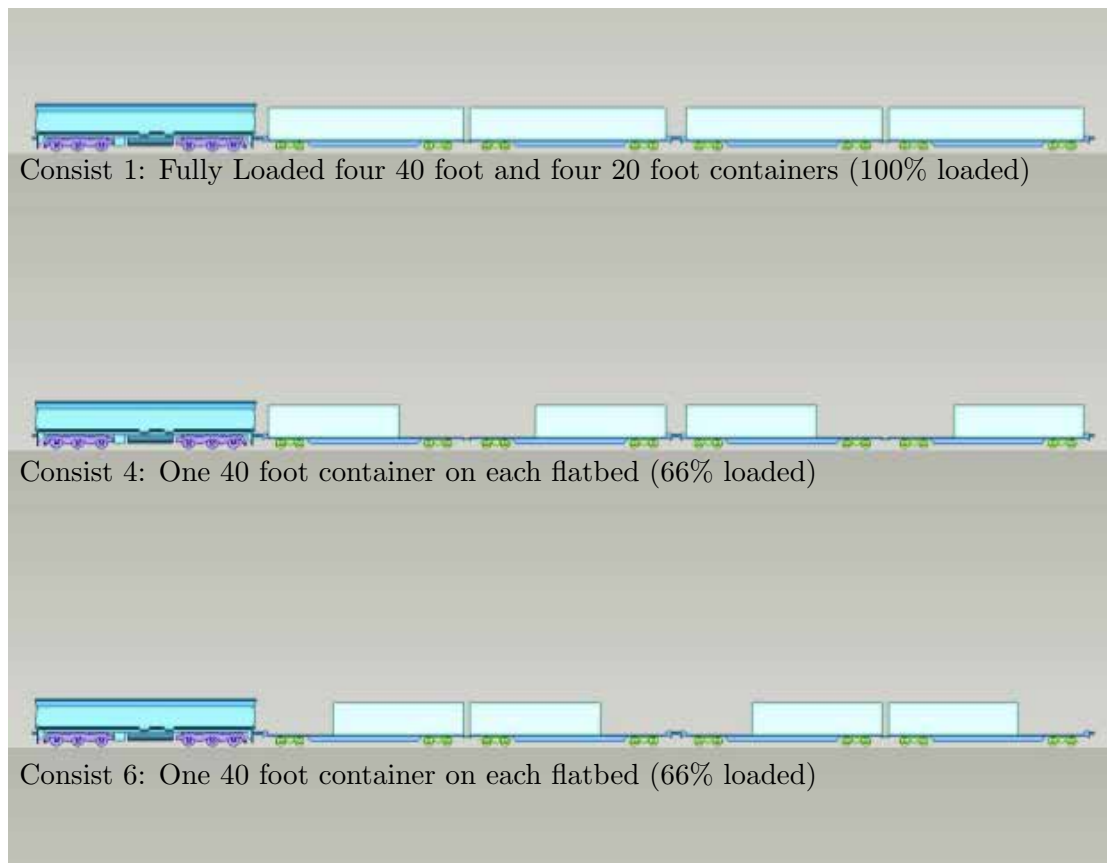


Figure 6.13: Diagrams of the container loading configurations and efficiencies to be tested at the TRAIN rig for the aerodynamic load experiments.

pressure taps at the container mid-height placed between pressure taps on the vertical loops created a ring of pressure taps around the container midheight, loop 8.

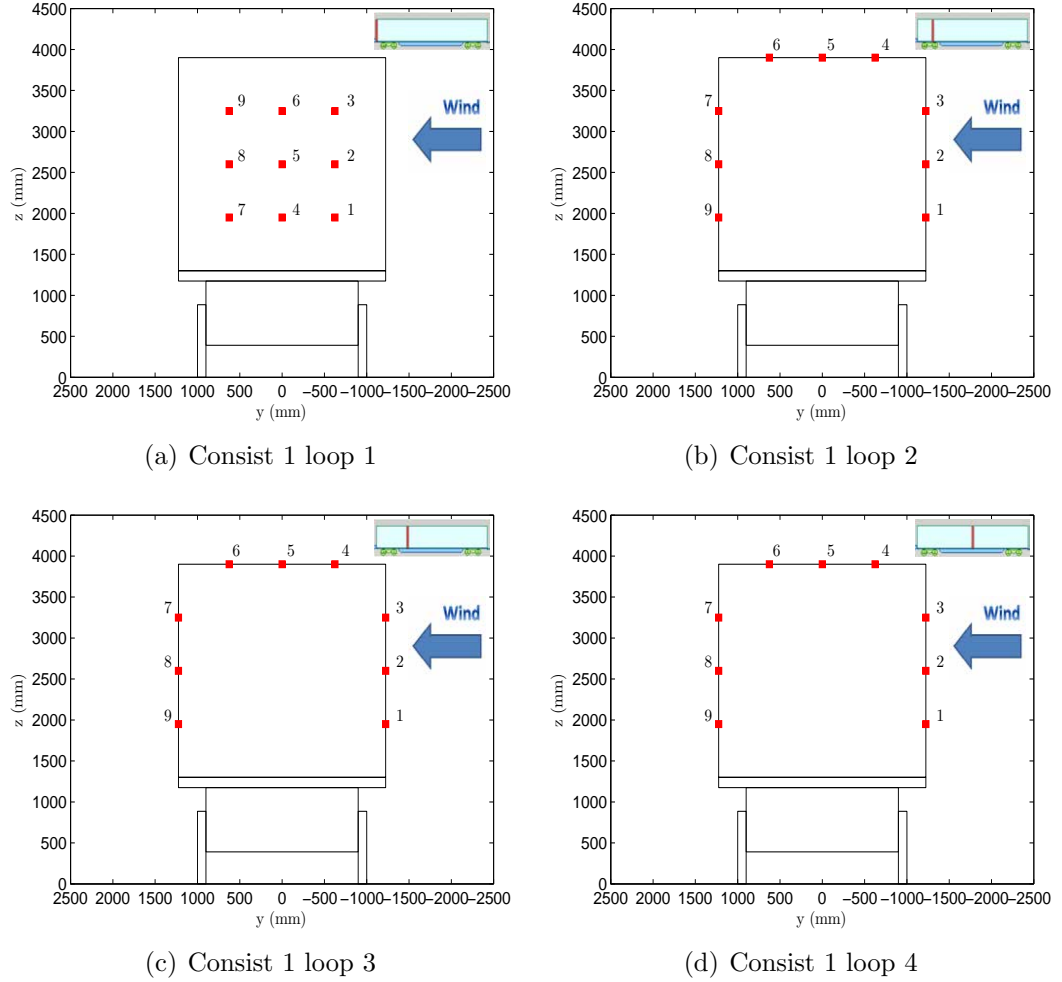


Figure 6.14: Pressure tapping positions on loops 1 to 4 for consist 1. In the crosswind test section the wind is directed from right to left. The direction of train travel is out of the page.

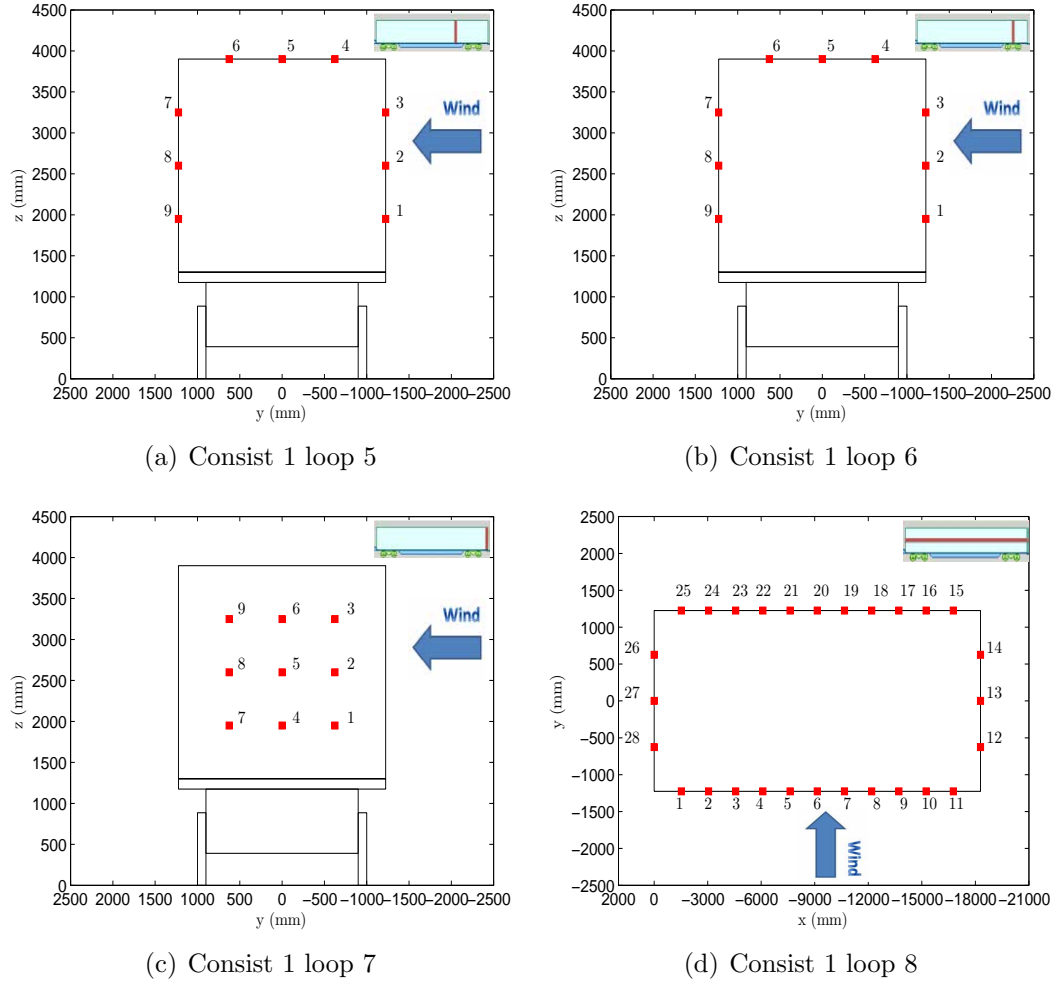


Figure 6.15: Pressure tapping positions on loops 5 to 8 for consist 1. In the crosswind test section the wind is directed from right to left. The direction of train travel is out of the page for loops 5, 6 and 7 and from right to left for loop 8.

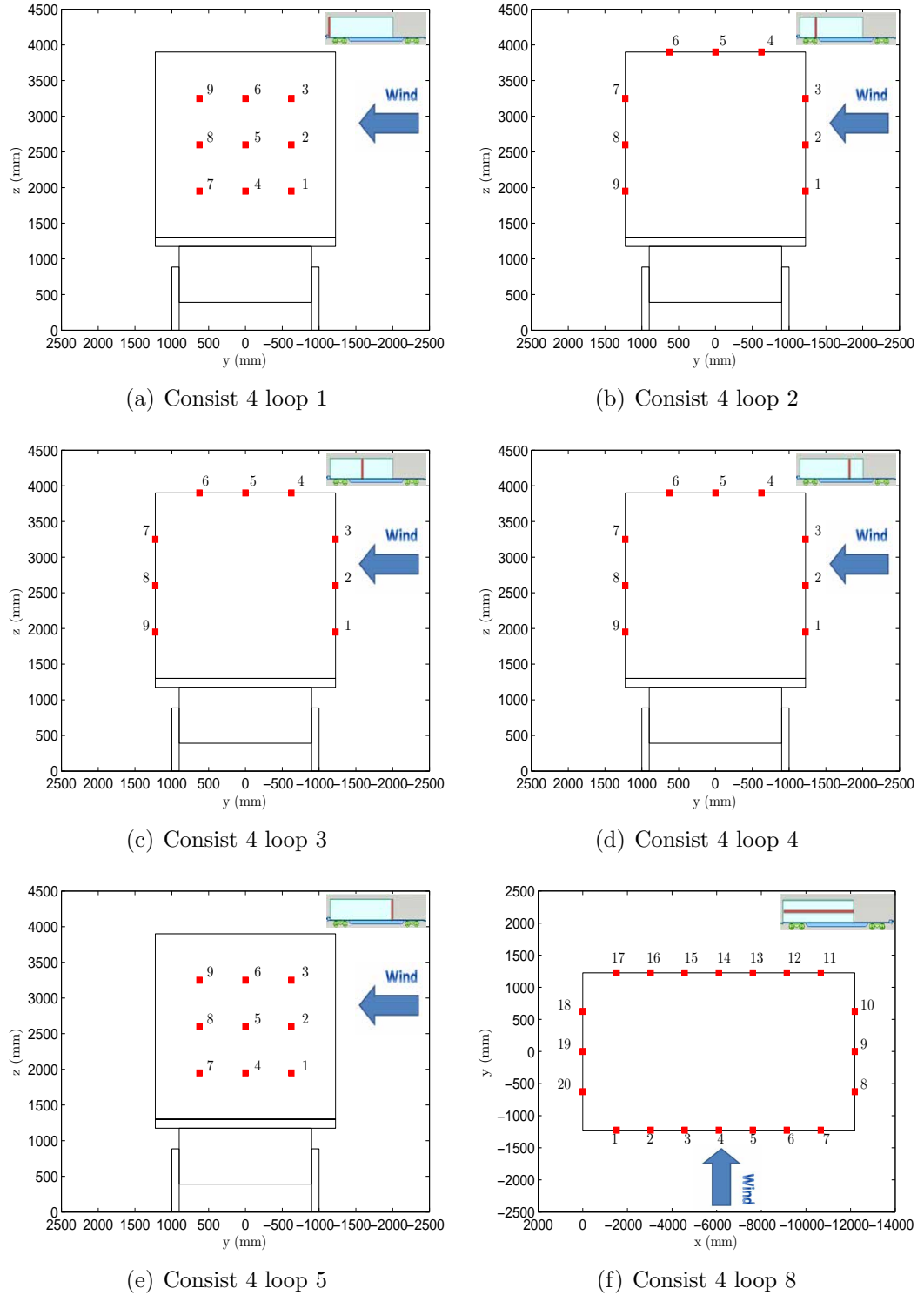
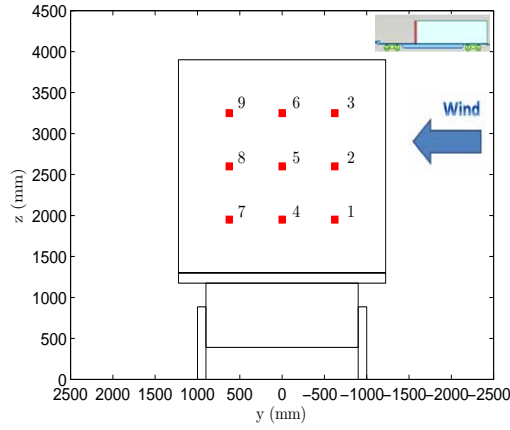
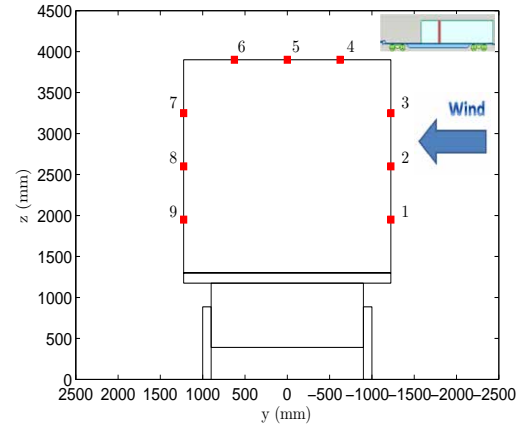


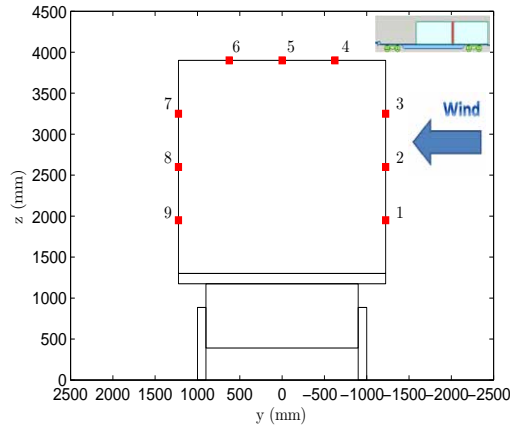
Figure 6.16: Pressure tapping positions on loops 1 to 8 for consist 4. In the crosswind test section the wind is directed from right to left. The direction of train travel is out of the page.



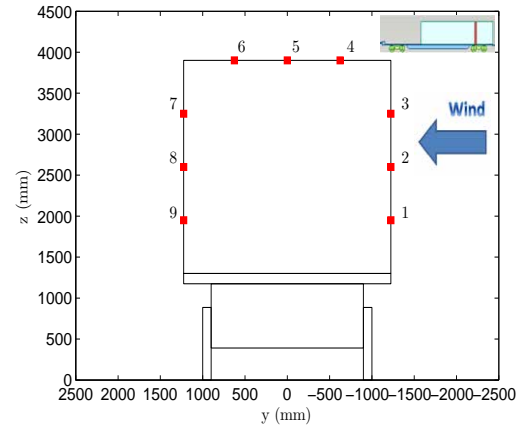
(a) Consist 6 loop 1



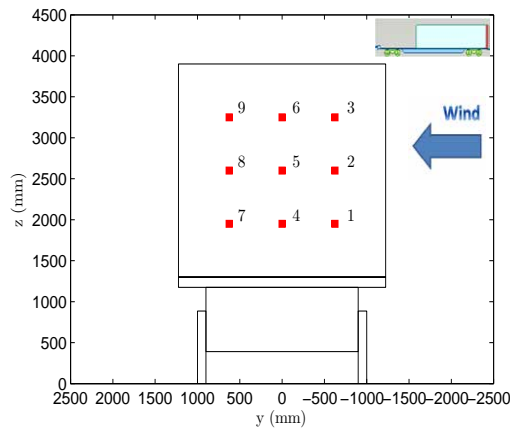
(b) Consist 6 loop 2



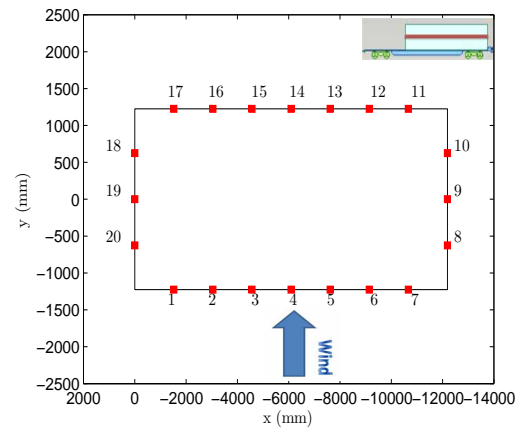
(c) Consist 6 loop 3



(d) Consist 6 loop 4



(e) Consist 6 loop 5



(f) Consist 6 loop 8

Figure 6.17: Pressure tapping positions on loops 1 to 8 for consist 6. In the crosswind test section the wind is directed from right to left. The direction of train travel is out of the page.

6.3.1.4 On-board reference pressure system

The pressure transducer reference pressure ports are connected via silicon tubing to a manifold which in turn is connected to a sealed container (figure 6.9). Connecting the pressure transducers to a manifold attached to a sealed container allowed a common reference pressure for all fifteen pressure transducers monitored at once by the data logger. Between the manifold and sealed container is a splitting point, created by two cylindrical metal tubing adapters glued into the container wall linked by a small piece of silicon tubing. The splitting point enabled the sealed container to be vented after every run, preventing a reference pressure drift (section 6.5) (Dorigatti, 2013).

6.3.1.5 Light detector

The sixteenth channel of the data logger is fitted with a light detecting phototransistor VISHAY-TEPT5600 sensor (Vishay, 2011) which is mounted into the container wall (figure 6.10). The phototransistor was powered and monitored by the data logger alongside the pressure transducers. A series of light sources positioned at specified locations along the track act as position finders (section 6.4.2.3). The sixteenth channel was calibrated so the phototransistor recorded a constant ~ 4.6 Volts when in normal lighting falling to ~ 0 Volts when exposed to a strong light. During the data processing it is possible to use the light detector time history for trimming raw data and isolating the portion of time histories associated to the train travelling within the open air test section or crosswind generator (chapter 7).

6.4 Experiment setup

6.4.1 Coordinate system and measuring positions

A coordinate system is defined as a right hand screw system (figure 6.18) such that the x-axis is aligned in the direction of travel, with the origin taken to be when measured tap enters the crosswind generator, indicated by a series of light sources and on-board light detector. The y-axis is the horizontal plane perpendicular to the track direction, measured from the centre of track measured in the wind direction and the z-axis is in the vertical direction measured upwards from the top of the rail. Figure 6.18 illustrates the reference system adopted for the aerodynamic load experiments, shown in figure 6.18 for the crosswind test section. The reference Cobra probe position, discussed in section 6.2.1, is also shown in relation to the model in the crosswind test section.

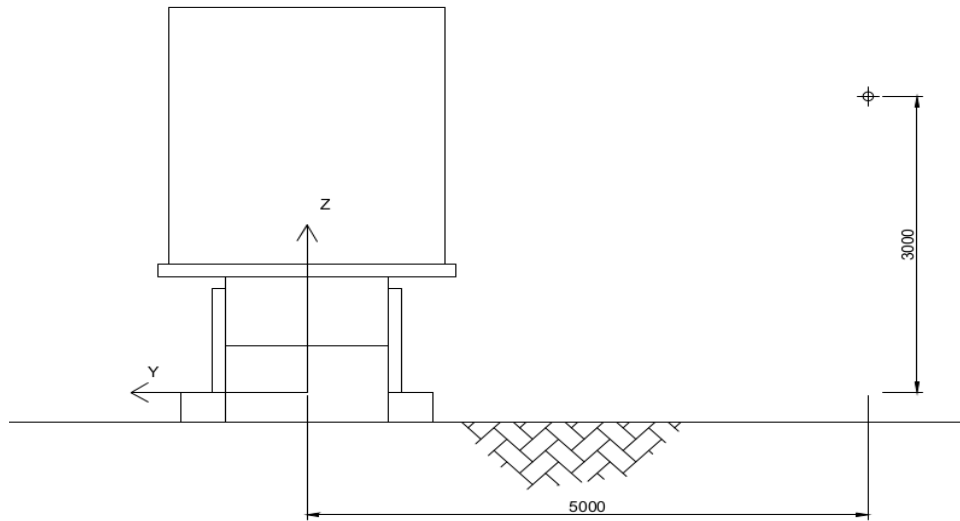


Figure 6.18: The coordinate system defined for the crosswind experiments at the TRAIN rig. The positive x-direction is measured into the page. The direction of train travel, for this figure, is in the negative x-direction out of the page. The Cobra probe reference position is also shown in relation to the model in the crosswind test section. All dimensions are given as the relative full scale measurements in mm.

6.4.2 Trackside instrumentation

6.4.2.1 Cobra probes

Localised crosswind velocity and static pressure measurements were made using Series 100 Cobra probes (TFI, 2011). The probes, introduced in detail in section 3.2.3.2.1, were used to initially carry out the flow characterisation retest (section 6.2.1), then as a method of monitoring wind conditions at a specified reference position during the actual crosswind experiments.

The reference probe is mounted at a reference position 4.775m from the crosswind generator train entrance portal at a distance of 0.2m upstream of the tracks, measured at the reference height of 0.12m. The reference position, also used in the crosswind flow characterisation as position 16 (figures 6.4 - 6.5), provides a comparison from which to extrapolate out run to run variation in flow speed and static pressure. The probe is set up such that the central measuring hole is placed at the specified measuring position, as in section 3.2.3.2.1. The probe is set up at the beginning of each test day, with measuring positions and alignment checked to an accuracy of $\pm 1\text{mm}$ and $\pm 2^\circ$ respectively.

The Cobra probe is mounted into a specifically designed probe holder which is in turn mounted through the crosswind generator floor and secured to the TRAIN rig structure (figure 6.19(a)). Reference pressure tubing is vented to a location out of the flow itself underneath the TRAIN rig apparatus, 8m from the crosswind generator (figure 6.19(b)).

6.4.2.2 Photoelectric position finders

The model speed was altered by pre-determining the tension in the firing cable, which in turn was altered for different loading efficiencies in relation to model weight. Model speed was measured using a series of opposing ‘Sick’ photoelectric position finders

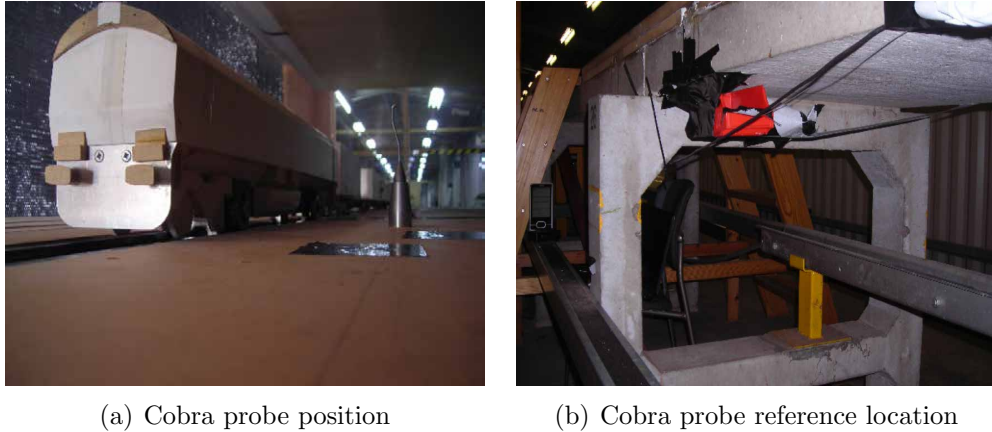


Figure 6.19: The Cobra probe in position within the crosswind generator and the pressure tubing to vent the reference of port out of the flow underneath the rig.

and reflectors along the TRAIN rig trackside. The position finders were separated by 1m and located at a central position 1.5m from the entrance and exit of the crosswind generator (figure 6.20(b)). Speed calculation and recording are undertaken as in section 3.2.3.2.2.

6.4.2.3 Light sensor

As discussed, a light detector fitted to the sixteenth channel of the data logger is used as a position finder in raw data time histories. A series of light sources, in the form of covered torches with a slit allowing a focussed light source, are positioned close to the entrance and exit of the crosswind generator (figures 6.20(c)-6.20(d)). The method of aligning data using the light detector is discussed in chapter 7.

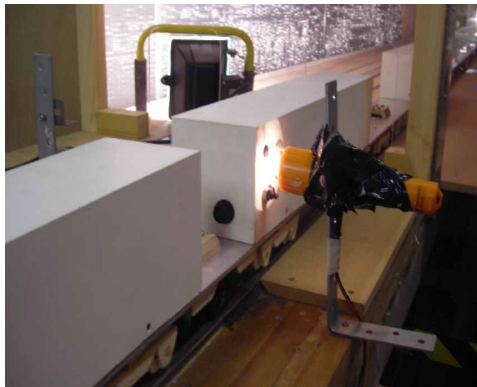
For the open air surface pressure tests the light detector channel is used to calculate train speed in the open air test section. The train speed calculated by using the light detector was compared to a series of additional train speed experiments using photoelectric position finders and differences were found to be within experimental uncertainty ($\pm 0.5\text{m/s}$).



(a) Equipment under TRAIN rig



(b) Photoelectric Position Finders



(c) Light source before crosswind generator



(d) Light source after crosswind generator

Figure 6.20: Images of the equipment under the TRAIN rig, the ‘Sick’ photoelectric position finders and the light source positions.

6.4.2.4 Ambient condition monitors

Ambient conditions were monitored using an Oregon Scientific BAR208HGA weather station to measure temperature ($\pm 1^\circ\text{C}$) and relative humidity ($\pm 1\%$). A GBP3300 Digital Barometer measured atmospheric pressure ($\pm 1\text{mb}/100\text{Pa}$). Sensors to measure ambient conditions were placed on a TRAIN rig supporting pillar next to the experiment setup and measurements recorded before each run manually into an Excel spreadsheet.

6.5 Experiment methodology

Moving model experiments to assess the surface pressure distribution on a container, measured in open air and crosswind situations, entailed carrying out multiple series of measurements for each train consist through each measuring zone. As the data logger only has sixteen channels the number of pressure transducers recorded simultaneously is limited. Therefore, for each consist the pressure tapping loops are divided into a series of tapping setups. For consist 1 the 75 pressure taps are divided into six setups, and similarly for consists 4 and 6 the 53 pressure taps are divided into four setups.

In general 15 repeats were carried out for each tapping setup to create ensemble averages in line with TSI standards and previous ensemble stability experiments using the crosswind generator (TSI, 2008; Dorigatti, 2013). The number of repeats was altered to 20 runs for the first experiment setup for consist 1 to assess ensemble stability for the freight train in comparison to a Class 390 (appendix D).

Prior to testing each tapping setup the measuring container is opened and pressure transducers connected to appropriate tapping. Before closing the container the laptop was connected via the USB cable and a live transducer monitoring test undertaken to ensure all connections were properly made. At the beginning and half way through each day a 15 second test was undertaken to measure the zero pressure offset voltage of

each transducer in the open air. For this test the reference pressure vent was opened, thus the pressure transducer was recording the ambient pressure on both sides, giving a zero pressure offset voltage used for raw data conversion (section 7.3.2).

As discussed, the reference pressure is provided by an on-board sealed container. Dorigatti (2013) noted the sealed container was susceptible to a small drift caused by variations in ambient temperature ($\pm 2\text{Pa}$). For this study the small duration of each run ensured drift was minimised, typically below the instrumentation accuracy (Dorigatti, 2013). To negate any possible drift affects the reference pressure vent was opened after each experiment run and closed just before the TRAIN rig firing process.

The on-board data logger is automatically started following a countdown trigger, applied using the user software on a laptop. In general an 80 second countdown ensured enough time to disconnect the laptop, tension the TRAIN rig and reset the photoelectric light gates. The data logger was sampled at 4000Hz for 40 seconds. For a 4000Hz sampling frequency and a train speed of 20.8m/s, a time of ~ 0.3 seconds was taken to travel through the 6.35m crosswind generator, thus ~ 1220 samples recorded. The sampling time allowed a period of 10 seconds before the model was fired and a period following the model coming to rest in the braking zone. The additional measurements taken when the train was at rest enabled the raw data to be aligned for either the open air or crosswind experiments, while providing additional data needed for normalising pressures (section 7.4).

For this study a nominal yaw angle relative to the crosswind of 30° is chosen. This meant for a mean streamwise spanwise average crosswind velocity of 12m/s a nominal train speed of 20.8m/s is required to achieve this yaw angle (section 6.2.1). Dorigatti (2013) noted a model vehicle speed decay through the crosswind generator of $\sim 1.1\text{m/s}$, caused by friction and aerodynamic drag. Preliminary runs with the freight train showed a similar speed decay, however, a small dependence on container loading configuration was observed. Assuming a linear decrease in train speed through the crosswind generator, the train speed required at the first photoelectric light gate

should be $21.4 \pm 0.5 \text{ m/s}$, ensuring a yaw angle of $30^\circ \pm 1^\circ$.

To achieve this train speed in the crosswind generator meant the train passed through the open air test section at $24 \pm 0.5 \text{ m/s}$. A series of preliminary runs to find the launching tension required were completed; the tension required is dependent on model weight and varies between loading efficiencies (table 6.2).

Consist number	Tension required (kN)
1	8.43
4	8.38
6	8.38

Table 6.2: The tension required to achieve the desired train speed needed for each consist in each experiment test section.

The Reynolds number is calculated differently for the open air and crosswind test sections. For the open air section Reynolds number is calculated using train speed $V_{train} = 24 \text{ m/s}$, however for the crosswind generator the reference velocity is taken as the relative crosswind. Therefore, for an average train speed $V_{train} = 20.8 \text{ m/s}$ through the crosswind generator and an average onset wind velocity $\overline{u_{cwg}} = 12 \text{ m/s}$ the relative crosswind $\overline{V_{rel}} = 24 \text{ m/s}$; thus the reference velocity for both cases is the same. The Reynolds number for a 1/25th scale model with a characteristic height of 0.156m is defined as,

$$\text{Re} = \frac{V_{rel} L_{ref}}{\nu} = \frac{24 * 0.156}{0.000015} = 2.5 \times 10^5 \quad (6.1)$$

The Cobra probe measuring the instantaneous crosswind flow is monitored using TFI Device Control software on a laptop. The crosswind flow properties were recorded at a sampling frequency of 2000Hz for 240 seconds. This sampling frequency ensured the spectral content of the simulated wind could be assessed (Dorigatti, 2013). A 240 seconds sampling time was chosen to allow time for the fans to be turned on and run for a period at full power, in which time the TRAIN rig firing process will be completed, then record the fans powering down. Recording the whole process allowed the time histories to be aligned for data processing (section 7.3.3).

Chapter 7

Aerodynamic load experiment processing methodology

7.1 Introduction

Chapter 7 introduces the methodology of processing container surface pressure data collected in the open air and crosswind experiment in preparation for analysing results in chapter 8. Data processing methods developed by Sanquer et al. (2004); Quinn et al. (2007) and Dorigatti (2013) are adapted for container surface pressure measurements on the freight train (section 7.2). As in chapter 4, a series of computer scripts are developed in Matlab to convert raw voltage data to meaningful physical data (section 7.3). Throughout this study data is presented in a non-dimensionalised form; sections 7.4.1 and 7.4.2 discuss the process of normalising data with respect to the crosswind and open air test sections, respectively. Section 7.5 introduces the method developed by Sanquer et al. (2004); Quinn et al. (2007) of discretising a pressure tapped vehicle into smaller areas to create coefficients for forces and rolling moments. Finally section 7.6 calculates associated result uncertainties with respect to instrumentation and methods of collection.

7.2 Processing methodology

Dorigatti (2013) developed a series of methodologies for processing surface pressure data recorded in the crosswind generator. Sections 7.2.1 and 7.2.3 discuss development and comparison of data processing methods, outlining how methods have been developed further and applied to this study.

7.2.1 Quasi-steady methodology

The surface pressure distribution is presented in terms of a series of non-dimensionalised pressure coefficients, derived from time averaging the coefficient time history,

$$C_{P_{ij}}(t) = \frac{P_{ij}(t) - \overline{P}_{ST,SW}^*}{\frac{1}{2}\rho(\overline{V}_{rel,SW}^*)^2} \quad (7.1)$$

where t is time, derived from the sample number and sampling frequency (section 4.3),

$$t_{samp} = \frac{N_{samp} - 1}{f_{samp}} \quad (7.2)$$

where $N_{samp}=1,2,\dots$ is the sample number and f_{samp} is the sampling frequency, which for model scale surface pressure data $f_{samp}=4000\text{Hz}$. Following data realignment with respect to either the open air test section or crosswind generator, the time base is also shifted, aligned by the point at which the measured pressure tap enters the measuring section at $t = 0$, hence the ‘*samp*’ subscript is dropped.

The index ij is used to identify pressure taps such that j is the tapping loop and i is the associated tap on that loop, according to the pressure tap layout in figures 6.14-6.17 (Dorigatti, 2013). $P_{ij}(t)$ is the instantaneous surface pressure at tap ij at time t and $\overline{P}_{ST,SW}^*$ is the corrected double averaged wind static reference pressure (Dorigatti,

2013). Air density ρ is calculated by (TSI, 2008),

$$\rho = \frac{P_{AMB}}{RT_{room}} \quad (7.3)$$

where the gas constant $R = 287\text{J}/(\text{kg}\cdot\text{K})$ and T_{room} is the temperature measured in Kelvin.

$\overline{V}_{rel,SW}^*$ is the corrected double averaged reference wind velocity relative to the train,

$$\overline{V}_{rel,SW}^* = \sqrt{(\overline{u_{cwg,SW}}^*)^2 + (V_{train,SW})^2} \quad (7.4)$$

where $\overline{u_{cwg,SW}}^*$ is the double corrected averaged streamwise velocity and $V_{train,SW}$ is the spanwise average train speed (Dorigatti, 2013).

Throughout chapters 7-8 many of the subscript/superscript and index notation used has previously been defined by Dorigatti (2013). When appropriate such notation will be defined in relation to the context presented for this study. Dorigatti (2013) uses the over bar notation to denote a time average and the subscript SW to denote a spanwise average over the crosswind test section. For this study the SW subscript is also used to denote the spanwise average over the open air test section. The $*$ superscript denotes when a crosswind variable has been corrected to account for streamwise gradients accessed within the crosswind flow characterisation (Dorigatti, 2013).

The pressure coefficient time history in equation 7.1 uses a corrected double averaged (time and spanwise) form of reference wind velocity relative to the train, negating any influences of inhomogeneity in the crosswind flow; a quasi-steady method frequently adopted in variable wind conditions (Dorigatti, 2013). The flow characterisation, presented in section 6.2.1, however exhibits limited spanwise uniformity in $\overline{u_{cwg}}$, with variations in turbulence intensities, relating to wind holes associated with $\overline{u_{cwg}}$ and the relative position in relation to fans. Due to the confined nature of the crosswind system within the building envelope, the fetch of the crosswind before the TRAIN rig

tracks is only 1m. The fetch distance is not large enough to negate the influence of the fans positioning on the crosswind flow. Dorigatti (2013) carried out an analysis to assess sensitivity of results to long time scale fluctuations and spanwise inhomogeneity of the relative crosswind. Results highlighted the influence of fluctuations in relative wind velocity on coefficient of pressure time histories and subsequent load coefficients (Dorigatti, 2013).

Dorigatti (2013) developed a modified method of calculation using a spanwise varying reference wind velocity, which gave comparable results to the quasi-steady methodology but reduced the influence of long time scale fluctuations; presented in section 7.2.2.

7.2.2 Modified methodology

Variations in mean relative wind velocity are created by long time scale fluctuations and spanwise inhomogeneity of mean horizontal velocity components ($\overline{\Delta u_{cwg}}$ and $\overline{\Delta v_{cwg}}$) and the decrease in train speed (ΔV_{train}) across the crosswind generator. Figure 7.1 illustrates the effect of variations on the magnitude of relative mean wind velocity $\overline{V_{rel}}$.

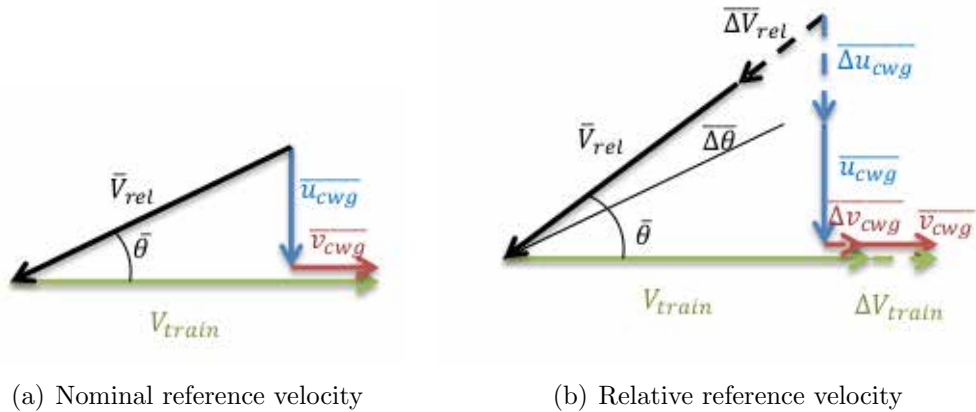


Figure 7.1: A vector diagram to show mean wind velocity relative to a moving vehicle for a) a nominal mean wind b) relative mean wind fluctuations.

Figure 7.1 also illustrates the influence of variations on the mean yaw angle $\overline{\theta}$ defined

as,

$$\overline{\theta} = \arctan \left(\frac{\overline{u_{\text{cwg}}}}{V_{\text{train}} - \overline{v_{\text{cwg}}}} \right) \quad (7.5)$$

where $\overline{u_{\text{cwg}}}$ and $\overline{v_{\text{cwg}}}$ are the nominal streamwise and lateral component of the mean crosswind and V_{train} is the train speed.

Dorigatti (2013) proposed a method to develop the quasi-steady methodology to include fluctuations in crosswind velocities and train speed. The modified methodology still adopts quasi-steady elements in relation to averaging turbulence induced short time scale wind fluctuations, however it includes characteristics of mean relative crosswind fluctuations by taking into account a linear decay in train speed and the relative fluctuations in $\overline{\Delta u_{\text{cwg}}}$ and $\overline{\Delta v_{\text{cwg}}}$ at each flow characterisation measuring point s_N (Dorigatti, 2013). Using figure 7.1(b) Dorigatti (2013) defines instantaneous values of streamwise u_{cwg} and lateral v_{cwg} components of crosswind velocity for an individual run r ,

$$u_{\text{cwg}}(r, t) = \overline{u_{\text{cwg}}}_{SW}(r) + \overline{\Delta u_{\text{cwg}}}(t) + u'_{\text{cwg}}(r, t) \quad (7.6)$$

$$v_{\text{cwg}}(r, t) = \overline{v_{\text{cwg}}}_{SW}(r) + \overline{\Delta v_{\text{cwg}}}(t) + v'_{\text{cwg}}(r, t) \quad (7.7)$$

where $\overline{u_{\text{cwg}}}_{SW}(r)$ denotes average velocity in both time and space, in the spanwise direction. $\overline{u_{\text{cwg}}}_{SW}(r)$ varies from run to run due to the stochastic nature of the wind simulation and is extrapolated from wind measurements undertaken for each run (Dorigatti, 2013). $\overline{\Delta u_{\text{cwg}}}(t)$ represents variations in the mean wind velocity with respect to $\overline{u_{\text{cwg}}}_{SW}(r)$; it is dependent on spanwise position, but doesn't include a turbulence contribution, thus is invariant from run to run (Dorigatti, 2013). $u'_{\text{cwg}}(r, t)$ denotes the turbulence induced fluctuations and therefore depends not only on spanwise position but each individual run (Dorigatti, 2013). Turbulence induced fluctuation terms cannot be controlled or predicted due to the stochastic nature of turbulence (Dorigatti, 2013). Therefore turbulence induced fluctuations are treated statistically, assuming a normal distribution about an average value $\overline{u'_{\text{cwg}}}$ (Dorigatti, 2013). Similar definitions are given for the lateral component of velocity v_{cwg} .

Similarly a value for the instantaneous train speed V_{train} for an individual run r is defined as,

$$V_{train}(r, t) = V_{train,SW}(r) + V_{train,GRAD}(r)(t - 0.5) \quad (7.8)$$

where $V_{train,GRAD}(r)$ is the gradient of velocity decrease through the crosswind generator, calculated by,

$$V_{train,GRAD}(r) = \frac{V_{train,EX} - V_{train,IN}}{L_{CW}} \quad (7.9)$$

where $V_{train,IN}$ is the train speed at the point at which loop j enters the crosswind generator, $V_{train,EX}$ is the train speed at the point at which loop j exits the crosswind generator and L_{CW} is the crosswind generator length.

From equation 7.5 it is clear the components of $V_{train}(r, t)$, $u_{cwg}(r, t)$ and $v_{cwg}(r, t)$ create fluctuations in yaw angle. The instantaneous yaw angle θ can therefore be defined as (Dorigatti, 2013),

$$\theta(r, t) = \overline{\theta}_{SW}(r) + \overline{\Delta\theta}(r, t) + \theta'(r, t) \quad (7.10)$$

where $\overline{\theta}_{SW}(r)$ is the average mean yaw angle across the span of the crosswind generator (equal to 30°). $\overline{\Delta\theta}(r, t)$ is the variation in yaw angle with respect to $\overline{\theta}_{SW}(r)$ and $\theta'(r, t)$ indicates turbulence induced fluctuations in yaw angle (Dorigatti, 2013).

The spanwise average terms $\overline{u_{cwg,SW}}$, $\overline{v_{cwg,SW}}$ and $\overline{\theta}_{SW}$ are by definition invariant with spanwise position but do vary from run to run, and thus are calculated from trackside measurements (Dorigatti, 2013). Conversely $\overline{\Delta u_{cwg}}$, $\overline{\Delta v_{cwg}}$ and $\overline{\Delta\theta}$, mean variations about spanwise averages, do vary with respect to spanwise position. Mean variations differ from turbulent fluctuations as these values can be measured in relation to flow characterisation values at set spanwise positions s_N .

By taking spanwise variations in mean relative crosswind velocities into account the surface pressure time histories for individual runs r are calculated for a series of span-

wise positions s_N , rather than a spanwise average (Dorigatti, 2013),

$$C_{P_{ij}}(s_N, \theta) = \frac{P_{ij}(s_N, \theta) - \bar{P}_{ST,SW}}{\frac{1}{2}\rho(\bar{V}_{rel}^*(s_N))^2} \quad (7.11)$$

where the relative wind velocity \bar{V}_{rel}^* is given by (Dorigatti, 2013),

$$\bar{V}_{rel}^*(s_N) = \sqrt{[\overline{u_{cwg,SW2}}^*(s_N)]^2 + [V_{train,SW2}(s_N) - \overline{v_{cwg,SW2}}^*(s_N)]^2} \quad (7.12)$$

where $SW2$ is an adjusted spanwise average calculated by dividing the crosswind generator length L_{CW} into a series of lengths $L_{CW_{s_N}}$, centred on flow characterisation measuring positions s_N , extending either side half way to neighbouring s_N , or to the crosswind generator edge.

Time histories are essentially deconstructed into a series of time histories for each spanwise position s_N with an associated yaw angle $\theta(r, s_N)$. Ensemble time averages are created by refinement of mean pressure coefficients to only accepting instantaneous values of C_p within the range $30^\circ \pm 2^\circ$, thus creating an ensemble time average coefficient of pressure $\overline{C_{P_{ij}}}$ with respect to an ensemble mean yaw angle $28^\circ < \bar{\theta}_{ENS} < 32^\circ$ at positions s_N (Cooper, 1993; Dorigatti, 2013),

$$\overline{C_{P_{ij}}} = \overline{C_{P_{ij}}(s_N, \bar{\theta}_{ENS})}_{|_{\bar{\theta}_{ENS} \in 30^\circ \pm 2^\circ}} \quad (7.13)$$

In relation to the original data processing methodology Dorigatti (2013) observed a difference of $\pm 3\%$ by calculating pressure coefficients using the modified methodology. Analysing ensemble pressure coefficient time histories highlighted that the modified methodology presented the greatest difference to the original methodology in areas with a large suction magnitude, associated with flow separation/recirculation (Dorigatti, 2013). It is hypothesised that regions of flow separation for the freight train will exhibit greater pressure coefficient magnitudes than observed for a high speed passenger train.

7.2.3 Modifications for this study

The modified methodology developed by Dorigatti (2013) is adapted for this study in relation to the open air and crosswind test sections. Adaptions to methodologies introduced in sections 7.2.1-7.2.2 are discussed in relation to the crosswind and open air test zones respectively.

7.2.3.1 Modifications to crosswind methodology

Dorigatti (2013) assumes a corrected spanwise average rather than a spanwise varying static pressure for calculating coefficient of pressure time histories (equation 7.11). The flow characterisation exhibits relative spanwise homogeneity for static pressure except in regions affected by the model entrance portals, therefore a spanwise average static pressure can be assumed, based on the run to run calculated value from the reference position (Dorigatti, 2013). However, the flow characterisation retest exhibits a small degree of variation for each run, resulting in a shift in ensemble static pressure from the original flow characterisation. To account for possible spanwise differences a spanwise varying static pressure calculation is adopted. Instantaneous values for static pressure for an individual run r are defined as,

$$P_{ST}(r, t) = \overline{P_{ST, SW}}(r) + \overline{\Delta P_{ST}}(t) + P'_{ST}(r, t) \quad (7.14)$$

where $\overline{P_{ST, SW}}(r)$ denotes average static pressure in both time and space, $\overline{\Delta P_{ST}}(t)$ represents variations in the mean wind velocity with respect to $\overline{P_{ST, SW}}(r)$ and $P'_{ST}(r, t)$ denotes turbulence induced fluctuations. Following the modified methodology accounting for spanwise varying static pressure, time histories for surface pressure coefficients are defined as,

$$C_{P_{ij}}(s_N, \Theta) = \frac{P_{ij}(s_N, \Theta) - P_{ST}(s_N, \Theta)}{\frac{1}{2}\rho(\overline{V}_{rel}^*(s_N))^2} \quad (7.15)$$

where the relative wind velocity \overline{V}_{rel}^* is defined in equation 7.12.

In relation to the modified methodology presented by Dorigatti (2013), a difference of $\pm 2\%$ is observed by calculating pressure coefficients using the modified methodology including variations in the crosswind static pressure. Similarly to the analysis of ensemble pressure coefficient time histories carried out by Dorigatti (2013), the further modified methodology presented the greatest difference in areas with a large suction magnitude, associated with flow separation/recirculation. Further smoothing of the pressure coefficient time histories is observed, exhibiting a reduced effect from the spanwise inhomogeneity of the crosswind flow.

7.2.3.2 Modifications for open air experiments

Surface pressure data measured in the open air section differs in processing methodology to the crosswind section due to lack of crosswind influence. Removing the crosswind influence and adopting a constant train speed $V_{train,SW}$, due to minimal deceleration in comparison to the crosswind section (section 7.3.1), the relative velocity reduces to,

$$\bar{V}_{relOA,SW}^* = \sqrt{(V_{train,SW})^2} \quad (7.16)$$

Similarly negating the crosswind effect removes the static pressure component P_{ST} , thus surface coefficient of pressure time histories become relative to the ambient pressure P_{AMB} , rather than P_{ST} (section 7.4.2). As train speed is assumed a nominal constant $V_{train,SW} = 24\text{m/s}$ (section 7.3.1), the original spanwise average coefficient of pressure time histories defined in equation 7.1 can be adapted for the open air test section,

$$C_{P_{ij}}(t) = \frac{P_{ij}(t) - P_{AMB}}{\frac{1}{2}\rho(\bar{V}_{relOA,SW}^*)^2} \quad (7.17)$$

where $\bar{V}_{relOA,SW}^*$ is as defined in equation 7.16. The ensemble calculation is defined as in Dorigatti (2013) for the original methodology.

7.3 Data conversion

7.3.1 Photoelectric position finders and light detector data

Photoelectric position finder and light detector data is used to align surface pressure measurements with respect to the appropriate test sections. Trackside position finder equipment is setup as in figure 7.2; multiple light sources correspond to different container positions to measure light detector data for all pressure tap configurations (figures 6.14-6.17).

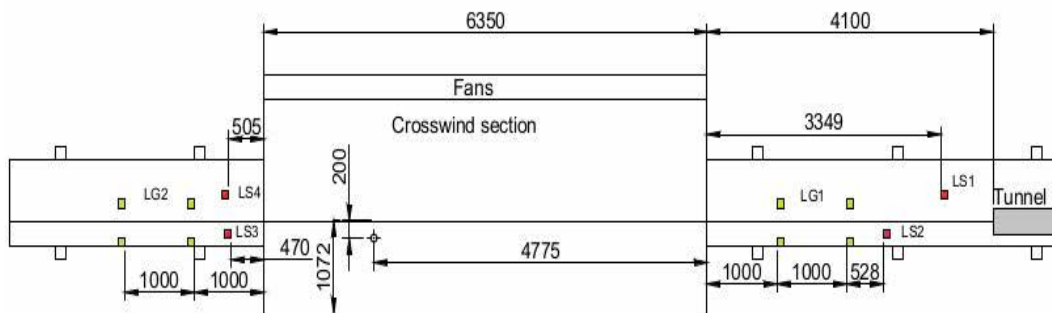


Figure 7.2: Positions of photoelectric position finders and light sources in the crosswind test zone. The photoelectric position finders LG1 and LG2 are shown in green and the light sources LS1-LS4 are shown in red. The crosswind generator and reference Cobra probe position are also shown. All dimensions are given in mm.

Analysis of trackside monitoring equipment data suggests the decrease in train speed differs depending on test section. For example, the deceleration through the open air test section is minimal, thus train speed is regarded as a constant speed through this zone (chapter 3). However through the crosswind generator deceleration increases, due to increased aerodynamic drag and friction forces created within the crosswind. The deceleration through the crosswind generator is assumed to be a linear decrease; shown to be an average deceleration of -3.5m/s^2 .

Assuming a linear decrease through the crosswind generator allows the instantaneous

train speed for an individual run r to be defined as,

$$V_{train}(r, \tau) = V_{train,GRAD}(r)\tau + V_{train,j,\tau_{LG1}}(r) \quad (7.18)$$

where $V_{train,GRAD}(r)$ is the gradient of velocity decrease through the crosswind generator, calculated by,

$$V_{train,GRAD}(r) = \frac{V_{train,j,\tau_{LG2}}(r) - V_{train,j,\tau_{LG1}}(r)}{L_{CW} + 3} \quad (7.19)$$

where $V_{train,\tau_{LG1}}(r)$ is the train speed as the nose reaches light gate 1 before the crosswind generator, $V_{train,\tau_{LG2}}(r)$ is the train speed as the nose reaches light gate 2 after the crosswind generator and L_{CW} is the crosswind generator length. τ is an adjusted time scale aligned with light gate 1 for the purpose of calculating the decrease in train speed for run r .

Assuming equation 7.18 it is possible to calculate the train speed as the Class 66 nose enters and exits the crosswind generator. Measuring the distance from the Class 66 nose to the relative measuring loop j allows the train speed as loop j enters and exits the crosswind generator to be calculated. This enables a shift in equation 7.18 to be carried out, shifting from τ to t ,

$$V_{train}(r, t) = V_{train,GRAD}(r)t + V_{train,j,t_{in}}(r) \quad (7.20)$$

where $V_{train,GRAD}(r)$ is the gradient of velocity decrease, as defined in equation 7.19. $V_{train,j,t_{in}}(r)$ is the train speed as loop j enters the crosswind generator. Train speed as loop j passes flow characterisation position s_N is calculated and substituted into equation 7.12 to calculate the resultant crosswind velocity at s_N for loop j on run r . The time at which loop j enters and exits the crosswind generator is used to trim crosswind pressure time histories for ease of analysis purposes.

Conversely, through the open air test section train speed was monitored by data logger

results. By analysing surface pressure and light detector data it is possible to pick out when the model is set in motion, when it leaves the acceleration zone and the point at which the train enters the 24m tunnel. Measuring the distance from the acceleration zone end to the tunnel allows an estimation of train speed through the open air test section. Analysing values of train speed with preliminary speed test results for the train with the data logger mounted, highlighted an average train speed of $24 \pm 2 \text{ m/s}$. Although it is not possible to calculate an instantaneous speed curve for the open air section, due the lack of additional photoelectric speed detectors, it is felt the minimal deceleration through this zone (-1.2 m/s^2) allows a nominal train speed of 24 m/s to be adopted for the open air surface pressure experiments. The error associated with this assumption is discussed in section 7.6. Similarly to crosswind data, the time at which loop j enters and exits the open air zone is used to trim pressure time histories.

7.3.2 Pressure transducer data

Figure 7.3 illustrates a typical trace of electronic signals recorded by the on-board data logger during a single run. Individual voltage traces $\text{Vol}_{ij,k}(t)$ for pressure transducers PT1 to PT15 are shown in colour, and the on-board light detector (LD) signal is shown in black. $\text{Vol}_{ij,k}(t)$ are the measured voltages where ij identifies the pressure tap and k identifies which pressure transducer was used for monitoring that tap, where $k = 1, \dots, 15$ (Dorigatti, 2013).

Experimental data is sampled by the data logger as a series of voltages from the pressure transducers at a frequency of 4000 Hz . Voltages are converted to pressure via conversion and calibration equations given by instrumentation manufacturers and calibration experiments.

Section 6.3.1.2 discusses the pressure transducer calibration methodology, with results given in appendix A. Pressure transducer data is converted from raw voltages $\text{Vol}_{ij,k}$

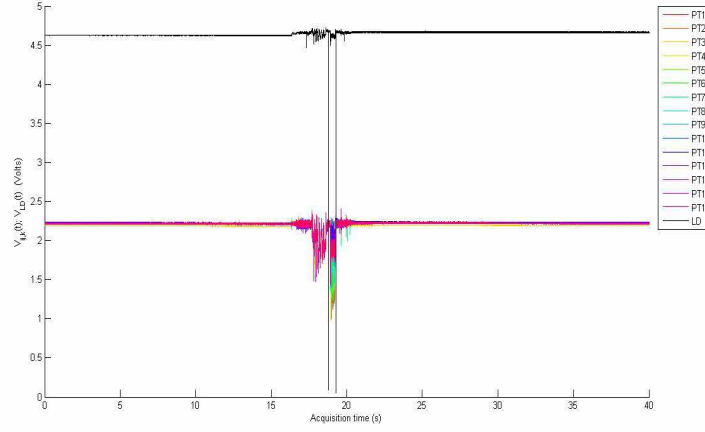


Figure 7.3: Time histories recorded by the on-board data logger for a single run. Pressure taps 1 to 15 are shown in colour and light detector data shown in black.

to pressure measurements $\Delta P_{ij}(t)$ using a series of cubic calibration curves,

$$\Delta P_{ij}(t) = C_{3,k} \Delta \text{Vol}_{ij,k}(t)^3 + C_{2,k} \Delta \text{Vol}_{ij,k}(t)^2 + C_{1,k} \Delta \text{Vol}_{ij,k}(t) \quad (7.21)$$

where $C_{1,k}$, $C_{2,k}$, $C_{3,k}$ are calibration coefficients associated with each transducer k (appendix A). $\Delta \text{Vol}_{ij,k}$ is the difference between the electronic signals recorded from the pressure transducers and the zero pressure offset,

$$\Delta \text{Vol}_{ij,k} = \text{Vol}_{ij,k} - \text{Vol}_{0,k} \quad (7.22)$$

The zero offset voltage $\text{Vol}_{0,k}$ calculates the zero pressure offset voltage for each pressure transducer in still ambient conditions. $\text{Vol}_{0,k}$ is calculated by taking a time average of pressure transducer data recorded for 15 seconds at 4000Hz with the reference pressure vent opened, thus recording ambient pressure on both sides of the pressure transducer, effectively giving a zero pressure offset voltage. $\text{Vol}_{0,k}$ is measured at the beginning and half way through each day to account for any differences to pressure transducers from variations such as differences in mean battery voltage.

Pressure measurements $\Delta P_{ij}(t)$ in equation 7.21 are effectively changes in pressure against the reference pressure, P_{RES} , which for the moving model is provided by a

sealed reservoir (Dorigatti, 2013),

$$\Delta P_{ij}(t) = P_{ij}(t) - P_{RES} \quad (7.23)$$

The drift associated with P_{RES} is minimal ($\pm 2\text{Pa}$, section 6.5), therefore P_{RES} is assumed constant for each experimental run.

In figure 7.3 pressures measured before and after the experimental run are effectively constant. In these regions the measured pressure is the atmospheric pressure P_{AMB} against the reference pressure P_{RES} . For analysis purposes (section 7.4) a 5 second time average value is calculated by averaging $\Delta P_{ij}(t_{samp})$ from $t_{samp} = 2$ seconds to $t_{samp} = 7$ seconds of the initial time history,

$$\Delta P_{ij,0} = \overline{\Delta P_{ij}(t)} \Big|_{2 < t_{samp} < 7} = P_{AMB} - P_{RES} \quad (7.24)$$

Dorigatti (2013) observed a resonant peak in pressure time history spectra, for the trimmed period when the train was in the crosswind generator, concluding that surface pressure measurements are affected by an interference caused by the fan blade passing frequency ($\sim 135\text{Hz}$). Following the same analysis for freight data highlighted similar interferences at frequencies $\sim 135\text{Hz}$. Applying a numerical Butterworth low pass filter at 117Hz removed the fan blade interference from trimmed time histories (Dorigatti, 2013).

7.3.3 Cobra probe data

Monitored crosswind data measured by Cobra probes is outputted to the user in a converted form of three components of velocity $u_{loc}(\tau)$, $v_{loc}(\tau)$, $w_{loc}(\tau)$ and differential static pressure $\Delta P_{ST,loc}(\tau)$, as discussed in section 4.2.1. Cobra probes record data continuously in an analogue format which is digitally sampled at a data acquisition rate of 4000Hz , converted from voltage signals to meaningful variables by the TFI

data logger and outputted at the sampling rate of 2000Hz. Section 4.2.1 discusses the method of file conversion from .TH* to .ap format for analysis purposes.

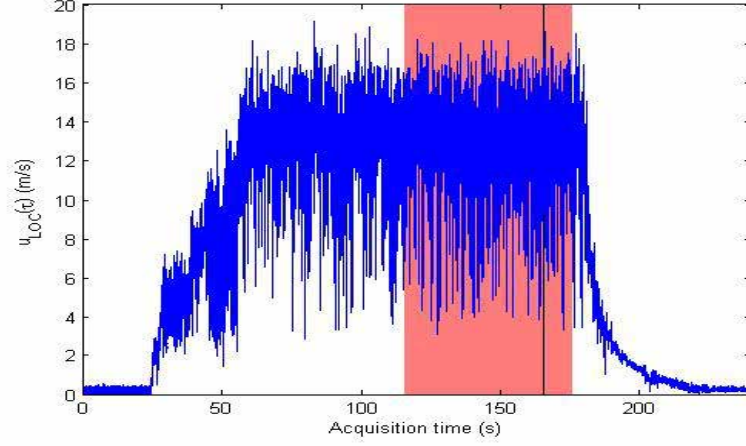


Figure 7.4: An example of a crosswind velocity u_{loc} time history recorded by the reference Cobra probe. The black line indicates when the train enters the crosswind generator and the shaded area shows data used to create the average $\overline{u_{loc}} = \overline{u_{loc}(\tau)} \Big|_{\tau_{60,1} < \tau < \tau_{60,2}}$

The probe was setup to record measurements for 240 seconds to enable time for the whole crosswind firing process to be completed, as discussed in section 6.5 (figure 7.4). Effectively for each run there is a period of still air, a period where the fans power up, followed by a period of running at maximum power, before powering down and finally returning to a still air situation. Figure 7.4 also shows the time at which the model enters the crosswind generator. Using the model entrance time τ_{IN} as a position finder allows the Cobra probe data to be trimmed to 50 seconds before τ_{IN} and 10 seconds following τ_{IN} , highlighted in figure 7.4,

$$u_{cwg,loc}(\tau) = u_{loc}(\tau) \Big|_{\tau_{60,1} < \tau < \tau_{60,2}} \quad (7.25)$$

$$v_{cwg,loc}(\tau) = v_{loc}(\tau) \Big|_{\tau_{60,1} < \tau < \tau_{60,2}} \quad (7.26)$$

$$\Delta P_{ST,loc}(\tau) = \Delta P_{ST,loc}(\tau) \Big|_{\tau_{60,1} < \tau < \tau_{60,2}} \quad (7.27)$$

This period of full power crosswind data is subsequently averaged to $\overline{u_{cwg,loc}}$, $\overline{v_{cwg,loc}}$ and

$\overline{P_{ST,loc}}$. Dorigatti (2013) defined a series of spanwise and streamwise data correction methods to calculate reference velocities and static pressure for normalising surface pressure data. Reference average crosswind velocities are calculated as a function of spanwise position s_N , with respect to each flow characterisation measuring position. By calculating a series of ratios of crosswind velocity and static pressure at each flow characterisation position s_N in relation to flow characterisation data recorded at the Cobra probe reference position, data is extrapolated from the local run to run measurements of streamwise crosswind velocities $\overline{u_{cwg,loc}}$, $\overline{v_{cwg,loc}}$ and static pressure $\overline{P_{ST,loc}}$ (Dorigatti, 2013). Effectively this creates a spanwise correction for each flow characterisation position s_N . Similarly Dorigatti (2013) analysed the flow characterisation to create streamwise velocity and pressure gradients, correcting data in the streamwise direction to account for the Cobra probe reference position, $d = 0.2\text{m}$ upstream from centre of track. Although the along wind velocity gradient is not defined for each spanwise position it can be assumed invariant across the crosswind generator as d is small in relation to the test section. For v_{cwg} no along wind gradient correction is applied (Dorigatti, 2013).

7.4 Non-dimensionalised variables

Surface pressure data is presented in terms of a series of non-dimensionalised pressure coefficients, derived from time averaging pressure coefficient time histories. Derivation of non-dimensionalised coefficients for the open air and crosswind sections differ depending on processing methodology applied (section 7.2.3).

7.4.1 Pressure coefficient measured through the crosswind

Once voltage data has been processed the pressure coefficient time histories for pressure tapping ij are calculated as,

$$C_{P_{ij}}(s_N, \theta)|_r = \frac{\Delta P_{ij}(s_N, \theta)|_r - \Delta P_{ij,0}|_r - \Delta P_{ST}^*(s_N)|_r}{\frac{1}{2}\rho_r \left([\overline{u_{cwg_{SW2}}}(s_N)|_r]^2 + [V_{train,SW2}(s_N)|_r - \overline{v_{cwg_{SW2}}}(s_N)|_r]^2 \right)} \quad (7.28)$$

where r is the individual time history. By substituting equations 7.23 and 7.24 into 7.28 it is possible to reduce the number of variables (Dorigatti, 2013),

$$C_{P_{ij}}(s_N, \theta)|_r = \frac{P_{ij}(s_N, \theta)|_r - P_{RES}|_r - (P_{AMB}|_r - P_{RES}|_r) - (P_{ST}^*(s_N)|_r - P_{AMB}|_r)}{\frac{1}{2}\rho_r \left([\overline{u_{cwg_{SW2}}}(s_N)|_r]^2 + [V_{train,SW2}(s_N)|_r - \overline{v_{cwg_{SW2}}}(s_N)|_r]^2 \right)} \quad (7.29)$$

$$\Rightarrow C_{P_{ij}}(s_N, \theta)|_r = \frac{P_{ij}(s_N, \theta)|_r - P_{ST}^*(s_N)|_r}{\frac{1}{2}\rho_r \left([\overline{u_{cwg_{SW2}}}(s_N)|_r]^2 + [V_{train,SW2}(s_N)|_r - \overline{v_{cwg_{SW2}}}(s_N)|_r]^2 \right)} \quad (7.30)$$

Equation 7.30 is of the form proposed by Dorigatti (2013) (equation 7.11), however the corrected static pressure P_{ST}^* is a function of spanwise position, not a spanwise average, accounting for changes in P_{ST} observed during the flow characterisation retest.

7.4.2 Pressure coefficient measured through the open air

A similar process is followed for the open air experiments, however the static pressure term is removed as there is no crosswind component. Therefore, pressure coefficient time histories measured in open air for pressure tapping ij are calculated as,

$$C_{P_{ij}}(t)|_r = \frac{P_{ij}(t)|_r - P_{AMB}|_r}{\frac{1}{2}\rho_r (V_{train,SW})^2} \quad (7.31)$$

where $V_{train,SW}$ is the average train speed through the open air section, set for this study as a nominal value $V_{train,SW} = 24\text{m/s}$.

7.5 Aerodynamic forces and moments

Non-dimensionalised aerodynamic coefficients for drag, side and lift forces and the rolling moment, are measured about two reference systems. The container reference system about the centre of the container base and leeward container base edge, and the track system about the centre of track (x-axis) and leeward rail, are shown in figure 7.7. The aerodynamic load coefficients are examined using average surface pressure coefficient data through a method developed by Sanquer et al. (2004); Quinn et al. (2007) and Dorigatti (2013). The reference system defined in figure 6.18 implies the non-dimensional coefficients are given as (Dorigatti, 2013),

$$C_X = \frac{F_X}{\frac{1}{2}\rho V_{ref}^2 A_{ref}} \quad (7.32)$$

$$C_Y = \frac{F_Y}{\frac{1}{2}\rho V_{ref}^2 A_{ref}} \quad (7.33)$$

$$C_Z = \frac{F_Z(\Theta)}{\frac{1}{2}\rho V_{ref}^2 A_{ref}} \quad (7.34)$$

$$C_{M_X} = \frac{M_X}{\frac{1}{2}\rho V_{ref}^2 A_{ref} H_{ref}} \quad (7.35)$$

$$C_{M_{X,lee}} = \frac{M_{X,lee}}{\frac{1}{2}\rho V_{ref}^2 A_{ref} H_{ref}} \quad (7.36)$$

where F_X , F_Y , F_Z are drag, side and lift forces respectively and M_X , $M_{X,lee}$ are rolling moment forces. ρ is as defined previously for equation 7.1. V_{ref} , A_{ref} and H_{ref} are reference values for relative velocity, as defined in equation 7.12, and the measuring container side area and height, respectively. For this study A_{ref} and H_{ref} are defined for the measuring container, not including the wagon (section 6.3.1.3), to assess loading configuration and crosswind influence on a loaded container. Therefore, for drag A_{ref} is the container nominal front area 6.31m^2 , and for other load coefficients A_{ref} is the nominal side area of the container, which for partially loaded consists is the 12.192m^2 container with a total side area of 31.58m^2 and for the fully loaded consist is a 12.192m^2 container and a 6.096m^2 container with a total side area of 47.37m^2 . H_{ref} is the nominal container

height which for all consists is 2.590m.

Quinn et al. (2007) developed a method to estimate relative non dimensional force coefficients through integrating surface pressure coefficients on a discretised geometry of a vehicle surface. Discretised areas are formed by creating a rectangle centred on each tapping point, extending halfway to neighbouring tapping points or to container edges for outer tapping points. Figure 7.5 illustrates the method of discretising the container geometry for the 12.192m container. The discretised area dimensions are given in terms of a full scale container in table 7.1. The method of discretisation is continued for the 12.192m and 6.096m containers together.

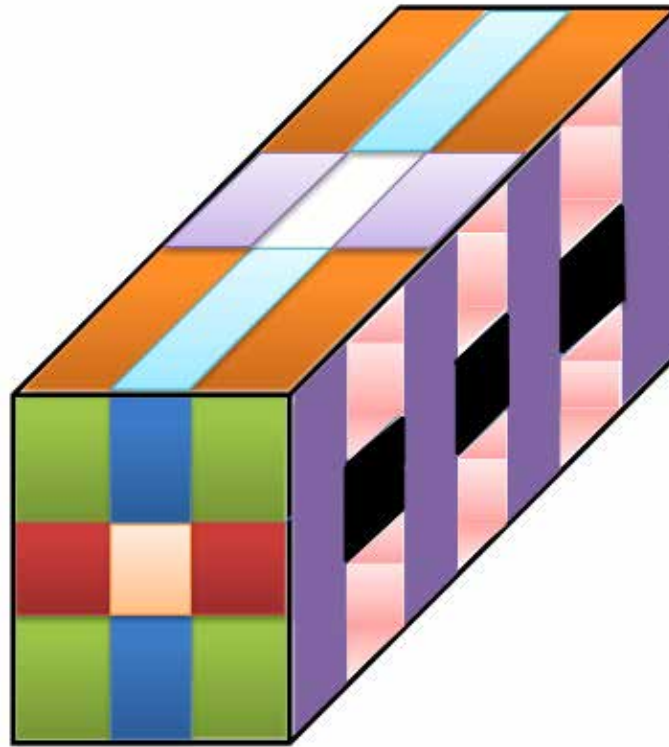


Figure 7.5: The method of discretising the container geometry shown here for the 12.192m container. The method is extended for the 12.192m and 6.096m container together. The dimensions of the discretised areas are given in table 7.1.

Figure 7.6 shows the discretised container geometry for the 12.192m container and the combination of the 6.096m and 12.192m container. The pressure tap distribution











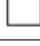
Colour	Dimensions (m)		
	x	y	z
	×	0.91	0.97
	×	0.61	0.97
	×	0.61	0.65
	×	0.91	0.65
	2.29	×	2.59
	1.52	×	1.48
	1.52	×	0.99
	4.57	0.91	×
	4.57	0.61	×
	3.05	0.91	×
	3.05	0.61	×

Table 7.1: Dimensions for the different area sizes of the container discretised geometry. The dimensions are given in terms of a full scale container. The method of discretisation is continued for the 12.192m and 6.096m container together.

and discretised area of influence, A_{ij} , associated with each pressure tap are defined. As part of this study different geometry discretisation methods were tested, however aerodynamic load coefficients for each method were within the estimated bounds of uncertainty defined in section 7.6.

The overall load coefficients can be defined as (Quinn et al., 2007; Dorigatti, 2013),

$$C_X = \frac{\sum_i \overline{C_{P_{ij}}} A_{ij} (\mathbf{n}_{ij} \cdot \mathbf{x})}{A_{ref}} \quad (7.37)$$

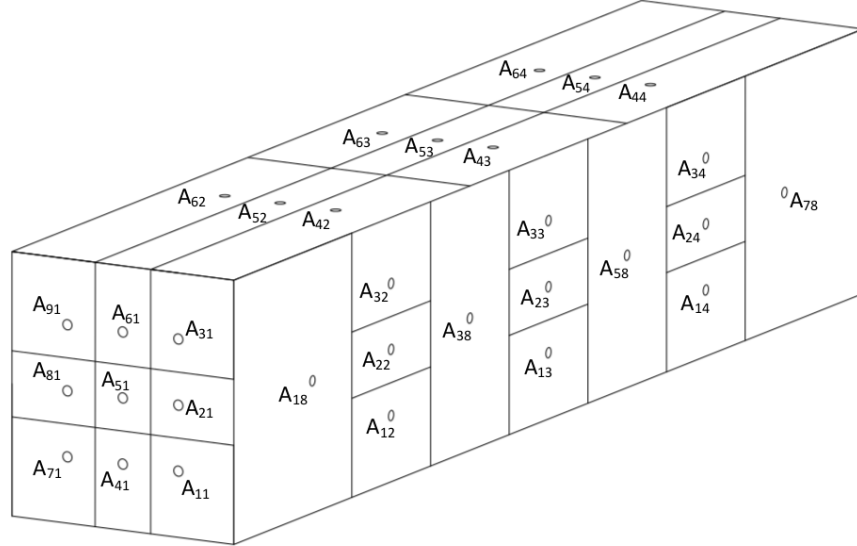
$$C_Y = \frac{\sum_i \overline{C_{P_{ij}}} A_{ij} (\mathbf{n}_{ij} \cdot \mathbf{y})}{A_{ref}} \quad (7.38)$$

$$C_Z = \frac{\sum_i \overline{C_{P_{ij}}} A_{ij} (\mathbf{n}_{ij} \cdot \mathbf{z})}{A_{ref}} \quad (7.39)$$

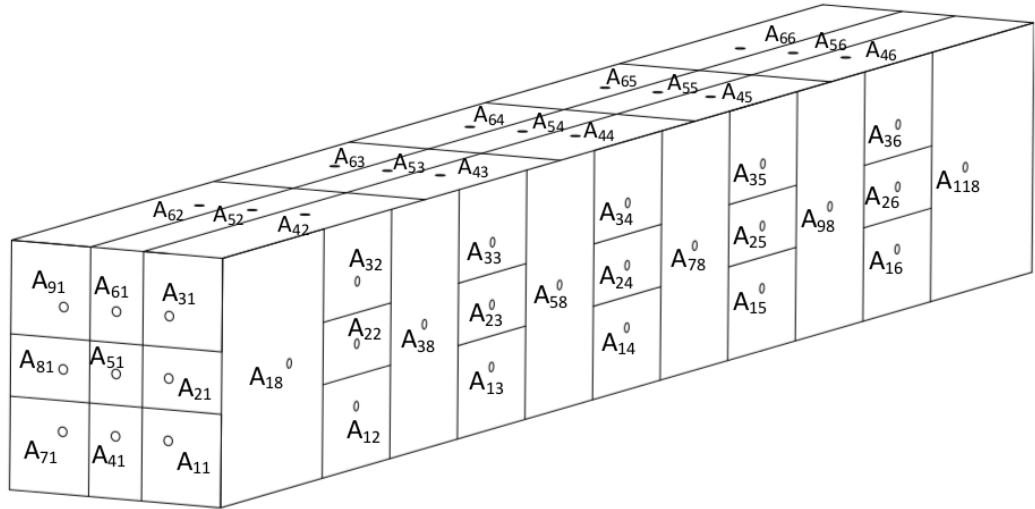
$$C_{M_X} = \frac{\sum_i \overline{C_{P_{ij}}} A_{ij} \frac{\|\mathbf{d}_{ij} \times \mathbf{n}_{ij}\|}{\mathbf{x}}}{A_{ref} H_{ref}} \quad (7.40)$$

$$C_{M_{X,lee}} = \frac{\sum_i \overline{C_{P_{ij}}} A_{ij} \frac{\|\tilde{\mathbf{d}}_{ij} \times \mathbf{n}_{ij}\|}{\mathbf{x}}}{A_{ref} H_{ref}} \quad (7.41)$$

where $\overline{C_{P_{ij}}}$ is the ensemble average pressure coefficient for each pressure tapping as-



(a) Pressure taps on 12.192m container



(b) Pressure taps on 12.192m and 6.096m containers

Figure 7.6: Pressure tapping positions and associated discretised area to each tapping point. The container is rotated about the 3rd wagon to create the loading configurations and pressure loops seen in figures 6.14-6.17.

sociated with discretised area A_{ij} . The aerodynamic load coefficients are calculated with respect to two reference systems, shown in figure 7.7. As no pressure taps are placed in the container base a reference system about the container is adopted (figure 7.7(a)), to assess the influence of container loading configuration on the aerodynamic load measured on the container. A second reference system about the centre of track and leeward rail also used to calculate the aerodynamic load on the container with respect to the track (figure 7.7(b)), providing a comparison to current safety standards (TSI, 2008). Assessing figure 7.7, \mathbf{n}_{ij} is the normal unit vector associated with discretised area A_{ij} (directed inwards into the body), and \mathbf{x} , \mathbf{y} and \mathbf{z} are the unit vectors associated with axes X , Y and Z (Dorigatti, 2013). \mathbf{d}_{ij} and $\tilde{\mathbf{d}}_{ij}$ are vectors perpendicular to the longitudinal axis X and container base leeward edge, directed from the pressure tap PT_{ij} (Dorigatti, 2013).

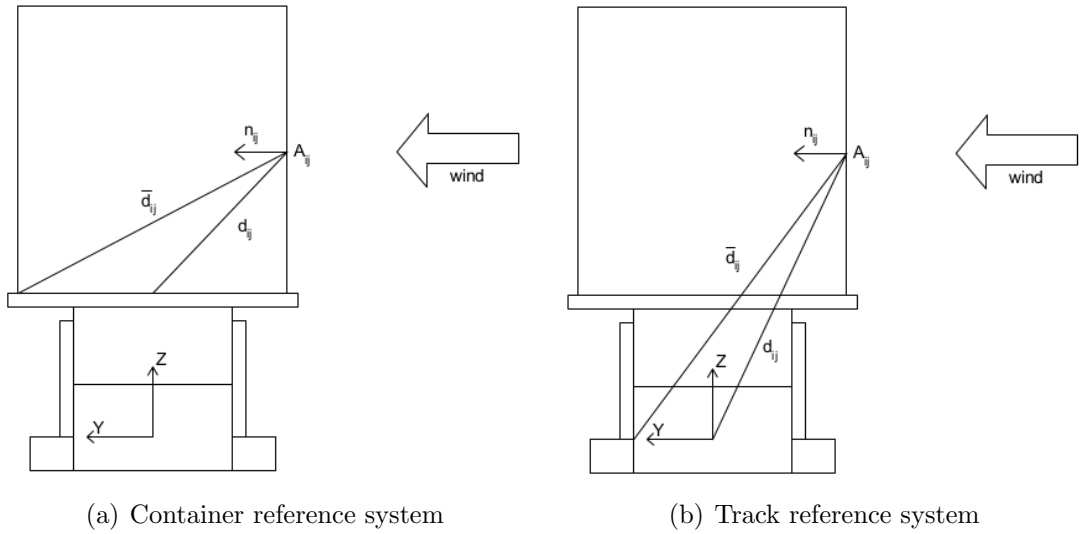


Figure 7.7: The reference systems used for calculating load coefficients on the discretised container surface. Figure 7.7(a) illustrates the container base reference system and figure 7.7(b) illustrates the reference system about the centre of track and leeward rail.

7.6 Uncertainty analysis

An uncertainty analysis for the mean surface pressure coefficients and aerodynamic load coefficients is presented in appendix B for the open air and crosswind test sections, the results of which are presented here. Estimate values for the total uncertainty are calculated by a methodology developed by Taylor (1997) and Tavoularis (2005), taking into account the uncertainty associated with the equipment used to take the measurements, through propagation of error theory (bias limit), as well as a quantification of the random uncertainty of results. Dorigatti (2013) applied the uncertainty analysis methodology to mean pressure and aerodynamic load coefficients measured at the TRAIN rig facility. The uncertainties associated to the aerodynamic load experiments are calculated in terms of mean pressure and aerodynamic load coefficients, with respect to the results presented in chapter 8. The method of calculating uncertainties, adopted from Dorigatti (2013), initially calculates the uncertainty of mean pressure coefficients, then by applying propagation theory, the uncertainty of aerodynamic load coefficients.

7.6.1 Mean pressure coefficients

The mean pressure coefficient is calculated for each pressure tap on the measuring container surface for consists 1, 4 and 6 in both the open air and crosswind test sections. In appendix B the total uncertainty for each pressure tap is given as the sum of the bias limit and random uncertainty. Estimate values for the mean and maximum total uncertainty for each consist in the open air and crosswind sections are shown in table 7.2.

		Total uncertainty	
		Mean	Maximum
Consist 1	open air	0.023	0.030
	crosswind	0.045	0.114
Consist 4	open air	0.025	0.028
	crosswind	0.048	0.144
Consist 6	open air	0.025	0.032
	crosswind	0.052	0.132

Table 7.2: A table of mean and maximum total uncertainties for mean pressure coefficients for all consists tested in the aerodynamic load experiments.

7.6.2 Aerodynamic load coefficients

The uncertainties associated with the mean aerodynamic load coefficients are estimated relative to the uncertainties calculated for the mean pressure coefficients. The un-

		C_X	C_Y	C_Z	C_{M_X}	$C_{M_{X,lee}}$
Consist 1	open air	0.012	0.008	0.006	0.006	0.007
	crosswind	×	0.016	0.018	0.014	0.016
Consist 4	open air	0.012	0.011	0.008	0.008	0.009
	crosswind	×	0.022	0.029	0.022	0.026
Consist 6	open air	0.013	0.012	0.008	0.008	0.009
	crosswind	×	0.022	0.028	0.022	0.025

Table 7.3: A table of mean total uncertainties for aerodynamic load coefficients in the open air and crosswind test sections.

certainties are calculated by applying propagation of error theory to the aerodynamic load coefficient equations (equations 7.37-7.41), and assuming the loads calculated for the discretised area associated to each pressure tap are independent (appendix B). The uncertainties for aerodynamic load coefficients in the open air and crosswind sections are shown in table 7.3.

The values in table 7.3 provide an estimate to the uncertainties for each aerodynamic load coefficient. The uncertainties are considered to be less than the true error, as the calculation does not account for the uncertainty introduced through discretising the container geometry, and by the assumption of pressure uniformity across each discretised area in the pressure integration process (Dorigatti, 2013).

Chapter 8

Aerodynamic load analysis, results and discussion

8.1 Introduction

In chapter 8 the analysis and results from the freight aerodynamic load experiments are discussed. Results are presented in terms of the open air (section 8.2) and crosswind (section 8.3) test sections. Firstly a series of individual pressure coefficient time histories are analysed to assess the stability of the on-board data logger system in relation to each test section (section 8.2.1 and 8.3.1). Mean ensemble pressure coefficients are calculated for each pressure tap. The analysis is split into a series of individual container surfaces, presented in sections 8.2.2 and 8.3.2. Aerodynamic load coefficients are calculated by discrete integration of mean pressure coefficients across the container surface. The results are analysed to assess the influence of container loading efficiency on aerodynamic load magnitudes and compared with previous freight studies in sections 8.2.3 and 8.3.3. A discussion of Reynolds number effects and the influencing factors on uncertainty are presented in section 8.4. Finally general conclusions are drawn in section 8.4.3.

8.2 Open air results and analysis

8.2.1 Surface pressure distribution

Mean pressure coefficients for the moving model open air aerodynamic load experiments are defined as,

$$\overline{C_{P_{ij}}} = \overline{C_{P_{ij}}(t)}|_{t_0 < t < t_1} \quad (8.1)$$

where t_0 and t_1 are the time at which the train enters and exits the open air test section respectively. Unlike the crosswind experiments, the open air mean pressure coefficients are calculated for the whole open air test section length.

Figures 8.1-8.3 give examples of the typical evolution of pressure coefficient as the train travels through the open air section. Loop 2 was chosen for this representation to provide a comparison of results with the crosswind measurements presented in section 8.3.1; the largest degree of variation in pressure coefficient is observed for taps on this loop. For each consist a series of 15 individual runs are plotted with the corresponding ensemble average time series.

The results presented in figures 8.1-8.3 are representative of all taps monitored on the container for all consists measured in the open air test section. In general, good consistency is observed in pressure coefficient time histories; remaining relatively constant in the open air section. Similarly to the crosswind data, for each individual run there are a series of high frequency fluctuations of similar amplitude, but without synchronicity, about the ensemble pressure coefficient. It is thought these fluctuations are created by the turbulent nature of the boundary layer flow developing around the train.

The mean pressure coefficients, as calculated by equation 8.1, for all consists are presented in tables 8.1-8.3, with the associated standard deviation. A series of figures to show the mean pressure coefficient distribution for each loop as a series of container cross sections for all consists are presented in figures 8.4-8.12. For each plot the wagon cross section illustrates the pressure tap positions on the container surface. Bounds to

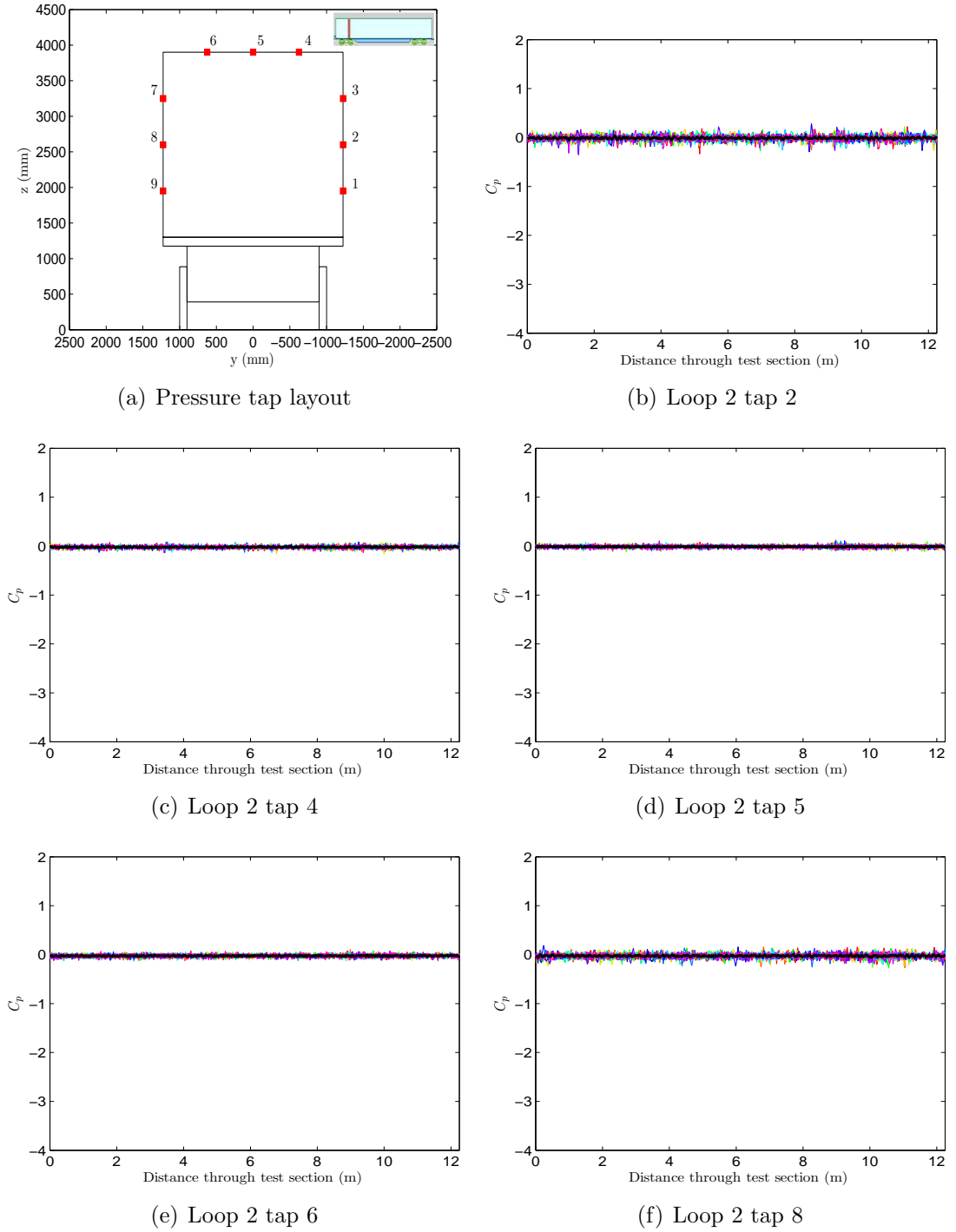


Figure 8.1: Examples of the typical evolution of pressure coefficient as the train travels within the open air section. A series of 15 individual runs are plotted with corresponding ensemble average time series for consist 1 loop 2.

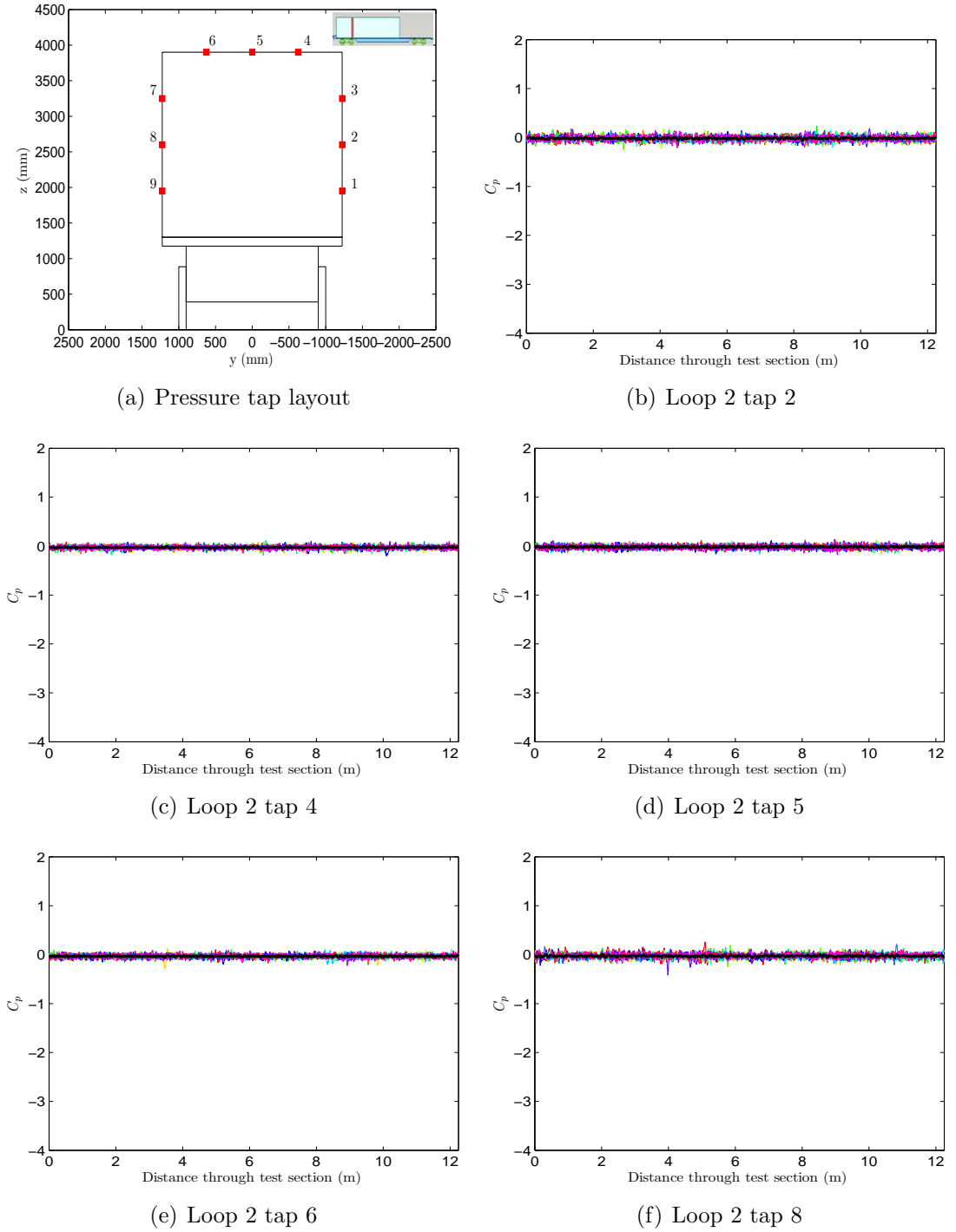


Figure 8.2: Examples of the typical evolution of pressure coefficient as the train travels within the open air section. A series of 15 individual runs are plotted with corresponding ensemble average time series for consist 4 loop 2.

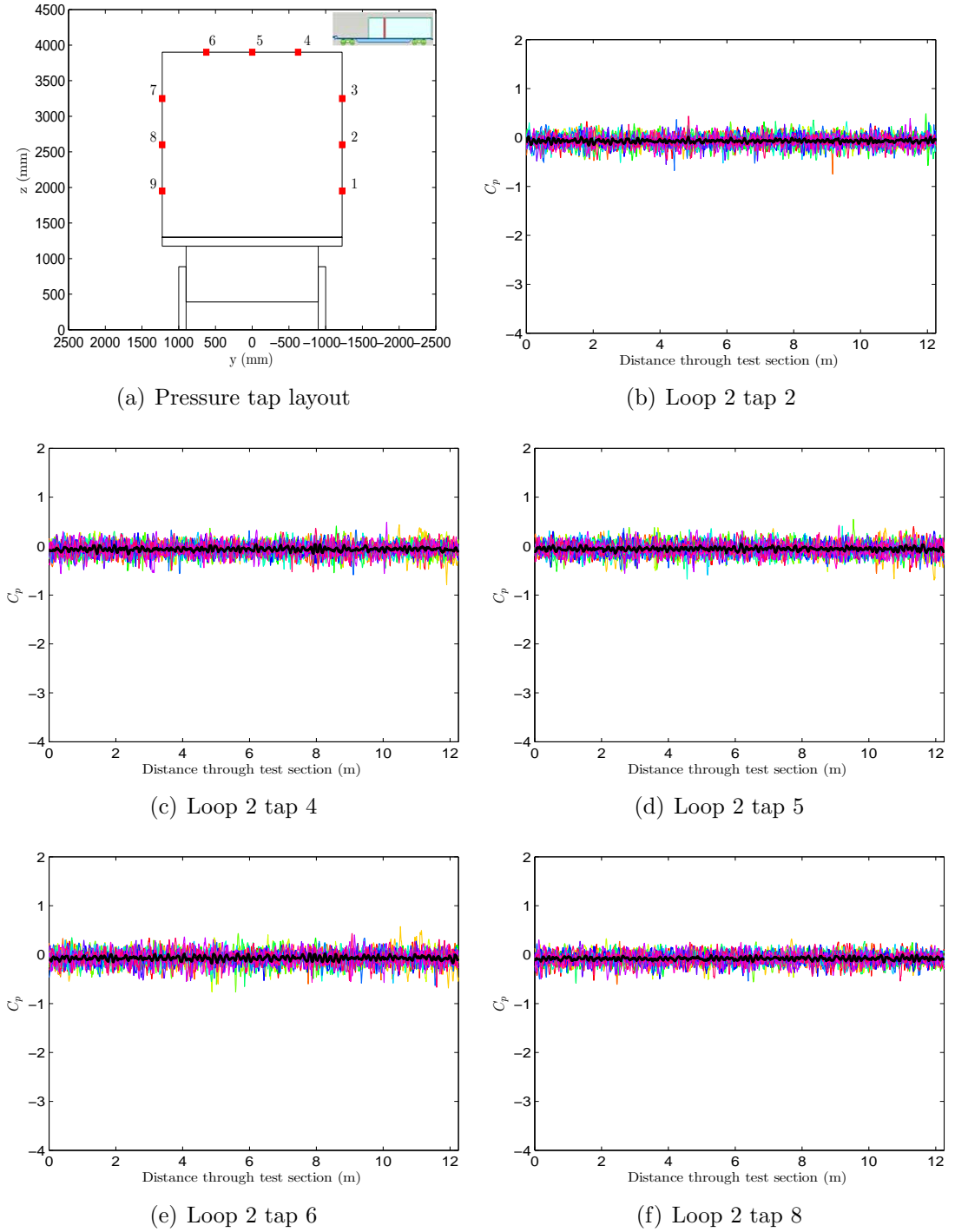
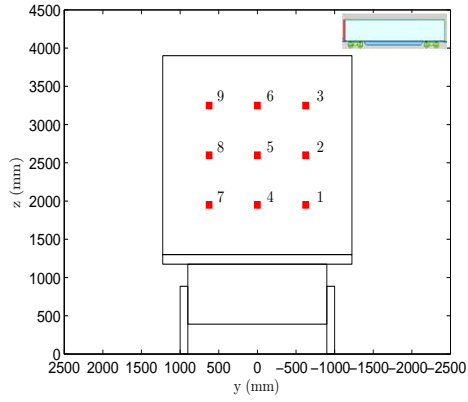


Figure 8.3: Examples of the typical evolution of pressure coefficient as the train travels within the open air section. A series of 15 individual runs are plotted with corresponding ensemble average time series for consist 6 loop 2.

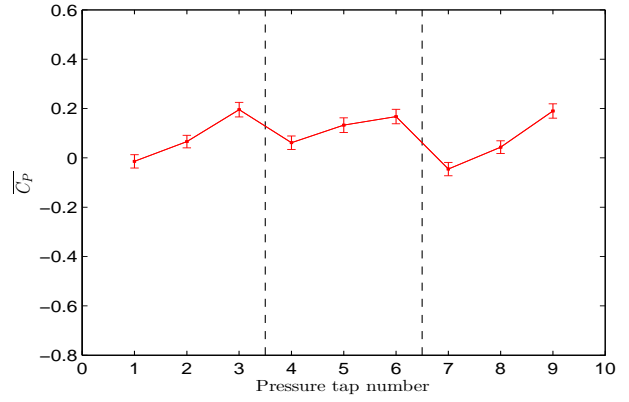
the associated uncertainty for each pressure transducer are also plotted in accordance to which pressure tap the transducer was connected.

Consist 1														
Tap	Loop													
	1		2		3		4		5		6		7	
	Mean	Std	Mean	Std	Mean	Std	Mean	Std	Mean	Std	Mean	Std	Mean	Std
1	-0.014	0.027	-0.022	0.016	-0.022	0.012	-0.027	0.009	-0.024	0.008	-0.019	0.010	-0.019	0.007
2	0.066	0.026	-0.011	0.012	-0.012	0.010	-0.018	0.009	-0.020	0.007	-0.013	0.011	-0.022	0.007
3	0.196	0.034	-0.009	0.008	-0.014	0.007	-0.023	0.008	-0.019	0.006	-0.021	0.009	-0.016	0.007
4	0.061	0.021	-0.020	0.006	-0.010	0.006	-0.025	0.006	-0.016	0.004	-0.030	0.005	-0.009	0.007
5	0.133	0.026	-0.012	0.006	-0.012	0.005	-0.016	0.006	-0.013	0.004	-0.011	0.004	-0.008	0.007
6	0.168	0.021	-0.025	0.007	-0.013	0.005	-0.033	0.006	-0.019	0.005	-0.017	0.005	-0.006	0.007
7	-0.045	0.029	-0.023	0.008	-0.018	0.006	-0.002	0.007	-0.002	0.007	-0.003	0.006	-0.022	0.007
8	0.044	0.027	-0.025	0.011	-0.021	0.009	-0.008	0.007	-0.012	0.007	-0.001	0.007	-0.026	0.006
9	0.190	0.032	-0.024	0.014	-0.025	0.009	-0.014	0.008	-0.003	0.008	-0.002	0.007	-0.027	0.006

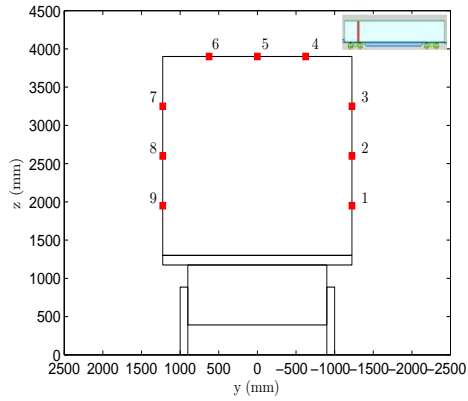
Table 8.1: Mean pressure coefficients and the standard deviation for consist 1 in the open air test section, on all vertical loops with taps 1 to 9.



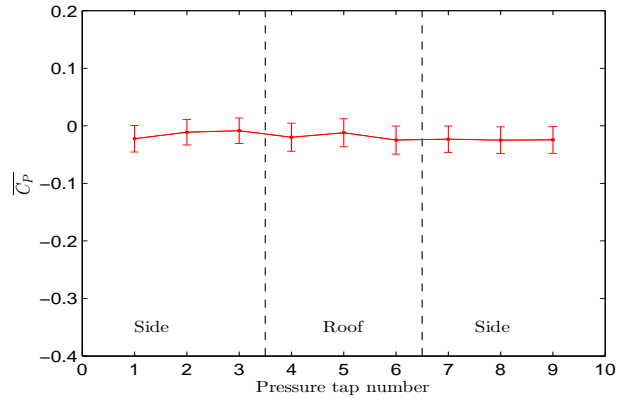
(a) Loop 1 pressure tap layout



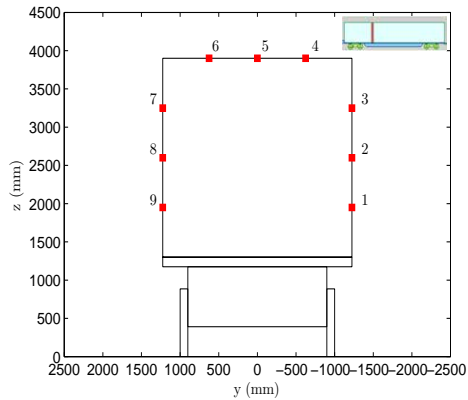
(b) Loop 1 coefficient of pressure



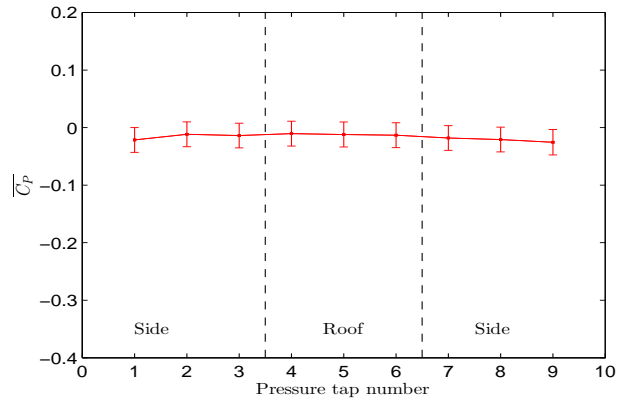
(c) Loop 2 pressure tap layout



(d) Loop 2 coefficient of pressure

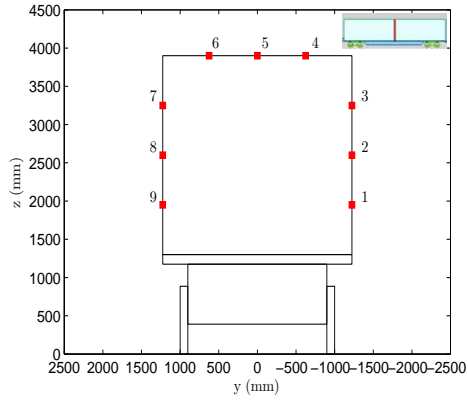


(e) Loop 3 pressure tap layout

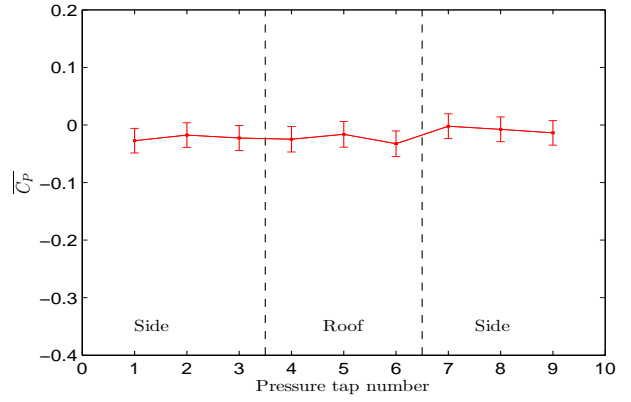


(f) Loop 3 coefficient of pressure

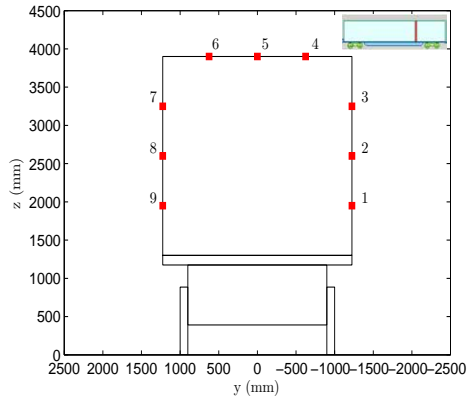
Figure 8.4: Mean surface pressure coefficient distribution with associated uncertainty error bounds for consist 1 loops 1, 2 and 3. For each loop a diagram of pressure tapping positions is provided.



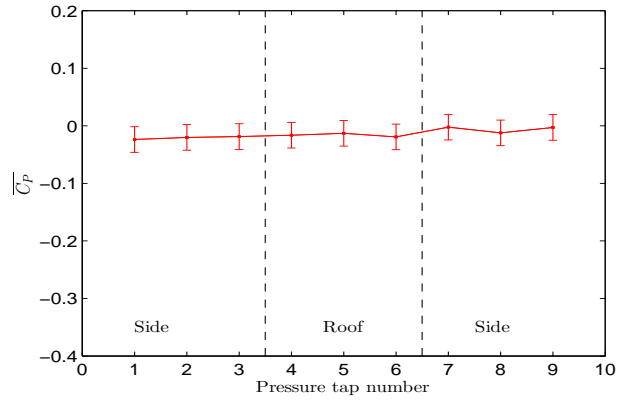
(a) Loop 4 pressure tap layout



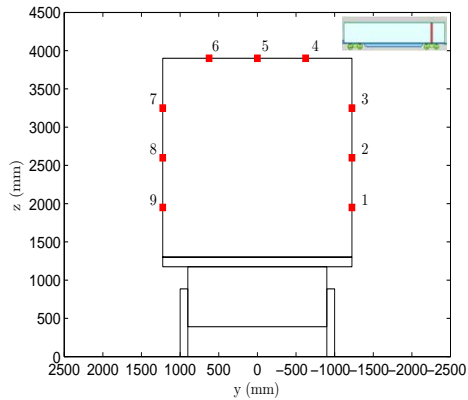
(b) Loop 4 coefficient of pressure



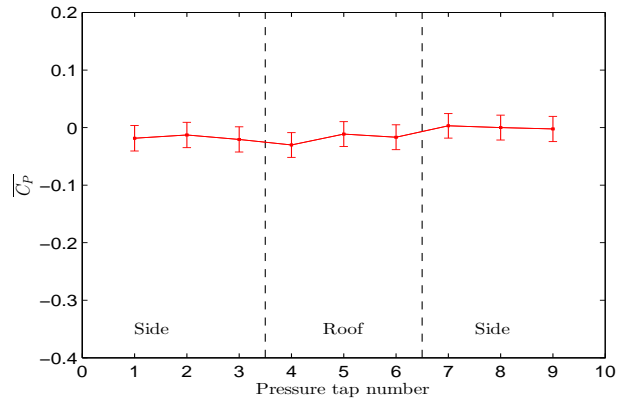
(c) Loop 5 pressure tap layout



(d) Loop 5 coefficient of pressure

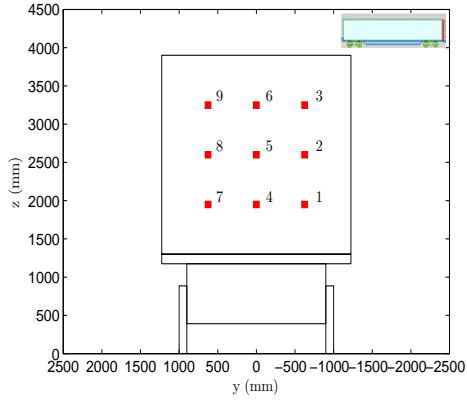


(e) Loop 6 pressure tap layout

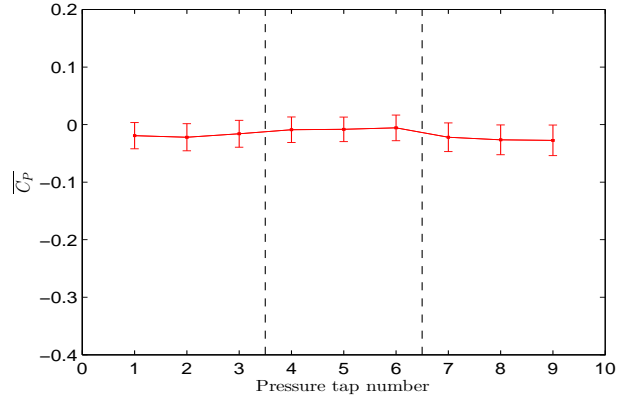


(f) Loop 6 coefficient of pressure

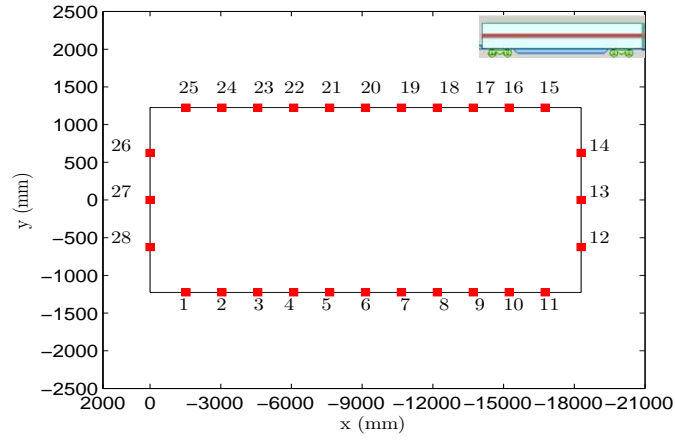
Figure 8.5: Mean surface pressure coefficient distribution with associated uncertainty error bounds for consist 1 loops 4, 5 and 6. For each loop a diagram of pressure tapping positions is provided.



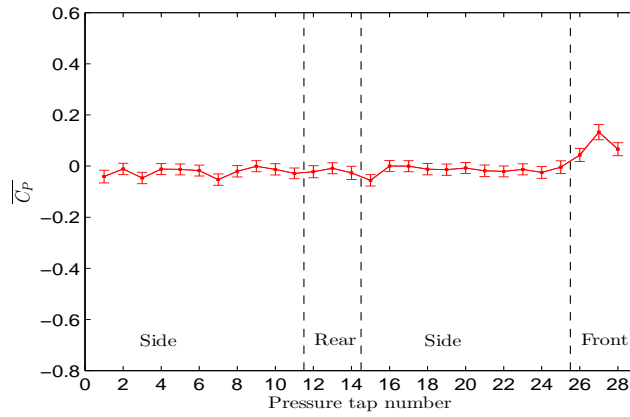
(a) Loop 7 pressure tap layout



(b) Loop 7 coefficient of pressure



(c) Loop 8 pressure tap layout



(d) Loop 8 coefficient of pressure

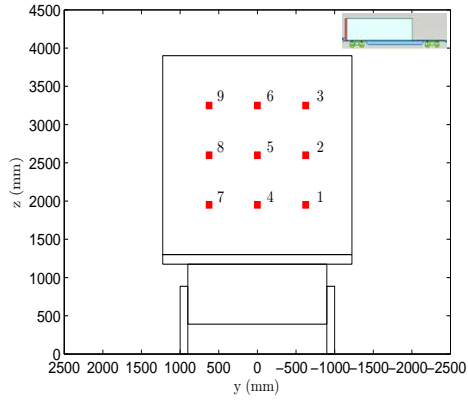
Figure 8.6: Mean surface pressure coefficient distribution with associated uncertainty error bounds for consist 1 loops 7 and 8. For each loop a diagram of pressure tapping positions is provided.

Tap	Consist 4									
	Loop									
	1		2		3		4		5	
	Mean	Std	Mean	Std	Mean	Std	Mean	Std	Mean	Std
1	0.007	0.026	-0.030	0.013	-0.033	0.010	-0.040	0.010	-0.082	0.006
2	0.067	0.027	-0.017	0.012	-0.017	0.010	-0.031	0.009	-0.084	0.006
3	0.152	0.028	-0.017	0.010	-0.019	0.008	-0.036	0.009	-0.087	0.006
4	0.059	0.022	-0.027	0.008	-0.016	0.007	-0.045	0.006	-0.081	0.005
5	0.095	0.023	-0.017	0.008	-0.018	0.005	-0.026	0.006	-0.084	0.006
6	0.129	0.024	-0.032	0.008	-0.019	0.007	-0.031	0.006	-0.089	0.006
7	-0.018	0.024	-0.026	0.011	-0.024	0.008	-0.015	0.008	-0.082	0.007
8	0.055	0.024	-0.028	0.012	-0.030	0.009	-0.019	0.008	-0.086	0.005
9	0.157	0.029	-0.031	0.013	-0.036	0.010	-0.027	0.008	-0.090	0.006

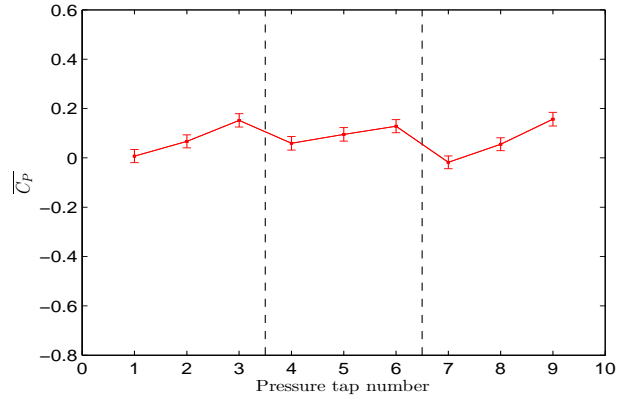
Table 8.2: Mean pressure coefficients and the standard deviation for consist 4 in the open air test section, on all vertical loops with taps 1 to 9.

Tap	Consist 6									
	Loop									
	1		2		3		4		5	
	Mean	Std	Mean	Std	Mean	Std	Mean	Std	Mean	Std
1	0.395	0.029	-0.075	0.024	-0.035	0.013	-0.040	0.011	-0.042	0.010
2	0.446	0.034	-0.070	0.028	-0.035	0.016	-0.037	0.013	-0.074	0.012
3	0.485	0.043	-0.079	0.038	-0.037	0.018	-0.057	0.012	-0.023	0.022
4	0.435	0.024	-0.065	0.033	-0.031	0.017	-0.041	0.010	-0.029	0.010
5	0.469	0.027	-0.058	0.032	-0.026	0.009	-0.023	0.011	-0.020	0.017
6	0.476	0.031	-0.070	0.038	-0.033	0.016	-0.027	0.011	-0.010	0.019
7	0.382	0.030	-0.087	0.031	-0.040	0.021	-0.022	0.014	-0.012	0.011
8	0.434	0.034	-0.081	0.028	-0.037	0.017	-0.026	0.013	-0.006	0.012
9	0.457	0.037	-0.090	0.029	-0.042	0.014	-0.024	0.012	-0.029	0.015

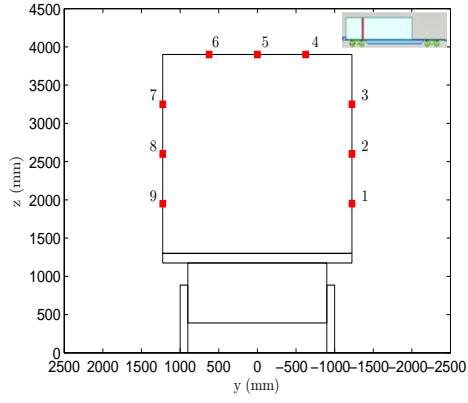
Table 8.3: Mean pressure coefficients and the standard deviation for consist 6 in the open air test section, on all vertical loops with taps 1 to 9.



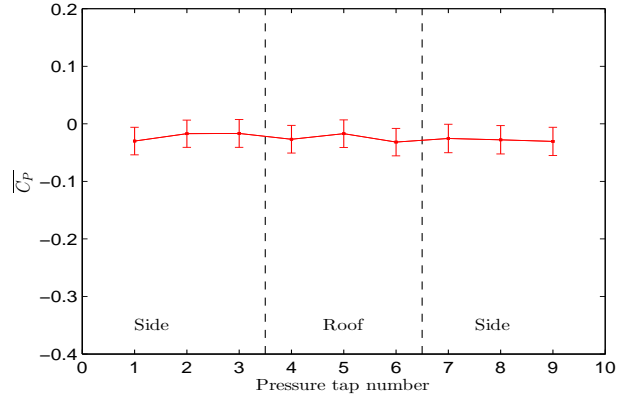
(a) Loop 1 pressure tap layout



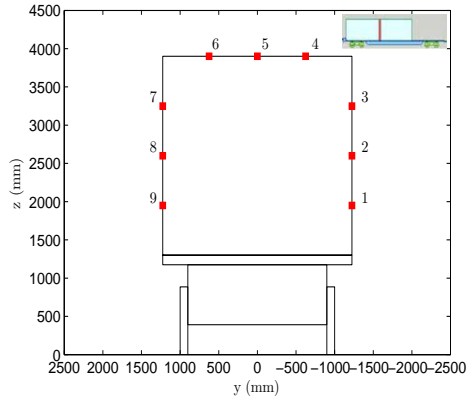
(b) Loop 1 coefficient of pressure



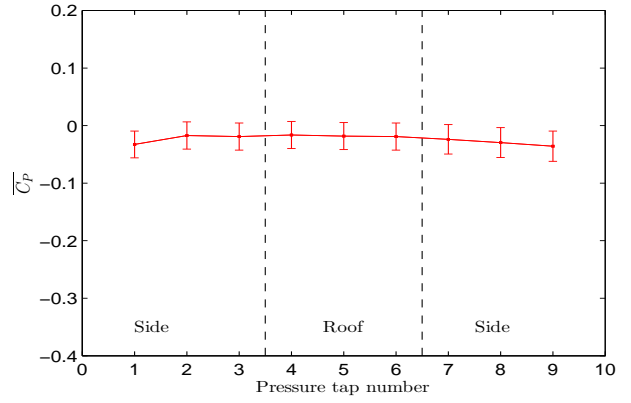
(c) Loop 2 pressure tap layout



(d) Loop 2 coefficient of pressure



(e) Loop 3 pressure tap layout



(f) Loop 3 coefficient of pressure

Figure 8.7: Mean surface pressure coefficient distribution with associated uncertainty error bounds for consist 4 loops 1, 2 and 3. For each loop a diagram of pressure tapping positions is provided.

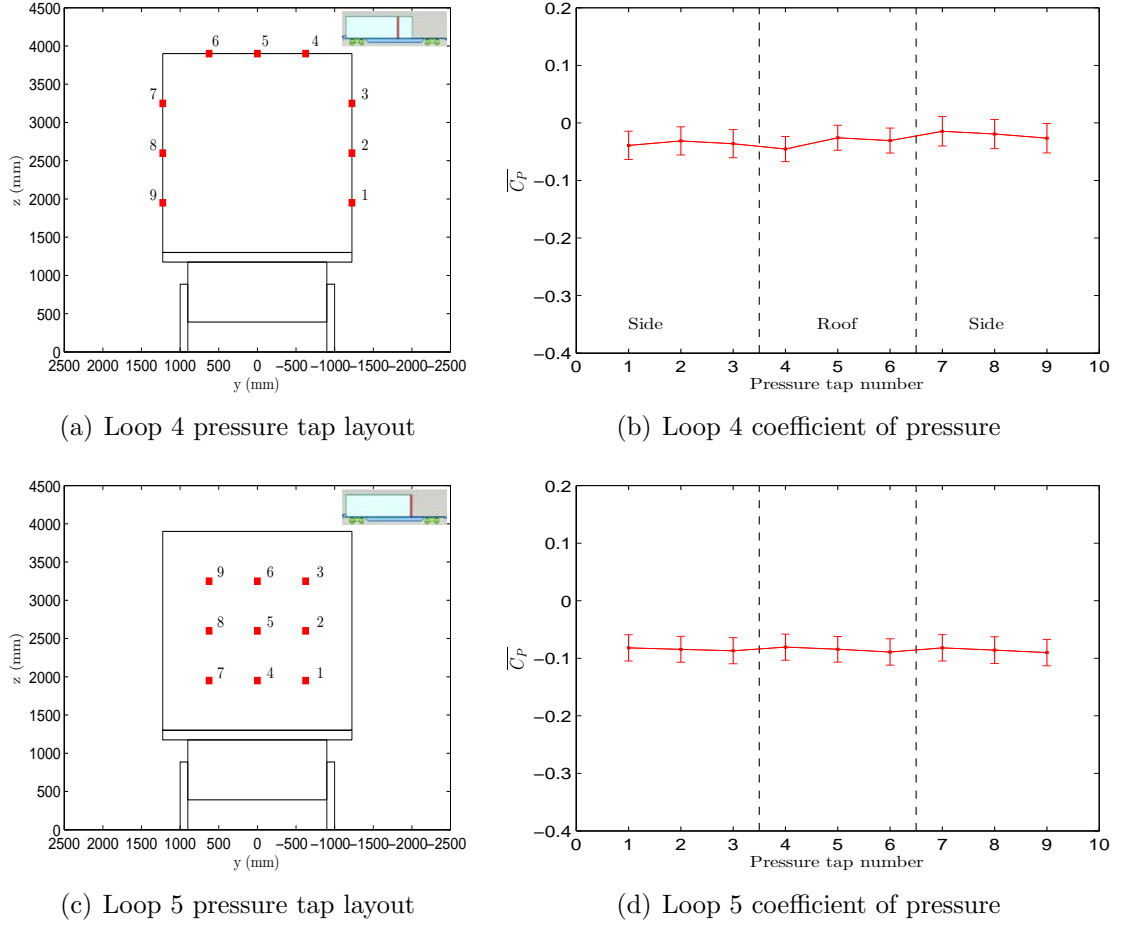
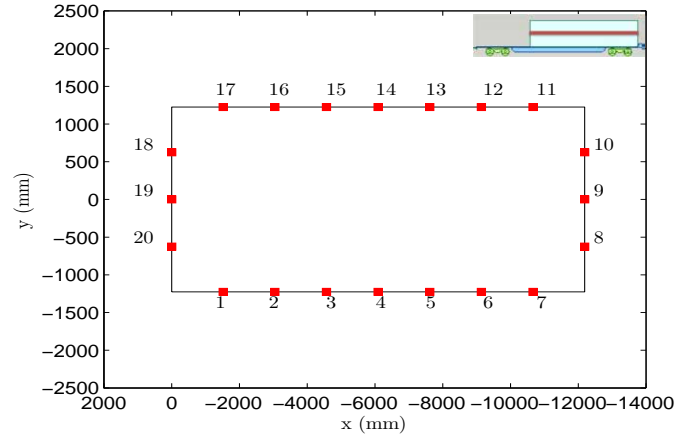
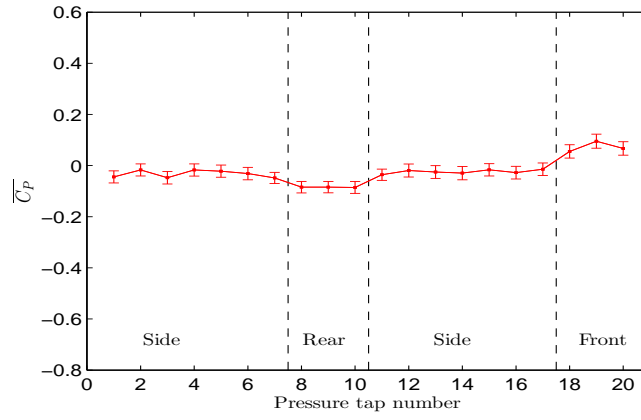


Figure 8.8: Mean surface pressure coefficient distribution with associated uncertainty error bounds for consist 4 loops 4 and 5. For each loop a diagram of pressure tapping positions is provided.



(a) Loop 8 pressure tap layout



(b) Loop 8 coefficient of pressure

Figure 8.9: Mean surface pressure coefficient distribution with associated uncertainty error bounds for consist 4 loop 8. For each loop a diagram of pressure tapping positions is provided.

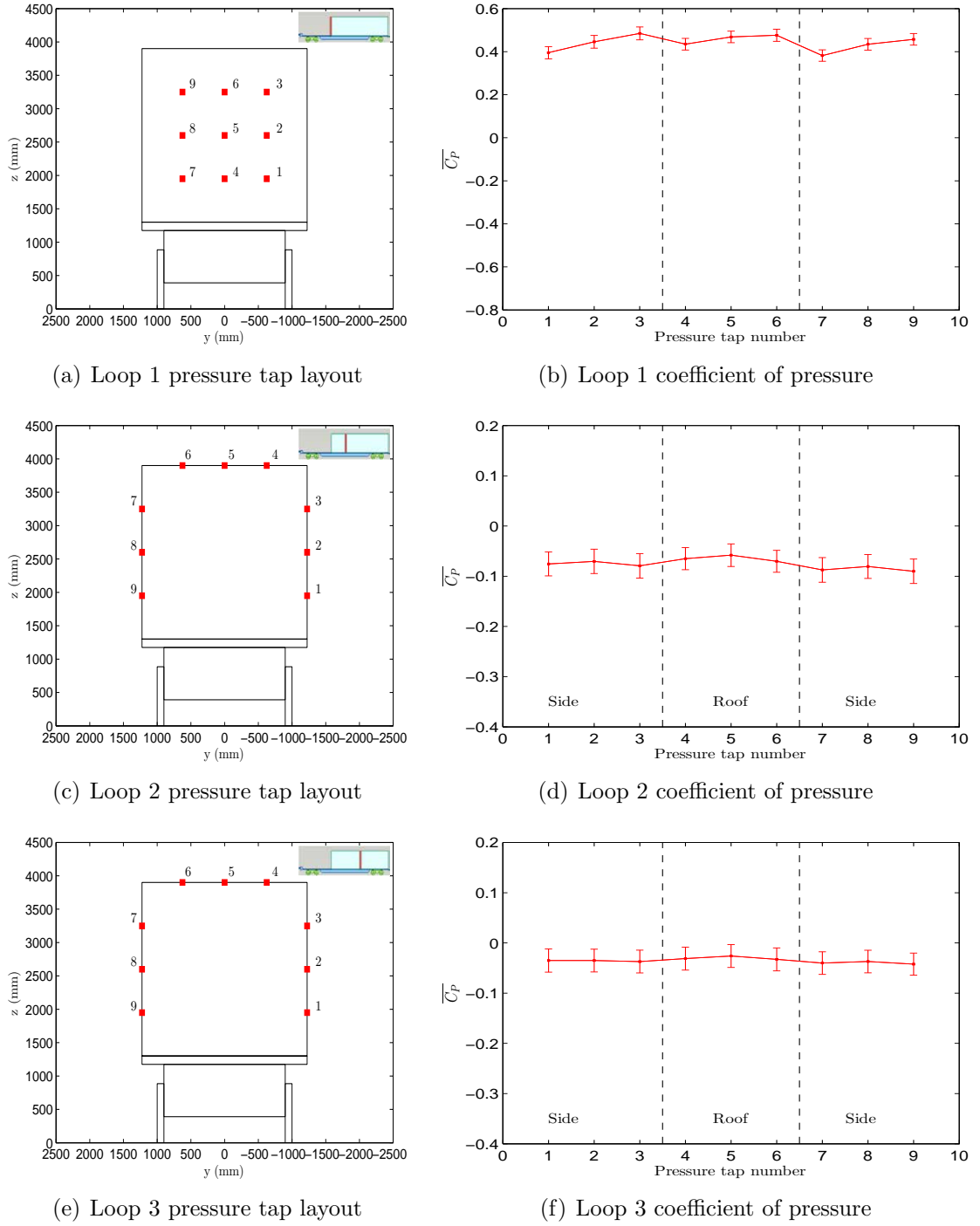


Figure 8.10: Mean surface pressure coefficient distribution with associated uncertainty error bounds for consist 6 loops 1, 2 and 3. For each loop a diagram of pressure tapping positions is provided.

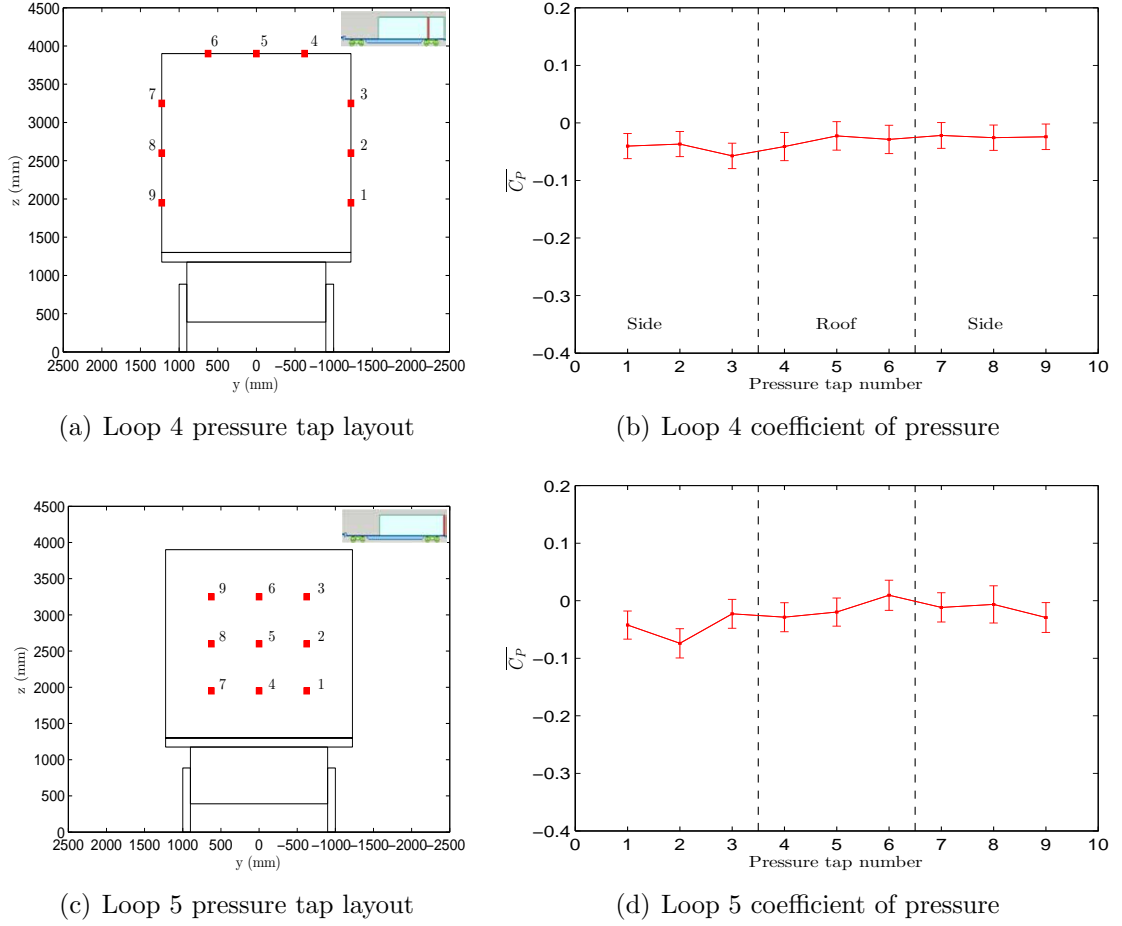
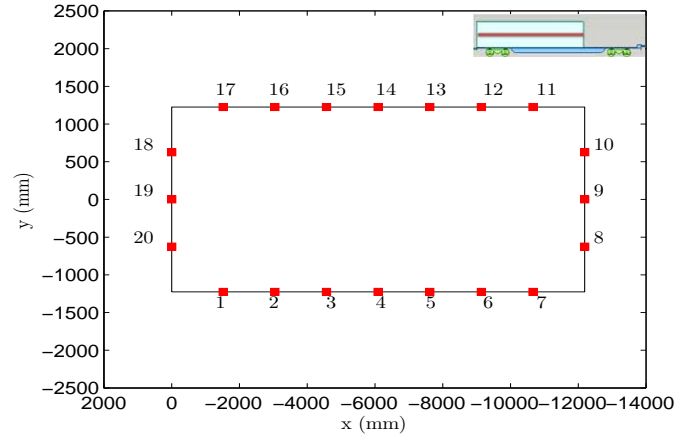
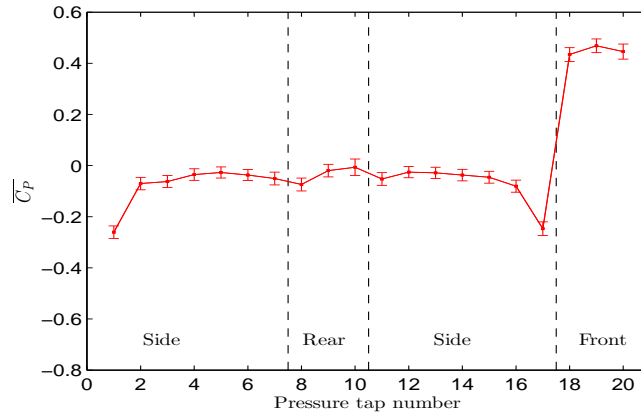


Figure 8.11: Mean surface pressure coefficient distribution with associated uncertainty error bounds for consist 6 loops 4 and 5. For each loop a diagram of pressure tapping positions is provided.



(a) Loop 8 pressure tap layout



(b) Loop 8 coefficient of pressure

Figure 8.12: Mean surface pressure coefficient distribution with associated uncertainty error bounds for consist 6 loop 8. For each loop a diagram of pressure tapping positions is provided.

8.2.2 Analysis of surface pressure distribution

The mean pressure coefficient distribution and associated error bounds for each container loading configuration examined in the open air test section are plotted in figures 8.4-8.12. The flatbed wagon and container full scale dimensions are given with pressure tap positions. Values of positive coefficient of pressure indicate areas of stagnation, whereas, values of negative pressure coefficient are representative of areas of suction. A series of flow patterns can be identified developing along the container length. Variations in these flow patterns are observed for the different consists examined; exhibiting a dependence on container loading configuration. In sections 8.2.2.1-8.2.2.4 these flow patterns are discussed in relation to the different container faces.

8.2.2.1 Lead face

The largest variations in pressure distribution are observed on the container lead face, shown to be highly dependent on container loading configuration. For all consists a region of stagnation is observed at the lead face. The large space in front of the measuring container in consist 6 creates a region of stagnation, with positive pressure on the lead face, exhibiting a greater magnitude than consists 1 and 4. The container loaded onto the wagon in front of the measuring container creates a shielding influence on the measuring container for consist 1 and 4, creating the differences observed between consist 6 and consists 1 and 4. The shielding effect is discussed in detail in regards to the crosswind test section in section 8.3.2.1.

Consist 1 exhibits a uniform distribution in pressure with relatively stable values. Consists 4 and 6 however exhibit a pressure gradient on the lead face, with pressure coefficients of a greater magnitude towards the roof edge. It is suggested that increased boundary layer slipstream velocities, created by lower loading efficiencies in consists 4 and 6, create greater positive pressure magnitudes when the flow impinges with the lead face of the measuring container. Values of pressure coefficient are larger towards

the roof edge than the container base, as boundary layer flow across the roof is drawn into the gap, impinging with the upper section of the lead face.

8.2.2.2 Side faces

The flow pattern on the container side faces for all consists exhibit very similar flow development of weak suction. The flow created is symmetric and relatively uniform in distribution and magnitudes. Small variations in pressure coefficient across the side faces lie within the associated error bounds for each tapping point. The largest variations occur for consist 6 loop 2, suggesting the magnitude of the flow separation from the leading face edges is increased due to the space in front of the measuring container. Values for standard deviation for all pressure taps measured on consist 6 are higher than for consist 1 and 4, indicating the influence of increased boundary layer growth with higher turbulence intensity levels for consist 6 in comparison to consists 1 and 4. In general, greater negative pressure magnitudes are observed for consists 4 and 6 in comparison to consist 1, highlighting the influence of container loading efficiencies as discussed previously.

8.2.2.3 Roof

The roof flow exhibits similar flow development to the side faces. A weak suction is observed over the container roof for all consists. Pressure coefficient values are generally lower for loop 2 in comparison to loops 3 and 4, related to a flow separation from the leading roof edge. This feature is most prominent for consist 6 due to the large space before the measured container, creating a larger flow deformation at the leading container edges. For all other loops pressure coefficients remain stable in magnitude, thus it is hypothesised that any flow recirculation remains closely bounded to the leading edge.

8.2.2.4 Rear face

Similarly to the lead face, the flow pattern observed on the container rear face is highly dependent on container loading configuration. The rear face is characterised by an area of suction, however, the distribution of negative pressure magnitudes is dependent on loading configuration and the space size following the measuring container.

The largest space behind the measuring container occurs for consist 4. The pressure distribution on the rear face remains relatively uniform with similar magnitudes across the whole face, but greater in magnitude than consists 1 and 6. Conversely, for the smaller space size between containers in consists 1 and 6 there is a large degree of variation in pressure distribution and magnitude across the rear face. The flow is symmetric with larger negative magnitudes at pressure taps towards the face edges than in the centre, hypothesised to be related to a shearing effect at the face edges. In the centre of the rear face for consists 1 and 6 there is a pressure gradient from the container base to the roof, suggesting a movement of flow upwards through the gap between containers. For consist 4 the large space following the measuring container negates the suction influence seen within the small gap, and thus a uniform pressure distribution is observed.

8.2.3 Overall aerodynamic load coefficients

The overall mean aerodynamic load coefficients are calculated as the discrete integral of forces acting on each pressure tap area, through applying equations 7.37-7.41. The model surface area is divided into a number of smaller areas associated with each pressure tapping (figure 7.6) and the forces on each pressure tap area calculated using the mean ensemble pressure coefficients.

Figure 8.13 and table 8.4 show estimated values calculated for aerodynamic load coefficients on the measuring container for consists 1, 4 and 6 in the open air test section.

The reference systems adopted are the same as in the crosswind section for continuity. Negative values for moments C_{M_X} and $C_{M_{X,lee}}$ correspond to moments that overturn the vehicle (Dorigatti, 2013).

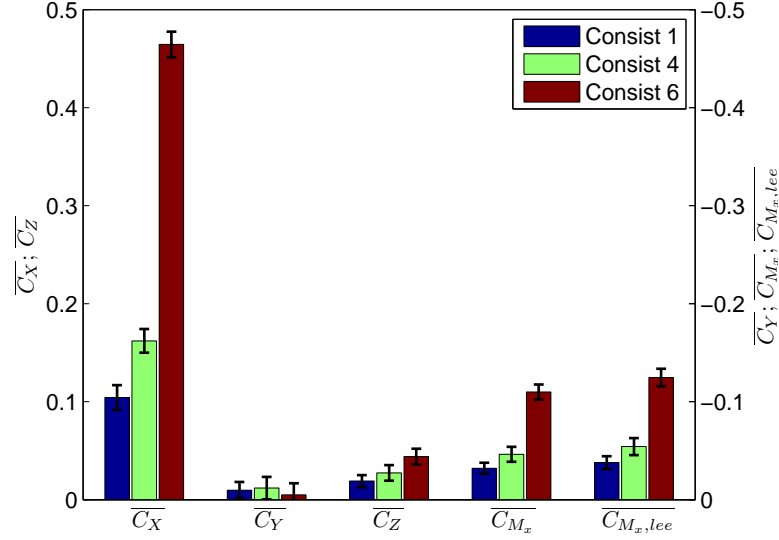


Figure 8.13: Estimated values for the aerodynamic load coefficients C_X , C_Y , C_Z , C_{M_X} and $C_{M_{X,lee}}$ in the open air test section. A conventional axis is adopted for C_X , C_Z and an inverted axis for C_Y , C_{M_X} and $C_{M_{X,lee}}$. The values for roll moments are given with respect a reference system about the centre of the measuring container and a leeward base edge. The associated uncertainty bounds for each coefficient are also plotted.

	Consist 1		Consist 4		Consist 6	
	Container reference	Track reference	Container reference	Track reference	Container reference	Track reference
C_X	0.10	0.10	0.16	0.16	0.46	0.46
C_Y	-0.01	-0.01	-0.01	-0.01	-0.01	-0.01
C_Z	0.02	-0.02	0.03	0.03	0.04	0.04
C_{M_X}	-0.03	-0.05	-0.05	-0.07	-0.11	-0.17
$C_{M_{X,lee}}$	-0.04	-0.05	-0.05	-0.07	-0.12	-0.18

Table 8.4: Aerodynamic load coefficients for consists 1, 4 and 6 C_X , C_Y , C_Z , C_{M_X} and $C_{M_{X,lee}}$ with respect to a container and track reference system in the open air test section. The values for roll moments are given with respect to either a reference system about the centre of the measuring container and a leeward base edge or a reference system about the centre of track and leeward rail.

Magnitudes of all aerodynamic load coefficients, except drag, for all consists tested are small, exhibiting values close to zero. However, figure 8.13 illustrates clear differences in force and roll moment coefficients as container loading configuration varies. In general,

larger magnitudes of aerodynamic coefficients are observed as the container loading efficiency is reduced and the space size in front of the measuring container is increased. The container loaded onto the wagon in front of the measuring container for consists 1 and 4 has a shielding effect, whereas forces acting on the measuring container in consist 6 have a greater influence from slipstream velocities within the boundary layer around the train. Consist 6 exhibits larger magnitudes for C_Y and C_Z in comparison to consists 1 and 4, due to flow separation from unshielded leading edges.

Values exhibited for C_X are larger than other aerodynamic load coefficients and show clear dependence on container loading configuration. In section 8.2.2, an analysis of flow development on the lead and rear faces highlighted the influence of spaces between loaded containers in front and behind the measuring container. The large space in front of the measuring container for consist 6 creates a region of stagnation on the measuring container lead face, with pressure coefficient magnitudes larger than either consist 1 or 4. The large space behind the measuring container for consist 4 creates an area of suction on the rear face of the measuring container, with a larger magnitude than either consist 1 or 6. However, the magnitude of the area of suction for consist 4 is not as large as the magnitude of the stagnation on the lead face of consist 6. Therefore, in calculating the drag coefficient the magnitude of C_X for consist 6 is larger than consist 4, which in turn is larger than consist 1; exhibiting clear dependence on container loading configuration. The magnitude of C_X is compared with Beagles and Fletcher (2013) for a yaw angle of 0° ; effectively measuring the aerodynamic load coefficients for a moving train without a crosswind simulation. Beagles and Fletcher (2013) tested a series of container loading efficiencies and found values for C_X at 0° ranged from 0.05 to 0.3. The magnitude of C_X for consist 1 and 4 compare well with similar container loading configurations presented in Beagles and Fletcher (2013), whereas the value for consist 6 is higher than any values presented in Beagles and Fletcher (2013). For the 0° yaw angle the aerodynamic forces exerted on the container are from flow in the boundary layer, therefore correct boundary layer development is important to

modelling the flow correctly. The results presented in Beagles and Fletcher (2013) are from wind tunnel tests on a series of consists made with a different number of wagons and container loading configurations but no locomotive. Full scale results presented in chapter 5 highlighted a key influence from locomotive type on subsequent boundary layer development. Therefore, the differences in values of C_X for results presented in this study are likely to be created due to differences in the method of modelling the freight train.

It should be noted that no pressure taps were placed in the container base. Due to the method of container attachment the flatbed wagon was modelled as a solid loading base to assesses forces on the container, not the container and wagon as a system. If a spine loading system was adopted for the flatbed wagon, pressure taps in the container base would be needed to account for the influence of flow underneath the wagon. This issue is discussed further in section 8.3.3; however, no significant changes to results are expected in relation to the general pattern between container loading configuration, for the situation of pressure taps in the container base or not.

C_{M_X} and $C_{M_{X,lee}}$ show a similar behaviour of increasing magnitude as the container loading efficiency is reduced. The moments in figure 8.13 are taken about the centre and leeward edge of the container base. Contrary to previous crosswind studies the moments are shifted from the conventional centre of track $x = 0$ and leeward rail, at height $z = 0$, to the centre and leeward edge of the container base, to measure the aerodynamic load coefficients for just the container, and not the container and wagon as a system. A comparison of both reference systems for calculating the roll moments reveals that values for the track reference system are larger than values for measurements taken just about the container, as shown in table 8.4.

In light of the 2008 UK crosswind incidents, RSSB (2012) carried out a series of wind tunnel experiments using a FEA-B flatbed wagon loaded with a 12.192m and 6.096m container and a HYA coal hopper wagon. The measured wagon was positioned in a consist with an unloaded FEA-B flatbed wagon either end of the measured wagon.

The study analysed results considering measurements for both the container and wagon using the reference system to measure roll moments about the leeward rail, as well as measurements for just the container using the reference system about leeward container base edge. Results were used to create a series of recommendations for the UK standard GM/RT 2142 (RSSB, 2009).

The container freight crosswind experiments conducted by RSSB (2012) include data measured at a yaw angle of 0° . The exact setup within RSSB (2012) is not replicated in this study, however, by using values for consists 1, 4 and 6 it is possible to draw some comparisons in the results for $C_{M_{X,lee}}$. Results show magnitudes for $C_{M_{X,lee}}$ are close to zero for measurements taken as a wagon and container system and measurements taken for just the container. For all consists measured within this study the values for $C_{M_{X,lee}}$ are larger in magnitude than those presented in RSSB (2012). It is suggested that the influence of boundary development within a complete train consist, including a locomotive and other wagons loaded with containers, increases boundary layer slipstream velocities, which in turn increase the magnitude of forces measured on the container surface. The comparison with RSSB (2012) is continued in section 8.3.3 for the crosswind results.

8.3 Crosswind results and analysis

8.3.1 Surface pressure distribution

The mean pressure coefficient for the moving model crosswind aerodynamic load experiments is defined as,

$$\overline{C_{P_{ij}}} = \overline{C_{P_{ij}}(s_N, \bar{\theta}_{\text{ENS}})}_{\text{ENS}} \Big|_{\bar{\theta}_{\text{ENS}} \in 30^\circ \pm 2^\circ} \quad (8.2)$$

Individual time histories are essentially deconstructed into a series of time histories for each spanwise position s_N , with an associated yaw angle $\theta(r, s_N)$. Ensemble time averages are created by refinement of mean pressure coefficients to only accepting instantaneous values of C_p within the range $\theta = 30^\circ \pm 2^\circ$, thus creating an ensemble time average coefficient of pressure $\overline{C_{P_{ij}}}$ with respect to an ensemble mean yaw angle $28^\circ < \bar{\theta}_{\text{ENS}} < 32^\circ$ at positions s_N (Cooper, 1993; Dorigatti, 2013).

Figures 8.14-8.16 give examples of the typical pressure coefficient evolution as the train travels through the crosswind test section. Loop 2 was chosen for this comparison as the largest degree of variation in pressure coefficient is observed for taps on this loop. A series of 15 individual pressure coefficient time histories are plotted with the corresponding deconstructed ensemble average. The areas highlighted in green are those in which the ensemble mean yaw angle $28^\circ < \bar{\theta}_{\text{ENS}} < 32^\circ$. Variations in pressure coefficient at both ends of time histories are created by the vehicle transition when entering and exiting the crosswind test section. Dorigatti (2013) concluded that data from the transitional zones offers the possibility to investigate transient aerodynamic phenomena, such as gust analysis; however, such effects are not considered in this study.

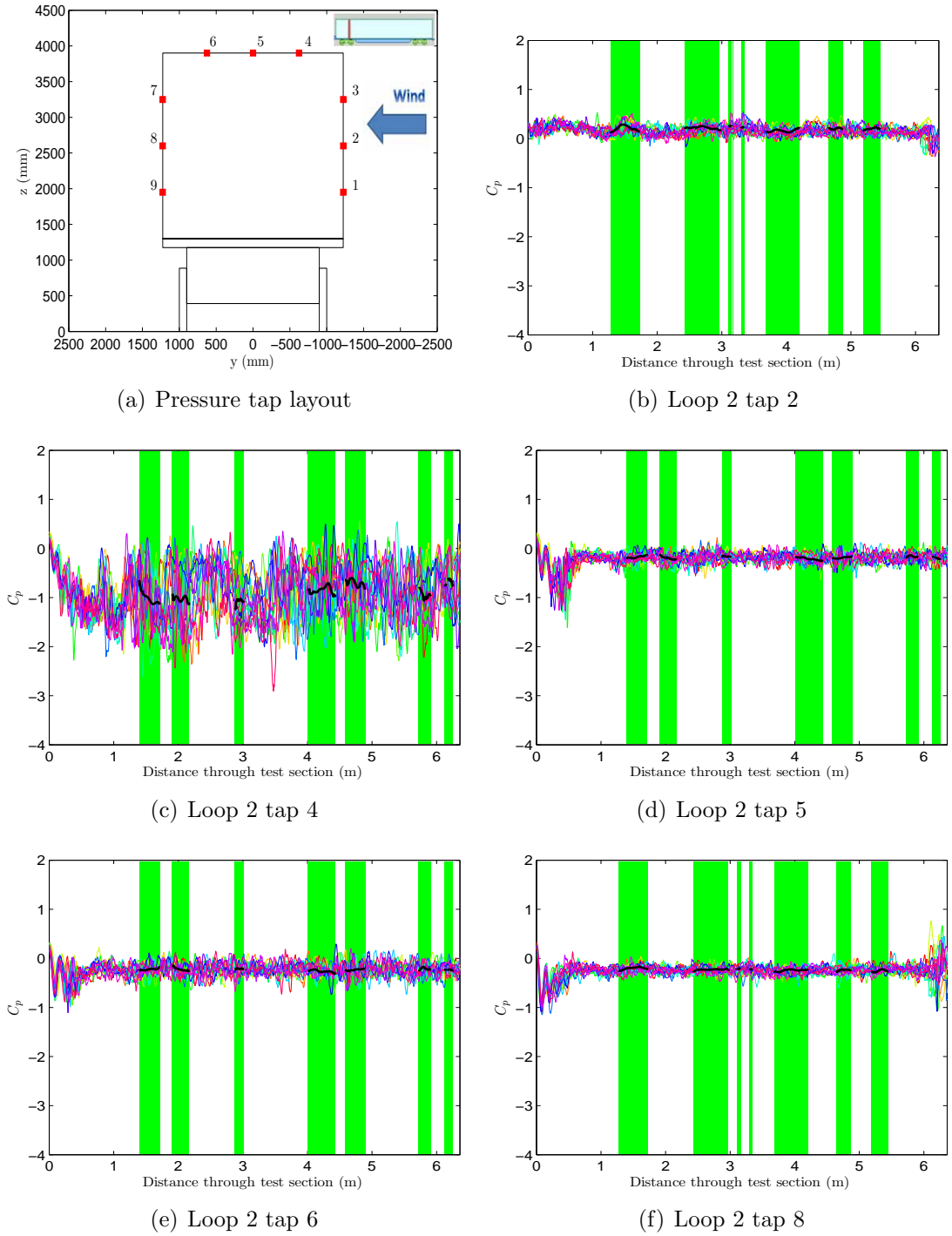


Figure 8.14: Examples of the typical evolution of pressure coefficient as the train travels within the crosswind generator. A series of 15 individual runs are plotted with corresponding deconstructed ensemble average time series for consist 1 loop 2. Areas highlighted green are where the ensemble mean yaw angle $28^\circ < \bar{\theta}_{\text{ENS}} < 32^\circ$.

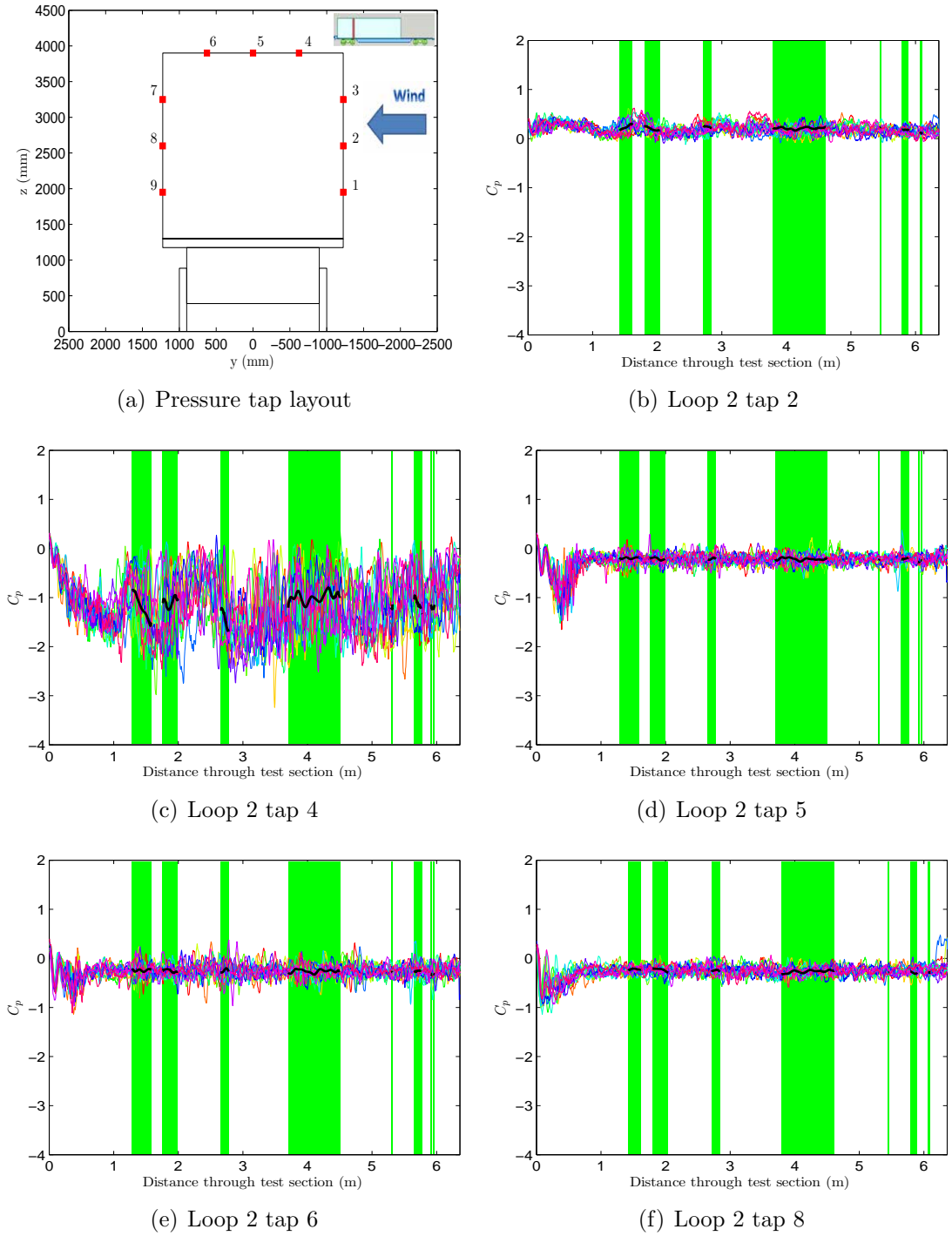


Figure 8.15: Examples of the typical evolution of pressure coefficient as the train travels within the crosswind generator. A series of 15 individual runs are plotted with corresponding deconstructed ensemble average time series for consist 4 loop 2. Areas highlighted green are where the ensemble mean yaw angle $28^\circ < \bar{\theta}_{\text{ENS}} < 32^\circ$.

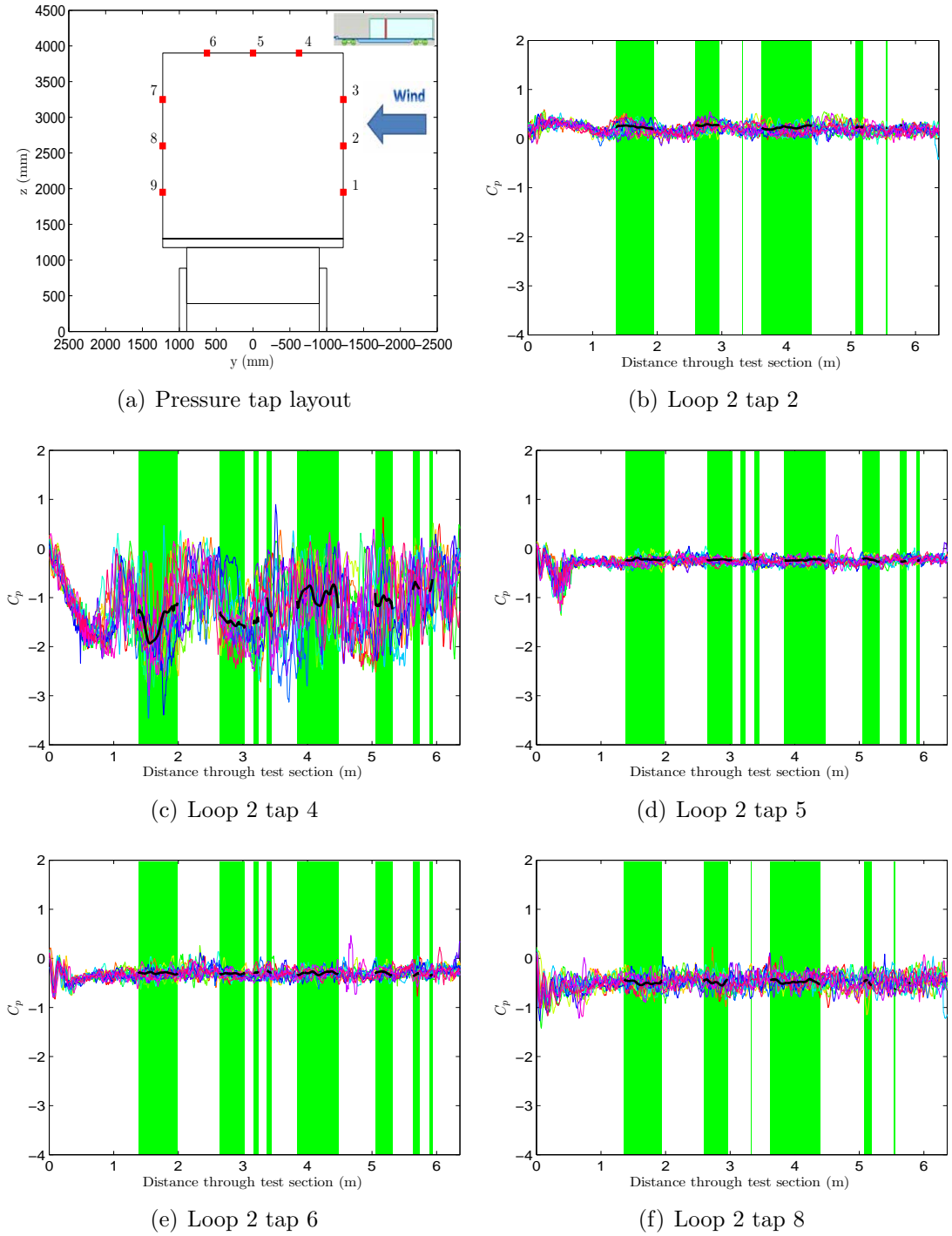


Figure 8.16: Examples of the typical evolution of pressure coefficient as the train travels within the crosswind generator. A series of 15 individual runs are plotted with corresponding deconstructed ensemble average time series for consist 6 loop 2. Areas highlighted green are where the ensemble mean yaw angle $28^\circ < \bar{\theta}_{\text{ENS}} < 32^\circ$.

Figures 8.14-8.16 are representative of all pressure taps monitored on the measuring container for all consists tested. In general, good consistency is observed for the pressure coefficient evolution within the central bounds of the crosswind test section (20% to 90% of crosswind generator length); and even for results outside the ensemble mean yaw angle $28^\circ < \bar{\theta}_{\text{ENS}} < 32^\circ$ bounds. For each individual run there are a series of random high frequency fluctuations, of similar amplitude, about the ensemble time series. These fluctuations are created by the turbulent nature of the flow developing around the train when subjected to the crosswind (Dorigatti, 2013). Larger fluctuation amplitudes observed in the individual time histories occur in combination with areas of the lowest values in pressure coefficient, figures 8.14(c), 8.15(c) and 8.16(c). Dorigatti (2013) concluded these areas are dominated by the presence of suction associated with vortices attached to the train surface, or of regions of recirculation characterised by an increased level of turbulence. In the freight data presented, these areas are located close to the measuring container edges, expected to be the source of large flow separations.

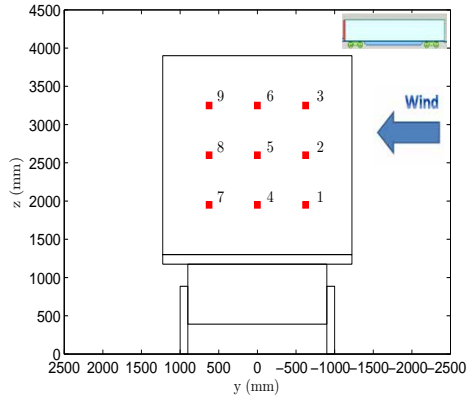
In figure 8.16(c) oscillations with a longer period, to the order of ~ 0.2 of the crosswind generator length, are observed in areas associated with suction peaks occurring. Dorigatti (2013) concluded these peaks were associated with spanwise inhomogeneity in the mean onset crosswind, creating variations in the resultant crosswind magnitude and yaw angle. As discussed, areas of low pressure associated with suction exhibit the largest fluctuations in pressure coefficient, which are enhanced by issues with spanwise inhomogeneity. The modified processing method, developed by Dorigatti (2013) and adopted in this study, negates much of the influence from spanwise inhomogeneity on the deconstructed ensemble coefficient of pressure time history (chapter 7).

The mean pressure coefficients for all consists are presented in tables 8.5-8.7, as calculated by equation 8.2. In figures 8.17-8.25 the mean pressure coefficient distribution for each measuring loop are presented as a series of container cross sections for all consists. In each plot the wagon cross section illustrates pressure tap positions on the container surface and the crosswind direction. Bounds to the associated uncertainty

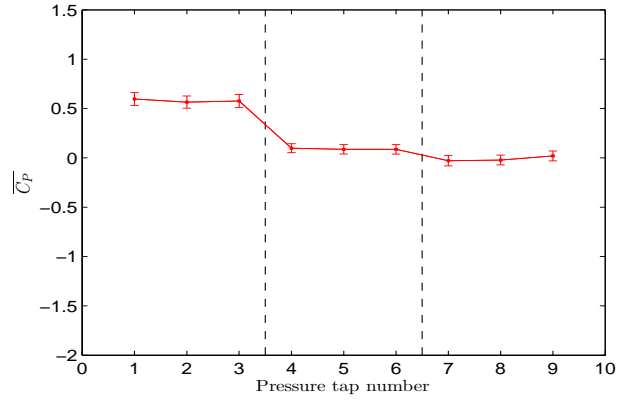
for each pressure transducer are also plotted in accordance to which pressure tap the transducer was connected. The mean pressure coefficients for loop 8 of each consist are presented as a cross section at the container mid height.

Consist 1														
Tap	Loop													
	1		2		3		4		5		6		7	
	Mean	Std	Mean	Std	Mean	Std	Mean	Std	Mean	Std	Mean	Std	Mean	Std
1	0.598	0.137	0.155	0.039	0.157	0.033	0.149	0.036	0.188	0.039	0.180	0.022	-0.440	0.053
2	0.565	0.117	0.195	0.048	0.194	0.041	0.184	0.048	0.211	0.044	0.203	0.032	-0.437	0.050
3	0.576	0.132	0.153	0.054	0.153	0.047	0.142	0.055	0.179	0.048	0.154	0.039	-0.290	0.070
4	0.098	0.059	-0.946	0.200	-0.787	0.116	-0.722	0.088	-0.511	0.065	-0.371	0.048	-0.248	0.057
5	0.087	0.059	-0.201	0.034	-0.393	0.120	-0.751	0.102	-0.654	0.085	-0.411	0.054	-0.295	0.048
6	0.086	0.071	-0.244	0.045	-0.117	0.042	-0.430	0.133	-0.549	0.105	-0.451	0.056	-0.160	0.066
7	-0.038	0.058	-0.262	0.060	-0.170	0.035	-0.155	0.035	-0.172	0.059	-0.167	0.043	-0.174	0.046
8	-0.031	0.047	-0.236	0.036	-0.161	0.032	-0.139	0.027	-0.162	0.046	-0.151	0.033	-0.191	0.049
9	0.010	0.075	-0.260	0.040	-0.180	0.032	-0.157	0.029	-0.161	0.047	-0.182	0.032	-0.158	0.055

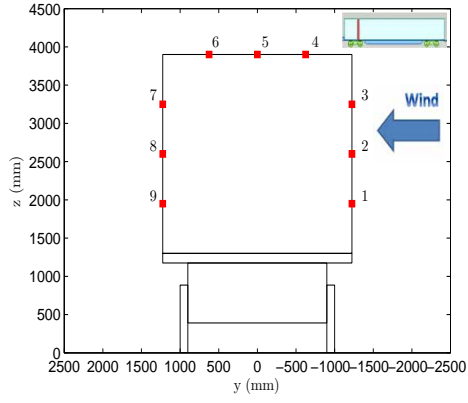
Table 8.5: Mean pressure coefficients and the standard deviation for consist 1 on all vertical loops for taps 1 to 9.



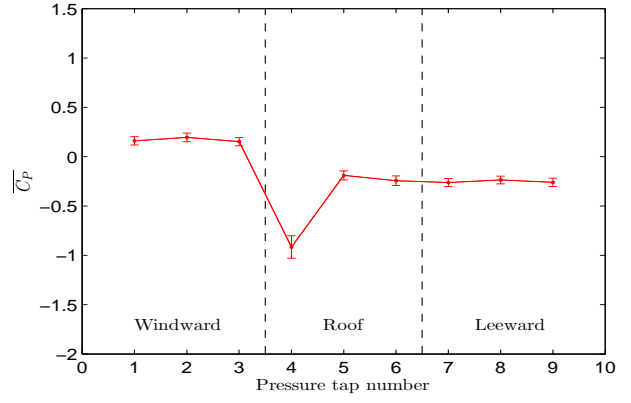
(a) Loop 1 pressure tap layout



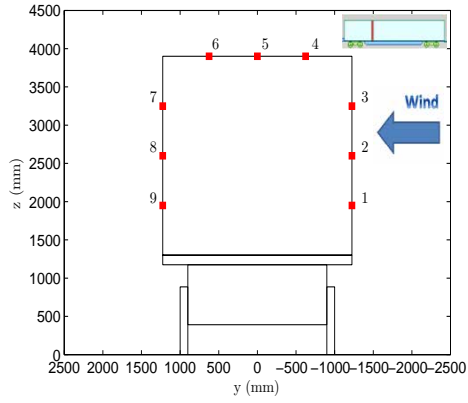
(b) Loop 1 coefficient of pressure



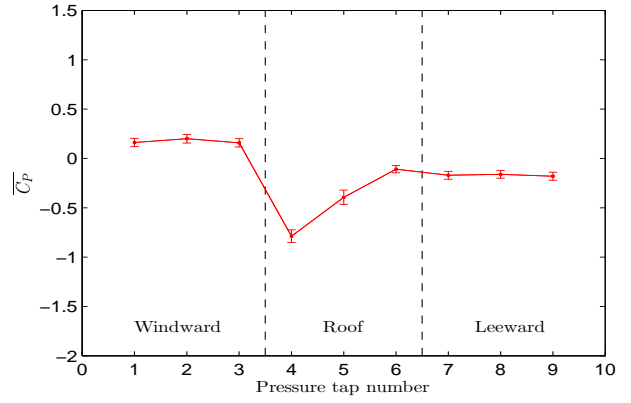
(c) Loop 2 pressure tap layout



(d) Loop 2 coefficient of pressure

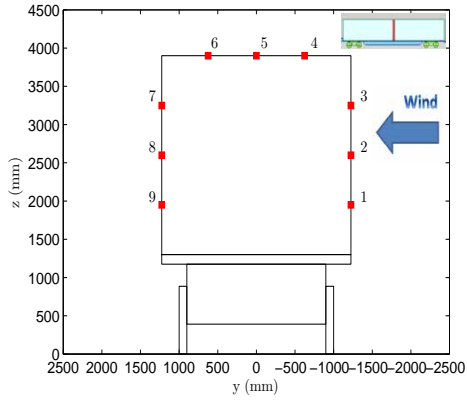


(e) Loop 3 pressure tap layout

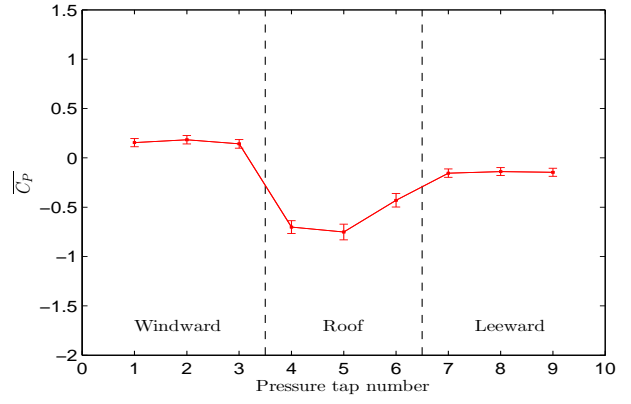


(f) Loop 3 coefficient of pressure

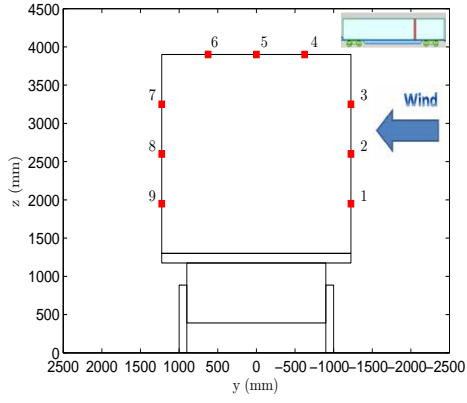
Figure 8.17: Mean surface pressure coefficient distribution with associated uncertainty error bounds for consist 1 loops 1, 2 and 3. For each loop a diagram of pressure tapping positions is provided.



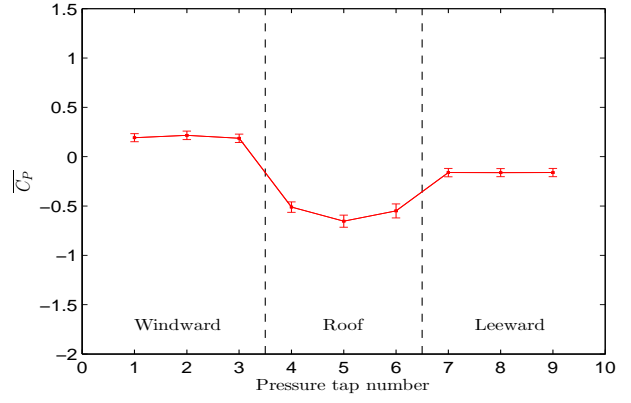
(a) Loop 4 pressure tap layout



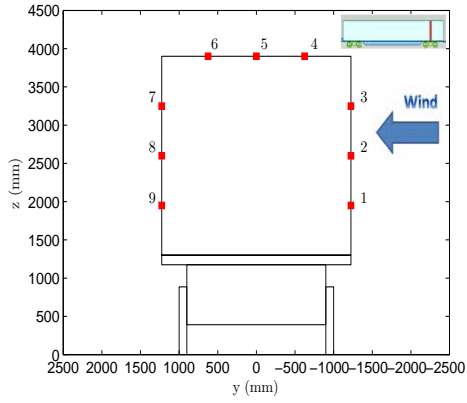
(b) Loop 4 coefficient of pressure



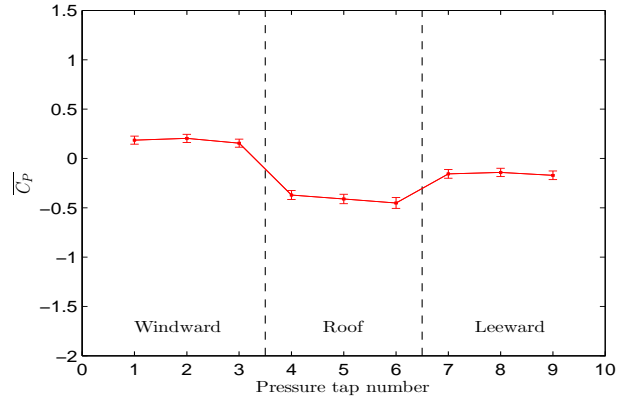
(c) Loop 5 pressure tap layout



(d) Loop 5 coefficient of pressure

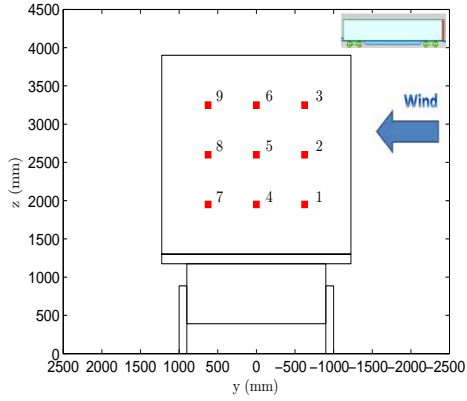


(e) Loop 6 pressure tap layout

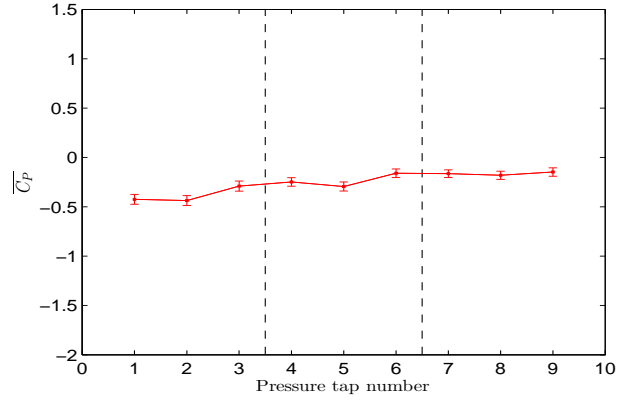


(f) Loop 6 coefficient of pressure

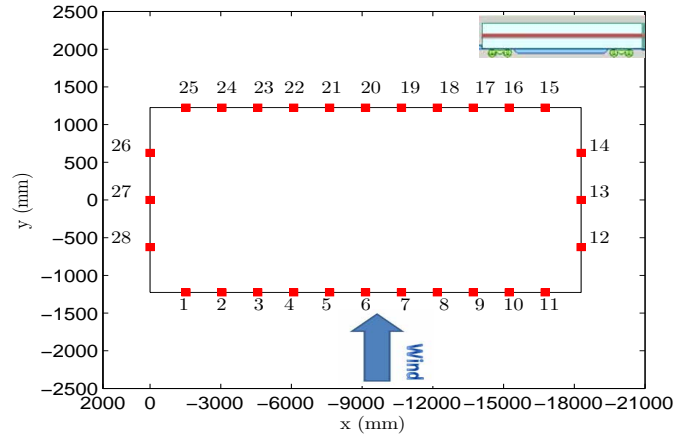
Figure 8.18: Mean surface pressure coefficient distribution with associated uncertainty error bounds for consist 1 loops 4, 5 and 6. For each loop a diagram of pressure tapping positions is provided.



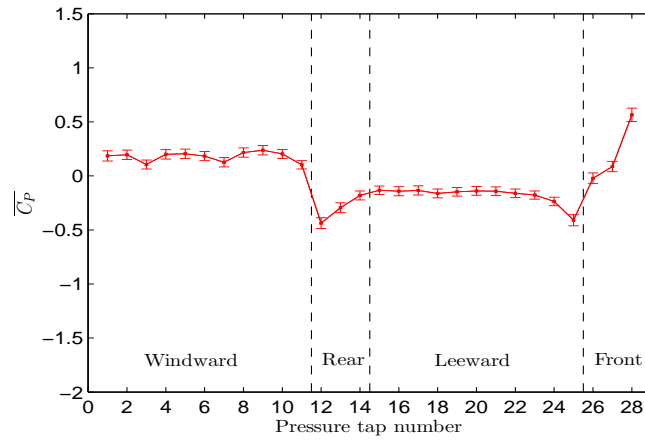
(a) Loop 7 pressure tap layout



(b) Loop 7 coefficient of pressure



(c) Loop 8 pressure tap layout



(d) Loop 8 coefficient of pressure

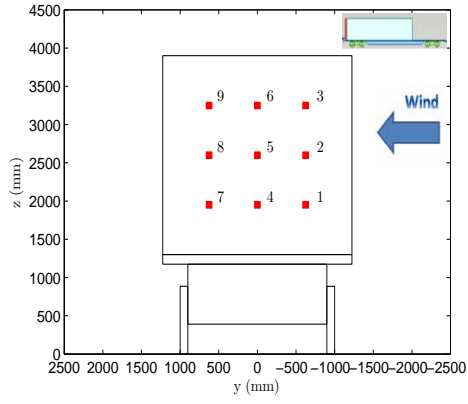
Figure 8.19: Mean surface pressure coefficient distribution with associated uncertainty error bounds for consist 1 loops 7 and 8. For each loop a diagram of pressure tapping positions is provided.

Tap	Consist 4									
	Loop									
	1		2		3		4		5	
	Mean	Std	Mean	Std	Mean	Std	Mean	Std	Mean	Std
1	0.620	0.127	0.165	0.042	0.148	0.040	0.112	0.042	-0.281	0.046
2	0.581	0.119	0.200	0.049	0.193	0.046	0.147	0.049	-0.280	0.046
3	0.564	0.138	0.128	0.054	0.139	0.050	0.112	0.050	-0.282	0.048
4	0.110	0.067	-1.200	0.305	-0.891	0.159	-0.617	0.094	-0.284	0.044
5	0.075	0.078	-0.235	0.045	-0.650	0.204	-0.794	0.130	-0.293	0.043
6	0.003	0.097	-0.273	0.067	-0.128	0.040	-0.399	0.138	-0.292	0.043
7	-0.021	0.097	-0.274	0.051	-0.165	0.040	-0.147	0.038	-0.309	0.045
8	-0.047	0.092	-0.262	0.043	-0.177	0.037	-0.144	0.030	-0.304	0.041
9	-0.112	0.124	-0.265	0.043	-0.206	0.038	-0.165	0.030	-0.326	0.044

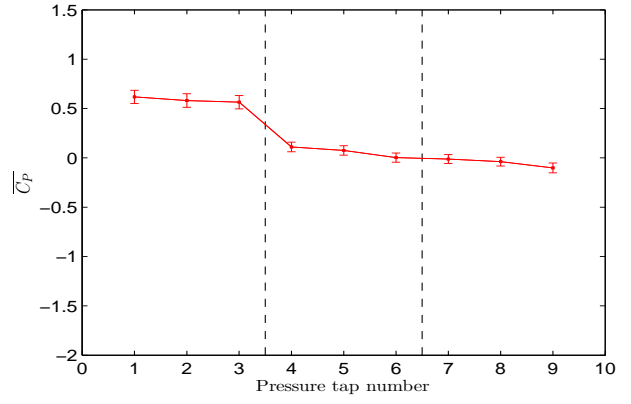
Table 8.6: Mean pressure coefficients and the standard deviation for consist 4 on all vertical loops for taps 1 to 9.

Tap	Consist 6									
	Loop									
	1		2		3		4		5	
	Mean	Std	Mean	Std	Mean	Std	Mean	Std	Mean	Std
1	0.940	0.120	0.215	0.039	0.236	0.045	0.198	0.035	-0.559	0.071
2	0.978	0.132	0.235	0.046	0.233	0.047	0.205	0.043	-0.537	0.057
3	0.898	0.126	0.137	0.045	0.167	0.048	0.109	0.039	-0.466	0.069
4	0.804	0.121	-1.201	0.364	-1.054	0.139	-0.703	0.104	-0.308	0.060
5	0.837	0.128	-0.243	0.027	-0.535	0.195	-0.833	0.107	-0.425	0.086
6	0.737	0.120	-0.299	0.035	-0.146	0.033	-0.387	0.163	-0.310	0.099
7	0.577	0.116	-0.527	0.106	-0.282	0.065	-0.200	0.049	-0.290	0.075
8	0.634	0.119	-0.500	0.070	-0.251	0.050	-0.200	0.032	-0.297	0.083
9	0.583	0.112	-0.586	0.072	-0.334	0.053	-0.241	0.035	-0.242	0.084

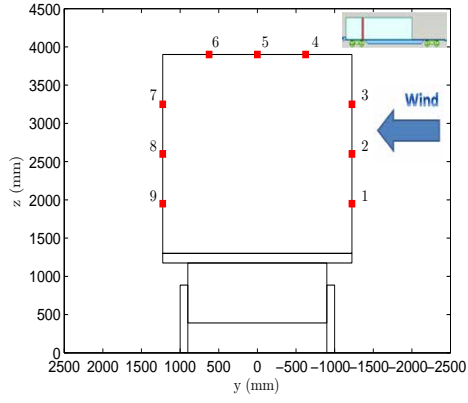
Table 8.7: Mean pressure coefficients and the standard deviation for consist 6 on all vertical loops for taps 1 to 9.



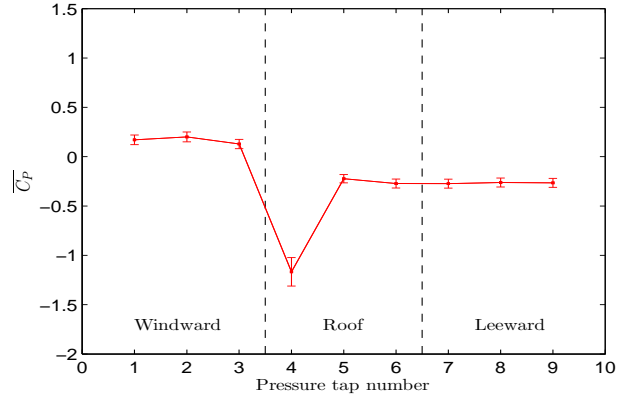
(a) Loop 1 pressure tap layout



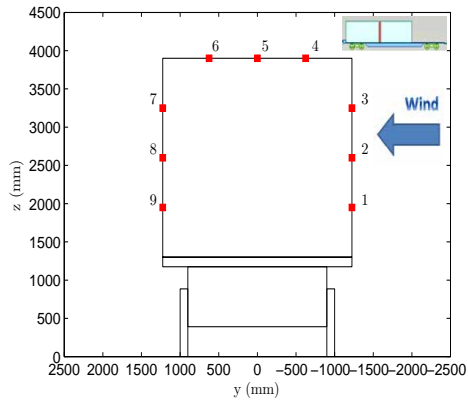
(b) Loop 1 coefficient of pressure



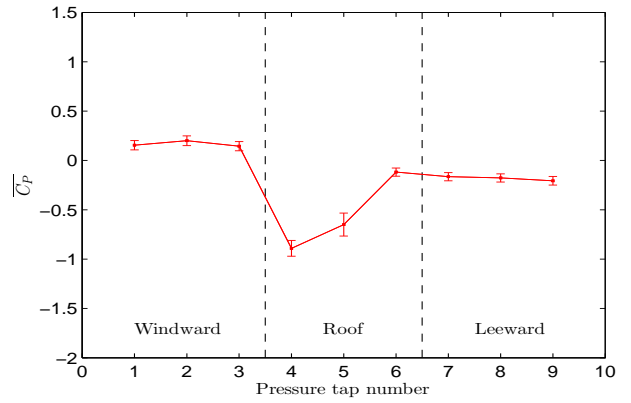
(c) Loop 2 pressure tap layout



(d) Loop 2 coefficient of pressure



(e) Loop 3 pressure tap layout



(f) Loop 3 coefficient of pressure

Figure 8.20: Mean surface pressure coefficient distribution with associated uncertainty error bounds for consist 4 loops 1, 2 and 3. For each loop a diagram of pressure tapping positions is provided.

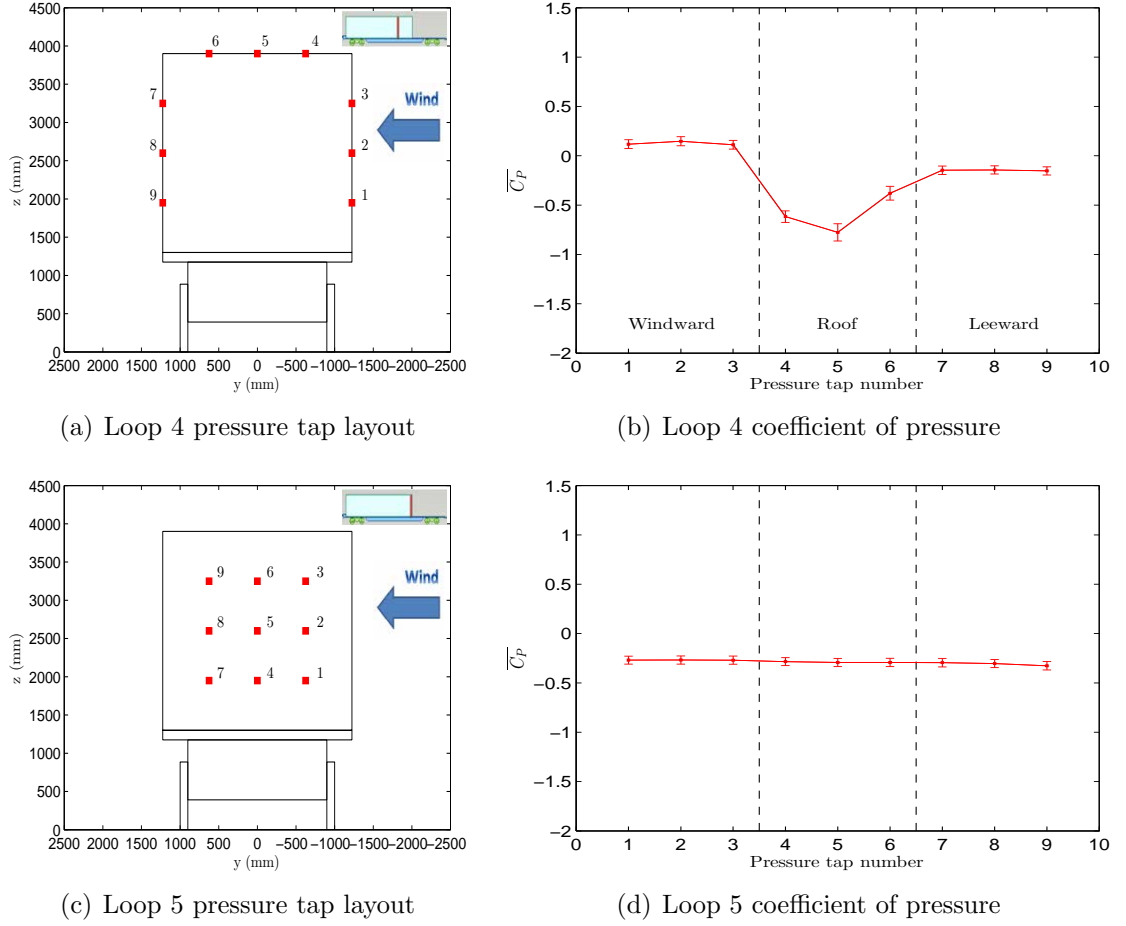
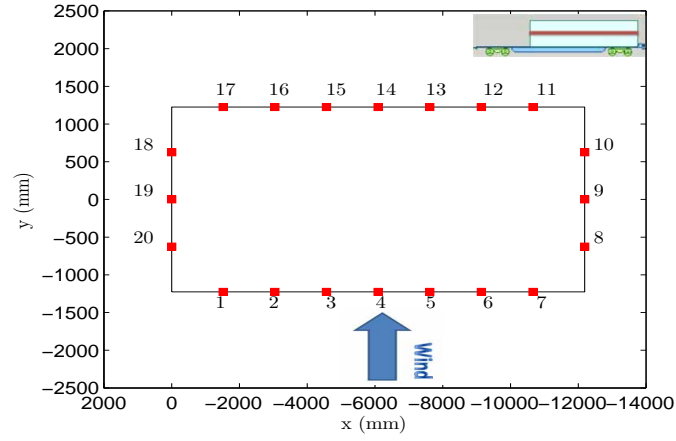
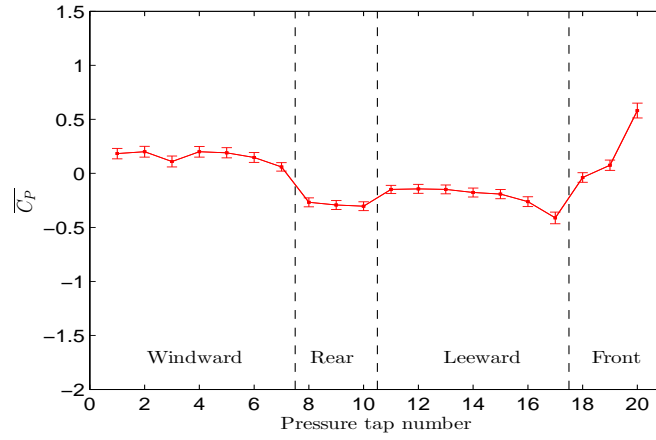


Figure 8.21: Mean surface pressure coefficient distribution with associated uncertainty error bounds for consist 4 loops 4 and 5. For each loop a diagram of pressure tapping positions is provided.

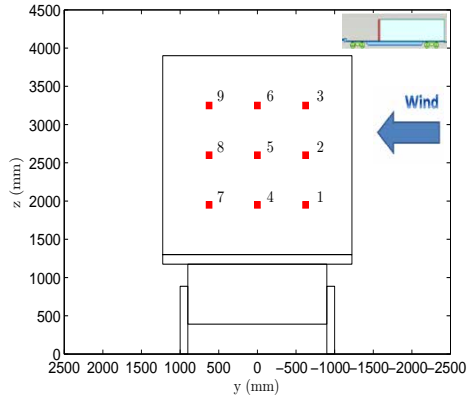


(a) Loop 8 pressure tap layout

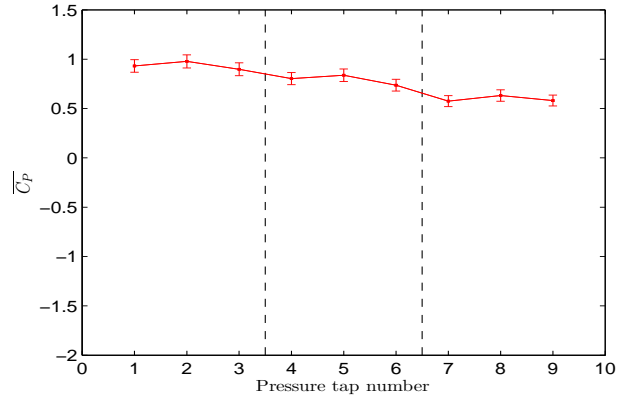


(b) Loop 8 coefficient of pressure

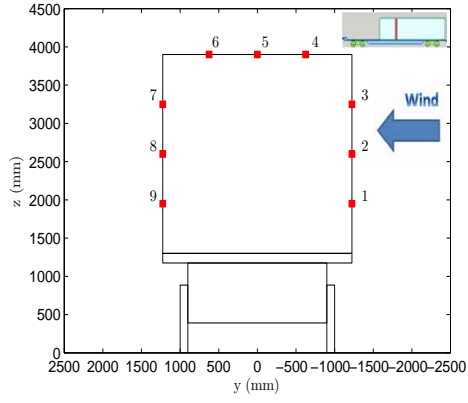
Figure 8.22: Mean surface pressure coefficient distribution with associated uncertainty error bounds for consist 4 loop 8. For each loop a diagram of pressure tapping positions is provided.



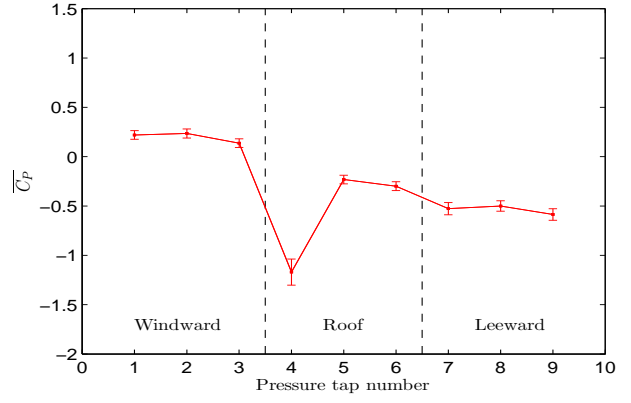
(a) Loop 1 pressure tap layout



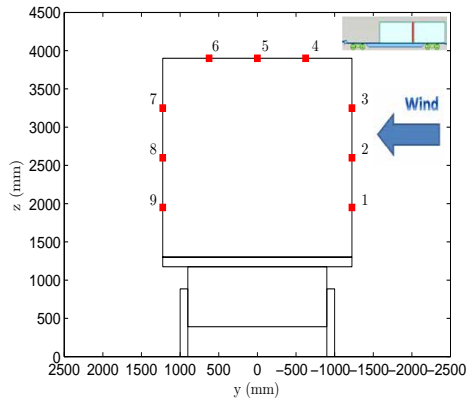
(b) Loop 1 coefficient of pressure



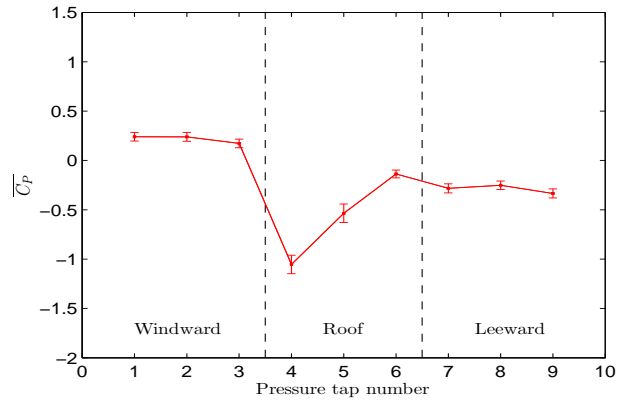
(c) Loop 2 pressure tap layout



(d) Loop 2 coefficient of pressure



(e) Loop 3 pressure tap layout



(f) Loop 3 coefficient of pressure

Figure 8.23: Mean surface pressure coefficient distribution with associated uncertainty error bounds for consist 6 loops 1, 2 and 3. For each loop a diagram of pressure tapping positions is provided.

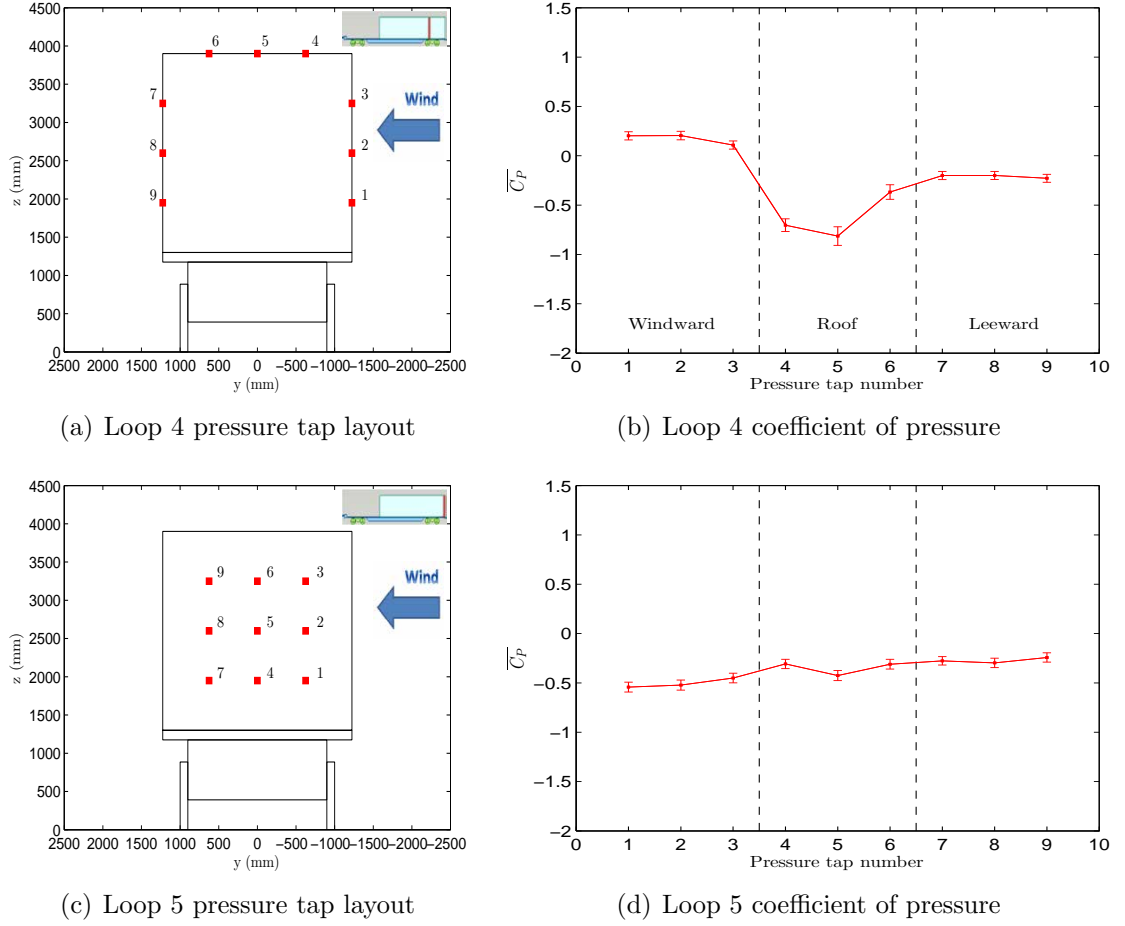
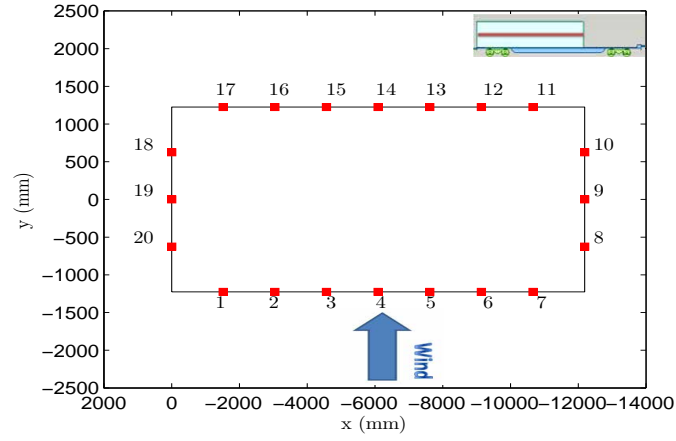
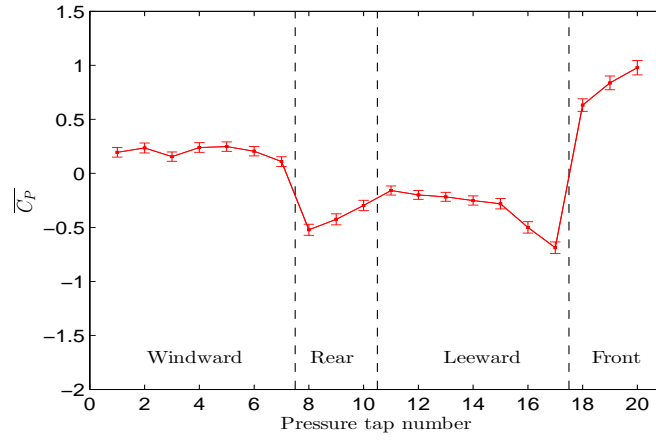


Figure 8.24: Mean surface pressure coefficient distribution with associated uncertainty error bounds for consist 6 loops 4 and 5. For each loop a diagram of pressure tapping positions is provided.



(a) Loop 8 pressure tap layout



(b) Loop 8 coefficient of pressure

Figure 8.25: Mean surface pressure coefficient distribution with associated uncertainty error bounds for consist 6 loops 8. For each loop a diagram of pressure tapping positions is provided.

8.3.2 Analysis of surface pressure distribution

The mean pressure coefficient distribution and associated error bounds for each container loading configuration are plotted in figures 8.17-8.25. The reference system introduced in chapter 6 is indicated in the wagon cross section plot as the wind direction; the flatbed wagon and container full scale dimensions are also given. Values of positive coefficient of pressure indicate areas of stagnation, whereas, values of negative pressure coefficient are representative of areas of suction. In general, results exhibit similar magnitudes to previous passenger studies (Baker and Sterling, 2009; Dorigatti, 2013); however, areas associated with large flow separation exhibit greater magnitudes of pressure coefficient than previously observed in passenger studies.

A series of flow patterns can be identified developing along the container length. Variations in these flow patterns are observed for the different consists examined, exhibiting a dependence on container loading configuration. These flow patterns are discussed in relation to the different container faces in sections 8.3.2.1-8.3.2.5.

8.3.2.1 Lead face

The flow pattern observed on the container lead face is highly dependent on container loading configuration. The large space between the container loaded on the second wagon and the measuring container on the third wagon in consist 6 creates a region of stagnation with positive pressure on the lead face. For consist 6 the largest magnitudes of pressure coefficient are exhibited for pressure taps closest to the windward edge. Toward the leeward edge on the lead face, the magnitude of pressure coefficients for consist 6 exhibits slightly larger values than measured in open air, without the crosswind influence (section 8.2.2.1). This suggests, although there is a large space in front of the measuring container, the influence of another container loaded onto the second wagon has a shielding effect on the container behind for a yaw angle of 30° .

The space between the container loaded onto the second wagon and the measuring

container for consists 1 and 4 is much smaller than for consist 6. However, similarly to consist 6, the largest magnitudes pressure coefficient are measured for pressure taps closest to the windward edge. In the centre of the lead face the pressure coefficient magnitude is close to zero, and towards the leeward edge small magnitudes of negative pressure coefficient are observed. The container loaded onto the second wagon creates a shielding effect on the measuring container, similar to the effect observed for consist 6. However, as the space between these containers is much smaller for consists 1 and 4 the shielding effect is increased. The negative pressure coefficient measured towards the leeward edge suggests a suction of flow from the gap between loaded containers. As the freight train moves through the crosswind, flow is directed through the gap between loaded containers. A positive pressure is measured for pressure taps closest to the windward edge, associated with the impinging crosswind, creating an area of stagnation. Flow out from the space between containers creates a suction effect, as measured at the leeward edge. Results measured at the rear face also suggest a movement of flow through the space between containers, dependent on loading configuration (section 8.3.2.5).

8.3.2.2 Windward face

The flow pattern on the windward face for all consists exhibits a relatively uniform area of stagnation with positive pressure. Small variations in pressure coefficient across the windward face lie within the associated error bounds for each tapping point. In chapter 5 the influence of container loading efficiency on boundary layer development highlighted pulse peaks in boundary layer velocities created by large spaces before a loaded container. The influence of container spacing is observed for windward face pressure coefficients. For consist 6 the influence of a large space, in comparison to consists 1 and 4, before the measuring container creates a pulse peak increase to the boundary layer velocity around the measuring container. Higher slipstream velocities within the boundary layer combine with the onset wind velocity to create a larger rela-

tive crosswind magnitude resulting in a larger pressure coefficient magnitude measured for consist 6 in comparison to consists 1 and 4. Consist 1 and 4 exhibit similar uniform pressure magnitudes and distribution across the windward face.

8.3.2.3 Roof

The flow pattern across the roof, for all consists, is characteristic of a roll vortex spreading across the roof, emanating from the windward corner of the lead face (Castro and Robins, 1977; Hemida and Baker, 2010). The roll vortex is characterised by a large negative peak at the pressure tap closest to the windward edge for loop 2 and uniform magnitudes for other pressure taps on loop 2. This peak is observed for all consists in figures 8.14(c)-8.16(c). The negative peak in pressure varies in intensity and position across the roof face, spreading towards the leeward edge as distance along the container from the lead face is increased. The flow separation creates unsteadiness in the pressure coefficient time history, observed in figures 8.14(c)-8.16(c). The lateral spread of the roll vortex creates increased standard deviation values across the container roof, emanating from the windward corner, as shown in tables 8.5-8.7. For consists 4 and 6 the flow pattern is visible for loop 4, closest to the container rear, however for consist 1 relatively uniform pressure magnitudes and distribution are observed for loop 6 (closest to the container rear). This suggests detachment of the roll vortex from the container roof towards the rear of the measuring container for consist 1. For all consists the magnitude of the suction peak on the roof represents the lowest values of pressure coefficient on the container surface.

The influence of container loading efficiency is also exhibited in the flow pattern across the roof. Pressure coefficient magnitudes across the roof for consist 6 are much larger than for consists 1 and 4. As discussed, the shielding effect of a container mounted close to the measuring container in consists 1 and 4 decreases the magnitude of key flow features created while travelling through a crosswind. The space before the measuring container in consist 6 negates any shielding effect for the windward corner at the lead

face, from which the roll vortex forms. The loading configuration creates increased slipstream velocities within the boundary layer, leading to a larger relative crosswind magnitude, which coupled with the unshielded windward corner leads to a roll vortex with a greater negative magnitude than for consists 1 and 4.

8.3.2.4 Leeward face

The flow pattern on the leeward face for all consists exhibits an area of suction with negative pressure. The pressure coefficients for consists 1 and 4 remain relatively uniform across the whole leeward face, except near the leeward lead face edge. This suggests complete detachment of vortices formed at the leeward lead face edge within a short distance of the edge (Dorigatti, 2013). For consist 4 a small pressure gradient from the lead to rear face is observed for loop 8 around the container centre. The pressure gradient is much smaller for consist 1, suggesting an influence from the container loading configuration on boundary layer development, influencing the suction region on the leeward face. A larger pressure gradient is also observed for consist 4 in comparison to consist 1 for measurements made for the train moving through the open air (section 8.2.2).

Consist 6 exhibits the largest variation in pressure coefficient on the leeward face. Following the leeward lead face edge there is a large suction peak covering pressure taps 16 and 17 on loop 8, extending vertically for all leeward taps on loop 2. The suction peak is associated with a vortex emanating from the leeward edge of the lead face. Pressure magnitudes measured for loops 3 and 4 suggest a steep pressure gradient toward the container rear. This gradient suggests complete detachment of leeward vortices by the container rear, with pressure coefficient magnitudes measured on loop 4 similar to leeward pressures measured for consists 1 and 4. The flow pattern observed is characteristic of a surface mounted cube under the influence of a crosswind and has been observed in freight crosswind studies previously (Hemida and Baker, 2010). Hemida and Baker (2010) found a series of large vortices, emanating from container

edges, become detached from the container surface and move downstream with the crosswind. The pressure gradients observed for the 30° yaw angle suggest vortices become detached and move away from the container surface, increasing in distance from the container surface as the distance from the container lead face is increased.

8.3.2.5 Rear face

Similarly to the lead face, the flow pattern observed on the container rear face is highly dependent on container loading configuration. The rear face is characterised by an area of suction, however, the distribution of negative pressure magnitudes is dependent on loading configuration and the space size following the measuring container.

The largest size space behind the measuring container occurs for consist 4. The pressure distribution on the rear face remains relatively uniform with similar magnitudes across the whole face. Conversely, for the smaller space between containers in consists 1 and 6 there is a large degree of variation in pressure distribution and magnitude across the rear face. At the windward edge there is a large negative peak towards the base of the rear face, decreasing in magnitude towards to container roof. Moving across the rear face the negative peak is seen to move up from the base pressure tap towards the middle pressure taps, with the pressure taps either side exhibiting a similar magnitude. It is hypothesised that flow is accelerated through the small gap between containers, with flow generally moving upwards in the gap. The impinging crosswind flow hits the lead face of the following container creating a positive pressure on the following container lead face and negative pressure on the measuring container rear face. Flow within the gap is drawn upwards and outwards by suction flow across the container roof and leeward face. This creates a negative pressure on both the lead and rear faces towards the leeward side within the small gap (section 8.3.2.1). For consist 4 the large space following the measuring container negates the suction influence seen within the small gap, and thus a uniform pressure distribution is observed.

The influence of container loading configuration is also observed between consists 1 and 6. For consist 6 the suction magnitudes at each pressure tap on the rear face are consistently 10% lower than for consist 1. It is hypothesised that the influence of increased boundary layer velocities, due to loading configuration for consist 6, increases the magnitude of suction within the small gap between containers. This creates an overall greater magnitude for the negative pressure distribution on the rear face of consist 6 in comparison to consist 1.

8.3.3 Overall aerodynamic load coefficients

The overall mean aerodynamic load coefficients are calculated as the discrete integral of forces acting on each pressure tap area, through applying equations 7.37-7.41. As discussed, the model surface area is divided into a number of smaller areas associated with each pressure tapping (figure 7.6). The forces on each pressure tap area were calculated using the mean ensemble pressure coefficients.

Figure 8.26 and table 8.8 show estimated values calculated for aerodynamic load coefficients on the measuring container for consists 1, 4 and 6. The values for roll moments are given in respect to either a reference system about the centre of the measuring container and a leeward base edge or a reference system about the centre of track and leeward rail. The reference systems ensure that negative values for moments C_{M_X} and $C_{M_{X,lee}}$ correspond to moments that overturn the vehicle (Dorigatti, 2013). Therefore, figure 8.26 includes a split vertical axis; a conventional axis is adopted for C_Y , C_Z and an inverted axis for C_{M_X} and $C_{M_{X,lee}}$.

The positive values for C_Y and C_Z indicate that that overall lateral and vertical forces are directed with the crosswind flow and upward respectively (Dorigatti, 2013). Similarly, negative values for moments C_{M_X} and $C_{M_{X,lee}}$ correspond to moments that overturn the vehicle. These results are characteristic of forces measured on a vehicle under the influence of a crosswind at a 30° yaw angle (Quinn et al., 2007; Baker and Sterling,

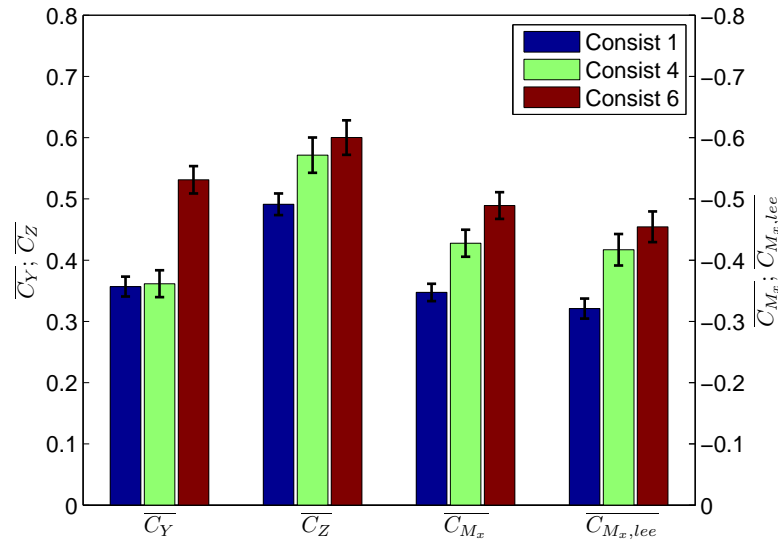


Figure 8.26: Estimated values for the aerodynamic load coefficients C_Y , C_Z , C_{M_X} and $C_{M_{X,lee}}$ in the crosswind test section. A conventional axis is adopted for C_Y , C_Z and an inverted axis for C_{M_X} and $C_{M_{X,lee}}$. The values for roll moments are given with respect a reference system about the centre of the measuring container and a leeward base edge. The associated uncertainty bounds for each coefficient are also plotted.

	Consist 1		Consist 4		Consist 6	
	Container reference	Track reference	Container reference	Track reference	Container reference	Track reference
C_Y	0.36	0.36	0.36	0.36	0.53	0.53
C_Z	0.49	0.49	0.57	0.57	0.60	0.60
C_{M_X}	-0.35	-0.52	-0.43	-0.64	-0.49	-0.73
$C_{M_{X,lee}}$	-0.32	-0.50	-0.42	-0.63	-0.45	-0.71

Table 8.8: Aerodynamic load coefficients for consists 1, 4 and 6 C_Y , C_Z , C_{M_X} and $C_{M_{X,lee}}$ with respect to a container and track reference system in the crosswind test section. The values for roll moments are given with respect to either a reference system about the centre of the measuring container and a leeward base edge or a reference system about the centre of track and leeward rail.

2009; RSSB, 2012; Dorigatti, 2013).

Figure 8.26 illustrates clear differences in force and roll moment coefficients as container loading configuration varies. In general, larger magnitudes are observed as container loading efficiency is reduced. Although consists 4 and 6 have the same loading efficiency, the variation in loading pattern creates differences in force coefficients. Consist 6 has a large space before the measuring container in comparison to consist 4, which is relatively shielded by a container on the wagon in front. Forces acting on the measuring container in consist 6 have a greater influence from slipstream velocities within the boundary layer around the train.

C_Y for consists 1 and 4 has similar magnitude. In section 8.3.2.4 the influence of gap size between loaded containers was discussed; results showed increased flow separation from the leeward lead face edge for consist 6 in comparison to consist 1 and 4. The container loaded on the wagon in front of has a shielding effect on the measuring container, reducing the magnitude of C_Y in relation to consist 6, for which container leading edges are more susceptible to large flow separations.

Values for C_Z exhibit the general pattern of a larger magnitude as the container loading efficiency is reduced and gap size between containers increased. As discussed in section 8.2.3, it should be noted that no pressure taps are placed in the container base. Due to the method of container attachment the flatbed wagon was modelled as a solid loading base, to assesses forces on the container, not the container and wagon. If a spine loading system was adopted for the flatbed wagon, pressure taps would be needed in the container base to measure the flow underneath the wagon. It is suggested that as no changes occur to the flatbed wagon between loading configurations, the pressure coefficients measured on the container base would be similar for all consists tested. Thus, it is not expected that the exclusion of pressure taps from the container base would influence the general pattern, in relation to aerodynamic load coefficients, between different container loading configurations tested. Dorigatti (2013) observed negative pressure across the underbody of the Class 390 model, for both stationary

and moving model experiments. If the average pressure coefficient value of -0.25, recorded in the underbody region of the Class 390, is considered for the freight model; calculating the value for C_Z from equation 7.39, using the reference system defined in figure 7.5, the value for C_Z decreases in respect to the case with no underbody pressure coefficients considered.

C_{M_X} and $C_{M_{X,lee}}$ again exhibit similar behaviour of increasing magnitude as the container loading efficiency is reduced. The moments in figure 8.26 are taken about the centre and leeward edge of the container base. Contrary to previous crosswind studies the moments are shifted from the conventional centre of track $x = 0$ and leeward rail, at height $z = 0$, to the centre and leeward edge of the container base, as aerodynamic load coefficients are calculated just for the container. A comparison of both reference systems for calculating the roll moments reveals that values for the track reference system are larger than values for measurements taken just about the container, as shown in table 8.8.

In light of the 2008 UK crosswind incidents, RSSB (2012) carried out a series of wind tunnel experiments using a FEA-B flatbed wagon, loaded with a 12.192m and 6.096m container, and a HYA coal hopper wagon. The results for the yaw angle of 0° were considered in section 8.2.3 in relation to the train moving through a non-crosswind situation. RSSB (2012) compared aerodynamic load coefficients measured for a wagon and container system and for just the container alone. RSSB (2012) found results measured for the container and wagon together gave lower values for $C_{M_{X,lee}}$ in comparison to values measured for the container alone, across the whole range of yaw angles tested. At a yaw angle of 30° , for the container alone, the estimated value for $C_{M_{X,lee}} \simeq 0.78$, shown in figure 8.27 (RSSB, 2012). The exact setup within RSSB (2012) is not replicated in this study, however, by using values for $C_{M_{X,lee}}$ for consists 1, 4 and 6 it is possible to draw some comparisons.

In equation 7.41 the value for $C_{M_{X,lee}}$ is normalised by the container length, therefore the influence of container length on $C_{M_{X,lee}}$ is negated. As discussed, the values for

$C_{M_{X,lee}}$ are dependent on container loading efficiency and position. Considering the loading configuration tested in RSSB (2012), there is a large space in front and behind the measuring container. Comparing this to consists 1, 4 and 6 the influence of a space in front and behind the measuring container increases the estimated value of $C_{M_{X,lee}}$, with the largest differences occurring for a space in front of the measuring container. Therefore, the values for consist 6 are considered to offer the closest comparison to the setup in RSSB (2012). For the container base measuring system at a yaw angle of 30° the estimated value of $C_{M_{X,lee}} = 0.45$, exhibiting limited agreement with RSSB (2012). However, if the influence of an additional space behind the measuring container was considered, the value for $C_{M_{X,lee}}$ would increase, bringing the value of $C_{M_{X,lee}}$ closer to the value measured in RSSB (2012); although, as discussed the space behind a container is shown to be less of an influence on $C_{M_{X,lee}}$ than the space in front of a container.

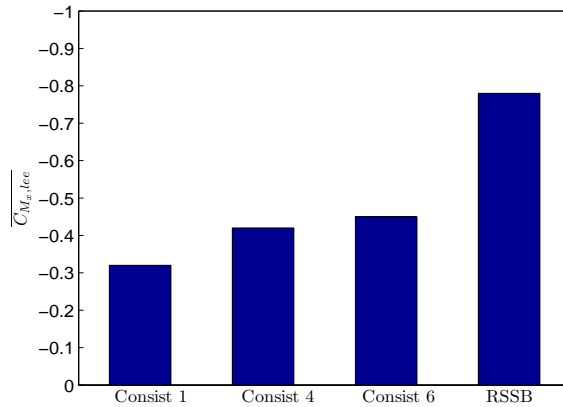


Figure 8.27: A comparison of $C_{M_{X,lee}}$ for consists 1, 4 and 6 with RSSB data measured for just the loaded container, not the container and wagon as a system (RSSB, 2012). Results are measured about the leeward container base edge reference system for a yaw angle of 30° .

8.4 Discussion

8.4.1 Reynolds number effect

In chapter 5 a comparison of slipstream development at different train speeds and with full scale data was undertaken to validate model scale results and analyse Reynolds number independence. Results showed good agreement for velocity and pressure magnitudes for both cases, indicating the validity of model scale experiments and Reynolds number independence for magnitudes. It was hypothesised that although key flow characteristics and the overall magnitude of velocities and pressures created are similar, smaller turbulent scales cannot be accurately modelled.

A similar analysis of Reynolds number independence is not possible for the aerodynamic load data sets collected. In light of analysis carried out in chapter 5 to compare the influence of container loading configuration on flow development, a similar approach was taken for the aerodynamic load experiments. Therefore, due to time constraints at the TRAIN rig it was not possible to conduct a Reynolds number independence study. Considering the Reynolds number equation; to alter the Reynolds number at the TRAIN rig only the resultant wind velocity could be changed, as the model size and air viscosity are fixed variables. To conduct a Reynolds number study either the onset wind velocity or train speed must be altered, through a range large enough to create a significant change in Reynolds number.

In the crosswind section the generator fan rotational speeds cannot be varied. By only altering the train speed there will be a difference to the resultant wind velocity but also the yaw angle. Therefore, it is not possible to conduct a suitable Reynolds number study for a moving model at the TRAIN rig. Dorigatti (2013) analysed the influence of Reynolds number by comparing moving model and static test cases for a yaw angle of 30° , with Reynolds numbers $Re=2 \times 10^5$ and $Re=1.2 \times 10^5$, respectively. By analysing critical Reynolds numbers Dorigatti (2013) concluded that no significant Reynolds

number effects were observed between the moving model and static experiments. However, the range of Reynolds numbers ($Re=1.2 \times 10^5 - 2 \times 10^5$) tested was relatively small in comparison to the Reynolds number of a full scale train ($Re \approx 5 \times 10^6$), raising questions over the validity of these tests. Quinn et al. (2007) carried out an aerodynamic load study on a bluff container section of a full scale lorry, mounted onto a series of force balances. By comparing roll moment results with the model scale container freight data, it is observed that at a yaw angle of 30° the container freight data lies within the bounds found for the bluff shaped lorry. The Reynolds number for the lorry is much larger than Reynolds number measured at the TRAIN rig. Therefore, although the vehicles in these studies are different it can be concluded that possible Reynolds number independence may be observed for aerodynamic load coefficients measured at model and full scale for a container freight train.

Conversely, a Reynolds number study for the open air aerodynamic load experiments is possible, as altering the model train speed would create a range of Reynolds numbers. However, as discussed in chapter 3, it was not possible to run the freight train at speeds of 30m/s due to model fragility, thus the range of Reynolds numbers for this test would be relatively small, again questioning the validity of the test.

8.4.2 Uncertainty analysis

Experimental uncertainties are introduced in chapter 7 and discussed at length in appendix B. The error bars for total uncertainties are plotted for each mean pressure coefficient and the aerodynamic load coefficients. The estimated total uncertainty is in general relatively constant for all container loading configurations. The total uncertainty for mean pressure coefficients is calculated as the sum of random uncertainties, calculated by measuring a normal distribution considering a confidence level of 95%, and bias limits, calculated through propagation of error theory of instrumentation accuracies. It is observed that the random uncertainty input is much less than the bias

limit, however, the random uncertainty increases as the container loading efficiency decreases. In general, the bias limits for all consists remain relatively constant for each test section. Bias limit values in the open air section are less than the crosswind section due to lack of additional uncertainty variables associated with the crosswind. Dorigatti (2013) observed that due to the method of calculating experiment uncertainties, the total uncertainty is not the actual error of results; rather a limit, with a high probability in which the actual error lies.

8.4.3 General concluding remarks

A series of conclusions can be drawn from the results and analysis presented in this chapter:

1. It is possible to measure the surface pressure on a freight container loaded onto a flatbed wagon using an on-board data logger and pressure monitoring system. The flow can be divided into a series of regions associated with each face of the measuring container. Results are compared with typical passenger train surface pressure coefficient magnitudes; similar values are observed for the freight container for a yaw angle of 30° . However, areas associated with large flow separation exhibit greater magnitudes than previously observed in passenger studies.
2. Good consistency is observed for the pressure coefficient evolution through the open air and crosswind test sections. High frequency fluctuations in pressure coefficient are created by the turbulent nature of the flow developing around the train.
3. Clear differences in surface pressure coefficients are observed for differing container loading configurations.
 - (a) The lead container face exhibits a region of stagnation, with magnitude dependent on container loading configuration. For all consists in the crosswind

section the largest magnitudes of pressure coefficient are measured closest to the windward edge, associated with the impinging crosswind. For consists 1 and 4 a pressure gradient across the lead face, from positive to negative pressure, suggests a suction of air from the gap between containers.

- (b) The rear face is characterised by an area of suction, however, the distribution of pressure is dependent on container loading configuration and the space size following the measuring container. For consist 4 the pressure distribution remains relatively uniform. Conversely, for consists 1 and 6 there is a large degree of variation in pressure distribution and magnitude across the rear face in both the open air and crosswind test sections. Flow is accelerated through the small gap between containers, with flow generally moving upwards. In the crosswind section, suction magnitudes for consist 6 are consistently 10% lower than for consist 1; hypothesised to be related to the influence of increased boundary layer velocities.
- (c) The flow across the roof in the crosswind test section, for all consists, is characteristic of a roll vortex spreading across the roof, emanating from the windward corner of the lead face. Results for consist 1 suggest detachment of the roll vortex from the container roof towards the rear of the measuring container. For all consists the magnitude of the suction peak on the roof represents the lowest values of pressure coefficient on the container surface. In the open air test section the flow is characterised by a region of suction, exhibiting lowest magnitude near the lead roof edge, associated with flow separation at the edge.
- (d) Flow at the container sides in the open air test section exhibits a region of weak suction for all consists tested. The flow created is symmetric and relatively uniform in distribution and magnitudes. In general pressure magnitudes are greater for consists 4 and 6 in comparison to consist 1, highlighting the influence of container loading efficiencies.

- (e) In the crosswind section the flow pattern on the windward face, for all consists, shows a relatively uniform area of stagnation. For consist 6 the influence of a large space, in comparison to consists 1 and 4, before the measuring container creates a flow separation at lead container edges, resulting in large pressure coefficient magnitudes.
 - (f) The flow pattern on the leeward face in the crosswind section, for all consists, exhibits an area of suction. Pressure coefficients for consists 1 and 4 remain relatively uniform across the whole leeward face, except near the leeward lead face edge, suggesting complete detachment of leeward vortices formed at the leeward lead face edge within a short distance of the edge. Consist 6 exhibits the largest variation in pressure coefficient, associated with detachment of vortices emanating from the leeward edge of the lead face. The pressure gradients observed for consist 6 suggest vortices become detached and move away from the container surface.
4. It is possible to calculate the overall mean aerodynamic load coefficients as a discrete integral of forces acting on each pressure tap area. Crosswind results are compared with typical passenger train aerodynamic load coefficients and shown to be characteristic of typical values measured for a yaw angle of 30° .
5. Clear differences in aerodynamic load coefficients are observed for differing container loading configurations in both the open air and crosswind test sections.
- (a) For open air results magnitudes of all aerodynamic load coefficients, for all consists tested, are small, exhibiting values close to zero. In general, larger magnitudes for aerodynamic load coefficients are observed as container loading efficiency is reduced.
 - (b) For crosswind results, larger magnitudes for aerodynamic load coefficients are observed as container loading efficiency is reduced and space size in front of the measuring container increased. For consists 1 and 4 the influence of a

container loaded closely on the wagon in front has a shielding effect on the measuring container. For consist 6 the measuring container is unshielded thus magnitudes for C_Y and C_Z are higher due to large flow separations.

- (c) Comparison of $C_{M_{X,lee}}$ with a previous container freight wind tunnel study found good agreement for the open air and crosswind results; however, the lack of boundary layer development in the wind tunnel study for the freight train was shown to give lower values than for the moving model employed in this study.

Chapter 9

Conclusions and recommendations for further work

9.1 Introduction

The main aim of this research was to characterise the aerodynamic flow around a container freight train and investigate how changing the container loading configuration affects the magnitude of aerodynamic forces measured on a container. In this section a series of conclusions are drawn in terms of the research aim and objectives stated in chapter 1. Each objective is presented in the following section with a discussion of the work carried out to meet the objective and the conclusions that can be drawn. Recommendations for further work on freight train aerodynamics are considered in section 9.3.

9.2 Conclusions

Objective 1: Carry out a thorough literature review on the aerodynamics of freight trains and bluff body vehicles to assess how the field of freight

train aerodynamics would most benefit from a focused model scale experimental study.

A thorough literature review is presented in chapter 2. The review draws together for the first time all relevant research for the understanding of freight train aerodynamics. In regards to this study the following conclusions were drawn from the literature review.

- It is clear that previous freight studies have tended to focus on drag reduction in relation to minimising fuel consumption. Freight slipstream research has been undertaken, but generally in small studies focused on defining new safety standards following an incident, or included in passenger train studies as a point of reference and comparison.
- The review indicated that a focused freight study was needed to characterise slipstream development for a common freight type, focused on a number of key loading configurations to create data sets, with a suitable ensemble size, to analyse the effects of loading configuration on flow development.
- A gap in the research was identified in understanding how freight trains fit within the TSI methodology. By constructing a suitable freight experimental study it was possible to carry out an analysis using the TSI standards to assess the suitability of the methodology in relation to freight slipstream development.
- The review highlighted that research in the field of measuring crosswind effects on freight trains is more active than research on freight slipstream development. However, as with slipstream research, crosswind research has predominantly focused on high speed passenger trains.
- Previous aerodynamic load studies have analysed the effect of crosswinds on a container and wagon as a complete system. The review indicated that following a series of incidents where containers were blown off freight trains that a focused study was needed to understand the influence of aerodynamic loads on a container loaded onto a freight train, rather than measuring the container and wagon as a

complete system.

Objective 2: Develop a moving model container freight train suitable for working at the TRAIN rig facility. The model should be able to have an interchangeable container loading configuration. A model container must be developed to include an on-board stand-alone pressure measuring system for measuring the surface pressure distribution on the container surface during moving model tests in both an open air and crosswind situation.

The TRAIN rig freight model development is described in chapter 3 and 6. A series of preliminary experiments to test the freight model are presented in appendix C.

- A 1/25th scale model freight train was designed and commissioned. Container freight was chosen for this study to reflect one of the largest sectors of freight transported in the UK and the relative ease for modelling purposes. The Class 66 locomotive was chosen for this study to reflect widespread use across the UK rail network and use in previous model scale experiments. The model was developed from an existing Class 66 model to include a long flat plate to simulate either four or eight FEA-B flatbed wagons. A series of interchangeable containers were commissioned to various scale ISO standard sizes, to enable a series of loading configurations to be tested. Essential geometric features of the Class 66 and FEA-B wagon were included on the model to enable a reliable comparison to full scale data.
- The model freight train was designed so that an on-board stand-alone pressure measuring system could be incorporated in a scale model container. The on-board system, developed as part of another PhD study (Dorigatti, 2013), was modified to be self-contained within a single container. The measuring container was designed to be detachable from the model, to allow a multitude of pressure tap and container loading configurations to be tested.

- A series of preliminary experiments, presented in appendix C, were carried out to analyse the suitability of the model in relation to the forces exerted on the model from the TRAIN rig firing procedure. Results found the model was capable of withstanding the firing procedure for train speeds of less than 25m/s, however the finer detailed components were susceptible to breaking and should be monitored on a regular basis.

Objective 3: Develop a test methodology for undertaking TRAIN rig moving model experiments to measure slipstream velocities and static pressure, as well as aerodynamic loads on a container surface in an open air and crosswind situation. The methodology should be designed to confirm to codes of practice where necessary.

The methodologies for carrying out slipstream and aerodynamic load experiments at the TRAIN rig with the freight model are introduced in chapter 3 and 6. As this study is the first freight model study conducted at the TRAIN rig facility, the experiment methods are adapted from well-established approaches, as well as more novel ideas to measure freight slipstreams and aerodynamic loads accurately, to enable a comparison to full scale data and provide data for CFD validation.

- A newly developed test procedure employed TFI Cobra probes (section 3.2.3.2.1) to measure three components of velocity and the static pressure of freight slipstreams. The probes were positioned and setup to enable essential flow structures and boundary layer development to be measured at a series of distances away from the model side and above the roof. Probes were also positioned at UK and European safety positions to meet TSI standards (3.2.3.1).
- A complex test procedure for the aerodynamic load experiments, developed from the methodology presented in Dorigatti (2013), was created for the freight train in the open air and crosswind test sections. The procedure enabled both the open air and crosswind measurements to be made during each individual experiment

run, presented in section 6.5. The test procedure and model design meant the surface pressure could be monitored by a self-contained on-board system, without the need for additional incorrectly modelled components.

- To meet the research aim of understanding aerodynamic flow development about a freight train, a series of container loading configurations were designed to simulate loading configurations observed in the full scale studies and represent loading efficiencies ranging from 100% to 0% (sections 3.2.2.4 and 6.3.1.3).
- For each experiment test case an appropriate train speed was selected in light of model stability and measuring instrumentation capability. To test the train speed in relation to the experiment methodologies a series of preliminary tests were carried out, presented in appendix C. For the slipstream experiments a train speed of 20m/s was chosen, whereas for the aerodynamic load experiments a train speed of 24m/s for the open air, and 20.8m/s for the crosswind section were chosen. For all cases the Reynolds number was below that of a full scale freight train, but sufficiently large enough to ensure flow structures created in the aerodynamic flow were representative of a full scale freight train.
- Trackside instrumentation and atmospheric monitoring systems were installed to be capable of measuring specific variables needed to calculate non-dimensional coefficients during the data analysis. The monitoring instruments provided information for an estimation of the uncertainty associated to the measured data.
- The newly developed TRAIN rig procedures enabled the maximum number of experiment runs performed in a day to be increased from 15 runs (Dorigatti, 2013) to on average 25 runs, with a maximum of 42 runs achieved in a day; without reducing the average data acceptance rate of at least 90%. Obviously due to the complexities of the aerodynamic load methodology, the number of runs completed in a day would be less than for the slipstream methodology.
- Previous studies have shown individual results to be highly variable, as flow is

dominated by large scale turbulent structures, thus the technique of ensemble averaging is required when studying train slipstreams (Sterling et al., 2008). A study of ensemble stability is presented in chapters 5 and 8, with a full analysis discussed in appendix D. Results show a series of 25 runs for slipstream experiments and 15 runs for aerodynamic load experiments to be suitable for obtaining statistically stable ensemble averages.

Objective 4: Undertake a series of moving model experiments in the open air to assess the influence of container loading configuration on slipstream development.

- Moving model experiments to measure freight slipstreams were carried out during May-June of 2012 and March 2013. The first round of experiments focused on the four wagon freight train, and following analysis, an additional set of experiments with the eight wagon train, formed the second round of slipstream experiments.
- Slipstream data was processed using well established techniques of ensemble analysis and normalisation. Novel adaptations to these techniques were made in relation to the Cobra probe drawbacks, presented in chapter 4 and 5.
- A series of Matlab scripts were designed and implemented to assist in data processing the slipstream measurements and provide suitable outputs for analysing the data (chapter 4). The Matlab scripts are made available as part of the complete freight data set and could be developed as a set of standardised scripts for the TRAIN rig facility.
- Part of the data processing methodology was to carry out an uncertainty analysis, presented in appendix B. The analysis calculated estimates for the bias limit of uncertainty for slipstream measurements as $\pm 2\%$, with a total uncertainty of $\pm 6\%$. Results exhibit similar uncertainty values to previous slipstream studies (Baker et al., 2012).

An in depth analysis of the slipstream velocities and static pressure is presented in chapter 5. The analysis initially focuses on the TRAIN rig model scale data, building an understanding of slipstream development for a container freight train, and assessing the characteristics of the aerodynamic flow. The key findings from this analysis are as follows.

- It is possible to present the slipstream results as a series of flow regions, as in previous passenger studies, albeit with differing flow development with these specific regions. Results were compared with typical passenger train magnitudes and large differences found in the nose and tail regions, hypothesised to be related to vehicle shape. Velocity and pressure magnitudes in the nose region are much larger than any values observed in train slipstream studies previously.
- Clear differences in slipstream development are observed for differing container loading configurations. For the coefficient of pressure a series of positive then negative peaks are observed about the Class 66 nose and container lead faces.
- Velocities within the boundary layer were shown to increase as the container loading efficiencies were decreased, with a series of pulse peaks relating to the change in pressure at the lead face of loaded containers.
- As discussed, two series of slipstream experiments using a four and eight wagon train were conducted. A key finding from the results was that for loading efficiencies of more than 50%, boundary layer growth stabilises rapidly within the first four wagon lengths. However, for loading efficiencies of less than 50%, continual boundary layer growth is observed until after five wagon lengths when boundary layer stabilisation occurs.
- Velocities in the lateral and vertical directions have magnitudes much larger than previously observed in passenger studies; increasing the overall magnitude by $\sim 10\%$. Flow directions at the Class 66 nose and container lead faces suggest the type of possible flow structures formed within the slipstream.

- A series of in depth analyses has been carried out in each of the flow regions identified. Analysis has highlighted differences created through decreased loading efficiencies, creating increased boundary layer growth, with a larger displacement thickness, and higher turbulence intensities. Autocorrelation analysis highlighted a possible vortex shedding emanating from the leading edge of the Class 66 nose above the roof. Integral time and length scales calculated through autocorrelation highlighted that limits of human instability, hypothesised by Sterling et al. (2008), are exceeded for the container freight train with a lower loading efficiency.

Objective 5: Collate together all previous full scale freight data sets. Carry out a comparison of model and full scale data to validate the TRAIN rig experiments and create a foundation of freight data to assess the suitability of TSI methodologies.

Full scale freight data sets were gathered together from previous freight studies (Sterling et al., 2008; Baker and Quinn, 2012). An in depth analysis of the slipstream velocities and static pressure is presented in chapter 5. A comparison of model and full scale data is carried out to analyse the influence of Reynolds number effects on flow development. Finally an analysis following the TSI methodology is presented to assess the suitability of the methodology in relation to freight trains. The key findings from this analysis are as follows.

- A comparison of model scale data at different train speeds and with full scale data was undertaken to validate TRAIN rig results and analyse Reynolds number independence. Results show good agreement for velocity and pressure magnitudes for both cases, indicating the validity of model scale experiments and Reynolds number independence for magnitudes. It is hypothesised that although key flow characteristics and the overall magnitude of velocities and pressures created are similar, smaller turbulent scales cannot be accurately modelled.
- An analysis of TSI and UK safety limits found results lie close to, but do not

break, existing limits; however proposed increases to train speeds would create slipstream velocities which do exceed TSI limits. The TSI methodology in relation to freight was questioned as to how differing freight types should be measured and whether large standard deviations created by including differing freight configurations are appropriate for this method of calculation. Velocity magnitudes recorded at UK safety positions are much larger than previously recorded values for passenger trains.

Objective 6: Undertake a series of moving model experiments in an open air and crosswind situation to measure the pressure distribution on a container surface to assess the influence of container loading configuration.

- Moving model experiments to measure the surface pressure distribution on a container were carried out during January-February 2013. A flow characterisation of the TRAIN rig crosswind generator was completed in December 2012, presented in chapter 6.
- Surface pressure data was processed using a methodology developed by Dorigatti (2013), adapted for this study. A series of Matlab scripts were designed to combine measurements taken in both the open air and crosswind test sections to assist in data processing the surface pressure measurements and provide suitable outputs for analysing the data (chapter 7). The Matlab scripts are made available as part of the complete freight data set and could be developed as a set of standardised scripts for the TRAIN rig facility.
- The uncertainty analysis, presented in appendix B, calculated estimates for the total uncertainty of aerodynamic load coefficients as $\pm 3\%$; however, results for the open air section were lower than for the crosswind section. Results exhibit similar uncertainty values to previous studies (Dorigatti, 2013).

An in depth analysis of the processed surface pressure data, following similar methodologies to previous aerodynamic load studies (Quinn et al., 2007; Dorigatti, 2013) is presented in chapter 8. The analysis initially focuses on the stability of individual surface pressure time histories, an analysis which is extended in appendix D. A discussion of the mean surface pressure coefficient distribution is undertaken for the open air and crosswind sections, identifying key flow characteristics and the influence of container loading configuration on flow development. Finally the values for aerodynamic load coefficients for the open air and crosswind sections are presented. A comparison with previous freight crosswind studies is carried out to analyse the suitability of using the TRAIN rig facility to measure the aerodynamic load on a container mounted onto a freight train. The key findings from this analysis are as follows.

- It is possible to measure the surface pressure on a freight container loaded into a flatbed wagon using an on-board data logger and pressure monitoring system. The flow can be divided into a series of regions associated with each face of the measuring container. Results were compared with typical passenger train surface pressure coefficient magnitudes and similar values observed for the freight container for a yaw angle of 30° .
- Clear differences in surface pressure coefficients are observed for differing container loading configurations. The lead container face exhibits a region of stagnation, the magnitude of which is dependent on container loading configuration. For consists 1 and 4 a pressure gradient across the lead face suggests a suction of flow from the gap between containers. Conversely the rear face is characterised by an area of suction, with flow accelerated through gap between containers. The flow across the roof in the crosswind test section, for all consists, is characteristic of a roll vortex spreading across the roof, emanating from the windward corner of the lead face. In the open air test section the flow across the roof and container sides is characterised by a region of weak suction, with an influence from container loading configuration. In the crosswind section the flow pattern on the windward

face, for all consists, exhibits a relatively uniform area of stagnation, whereas flow on the leeward face exhibits an area of suction. Pressure coefficients for consists 1 and 4 remain relatively uniform across the whole leeward face, except near the leeward lead face edge, suggesting complete detachment of vortices formed at the leeward lead face edge within a short distance of the edge. Consist 6 exhibits the largest variation in pressure coefficient, associated with detachment of vortices emanating from the leeward edge of the lead face.

- It is possible to calculate the overall mean aerodynamic load coefficients as a discrete integral of forces acting on each pressure tap area. Crosswind results were compared with typical passenger train aerodynamic load coefficients and shown to be characteristic of typical values measured for a yaw angle of 30° .
- A comparison of roll moments using different reference systems revealed that the values measured for roll moment about the leeward rail are larger than the values for measurements taken about the container leeward base edge.
- Clear differences in aerodynamic load coefficients were observed for differing container loading configurations in both the open air and crosswind test sections. For open air results magnitudes of all aerodynamic load coefficients, for all consists tested, were small. For crosswind results larger magnitudes for aerodynamic load coefficients were observed as container loading efficiency is reduced and space size in front of the measuring container increased. For consists 1 and 4 the influence of a container loaded closely on the wagon in front has a shielding effect on the measuring container, whereas for consist 6 the measuring container is unshielded, thus magnitudes for C_Y and C_Z are higher due to large flow separations.
- Comparison of $C_{M_{X,lee}}$ with a previous container freight wind tunnel study found good agreement for the open air and crosswind results, however, the lack of boundary layer development in the wind tunnel study for the freight train was shown to give lower values than for the moving model employed in this study.

Objective 7: Provide a data set of moving model container freight data for slipstream and aerodynamic loads to be used as a benchmark for CFD simulations.

- The model scale freight experiment data was made available to be used as a benchmark for CFD simulations. The data set has been used to validate a series of CFD simulations published and presented at the 2013 University of Birmingham 4th annual BEAR PGR conference (Flynn et al., 2013). The data has also been used to assist a French exchange student complete an undergraduate dissertation on how CFD can be used to analyse freight train slipstream development (Collin, 2013).

9.3 Recommendations for further work

1. The research in this study has focused on container freight, chosen to reflect the largest sector of rail freight in the UK. As discussed in chapter 3, the term freight train is used to describe a multitude of different wagon types. Analysis of other freight types carried out during this study highlighted the influence of ladders attached to the side of tanker wagons, creating a pulse increase to slipstream velocities. Further work should be carried out to assess flow development for other freight wagon types and analyse whether common flow characteristics exist. In chapter 5 the difference in slipstream development between a container freight train hauled by a Class 66 and a Class 92 was discussed. Further work should be carried out to characterise the influence on flow development from the locomotive type, testing newer locomotives such as the General Electric Class 70.
2. The results from the aerodynamic load experiments suggest that container loading configuration can greatly influence the magnitude of moments on a loaded container. The use of an on-board stand-alone data logger system was shown to be a suitable method for measuring surface pressures. An upgrade to the

on-board data logger system to increase the number of channels and pressure taps would allow the container surface to be discretised into smaller areas. This would reduce the effect of the assuming a uniform pressure distribution for each tapping area, thus reducing the experiment uncertainty. Further work should be undertaken by making measurements for an open spine wagon with pressure taps in the container base, to allow a more accurate comparison to previous freight wind tunnel experiments.

3. A detailed full scale experimental freight study is needed to allow further validation of the model scale data to be carried out. A specific study with a fixed container loading configuration, complying to TSI standards for ensemble size, is needed to create a base study from which model scale and CFD simulations can be validated. No previous full scale freight studies have had velocity measuring probes at a position close enough to the train side to measure the nose peak magnitude observed in the model scale data, presented in chapter 5. Carrying out an in depth full scale study would allow greater assessment of the Reynolds number effects created by modelling freight slipstream development in scale experiments.
4. The conclusions from this study are based on the idea of ensemble and statistical analysis. Further work is needed to inspect individual runs and characterise any visible flow structures. This analysis could be carried out in conjunction with a CFD study to visualise instantaneous flow development.
5. The analysis presented for the aerodynamic load experiments in chapter 8 focused on steady flow data, analysing the influence of container loading configuration. Further work should be carried out to assess the influence from unsteady flow data, by analysing peak pressure and aerodynamic load coefficient values, and observing any correlation between flow fluctuations. An additional analysis of the disregarded data from the crosswind entry and exit portals would allow an assessment of the influence of gusts on aerodynamic load coefficients.

6. The findings from this study on aerodynamic flow development for a container freight train should be used as a foundation to establish whether the codes of practice specified in the TSI or UK standards need updating, to be measured in relation to freight trains as well as high speed passenger trains. The results in chapter 5 imply freight trains already lie close to existing limits for slipstream velocities, and any possible increases in train speed would break these limits. As current limits are not defined with respect to safety, further work should be undertaken to assess whether the methodology and prescribed limits given in national standards give realistic limit values for the safety of passengers or trackside workers.

References

- ACIN (2014). Betz micromanometer - Factory standard for pressure calibration. Available at <http://www.acin.nl>. Last accessed on 27/01/2014.
- Ahmad, K., M. Khare, and K. Chaudhry (2005). Wind tunnel simulation studies on dispersion at urban street canyons and intersections—a review. *Journal of Wind Engineering and Industrial Aerodynamics Volume 93*(9), 697–717.
- Alam, F. and S. Watkins (2007a). Effects of Crosswinds on Double Stacked Container Wagons. In *16th Australasian Fluid Mechanics Conference (AFMC)*, pp. 758–761. School of Engineering, The University of Queensland.
- Alam, F. and S. Watkins (2007b). Lateral stability of double stacked container wagon under crosswinds. In *Proceedings of the International Conference on Mechanical engineering (ICME2007), Dhaka, Bangladesh*.
- Andersson, E., J. Häggström, M. Sima, and S. Stichel (2004). Assessment of train-overturning risk due to strong cross-winds. *Proceedings of the Institution of Mechanical Engineers, Part F: Journal of Rail and Rapid Transit Volume 218*(3), 213–223.
- Andrews, H. (1954). The measurement of train resistance. *ARCHIVE: Journal of the Institution of Locomotive Engineers 1911-1970 (vols 1-59) Volume 44*(237), 91–166.
- ATSB (2008). Rail Occurrence Investigation RO-2008-013. Technical report, ATSB Transport.

- Baker, C. (1985). The determination of topographical exposure factors for railway embankments. *Journal of Wind Engineering and Industrial Aerodynamics Volume 21*(1), 89–99.
- Baker, C. (1986). Train aerodynamic forces and moments from moving model experiments. *Journal of Wind Engineering and Industrial Aerodynamics Volume 24*(3), 227–251.
- Baker, C. (2001). Flow and dispersion in ground vehicle wakes. *Journal of Fluids and Structures Volume 15*(7), 1031–1060.
- Baker, C. (2010). The flow around high speed trains. *Journal of Wind Engineering and Industrial Aerodynamics Volume 98*(6-7), 277–298.
- Baker, C. (2013). A framework for the consideration of the effects of crosswinds on trains. *Journal of Wind Engineering and Industrial Aerodynamics Volume 123*, 130–142.
- Baker, C., S. Dalley, T. Johnson, A. Quinn, and N. Wright (2001). The slipstream and wake of a high-speed train. *Proceedings of the Institution of Mechanical Engineers, Part F: Journal of Rail and Rapid Transit Volume 215*(2), 83–99.
- Baker, C., H. Hemida, S. Iwnicki, G. Xie, and D. Ongaro (2011). Integration of crosswind forces into train dynamic modelling. *Proceedings of the Institution of Mechanical Engineers, Part F: Journal of Rail and Rapid Transit Volume 225*(2), 154–164.
- Baker, C., S. Jordan, T. Gilbert, A. Quinn, M. Sterling, T. Johnson, and J. Lane (2012). Transient aerodynamic pressures and forces on trackside and overhead structures due to passing trains. Part 1 Model scale experiments Part 2 Standards applications. *Proceedings of the Institution of Mechanical Engineers, Part F: Journal of Rail and Rapid Transit*.

- Baker, C., S. Jordan, T. Gilbert, M. Sterling, and A. Quinn (2012). RSSB Project T750 - Review of Euronorm Design Requirements For Trackside And Overhead Structures Subjected To Transient Aerodynamic Loads. Technical report, Birmingham Centre for Railway Research and Education.
- Baker, C. and A. Quinn (2012). Train slipstream measurements at Uffington on the Western Main Line. Technical report, Birmingham Centre for Railway Research and Education at the University of Birmingham.
- Baker, C. and M. Sterling (2009). Aerodynamic forces on multiple unit trains in cross winds. *Journal of Fluids Engineering Volume 131*, 101–103.
- Baker, C. J., A. Quinn, M. Sima, L. Hoefener, and R. Licciardello (2013a). Full-scale measurement and analysis of train slipstreams and wakes: Part 1 Ensemble averages. *Proceedings of the Institution of Mechanical Engineers, Part F: Journal of Rail and Rapid Transit Volume 0*, 1–17.
- Baker, C. J., A. Quinn, M. Sima, L. Hoefener, and R. Licciardello (2013b). Full-scale measurement and analysis of train slipstreams and wakes. Part 2 Gust analysis. *Proceedings of the Institution of Mechanical Engineers, Part F: Journal of Rail and Rapid Transit*.
- Bartlett, P. (2014). Class 66 photographs. Available at <http://paulbartlett.zenfolio.com/>. Last accessed on 11/04/2014.
- Beagles, A. and D. Fletcher (2013). The aerodynamics of freight; approaches to save fuel by optimising the utilisation of container trains. *Journal of Rail and Rapid Transit*, 1–9.
- Bernsteen, S. (1979). *A Theoretical Analysis of the Rolling Resistance of Railway Vehicles from Fundamental Mechanics*. Ph. D. thesis, Carnegie-Mellon University.

- Blackadar, A. K. and H. Tennekes (1968). Asymptotic similarity in neutral barotropic planetary boundary layers. *Journal of Atmospheric Sciences Volume 25*, 1015–1020.
- Box, G. P. and G. Jenkins (1970). Time Series Analysis: Forecasting and Control. *San Francisco: Holden-Day*.
- BR (August 1982). TM-AER-060 Slipstream Effects of Aerodynamically Rough Trains. Technical report, British Rail.
- BR (December 1993b). RR-AER-014 Trackside Safety Tests at Northallerton. Technical report, British Rail.
- BR (January 2002). AEATR-T&S-2001-214 and AEATR-T&S-2002-004 90 mph Freight Train Slipstream Tests – Stage 1, January 2002 90 mph Freight Train Slipstream Tests – Stage 2, January 2002. Technical report, British Rail.
- BR (March 1993a). LR-AER-072 Survey of Air Turbulence Studies for Transit Vans Carried on Carflats and the Effect on Pushchairs. Technical report, British Rail Research.
- Brockie, N. and C. Baker (1990). The aerodynamic drag of high speed trains. *Journal of Wind Engineering and Industrial Aerodynamics Volume 34* (3), 273–290.
- BSI (2005). Railway applications - Aerodynamics - Part 4: Requirements and test procedures for aerodynamics on open track. *BS EN 14067-4:2005 +A1:2009*.
- BST (2007). PSD Series - High Performance Regulated DC Power Supply (Digital Display). Available at <http://www.bstcaltek.com>. Last accessed on 04/07/2013.
- Castro, I. and A. Robins (1977). The flow around a surface-mounted cube in uniform and turbulent streams. *Journal of Fluid Mechanics Volume 79*(02), 307–335.
- CEN (2009). EN 14067-4 Railway applications - Aerodynamics Part 4: Requirements and test procedures for aerodynamics on open track. Technical report, CEN.

- Collin, Q. (2013). Numerical Simulations of Slipstream around freight trains. Master's thesis, University of Birmingham/Ensime.
- Cooper, K. (1993). Bluff-body aerodynamics as applied to vehicles. *Journal of Wind Engineering and Industrial Aerodynamics Volume 49*(1-3), 1–21.
- Cooper, R. (1984). Atmospheric turbulence with respect to moving ground vehicles. *Journal of wind engineering and industrial aerodynamics Volume 17*(2), 215–238.
- Davidson, P. (2004). *Turbulence: an introduction for scientists and engineers*. Oxford University Press, USA.
- Decatur (2013). Decatur Electronics Railmaster-VP. Available at <http://www.decatoureurope.com/>. Last accessed on 02/10/2013.
- Deeg, P., M. Jönsson, H. Kaltenbach, M. Schober, and M. Weise (2008). Cross-comparison of measurement techniques for the determination of train induced aerodynamic loads on the track bed. In *Proceedings of the BBAA VI, Milano, Italy*.
- Derrick, T. R., B. T. Bates, and J. S. Dufek (1994). Evaluation of time-series data sets using the Pearson product-moment correlation coefficient. *Medicine and science in sports and exercise Volume 26*(7), 919.
- DfT (2007). Delivering a sustainable railway. Technical report, Department for Transport.
- Diedrichs, B., M. Berg, and S. Krajnovic (2004). Large Eddy Simulations of a typical European high-speed train inside tunnels. In *2004 SAE World Congress, SAE Paper No. 2004-01-0229, Detroit, USA, 2004*.
- Donnelly, R. and C. Butcher (1990). New-generation ore wagons on the Mount Newman Mining railroad. *ARCHIVE: Proceedings of the Institution of Mechanical Engineers, Part F: Journal of Rail and Rapid Transit 1989-1996 (vols 203-210) Volume 204*(16), 55–61.

- Dorigatti, F. (2013). *Rail vehicles in crosswinds: analysis of steady and unsteady aerodynamic effects through static and moving model tests*. Ph. D. thesis, University of Birmingham.
- Durbin, P. and G. Medic (2007). *Fluid dynamics with a computational perspective*, Volume 10. Cambridge university press.
- Efron, B. and R. J. Tibshirani (1994). *An introduction to the bootstrap*, Volume 57. CRC press.
- Flynn, D., D. Soper, H. Hemida, and C. Baker (2013). Detached-eddy simulation of the slipstream of an operational freight train. In *University of Birmingham 4th annual BEAR PGR conference 2013*.
- Fox, P., P. Hall, and R. Pritchard (2008). *British Railways Locomotives & Coaching Stock 2008*. Platform 5, Sheffield.
- Garratt, J. R. (1994). *The atmospheric boundary layer*. Cambridge university press.
- Gawthorpe, R. (1994). Wind effects on ground transportation. *Journal of Wind Engineering and Industrial Aerodynamics Volume 52*, 73–92.
- George, W. (2004). Lectures in Turbulence for the 21st Century.
- Gibson, S. (2003). Allocation of capacity in the rail industry. *Utilities Policy Volume 11*(1), 39–42.
- Gil, N., C. Baker, and C. Roberts (2008). The Measurement of Train Slipstream Characteristics using a Rotating Rail Rig. In *6th Int. Colloq. on Bluff Body Aerodynamics and its Applications*.
- Gil, N., C. Baker, C. Roberts, and A. Quinn (2010). Passenger Train Slipstream Characterization Using a Rotating Rail Rig. *Journal of Fluids Engineering Volume 132*, 061401 1–11.

- Gill (2013). Gill Instruments: R3-50 3-Axis Ultrasonic Anemometer. Available at <http://www.gillinstruments.com/>. Last accessed 02/10/2013.
- Golovanevskiy, V. A., V. V. Chmovzh, and Y. V. Girka (2012). On the optimal model configuration for aerodynamic modeling of open cargo railway train. *Journal of Wind Engineering and Industrial Aerodynamics Volume 107*, 131–139.
- Haines, M. (2013). *The simulation of non-synoptic effects for wind damage studies*. Ph. D. thesis, University of Birmingham.
- Hemida, H. and C. Baker (2010). Large-eddy simulation of the flow around a freight wagon subjected to a crosswind. *Computers & Fluids Volume 39, Issue 10*, 1944–1956.
- Hemida, H., N. Gil, and C. Baker (2010). LES of the Slipstream of a Rotating Train. *Journal of Fluids Engineering Volume 132*, 051103.
- Honeywell (2013). Honeywell - 164PC01D37 differential pressure transducer. Available at <http://uk.farnell.com/honeywell-s-c/164pc01d37/pressure-sensor-0-10-h2o/dp/73187>. Last accessed 02/10/2013.
- ISO (2006). International Organization for Standardization (ISO), Freight containers, Volume 34 of ISO standards handbook, International Organization for Standardization, 4th edition, 2006. ISBN 92-67-10426-8.
- ITSV (2013). Wagon information. Available at: <http://www.ltsv.com>. Last accessed on 08/04/2014.
- Jordan, S., M. Sterling, and C. Baker (2009). Modelling the response of a standing person to the slipstream generated by a passenger train. *Proceedings of the Institution of Mechanical Engineers, Part F: Journal of Rail and Rapid Transit Volume 223, Issue 6(6)*, 567–579.

- Krönke, I. and H. Sockel (1994). Model tests about cross wind effects on containers and wagons in atmospheric boundary layers. *Journal of Wind Engineering and Industrial Aerodynamics Volume 52*, 109–119.
- Kundu, P. K. and I. M. Cohen (2010). *Fluid Mechanics*. Academic Press, San Diego, CA.
- Lai, Y. and C. Barkan (2006). Improving Energy Efficiency of Intermodal Trains Using Machine Vision and Operations Research Analysis. In *Proceedings of the 7th World Congress on Railway Research, Montreal*. Citeseer.
- Lukaszewicz, P. (2009). Running resistance and energy consumption of ore trains in Sweden. *Proceedings of the Institution of Mechanical Engineers, Part F: Journal of Rail and Rapid Transit Volume 223*(2), 189–197.
- MCC (2013). Measurement Computing USB-1616FS. Available at <http://www.mccdaq.com/usb-data-acquisition/USB-1616FS.aspx>. Last accessed 02/10/2013.
- McConville, A. (2008). *The physical simulation of thunderstorm downbursts*. Ph. D. thesis, University of Birmingham.
- Microsoft-Corporation (2013). Uffington Ordinance Survey map. Available at www.bing.com/maps/. Last accessed on 27/06/2013.
- Moran, P. and R. Hoxey (1979). A probe for sensing static pressure in two-dimensional flow. *Journal of Physics E: Scientific Instruments 12*(8), 752.
- Muld, T. (2010). Analysis of Flow Structures in Wake Flows for Train Aerodynamics. Technical report, Royal Institute of Technology, Department of Mechanics, SE-100 44 Stockholm, Sweden.
- Oke, T. (1988). Street design and urban canopy layer climate. *Energy and Buildings Volume 11*(1-3), 103–113.

- Östh, J. and S. Krajnović (2013). A study of the aerodynamics of a generic container freight wagon using large-eddy simulation. *Journal of Fluids and Structures*.
- Paterson, D. and C. Apelt (1990). Simulation of flow past a cube in a turbulent boundary layer. *Journal of Wind Engineering and Industrial Aerodynamics Volume 35*, 149–176.
- Paul, J. C., R. W. Johnson, and R. G. Yates (2009). Application of CFD to rail car and locomotive aerodynamics. In *The Aerodynamics of Heavy Vehicles II: Trucks, Buses, and Trains*, pp. 259–297. Springer.
- Peters, J. (1993). Effect of Reynolds number on the aerodynamic forces on a container model. *Journal of Wind Engineering and Industrial Aerodynamics Volume 49*(1-3), 431–438.
- Picard, A., R. Davis, M. Gläser, and K. Fujii (2008). Revised formula for the density of moist air (CIPM-2007). *Metrologia Volume 45*(2), 149.
- Polikar, R. (2006). The wavelet tutorial. Available at <http://users.rowan.edu/~polikar/WAVELETS/WTpart1.html>. Last accessed on 09/01/2014.
- Pope, C. (2006). Safety of slipstreams effects produced by trains. *A report prepared by Mott Macdonald, Ltd., for RSSB*.
- Quinn, A., M. Sterling, A. Robertson, and C. Baker (2007). An investigation of the wind-induced rolling moment on a commercial vehicle in the atmospheric boundary layer. *Proceedings of the Institution of Mechanical Engineers, Part D: Journal of Automobile Engineering Volume 221*(11), 1367–1379.
- Raghunathan, R. S., H.-D. Kim, and T. Setoguchi (2002). Aerodynamics of high-speed railway train. *Progress in Aerospace sciences Volume 38*(6), 469–514.
- RAIB (2009). Detachment of containers from freight wagons near Cheddington and Hardendale 1 March 2008. Technical report, DfT Accident Investigation.

- Read, M. (2014). FEA-B wagon photographs. Available at <http://ukrailwaypics.smugmug.com/>. Last accessed on 11/04/2014.
- Reynolds, O. (1895). On the dynamical theory of incompressible viscous fluids and the determination of the criterion. *Philosophical Transactions of the Royal Society of London. A Volume 186*, 123–164.
- Rochard, B. and F. Schmid (2000). A review of methods to measure and calculate train resistances. *Proceedings of the Institution of Mechanical Engineers, Part F: Journal of Rail and Rapid Transit Volume 214*(4), 185–199.
- RSSB (2001). Calculation of Enhanced Permissible Speeds for Tilting Trains, Railway Safety approved Code of Practice GC/RC 5521. Technical report, Rail Safety and Standards Board Limited, London.
- RSSB (2009). Resistance of Railway Vehicles to Roll-Over in Gales, Railway Group Standard GM/RT 2142. Technical report, Rail Safety and Standards Board Limited, London.
- RSSB (2012). Investigation of freight vehicle aerodynamic performance in accordance with GM/RT 2142 Resistance of Railway Vehicles to Roll-over in Gales. Technical report, Rail Safety and Standards Board Limited, London.
- Sanquer, S., C. Barre, M. D. de Virel, and L.-M. Cleon (2004). Effect of cross winds on high-speed trains: development of a new experimental methodology. *Journal of Wind Engineering and Industrial Aerodynamics Volume 92*(7), 535–545.
- Sanz-Andrés, A., A. Laverón, C. Baker, and A. Quinn (2004). Vehicle induced loads on pedestrian barriers. *Journal of wind engineering and industrial aerodynamics Volume 92*(5), 413–426.
- Sanz-Andrés, A., J. Santiago-Prowald, C. Baker, and A. Quinn (2003). Vehicle-induced

- loads on traffic sign panels. *Journal of Wind Engineering and Industrial Aerodynamics Volume 91*(7), 925–942.
- Saunders, J., S. Watkins, and R. Cassar (1993). Vortex optimisation of slotted tops and cavities of two different open rail wagons. *Journal of Wind Engineering and Industrial Aerodynamics Volume 49*(1-3), 421–430.
- Schulte-Werning, B., G. Matschke, R. Gregoire, and T. Johnson (1999). RAPIDE: A project of joint aerodynamics research of the European high-speed rail operators. In *World Congress on Railway Research*, pp. 19–23.
- Sensortechinics (2013). HCLA Series miniature amplified low pressure sensors - Data Sheet. Available at www.sensortechinics.com. Last accessed on 04/07/2013.
- Shah, K. and J. Ferziger (1997). A fluid mechanics view of wind engineering: Large eddy simulation of flow past a cubic obstacle. *Journal of wind engineering and industrial aerodynamics Volume 67*, 211–224.
- Soper, D., C. Baker, and M. Sterling (2013a). Slipstream development of a container freight train. In *International Workshop on Train Aerodynamics, Birmingham, UK*.
- Soper, D., C. Baker, and M. Sterling (2013b). The slipstream development of a container freight train. In *6th European and African Conference on Wind Engineering, Cambridge, UK*.
- Soper, D., C. Baker, and M. Sterling (2014). Assessing crosswind effects on a container freight train with differing container loading configurations. In *1st International Conference in Numerical and Experimental Aerodynamics of Road Vehicles and Trains, Bordeaux, France*.
- Sterling, M., C. Baker, S. Jordan, and T. Johnson (2008). A study of the slipstreams of high-speed passenger trains and freight trains. *Proceedings of the Institution of*

- Mechanical Engineers, Part F: Journal of Rail and Rapid Transit Volume 222*(2), 177–193.
- Stoesser, T., F. Mathey, J. Frohlich, and W. Rodi (2003). LES of flow over multiple cubes. *Ercoftac Bulletin Volume 56*, 15–19.
- Taghizadeh, S. (2000). Digital signal processing part3: discrete-time signals & systems case studies.
- Tavoularis, S. (2005). *Measurement in fluid mechanics*. Cambridge University Press.
- Taylor, J. R. (1997). *An introduction to error analysis: the study of uncertainties in physical measurements*. University science books.
- Temple, J. and S. Dalley (2001). RAPIDE Project; Analysis of the slipstream data. AEA Technology Rail AEATR-T&S-2001-197. Technical report, AEA Technology Rail.
- Temple, J. and T. Johnson (August 2008). Effective management of risk from slipstream effects at trackside and on platforms. Technical report, A report produced for Rail Safety and Standards Board.
- Temple, J. and T. Johnson (June 2003). Review of slipstream effects on platforms. Technical report, A report produced for Rail Safety and Standards Board.
- TFI (2011). Turbulent Flow Instrumentation - Cobra Probe - Getting started guide. Technical report, Turbulent Flow Instrumentation.
- Torrence, C. and G. Compo (1998). A practical guide to wavelet analysis. *Bulletin of the American Meteorological Society Volume 79*(1), 61–78.
- TSI (2008). COMMISSION DECISION of 21 February 2008 concerning the technical specification for interoperability relating to the rolling stock subsystem of the trans-European high-speed rail system. Technical report, Official Journal of the European Union.

- Uffington (2012). Tom Brown's School Museum Uffington, Available at www.museum.uffington.net. Last accessed 27/06/2013.
- Vishay (2011). Ambient Light Sensor - TEPT5600. Available at <http://www.vishay.com/>. Last accessed on 04/07/2013.
- Watkins, S., J. Saunders, and H. Kumar (1992). Aerodynamic drag reduction of goods trains. *Journal of Wind Engineering and Industrial Aerodynamics Volume 40*(2), 147–178.
- Woodburn, A. (2008). An investigation of container train service provision and load factors in Great Britain. *European Journal of Transport and Infrastructure Research Volume 11*(3), 147–165.
- Zajackowski, F. J. and L. J. Peltier (2011). Detached eddy simulation of atmospheric flow about a surface mounted cube at high Reynolds number. *Journal of Fluids Engineering Volume 133*, 031002–1.
- Ziehl-Abegg (2010). Technical Data - Axial Fans Series FC. Available at <http://www.ziehl-abegg.com>. Last accessed on 04/07/2013.

Appendix A

Instrumentation calibration

A.1 Introduction

This appendix discusses the calibration performed for the Cobra probes and differential pressure transducers used in this study. Section A.2.1 introduces a series of experiments undertaken to compare the University of Birmingham Cobra probes with each other, by measuring a previously well studied flow. The results discussed in section A.2.2 found four probes were broken, and were subsequently returned to TFI in Australia for recalibration. The recalibrated probes were then used as a base of comparison for the calibration of the other Cobra probes (section A.2.3). A discussion regarding the calibration of the Gill ultrasonic anemometers is given in section A.3.

The differential pressure transducers were calibrated statically using a Betz manometer (section A.4.1). A series of analysis to compare the calibration results in relation to the manufacturer limits (section A.4.2) and a cubic calibration (section A.4.3) are discussed. Finally, a discussion regarding the calibration for the pressure transducers used in the full scale experiments is given in section A.5.

A.2 TFI Cobra probe calibration

A.2.1 Calibration process

Series 100 Cobra probes have been employed throughout this study. The Cobra probes are supplied fully calibrated; however, recalibration every six months or following large temperature changes is required (TFI, 2011). The static calibration determines the voltage to pressure scaling factors used by internal pressure transducers (TFI, 2011). The University of Birmingham currently has eight Cobra probes. Two probes calibrated at 20m/s and 450Pa which are numbered 140 and 149, two probes calibrated at 36m/s and 450 Pa which are numbered 153 and 154 and four probes calibrated at 40m/s and 1000 Pa numbered as 252, 254, 263 and 265. In this study the four probes with higher calibration factors are used, to account for the high velocities and pressure magnitudes measured in the freight train slipstream. Prior to the experiments at the TRAIN rig facility, a series of probe comparisons were carried out to assess whether results fell within the calibration and accuracy bounds outlined by TFI. The experiment setup and results of these tests are presented here.

Two cases were used to examine the response of the Cobra probe. The University of Birmingham's downburst simulator was used to simulate a statistically stationary flow under a wind tunnel jet and a transient flow underneath a wind tunnel jet. The downburst simulator used for this test, pictured in figure A.1, is essentially a bank of fans creating a jet of air downward towards the floor, which can be controlled by a flap system to simulate a downburst type wind event (Haines, 2013).

For each test case the probes were aligned underneath the vertical jet created by the downburst simulator. The jet velocity has previously been measured at 13.7m/s using hot wires, calibrated to within manufacturer uncertainty bounds (McConville, 2008; Haines, 2013). The Cobra probes were positioned using a clamp stand and probe holder, such that the central measuring port was positioned at the centre of the vertical jet,



Figure A.1: The University of Birmingham downburst simulator (Haines, 2013).

with the central face of the Cobra probe head in a streamwise direction, as discussed in chapter 3.

In the stationary tests the fans were turned on and allowed to reach maximum rotational speed (30Hz), corresponding to a 13.7m/s jet speed. Once running at full power the fans remained on for five minutes, during which ten 20 second samples of data were taken for each probe. The turbulence intensity was within the range of the probes, for all cases 10%-20%.

Similarly for the transient test case ten 20 second samples were taken for each probe. In this case the sample was initiated when the fans were turned off. The fans were then turned on after six seconds, creating a time varying flow to be examined for each probe. For both test cases a sampling frequency of 2500Hz was chosen to be consistent with the experiment methodologies in this study. Individual samples proved to be very noisy signals, therefore a 1000 point moving average filter was applied, so as to examine the underlying signal.

Before the comparison experiment was undertaken a visual inspection of all probes was carried out, revealing possible blockage in the reference port for probe 140. Results from the experiment highlighted that probes 140, 154, 252 and 263 did not behave as expected, and were subsequently returned to TFI for recalibration. The probe

comparison experiments were carried out again following the return of the recalibrated probes, to assess the calibration of the probes that were not recalibrated by TFI.

A.2.2 Cobra probe comparison results

The results from the initial comparison experiments are presented for each channel u , v , w and p . An average time history was created for the stationary data by averaging across the ten individual runs. For the transient test, data was aligned to a common point relating to the transient portion of the flow, then ensemble averaged.

A.2.2.1 Stationary results

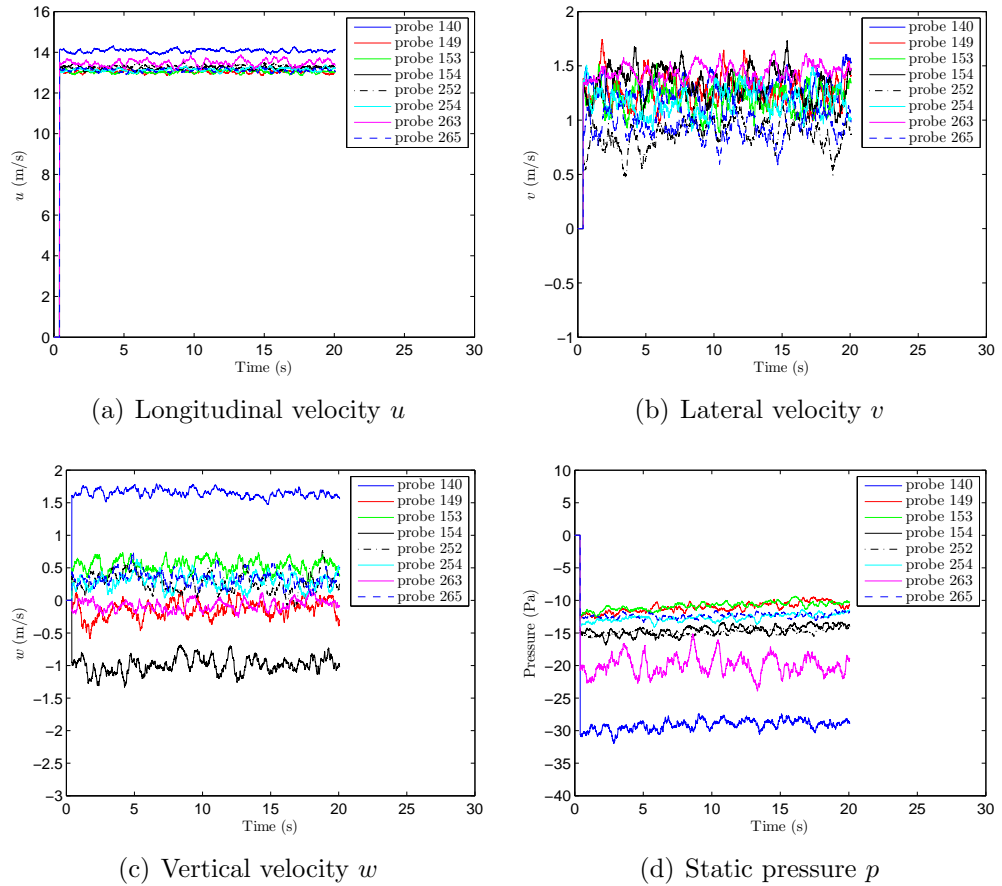


Figure A.2: A comparison of University of Birmingham Cobra probes within a stationary flow. The results show the ensemble time histories for u , v , w and p .

Figure A.2 illustrates the comparison of Cobra probes within a stationary flow. For u and v the ensemble time histories for each probe exhibit good agreement within the bounds of uncertainty suggested by TFI (TFI, 2011), except probes 140 and 263 which show a slightly high velocity reading. In the vertical plane w probe 140 exhibits a reading higher than other probes, and probes 154 and 263 are lower compared with other probes. Similarly for static pressure, probes 140 and 263 exhibit a much lower reading than other probes.

A.2.2.2 Transient results

A comparison of Cobra probe results for the transient test case is shown in figure A.3. For each probe u and v ensemble time histories exhibit good agreement within the bounds of uncertainty suggested by TFI (TFI, 2011), except probes 140 and 263 which exhibit slightly high readings, as in the stationary test case. For probe 252 there is an offset of 1m/s in u and for probe 263 an offset in v before the transient phenomenon. The offset for probe 263 builds into a number of peaks in the time history, shown to be in disagreement with other probes and generally not what would be expected of the flow. In the vertical plane probe 140 exhibits a higher reading, and probes 154 and 263 are lower compared with other probes. Probe 252 again exhibits an offset from 0m/s before the initiation of the flow, suggesting a calibration error. For static pressure, probes 140 and 263 exhibit a much lower reading than other probes, as seen for the stationary case in figure A.2.

A.2.2.3 Conclusions

The comparisons appeared to show that not all probes were behaving in the same manner, in the same flow to within the error margins specified. Probes 140, 154, 252 and 263 presented a problem in at least one of the four components u , v , w and p . A visual inspection of probe 140 revealed a possible blocked reference pressure port,

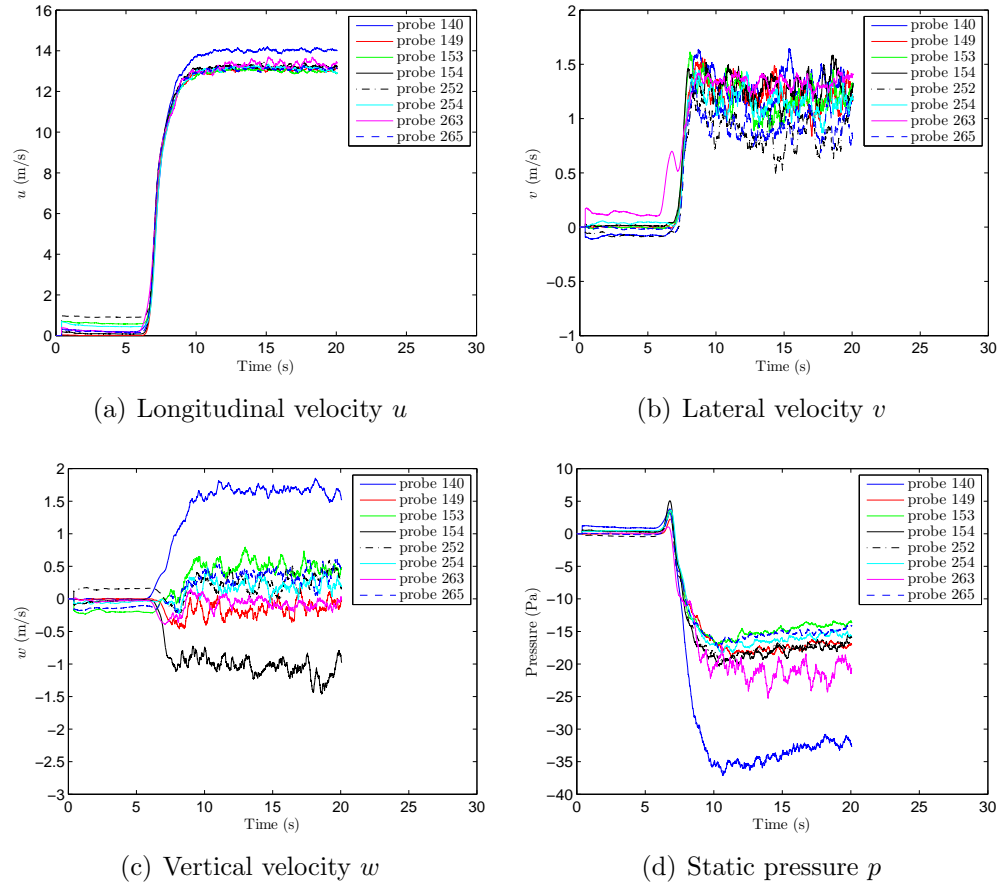


Figure A.3: A comparison of University of Birmingham Cobra probes within a transient flow. The results show the ensemble time histories for u , v , w and p .

however all other probes exhibited no signs of blockage. The probe comparison was carried out again using different a DAC box and cables, with similar results to those presented; suggesting the error was probe dependent and not a DAC box or cable problem.

A.2.3 Cobra probe calibration results

The probes presenting an error were returned to TFI for recalibration. Once recalibrated, the comparison experiment was repeated for probes 252, 263 and 265; the probes used at the TRAIN rig facility. Recalibrated probe results created a comparison with the non-recalibrated probe results, providing an assessment as to whether the non-recalibrated probe results were within the uncertainty bounds specified by the manufacturer with respect to recently calibrated probes. The results and analysis from the calibration comparison are presented in terms of a stationary and transient flow. It should be noted that due to another experiment being conducted at the same time as the Cobra probe comparison test, a retest of probe 254 was not possible.

A.2.3.1 Stationary results

Figure A.4 illustrates the comparison of Cobra probes within a stationary flow. For u and p good agreement is exhibited for all probes, to within the bounds of uncertainty suggested by TFI (TFI, 2011). In regards to the stationary flow, the recalibration by TFI has solved the issues with probes 252 and 263 presented in figure A.2.

A.2.3.2 Transient results

A comparison of Cobra probe results for the transient test case is shown in figure A.5. u and p ensemble time histories for each probe exhibit good agreement within the bounds of uncertainty suggested by TFI (TFI, 2011). As in the original tests, for probe 252

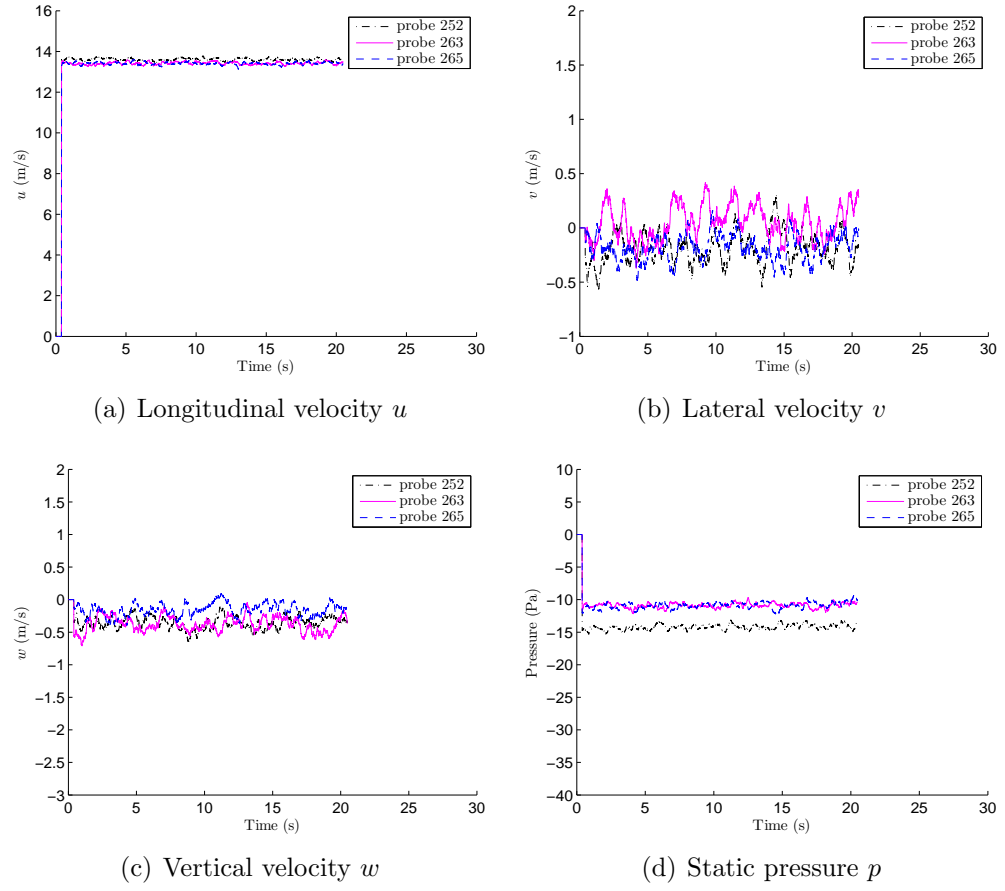


Figure A.4: A comparison of a stationary flow to assess the calibration of Cobra probes 252, 263 and 265 used at the TRAIN rig. The results show the ensemble time histories for u , v , w and p .

there is an offset of in u ; however it is reduced to 0.5m/s, within the TFI uncertainty bounds. In regards to the transient flow, the recalibration by TFI has solved the issues with probes 252 and 263 presented in figure A.3.

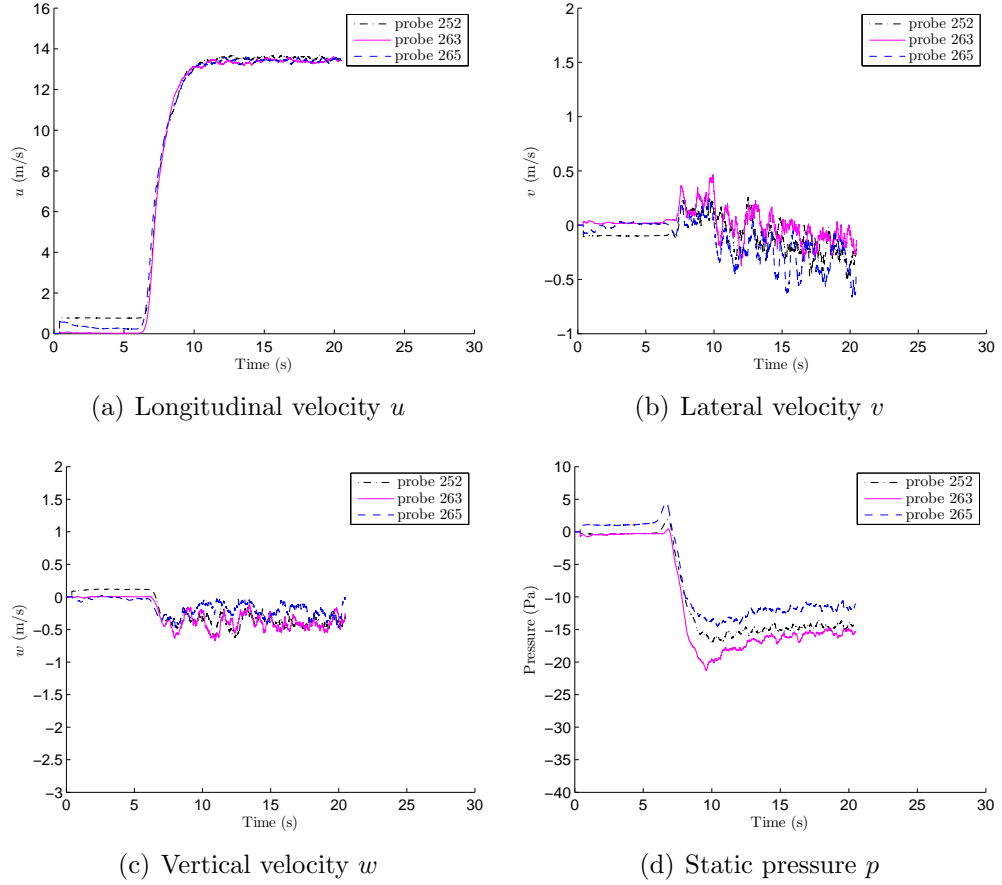


Figure A.5: A comparison of a transient flow to assess the calibration of Cobra probes 252, 263 and 265 used at the TRAIN rig. The results show the ensemble time histories for u , v , w and p .

A.2.3.3 Conclusions

The results in sections A.2.3.1-A.2.3.2 indicate good agreement for all probes in the u and p channels for both stationary and transient flows. In relation to the recalibrated probes it can be seen that the non-recalibrated probe 265 falls within TFI uncertainty bounds of the recalibrated results, suggesting a well calibrated state.

All stationary results lie within TFI uncertainty bounds of the previously measured

vertical jet velocity of 13.7m/s, suggesting the probes all exhibit a well calibrated state in relation to other calibrated measuring equipment. Figure A.6 illustrates the standard deviation of individual samples with respect to the ensemble for u and p for the stationary and transient cases. Results show a small run to run variation with respect to the ensemble, suggesting high repeatability of results and no sampling errors. It can be concluded that the TRAIN rig Cobra probes are suitably calibrated for the slipstream and aerodynamic load experiments presented within this study.

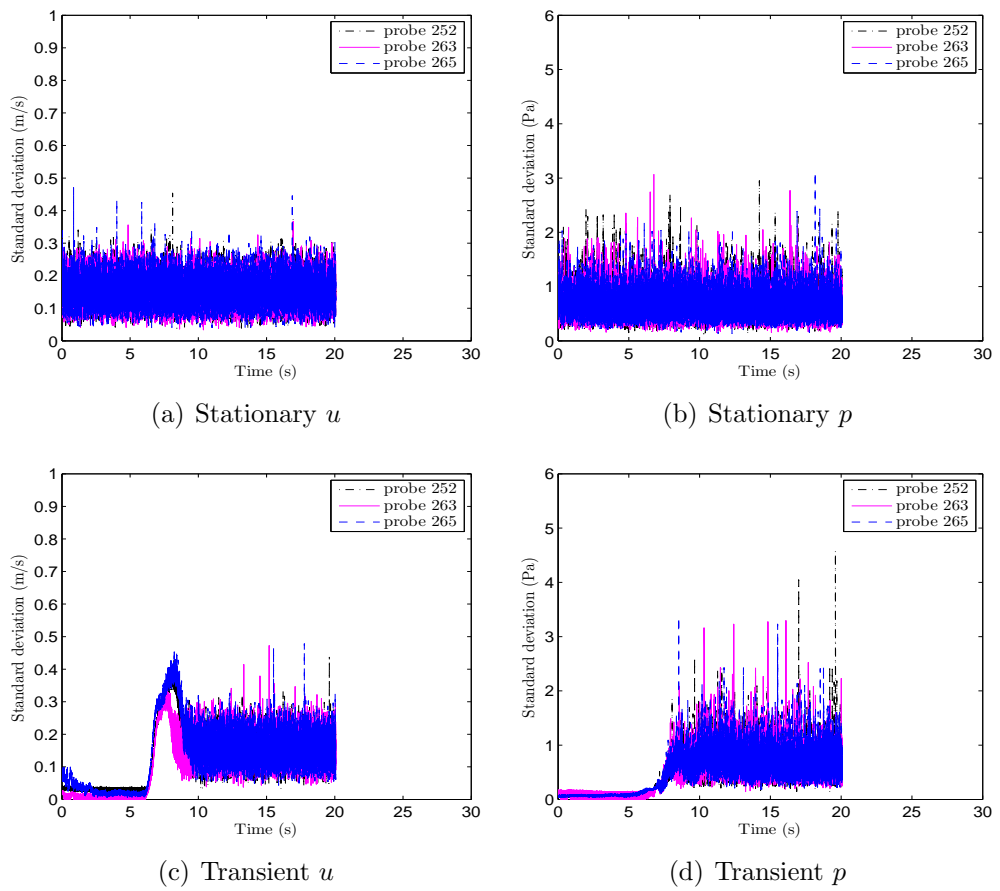


Figure A.6: Standard deviation of individual runs with respect to the ensemble mean for Cobra probes in a stationary and transient flow. The results are presented for the u and p channels.

A.3 Gill Instruments R3-50 ultrasonic anemometer calibration

Full scale slipstream velocities were measured using Gill Instruments R3-50 ultrasonic anemometers (Gill, 2013). The ultrasonic anemometer outputs voltage data proportional to the time taken for sonic pulses to pass between a pair of transducers, recorded at a frequency of 100Hz (Gill, 2013). The ultrasonic anemometer is supplied as factory calibrated and the characteristics of the anemometer should not change unless the measuring head is physically distorted. If the measuring head was distorted the zero measurement would give a false reading and a series of wind tunnel experiments, applying a known reference velocity, would be needed to recalibrate the anemometer. A simple test in still conditions was used to check whether the probes were still calibrated. Results showed no changes to the zero measurement, and subsequently no calibration issues. Therefore, the ultrasonic anemometers used in the Uffington test were set with the manufacturer calibration and provided results within the manufacturer error bounds.

A.4 Sensor Technics HCLA12X5PB calibration

A.4.1 Calibration process

The pressure transducers were calibrated using an Acin Instrumentation Betz micro manometer (ACIN, 2014). The Betz consists of a liquid J-manometer which has an accuracy of 1Pa and a resolution of $\pm 0.5\text{Pa}$ (ACIN, 2014). All the transducers were connected to the Betz in parallel using a closed pneumatic circuit. The transducer high pressure ports (HPP) were connected to a manual pump, attached in parallel to the Betz. Similarly the low pressure ports (LPP) were connected to the Betz low pressure port. The HCLA12X5PB pressure transducers used in the on-board pressure system

have a working range of $\pm 1250\text{Pa}$ (Sensortech, 2013). The Betz manual pump is used to apply a nominal differential pressure (ΔP_N) within the pressure transducer range; the nominal differential pressure is indicated on a screen on the Betz manometer. Once ΔP_N has stabilised, time histories of the voltage output $\text{Vol}_k(t)$ were recorded for 15 seconds for each pressure transducer using the on-board data logger system. The time histories for each pressure transducer were time averaged to give $\text{Vol}_{RT}(\Delta P_N)$. This process is repeated 27 times across the whole pressure transducer range, including 0Pa. The nominal differential pressure recorded at 0Pa provides the zero pressure offset, discussed in chapter 7. Effectively the zero pressure offset provides the voltage associated with no pressure difference across the pressure transducer, denoted as $\text{Vol}_{0,k}(t)$. The zero pressure offset differs slightly for each pressure transducer, and subsequently slightly from the manufacturers prescribed value of 2.25Volts, even for the same parallel supply unit in the on-board logger system, as shown in table A.1.

Pressure transducer	$\text{Vol}_{0,k}$
PT 1	2.260
PT 2	×
PT 3	×
PT 4	×
PT 5	×
PT 6	×
PT 7	2.255
PT 8	2.260
PT 9	2.260
PT 10	2.265
PT 11	2.257
PT 12	×
PT 13	×
PT 14	2.257

Table A.1: Zero offset voltages $\text{Vol}_{0,k}$ for pressure transducers PT1-PT14. The pressure taps with no data correspond to those broken in another experiment before the calibration was carried out.

The differences observed in zero pressure offset for each pressure transducer were monitored on a daily basis throughout the aerodynamic load experiments (chapter 6). The data is processed, as in chapter 7, with respect to the zero pressure offset $\text{Vol}_{0,k}$, to

give (Dorigatti, 2013),

$$\Delta \text{Vol}_k(\Delta P_N) = \text{Vol}_{RT}(\Delta P_N) - \text{Vol}_{0,k} \quad (\text{A.1})$$

The calibration data collected using the Betz manometer is shown in figure A.7. The results are plotted as a series of nominal differential pressures across the pressure transducer range against the corresponding time averaged voltage recorded. All pressure transducers follow a linear trend, as expected from the manufacturer specifications. It should be noted that only 7 of the 14 pressure transducers could be tested for this calibration. The transducers not tested were used within another study at the TRAIN rig, in which the transducers were taken beyond the working range and damaged. The implications of this are discussed in section A.4.4.

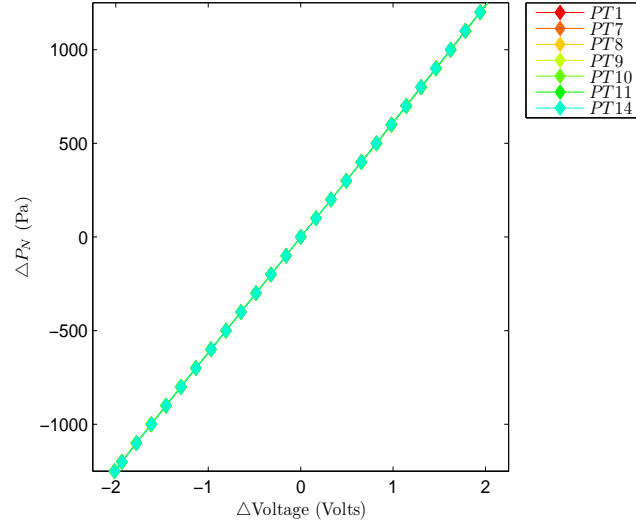


Figure A.7: Pressure calibration raw data as measured by the Betz manometer and on-board pressure measuring system.

A.4.2 Nominal linear calibration (NLC)

The nominal linear calibration is that defined by the manufacturer as,

$$\Delta P_{NLC,k}(t) = \Delta \text{Vol}_k(t) K_{NLC} \quad (\text{A.2})$$

where K_{NLC} is the nominal linear calibration factor given by the manufacturer for all Sensor Technics HCLA12X5PB pressure transducers with the range $\pm 1250\text{Pa}$. ΔP_{NLC} is the measurement of the differential pressure using this calibration method (Sensortecnics, 2013; Dorigatti, 2013).

The nominal linear calibration error associated with this calculation, as measured during the calibration, can be expressed as,

$$E_{NLC,k}(\Delta P_N) = \Delta P_{NLC,k} - \Delta P_N \quad (\text{A.3})$$

$E_{NLC,k}$ essentially assesses the difference between the calculated value of pressure from a certain voltage to the value of pressure measured by the Betz manometer. The error is calculated for each measured position in the pressure transducer range, shown in figure A.8.

The largest errors are shown to occur towards the pressure transducer limit values, of the order $\pm 15\text{Pa}$. Across the central portion of the transducer range between $\pm 1\text{Volts}$ the error for all pressure transducers tested is below $\pm 10\text{Pa}$.

A.4.3 Actual cubic calibration (ACC)

To reduce the error associated with the nominal linear calibration method a series of calibration curves can be fitted to the Betz results. Dorigatti (2013) compared a linear and cubic method of curve fitting to linearly interpolate results; concluding the cubic method presented the smallest error with respect to the measured data. The actual

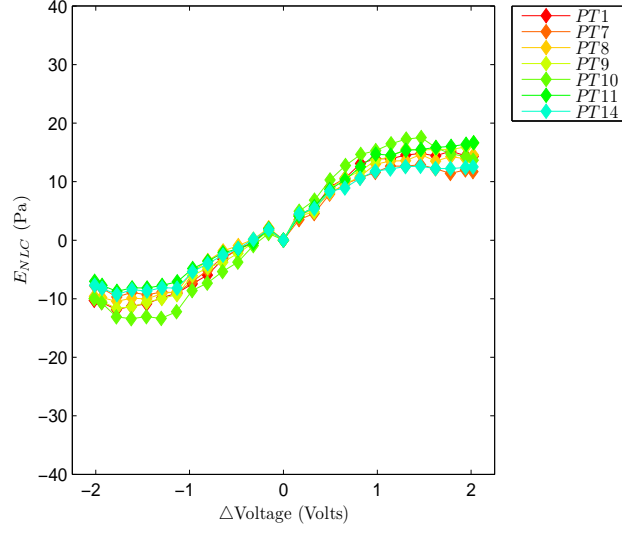


Figure A.8: Nominal linear calibration error $E_{NLC,k}$ associated with each pressure transducer.

cubic calibration curve for each pressure transducer is expressed as (Dorigatti, 2013),

$$\Delta P_{ACC,k}(t) = C_{3,k} \Delta \text{Vol}_k^3(t) + C_{2,k} \Delta \text{Vol}_k^2(t) + C_{1,k} \Delta \text{Vol}_k(t) \quad (\text{A.4})$$

where $\Delta P_{ACC,k}$ is the differential pressure measurement, and $C_{1,k}$, $C_{2,k}$ and $C_{3,k}$ are the cubic calibration coefficients obtained from fitting the cubic curve to the Betz calibration data. The calibration coefficients for each pressure transducer are given in table A.2.

The error associated with the actual cubic calibration can be calculated similarly to the nominal linear calibration as,

$$E_{ACC,k}(\Delta P_N) = \Delta P_{ACC,k} - \Delta P_N \quad (\text{A.5})$$

The associated errors calculated for each pressure transducer for the cubic calibration method are shown in figure A.9.

The method of cubic calibration has reduced the error associated to each pressure transducer in relation to the nominal linear calibration error. For all pressure trans-

	C_3 Pa/Vol ³	C_2 Pa/Vol ²	C_1 Pa/Vol
PT 1	1.402	-0.757	613.19
PT 2	×	×	×
PT 3	×	×	×
PT 4	×	×	×
PT 5	×	×	×
PT 6	×	×	×
PT 7	1.448	-0.654	614.36
PT 8	1.069	-0.843	614.70
PT 9	1.207	-0.972	613.54
PT 10	2.258	-0.674	609.96
PT 11	1.216	-1.495	614.23
PT 12	×	×	×
PT 13	×	×	×
PT 14	1.227	-0.787	615.07

Table A.2: Actual cubic calibration factors C_1 , C_2 and C_3 . The pressure transducers with no data correspond to those broken in another experiment before this calibration was carried out.

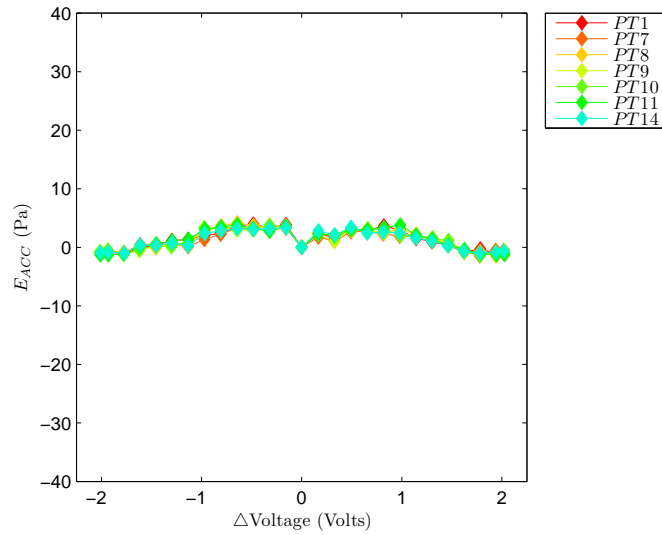


Figure A.9: Actual cubic calibration error $E_{ACC,k}$ associated with each pressure transducer.

ducers tested the errors are of a similar magnitude, with the maximum error across the whole pressure transducer range below $\pm 5\text{Pa}$.

A.4.4 Discussion

As discussed, only 7 of the 14 pressure transducers used in the on-board surface pressure system could be tested for the calibration. The transducers not tested were used within another study at the TRAIN rig, in which the transducers were taken beyond the working range and damaged. By analysing the results presented for the calibrated pressure transducers, it is suggested that the implications of only calibrating 7 transducers and using the standard manufacturer nominal linear calibration factor for the other 7 transducers, in relation to the overall results, is minimal.

The maximum nominal linear calibration error for the calibrated transducers was shown to be $\pm 15\text{Pa}$, reducing to $\pm 5\text{Pa}$ for the cubic calibration method. The errors are similar for all calibrated transducers, suggesting the maximum errors are similar to those that would have been found for the transducers not tested. For both the nominal and cubic calibration method the errors across the central portion of the transducer range, $\pm 1\text{Volts}$ corresponding to values of pressure $\pm 700\text{Pa}$, are smaller than error values outside this range. Analysing pressure measured in both the open air and crosswind test section, it can be seen that the majority of measurements made lie within the $\pm 700\text{Pa}$ bounds. Therefore, if the calibrated transducers are used a baseline for estimating the errors associated with the non-calibrated transducers; as the majority of pressures measured lie within the $\pm 700\text{Pa}$ bounds, which for the calibrated transducers corresponds to errors below the maximum error, it is hypothesised that the non-calibrated transducers will also lie within this error range, which is taken to be acceptable for this study.

A.5 Honeywell 164PC01D37 calibration

Honeywell 164PC01D37 differential pressure transducers used in the full scale experiment probes to measure static pressure were calibrated using a Betz micro manometer. The pressure system developed for the full scale experiments (section 3.3.2.2.2) was connected to a Betz micro manometer and tested using the methodology presented in section A.4. The calibration was carried out prior to undertaking the full scale experiments (Baker and Quinn, 2012). Results showed the Honeywell 164PC01D37 transducers gave linear measurements in the pressure transducer range, to within the manufacturers specified error bounds. The full scale pressure analysis presented in chapter 5 is given in terms of a nominal linear calibration, using the manufacturer calibration factor.

Appendix B

Uncertainty analysis

B.1 Introduction

In chapter 4 and 7 a discussion of the uncertainty associated with experimental data was presented. Estimate values for total error were given for the slipstream velocity and static pressure measurements, as well as surface pressure and aerodynamic load coefficients for a freight train running through an open air and crosswind situation. The uncertainty analysis is presented in this appendix. Section B.2 introduces the methodology adopted for calculating the total error associated with a measured variable. The uncertainty analysis is presented separately for the slipstream (section B.3) and aerodynamic load (section B.4) experiments.

B.2 Uncertainty analysis methodology

The true value of a physical or derived fluid property is in general an unknown quantity, estimated by recording a series of measurements. The difference between the measured and true value is defined as the measurement error, quantified by calculating the measurement uncertainty (Tavoularis, 2005). Dorigatti (2013) applied an

uncertainty analysis methodology developed by Taylor (1997) and Tavoularis (2005) to mean pressure and aerodynamic load coefficients measured at the TRAIN rig facility. In relation to other TRAIN rig studies (Baker et al., 2012), the uncertainty methodology applied in Dorigatti (2013) not only takes into account the uncertainty associated with the equipment used to take the measurements, but also a quantification of the random uncertainty of results. The method presented in Dorigatti (2013) for calculating uncertainty is adopted for this study for both the slipstream and aerodynamic load measurements. A discussion of the methodology developed by Taylor (1997) and Tavoularis (2005) is presented and applied in the following sections.

B.2.1 Bias limit

Throughout this study experimental data is presented in terms of non-dimensional coefficients. The coefficient is calculated using a series of variables recorded for each measurement made. To account for the combined influence of individual uncertainties associated to each variable, the theory of propagation of error is applied to calculate the coefficient uncertainty (Taylor, 1997).

The bias limit calculates the uncertainty of a measured variable by assessing the characteristics and performance limits of the employed experiment instrumentation. Taylor (1997) states that according to the propagation of error, the bias limit is defined as,

$$E_{BIAS} = \sqrt{\sum_k \left(\frac{\partial C_\xi}{\partial b_k} \delta b_k \right)^2} \quad (B.1)$$

where C_ξ is any non-dimensional coefficient calculated in this study. b_k indicates an individual quantity measured for the calculation of C_ξ , and δb_k represents the respective instrumentation uncertainty. Instrumentation uncertainty is caused by hysteresis and non-linearity, and is usually supplied in manufacturer specifications and considered to be a uniform distribution of uncertainty across the instrument range. For the

differential pressure transducers the bias error limit is non-linear and calculated as the maximum error from the calibration carried out in appendix A.

B.2.2 Random uncertainty

To account for the random variability relating to the run to run unsteadiness of the physical phenomenon measured, Dorigatti (2013) defines the random uncertainty by assuming a normal distribution and considering a confidence level of 95%,

$$E_{RND} = \pm 2 \frac{\sigma_{C_\xi}}{\sqrt{N}} \quad (\text{B.2})$$

where C_ξ is any non-dimensional coefficient calculated in this study, σ_{C_ξ} is the standard deviation with respect to the ensemble and N is the number of runs in the ensemble average.

B.2.3 Total uncertainty

The total uncertainty is defined as the sum of the bias and random uncertainties.

$$E_{TOT} = E_{BIAS} + E_{RND} \quad (\text{B.3})$$

As the bias and random uncertainty terms measure different quantities, the two terms are considered independent (Dorigatti, 2013).

B.3 Slipstream uncertainty analysis

The uncertainties associated with the slipstream experiments are calculated in terms of maximum values for velocities and static pressure, in line with the TSI methodology and previous slipstream studies (Gil et al., 2010; Baker et al., 2012). The method of

calculating uncertainties, adopted from the methodology presented for surface pressure coefficients in Dorigatti (2013), is presented in terms of a bias limit and random uncertainty for both slipstream velocities and static pressure. The slipstream uncertainty analysis is presented for the 181.25m train for consists 1, 3 and 5 and the full scale data.

B.3.1 Slipstream velocities

The maximum resultant slipstream velocity in the horizontal plane is calculated for each individual run, at each measuring position, for all container loading configurations tested on the 181.25m freight train and all configurations at full scale.

B.3.1.1 Bias limit

The uncertainty for each measuring instrument is given in table B.1 in terms of model and full scale data. As the uncertainty calculation focuses on the maximum resultant slipstream velocity in the horizontal plane, by propagation of error, the manufacturer specifications are used to calculate the accuracy of resultant velocity measurements,

$$\begin{aligned}
 \delta u_{res} &= \sqrt{\left(\left(\frac{u}{\sqrt{u^2 + v^2}}\right) \delta u\right)^2 + \left(\left(\frac{v}{\sqrt{u^2 + v^2}}\right) \delta v\right)^2} \\
 &= \sqrt{\left(\left(\frac{u^2}{u^2 + v^2}\right) \delta u^2\right) + \left(\left(\frac{v^2}{u^2 + v^2}\right) \delta v^2\right)} \\
 &= \sqrt{\left(\frac{u^2 + v^2}{u^2 + v^2}\right) \delta u^2} = 0.3\text{m/s}
 \end{aligned}$$

The bias limits for each container loading configuration at model scale and for all consists at full scale are shown in figure B.1(a). The mean and maximum bias limit value for all configurations are shown in table B.2.

		Accuracy	Instrumentation	Source of information
Model scale data	$\delta \Delta P_{ST}$	$\pm 5\text{Pa}$	Cobra probe	Manufacturer specifications
	δu	0.3 m/s	Cobra probe	Manufacturer specifications
	δv	0.3 m/s	Cobra probe	Manufacturer specifications
	δw	0.3 m/s	Cobra probe	Manufacturer specifications
	δu_{res}	0.3 m/s	Cobra probe	Manufacturer specifications
	δV_{train}	0.1 m/s	Trackside speed measuring devices	Manufacturer specifications
Full scale data	δu	0.1 m/s	Ultrasonic anemometer	Manufacturer specifications
	δv	0.1 m/s	Ultrasonic anemometer	Manufacturer specifications
	δu_{res}	0.1 m/s	Ultrasonic anemometer	Manufacturer specifications
	δV_{train}	0.25 m/s	Handheld speed gun	Manufacturer specifications

Table B.1: A table of measuring instrument accuracies for the slipstream velocity experiments.

B.3.1.2 Random uncertainty

The random uncertainty for the slipstream velocity measurements are calculated in terms of a normal distribution, considering a confidence level of 95%. The standard deviation is calculated with respect to individual resultant velocity measurements for each run in relation to the ensemble. It should be noted for full scale measurements, due to different freight types for each run, that the random uncertainty value is considered an over estimate of the random uncertainty in relation to a calculation considering individual freight types.

The random uncertainties for all configurations are shown in figure B.1(b) and the mean and maximum random uncertainty value shown in table B.2.

B.3.1.3 Total uncertainty

The total uncertainty for each consist is given as the sum of the bias limit and random uncertainty. Values for the total uncertainty at each probe position for all test configurations are shown in figure B.1(c). The mean and maximum total uncertainty values for the slipstream velocity measurements at both model and full scale are shown in table B.2.

The values in table B.1 provide an estimate to the uncertainties for slipstream velocity measurements at model and full scale. The uncertainties are considered to be conservative estimations to the true error. The values for bias limit for all consists at

	Bias limit		Random uncertainty		Total uncertainty	
	Mean	Maximum	Mean	Maximum	Mean	Maximum
Consist 1	0.016	0.017	0.053	0.092	0.069	0.108
Consist 3	0.016	0.017	0.047	0.074	0.063	0.090
Consist 5	0.016	0.017	0.047	0.073	0.063	0.089
Full scale	0.003	×	0.094	×	0.098	×

Table B.2: A table of mean and maximum bias, random and total uncertainties for slipstream velocities for each container loading configuration at model scale and mean values at full scale.

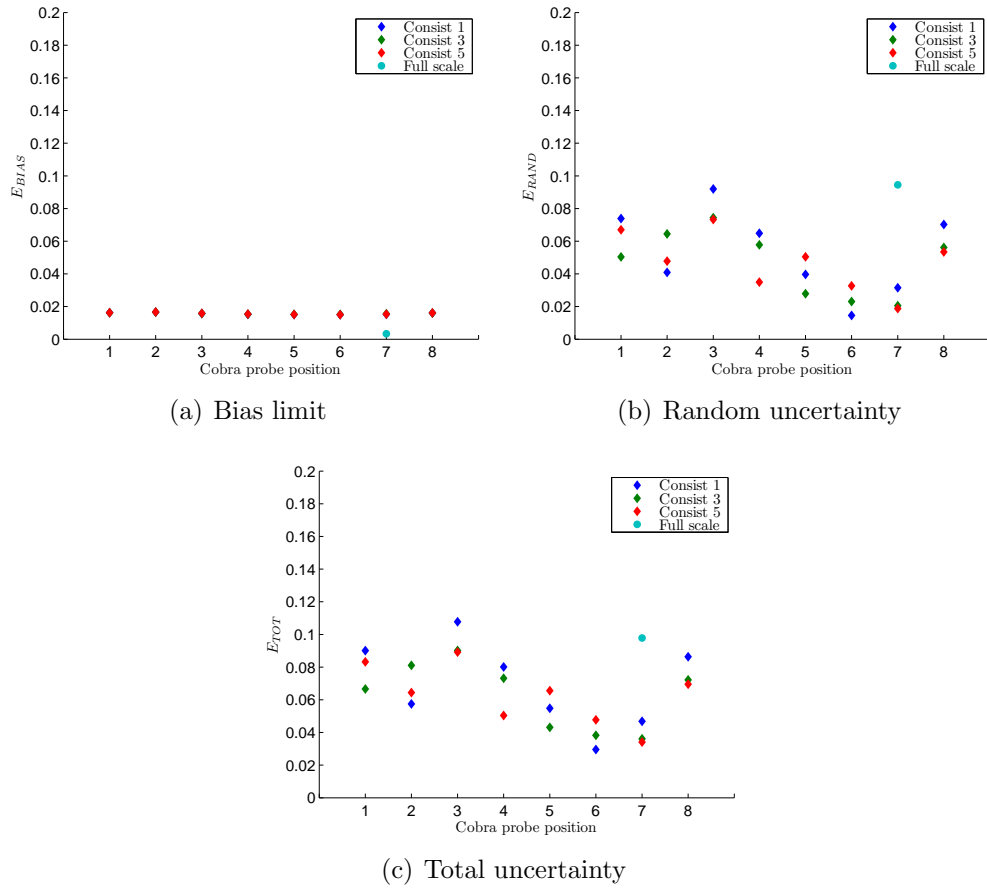


Figure B.1: The bias limit, random uncertainties and total uncertainties for slipstream velocity measurements at model scale for consists 1, 3 and 5 on the 181.25m freight train and at full scale.

both model and full scale are relatively small in comparison to the random uncertainty. At model scale run to run differences in flow development lead to a larger standard deviation of maximum resultant velocity values. At full scale the lack of consistent freight types creates different flow development for each run measured, creating a large standard deviation of maximum resultant velocity values. The position and magnitude of the resultant velocity is dependent on train type and loading configuration. At model scale the maximum resultant velocity is measured in the nose region, whereas at full scale values are either measured in the nose or boundary layer regions. It is hypothesised that if a single freight configuration was tested for a number of runs, that the random uncertainty values for full scale data would be similar to model scale. Previous slipstream studies have only calculated the bias limit as a measure for uncertainty (Baker et al., 2012), exhibiting similar results to the bias limits shown in table B.2. By including the random uncertainty, a measure of the unpredictability of flow development is included in the total uncertainty calculation.

B.3.2 Static pressure

The maximum and minimum pressure coefficient values are calculated for each container loading configuration at model scale for the 181.25m freight train, and each run at full scale. The uncertainties are calculated for both maximum and minimum pressure coefficient values and an average uncertainty value calculated.

B.3.2.1 Bias limit

The uncertainty for each measuring instrument is given in table B.3 in terms of model and full scale data. The value for air density is calculated through propagation of error theory in relation to the ideal gas law equation. The environmental pressure was measured using a Greisinger Electronic GPB 3300 station to an accuracy of 200Pa, and the temperature measured using an Oregon Scientific BAR208HG weather station to an

estimated accuracy of 1K. By propagation of error analysis the uncertainty associated to the air density is,

$$\begin{aligned}\delta\rho &= \sqrt{\left(\left(\frac{1}{RT_{room}}\right) * \delta P_{AMB}\right)^2 + \left(\left(\frac{-P_{AMB}}{RT_{room}^2}\right) * \delta T_{room}\right)^2} \\ &= 0.004\% * 1.23 = 0.005\text{kg/m}^3\end{aligned}\quad (\text{B.4})$$

It should be noted that the value of density is measured using the ideal gas law which does not take into account humidity. The process has been repeated with the ideal gas law form that does include humidity and no significant differences observed. The pressure transducers used in the full scale experiments are considered to have a linear response across the transducer range.

		Accuracy	Instrumentation	Source of information
Model scale data	$\delta \triangle P$	$\pm 5\text{Pa}$	Cobra probe	Manufacturer specifications
	δV_{train}	0.1 m/s	Trackside speed measuring devices	Manufacturer specifications
	$\delta\rho$	0.005 kg/m ³	Derived from ambient conditions	Manufacturer specifications
Full scale data	$\delta \triangle P_0$	$\pm 5\text{Pa}$	Trackside pressure transducers	Manufacturer specifications
	$\delta \triangle P$	$\pm 5\text{Pa}$	Trackside pressure transducers	Manufacturer specifications
	δV_{train}	0.25 m/s	Handheld speed gun	Manufacturer specifications
	$\delta\rho$	0.005 kg/m ³	Derived from ambient conditions	Manufacturer specifications

Table B.3: A table of measuring instrument accuracies for the slipstream static pressure experiments.

The bias limits for each container loading configuration at model scale and for all consists at full scale are shown in figure B.2(a). The mean and maximum bias limit value for all configurations are shown in table B.4.

B.3.2.2 Random uncertainty

The random uncertainty for the slipstream static pressure measurements are calculated in terms of a normal distribution, considering a confidence level of 95%. Unlike the slipstream velocity measurements where the maximum resultant velocity was measured at different points along the train, all maximum and minimum pressure values were measured in the Class 66 nose region at model and full scale. Therefore, values for the random uncertainty should be comparable at model and full scale.

The random uncertainties for all configurations tested are shown in figure B.2(b) and the mean and maximum random uncertainty values shown in table B.4.

B.3.2.3 Total uncertainty

The total uncertainty for each consist is given as the sum of the bias limit and random uncertainty. Values for the total uncertainty at each probe position for all configurations tested are shown in figure B.2(c). The mean and maximum total uncertainty value for the slipstream pressure measurements at both model and full scale are shown in table B.4.

	Bias limit		Random uncertainty		Total uncertainty	
	Mean	Maximum	Mean	Maximum	Mean	Maximum
Consist 1	0.020	0.021	0.030	0.041	0.051	0.061
Consist 3	0.021	0.022	0.030	0.045	0.051	0.066
Consist 5	0.020	0.022	0.026	0.033	0.047	0.055
Full scale	0.015	×	0.030	×	0.045	×

Table B.4: A table of mean and maximum bias, random and total uncertainties for slipstream static pressure for each container loading configuration at model scale and mean values at full scale.

The bias limit for model scale data is larger than full scale due to differences in measuring instrumentation accuracies. Values for bias limits are similar to those previously measured in model scale slipstream studies (Baker et al., 2012). As discussed, as maximum and minimum static pressure measurements are made in the Class 66 nose region, results for random uncertainties should be similar at model and full scale. Results in table B.4 show good agreement between model and full scale random uncertainties; values are relatively small suggesting good agreement between maximum and minimum values of individual runs. In comparison to slipstream velocities the values for random uncertainty in static pressure are smaller. Similarly to slipstream velocity uncertainties, by including the random uncertainty, a measure of the unpredictability of flow development is included in the total uncertainty calculation.

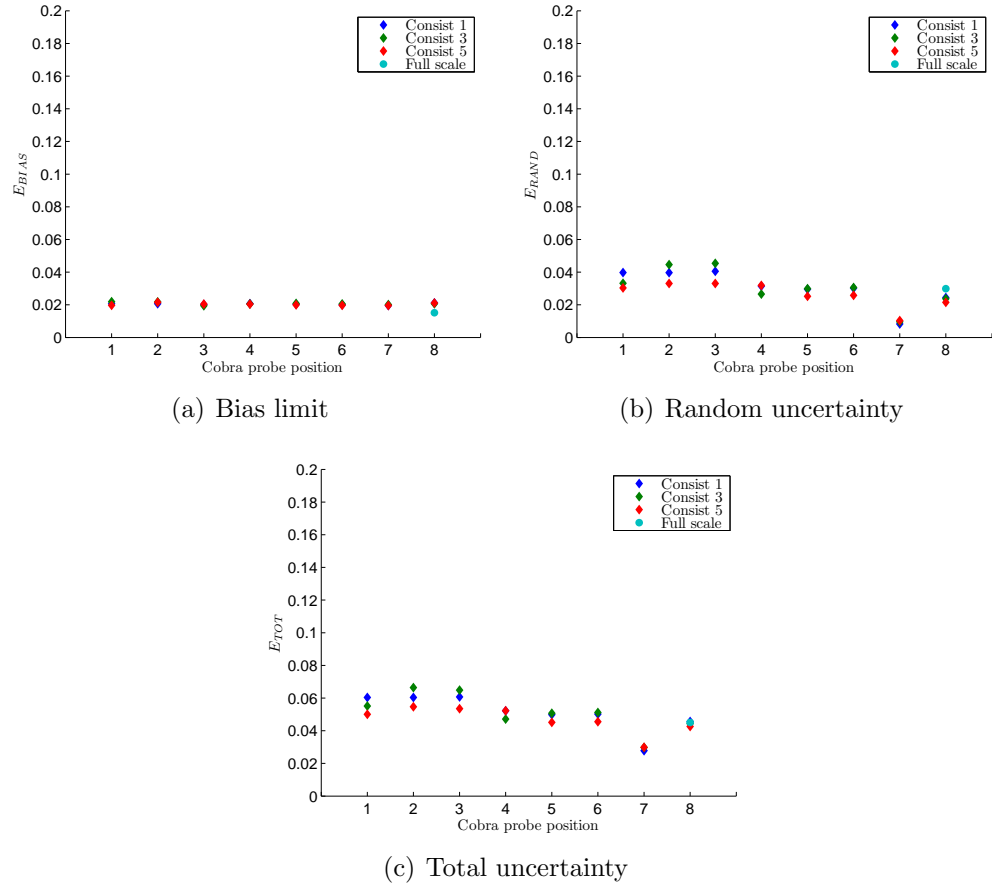


Figure B.2: The bias limit, random uncertainties and total uncertainties for slipstream static pressure measurements at model scale for consists 1, 3 and 5 on the 181.25m freight train and at full scale.

B.4 Aerodynamic load uncertainty methodology

The uncertainties associated to the aerodynamic load experiments are calculated in terms of mean pressure and aerodynamic load coefficients, with respect to the results presented in chapter 8. The method of calculating uncertainties, adopted from Dorigatti (2013), initially calculates the uncertainty of mean pressure coefficients, then, by applying propagation theory, the uncertainty of aerodynamic load coefficients.

B.4.1 Mean pressure coefficients

The mean pressure coefficient is calculated for each pressure tap on the measuring container surface for consists 1, 4 and 6 in both the open air and crosswind test sections.

B.4.1.1 Bias limit

The uncertainty for each measuring instrument is given in table B.5. As discussed previously, the air density was calculated through the propagation of error theory in relation to the ideal gas law equation. Similarly, the measurements of the crosswind velocities and static pressure, made with the Cobra probes, were extrapolated for each spanwise position. Therefore, using propagation theory the Cobra probe accuracies presented in table B.5 are used to calculate the uncertainty of the coefficient of pressure. To account for the non-linearity of the pressure transducers, a calibration is undertaken in appendix A, and maximal errors used as a measure of uncertainty. It should be noted that for the crosswind experiment multiple measurements are made with the on-board pressure transducers and Cobra probes. The repeated measurements are all considered independent, as measured in either separate portions of an individual run or independently measured by the instrumentation.

The bias limits for each pressure tap are shown in figures B.3-B.5 and the mean and maximum bias limit values for the open air and crosswind sections shown in table B.6.

	Accuracy	Instrumentation	Source of information
$\delta \triangle P_{ij}(S_N, \theta)$	$\pm 5 \text{ Pa}$	On-board pressure transducers	Static calibration
$\delta \triangle P_{ij,0}$	$\pm 3 \text{ Pa}$	On-board pressure transducers	Static calibration
$\delta \triangle P_{ST,loc}$	$\pm 9.5 \text{ Pa}$	Derived from Cobra probe measurements	Manufacturer specifications
$\delta \overline{u_{cwg,loc}}$	0.53 m/s	Derived from Cobra probe measurements	Manufacturer specifications
$\delta \overline{v_{cwg,loc}}$	0.53 m/s	Derived from Cobra probe measurements	Manufacturer specifications
$\delta V_{train}(S_N)$	0.1 m/s	Trackside speed measuring devices	Manufacturer specifications
$\delta \rho$	0.005 kg/m ³	Derived from ambient conditions	Manufacturer specifications

Table B.5: A table of measuring instrument accuracies for the aerodynamic load experiments.

B.4.1.2 Random uncertainty

The random uncertainty for the mean surface pressure coefficients in the open air and crosswind sections are calculated in terms of a normal distribution, considering a confidence level of 95%. The standard deviation is calculated with respect to individual mean pressure coefficients for each run in relation to the ensemble.

The random uncertainties for each pressure tap are shown in figures B.3-B.5. The mean and maximum random uncertainty values for the open air and crosswind sections are shown in table B.6.

B.4.1.3 Total uncertainty

The total uncertainty for each pressure tap is given as the sum of the bias limit and random uncertainty. Values for the total uncertainty for each pressure tap are shown in figures B.3-B.5. The mean and maximum total uncertainty value for the open air and crosswind sections for each consist are shown in table B.6.

The estimated total uncertainty is relatively constant for all container loading configurations. It is observed that the random uncertainty input is much less than the bias limit, however, the random uncertainty increases as the container loading efficiency decreases. In general, the bias limits for all consists remain relatively constant for each test section, as would be expected, as following equation B.1 all the input variables are similar. Bias limit values in the open air section are less than the crosswind section due

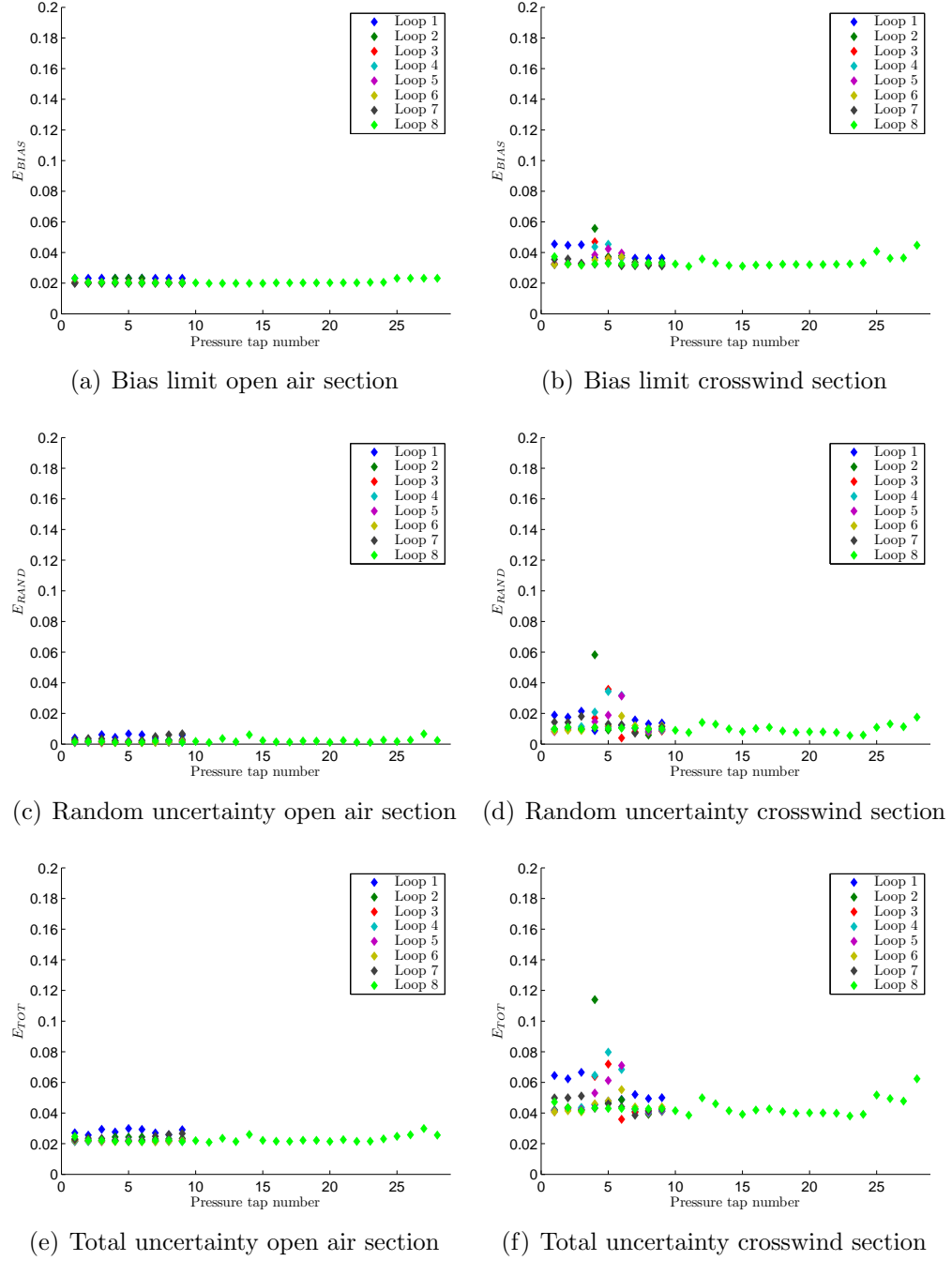


Figure B.3: The bias limit, random uncertainties and total uncertainties for consist 1 in the open air and crosswind test sections.

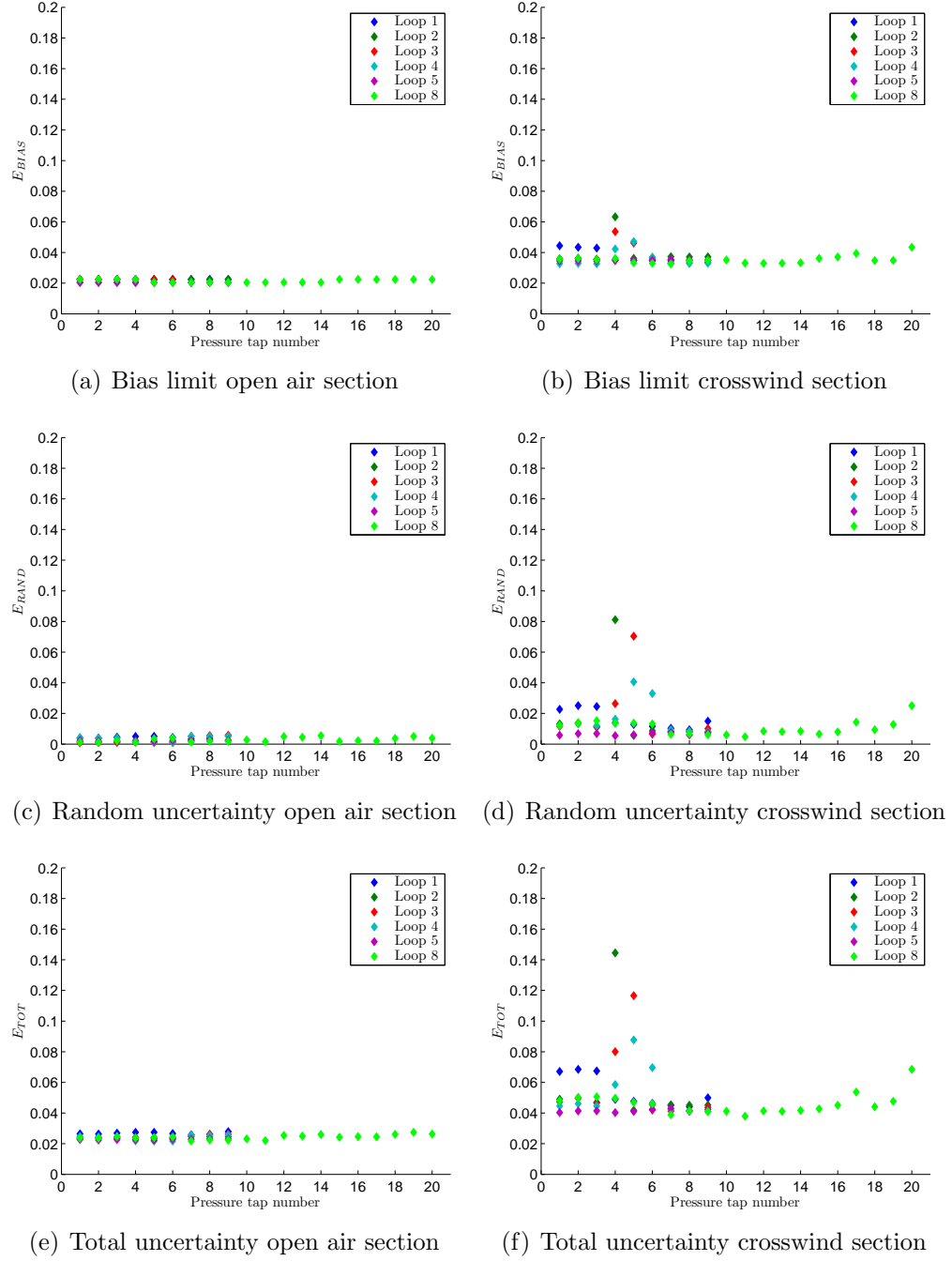


Figure B.4: The bias limit, random uncertainties and total uncertainties for consist 4 in the open air and crosswind test sections.

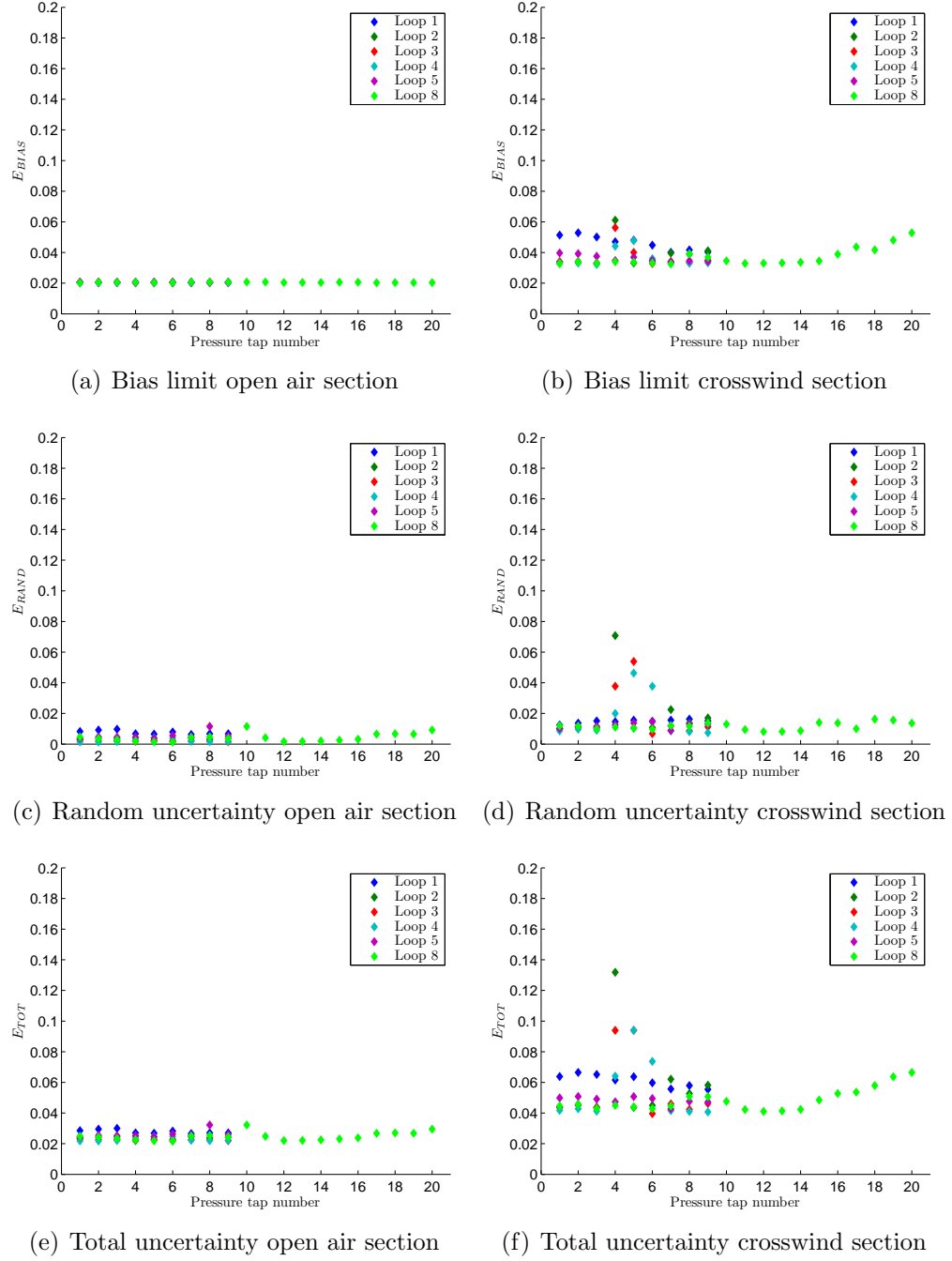


Figure B.5: The bias limit, random uncertainties and total uncertainties for consist 6 in the open air and crosswind test sections.

		Bias limit		Random uncertainty		Total uncertainty	
		Mean	Maximum	Mean	Maximum	Mean	Maximum
Consist 1	open air	0.021	0.023	0.002	0.007	0.023	0.030
	crosswind	0.034	0.056	0.011	0.058	0.045	0.114
Consist 4	open air	0.022	0.022	0.003	0.006	0.025	0.028
	crosswind	0.036	0.063	0.012	0.081	0.048	0.144
Consist 6	open air	0.020	0.021	0.005	0.012	0.025	0.032
	crosswind	0.038	0.061	0.014	0.071	0.052	0.132

Table B.6: A table of mean and maximum bias, random and total uncertainties for mean pressure coefficients.

to the lack of additional uncertainty variables associated with the crosswind. Similarly, values for random uncertainty in the open air are less than in the crosswind section, highlighting the stability of surface pressures in a non-crosswind situation.

B.4.2 Aerodynamic load coefficients

The uncertainties associated with the mean aerodynamic load coefficients are estimated relative to the uncertainties calculated for the mean pressure coefficients. Applying propagation theory to the aerodynamic load coefficient equations, defined in chapter 7, and assuming the load calculated for the discretised area associated to each pressure tap are independent, the uncertainty of the mean aerodynamic load coefficients can be defined as (Dorigatti, 2013),

$$E_{LOAD} = \sqrt{\sum_i \left(\sum_j \left(\frac{\partial C_\xi}{\partial C_{P_{ij}}} E_{TOT_{ij}} \right) \right)^2} \quad (B.5)$$

The uncertainties for aerodynamic load coefficients in the open air and crosswind sections are shown in table B.7.

The values in table B.7 provide an estimate to the uncertainties for each aerodynamic load coefficient. The uncertainties are considered to be less than the true error, as the calculation does not account for the uncertainty introduced through discretising the container geometry and by the assumption of pressure uniformity across each dis-

		C_X	C_Y	C_Z	C_{M_X}	$C_{M_{X,lee}}$
Consist 1	open air	0.012	0.008	0.006	0.006	0.007
	crosswind	×	0.016	0.018	0.014	0.016
Consist 4	open air	0.012	0.011	0.008	0.008	0.009
	crosswind	×	0.022	0.029	0.022	0.026
Consist 6	open air	0.013	0.012	0.008	0.008	0.009
	crosswind	×	0.022	0.028	0.022	0.025

Table B.7: A table of mean total uncertainties for aerodynamic load coefficients for the open air and crosswind test sections.

cretised area in the pressure integration process (Dorigatti, 2013). The uncertainty process was repeated for two further container discretisation methods and minimal differences observed between each. Dorigatti (2013) cited that a possible measure to assess the influence of the assumptions made through discretising the container surface would be to carry out the experiments using a force balance; however, the adoption of the alternative measuring instrumentation will change the value of E_{TOT} used in the calculation of aerodynamic load uncertainties.

Appendix C

Preliminary model scale experiments

C.1 Introduction

A series of preliminary experiments were designed and conducted to test the TRAIN rig facility and freight model, while analysing the suitability of the slipstream and aerodynamic load experiment setups (chapter 3 and 6) for different loading efficiencies. By analysing results of a series of preliminary experiments it was possible to make small amendments to the experiment methodologies for application within this study. Section C.2 introduces the preliminary experiment setup and methodology used. In section C.3 the preliminary experiment results are analysed and recommendations made in relation the final experiment setups and methodologies. Finally conclusions about the preliminary experiment findings are drawn in section C.4.

C.2 Experiment setup

The experiment setup and methodology adopted for the preliminary experiments was the foundations for the main series of experiments. A number of differences between

methodologies are discussed in the following sections; however, parts of the methods that are not altered are not presented again here, and can found in chapter 3 and 6.

Throughout this preliminary study consists 1 and 5 (figure 3.8) are used to represent a cross section of loading efficiencies; hypothesised to provide the largest spread in slipstream velocities. By conducting a series of preliminary experiments with differing loading efficiencies, it was possible to analyse the experiment methodology and the suitability of the model in relation to this method. The preliminary studies were undertaken before the 181.25m eight wagon freight train was developed, thus all experiments are carried out using the 101.25m four wagon freight train. Consist 1 was chosen to represent the heaviest loading configuration, providing a suitable test for the TRAIN rig firing and braking mechanisms. Consist 1 also provided a test configuration for the aerodynamic load experiments. Consist 5 was hypothesised to create slipstream velocities and pressures with the largest magnitudes in comparison to the other proposed loading efficiencies to be tested (figure 3.8), providing a suitable test for the Cobra probes and trackside equipment. In the preliminary slipstream experiments, 25 runs for consist 1 and 43 runs for consist 5 were completed. For the aerodynamic load preliminary experiment, 5 runs using consist 1 were carried out.

C.2.1 Slipstream experiment

The slipstream preliminary experiment setup set the foundations for the main experiments. The differences between preliminary and main slipstream experiments are discussed here; however, where no changes were made the experiment setup is as presented in chapter 3. Cobra probes were positioned at various distances from the train side to assess the suitability of the probe within a freight slipstream. The positions are shown in table C.1. The train speed was record by photoelectric light sensors and the ambient conditions were monitored. A light source and detector were positioned at the trackside in line with the Cobra probe measuring head to act as a position finder

for the train nose in the Cobra probe data files. The position finder data was used to justify the choice of the data alignment method (section 4.4). The light sensor consists of a torch with 1mm slitted cover and a Vishay Intertechnology Inc. phototransistor sensor (VISHAY-TEPT5600) (Vishay, 2011).

Probe number	Cobra Probe positions	
	Height (mm)	Distance from track centre (mm)
1	4500	0
2	2250	1750
3	2250	2375
4	2250	3000

Table C.1: Cobra probe measuring positions for the slipstream preliminary experiments.

An initial series of test firings were conducted to calculate the tension needed to create the required train speed; creating in effect a curve of tension against train speed for each train consist (table 3.2). Initially a train speed of $V_{train} = 33.5 \pm 0.5\text{m/s}$ was chosen, reflecting maximum UK freight train running speed (Temple and Johnson, 2003; Sterling et al., 2008). However, following five runs the train speed was reduced to $V_{train} = 25 \pm 0.5\text{m/s}$, as it was felt the model was unsuitable for a train speed of $V_{train} = 33.5\text{m/s}$, due to balsa wood components becoming loose.

C.2.2 Aerodynamic load experiment

The aim of these experiments was to assess the suitability of the model and measuring container under the loads experienced during the TRAIN rig firing process, and to ensure that surface pressures recorded by the on-board data logger would lie within the pressure transducer range. The aerodynamic load experiment setup is as discussed in chapter 6, however, the series of light sources acting as position finders were not included for the preliminary tests. A finding from the preliminary experiments was the need for additional train position finders in the crosswind generator section; thus the light sources were included for the main experiments. The train speed was recorded by photoelectric light sensors in the crosswind section and extrapolated from on-board

data for the open air section. Results from the open air section match train speed results from the slipstream experiments. The ambient conditions were monitored and recorded.

For the preliminary study consist 1 was loaded with the measuring container on the third wagon, such that the container end fitted with the pressure tap array was facing into the direction of travel. Following analysis of the results (section C.3.2), it was felt that additional variations to the measuring container position were not necessary.

Due to the additional weight of the on-board equipment within the measuring container, a further series of test firings were undertaken to calculate the tension needed to create the required train speed (table 6.2). A train speed of $V_{train} = 20.8 \pm 0.5 \text{ m/s}$ was chosen, as discussed, to create the appropriate yaw angle of 30° in the crosswind test section.

C.3 Preliminary experiment results

C.3.1 Slipstream experiment

For each loading configuration results showed it was possible for the train to run at the desired train speed past the Cobra probe setup. Following the preliminary experiments for each consist, the train was removed from the track and observed externally. No damage was observed to the model as a result of the forces incurred during the firing and braking processes.

Preliminary experimental data was aligned with respect to the train nose. The light source was positioned so that the light beam was in line with the measuring face of the Cobra probe head, creating an event finder for the train nose, as shown in figure C.1. The fall in voltage data corresponds with breaking the light beam, associated with the train passing. Similarly the rise and fall in voltage data, seen $\sim 20\text{m}$, corresponds to the small gap between the Class 66 locomotive and the container loaded onto the first

wagon. Results show the zero crossing between the maximum positive and negative pressure peaks to be the point at which the train nose passes the Cobra probes.

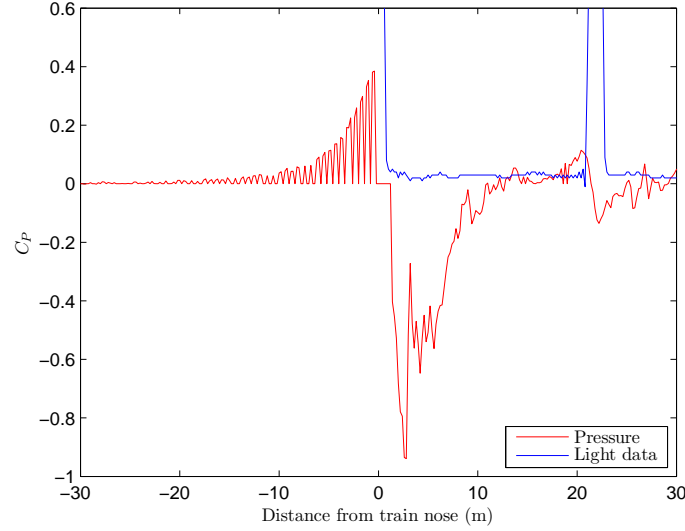


Figure C.1: Nose region coefficient of pressure data for an individual run (red) plotted with the voltage data from the nose region position finder (blue). The Cobra probe drop outs can be observed before the positive pressure peak as a series of zeroes. The drop outs are ignored in the slipstream analysis presented in chapter 5.

Data recorded was analysed, as in chapter 4, and ensemble averages for velocities and coefficient of pressure calculated. For consist 1 nine runs of useable data were recorded, whereas for consist 5 nineteen runs of useable data were recorded. Figure C.2 shows the normalised ensemble longitudinal velocity U and ensemble coefficient of pressure for each loading configuration at probe positions 2 to 4. The horizontal axis shown in figure C.2 is given in terms of full scale distance from the train nose, with negative values corresponding to distances ahead of the train nose.

An initial result from the slipstream data was the existence of high longitudinal slipstream velocities around the train nose, in the region of 120% of train speed close to the train side. Slipstream velocities of this magnitude have not previously been observed in passenger studies (Baker et al., 2001; Sterling et al., 2008). It was concluded that the high nose peak magnitude was related to the relatively non-aerodynamic shape of a Class 66 locomotive. The high longitudinal velocity magnitudes are of similar order to

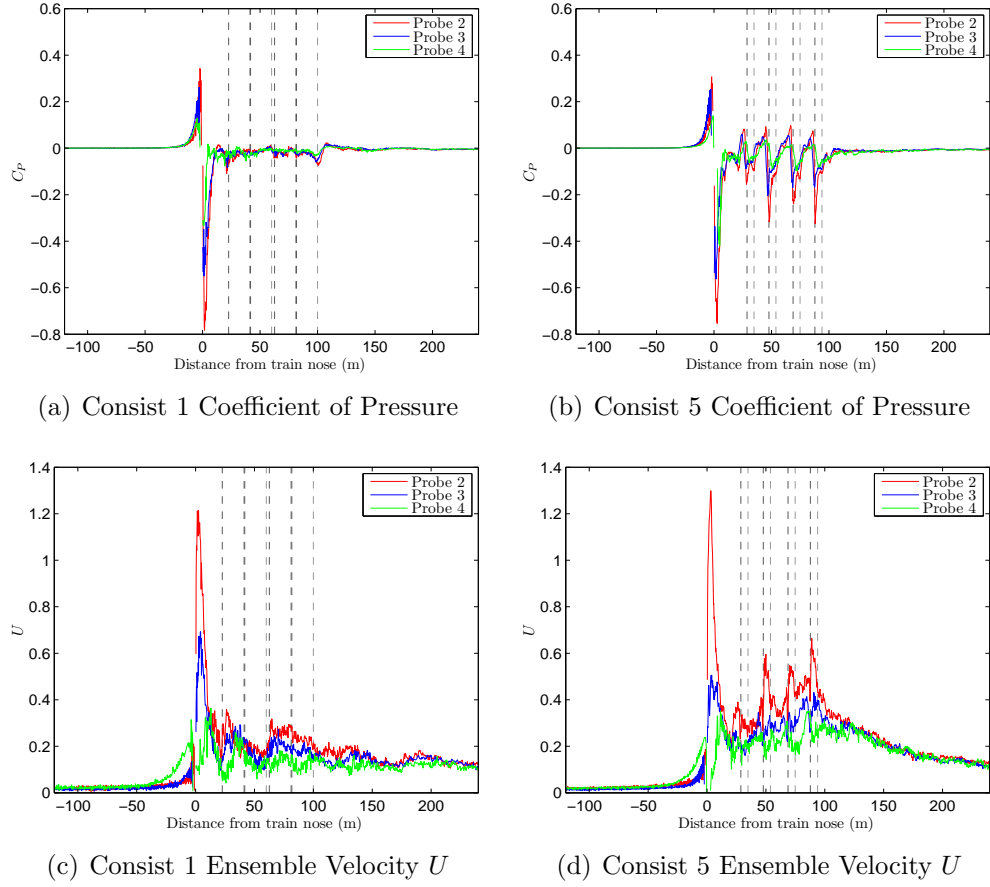


Figure C.2: Coefficient of pressure and normalised ensemble longitudinal velocity U results from the preliminary experiments for consists 1 and 5 recorded at train speed 25m/s for probes 2 (blue), 3 (red) and 4 (green). The vertical dashed lines indicate the front (black) and rear (grey) faces of the containers.

the maximum velocity cap of the Cobra probe operational range, creating lower data acceptance, resulting in no data recorded for half the runs undertaken (section 5.7).

Figure C.2 shows clear differences between loading configurations in both pressure and velocity. The influence of spaces in consist 5 between loaded containers for the coefficient of pressure creates a series of peaks, similar to those in the nose region, about the lead face of each container, whereas for consist 1 the coefficient of pressure remains relatively constant following the nose region. These observations are reflected in the boundary layer region of normalised ensemble longitudinal velocity U . For consist 5 a continual growth in velocity is witnessed with clear peaks close to the train side at container leading faces, whereas for consist 1 velocity remains relatively stable along the train length. The results highlight an issue of boundary layer development; for a container loading efficiency of less than 50% the transition between boundary growth and stability is not observed. By comparing the tension required to achieve the desired train speed for each container loading configuration (table 3.2), it was possible to design a freight model to include eight wagons, capable of working within the bounds of the TRAIN rig system and providing the opportunity to observe full boundary layer development for loading efficiencies of less than 50%.

C.3.2 Aerodynamic load experiment

Following the installation of the on-board data logger into the measuring container, the system was attached to the train for testing. Initially the crosswind generator fans were turned on and allowed to power up to full speed. The train was slowly pushed into the centre of the crosswind generator and held in place for 30 seconds, before being pushed out of the section. This process was repeated a number of times. The test showed the measuring container was securely attached to the train and was unlikely to become detached under the crosswind influence.

A series of five experiment runs were then completed using the methodology discussed

in chapter 6. Results showed it was possible for the train carrying the measuring container to run at the desired train speed through the open air and crosswind test sections. Following the experiments the measuring container was removed from the train and observed both externally and internally. No damage was observed to the measuring container or the model as a result of the forces incurred during the firing and braking processes; however it was noted that the initial mounting of the data logger did have a small amount of movement within the measuring container. For the main crosswind experiments additional internal bracing was placed within the container to stabilise the data logger.

Data recorded in the crosswind section was analysed, as in chapter 7, and ensemble averages calculated. As discussed, the lack of light sources acting as position finders created problems for aligning the crosswind data; thus an adaption to the experiment methodology was carried out to include light sources for the main experiments. The results are shown in figures C.3-C.4 for a pressure tap on each face tested. The areas highlighted in green are where the ensemble mean yaw angle $28^\circ < \overline{\theta}_{\text{ENS}} < 32^\circ$. Variations in the pressure coefficient at both ends of the time histories are created by the vehicle transition when entering and exiting the crosswind generator (Dorigatti, 2013).

The results shown are representative of all taps monitored during the preliminary experiments. In general good consistency is observed in pressure coefficient evolution within the central bounds of the crosswind generator (20% to 90% of crosswind generator length), and even when outside the ensemble mean yaw angle $28^\circ < \overline{\theta}_{\text{ENS}} < 32^\circ$ bounds. For each individual run there are a series of random high frequency fluctuations of similar amplitude about the ensemble pressure coefficient. These fluctuations are created by the turbulent nature of the flow developing around the train when subjected to the crosswind. For all tests the pressures measured were within the pressure transducer range, therefore no changes were required for the main experiments. The method of using an on-board measuring system and data logger within a model

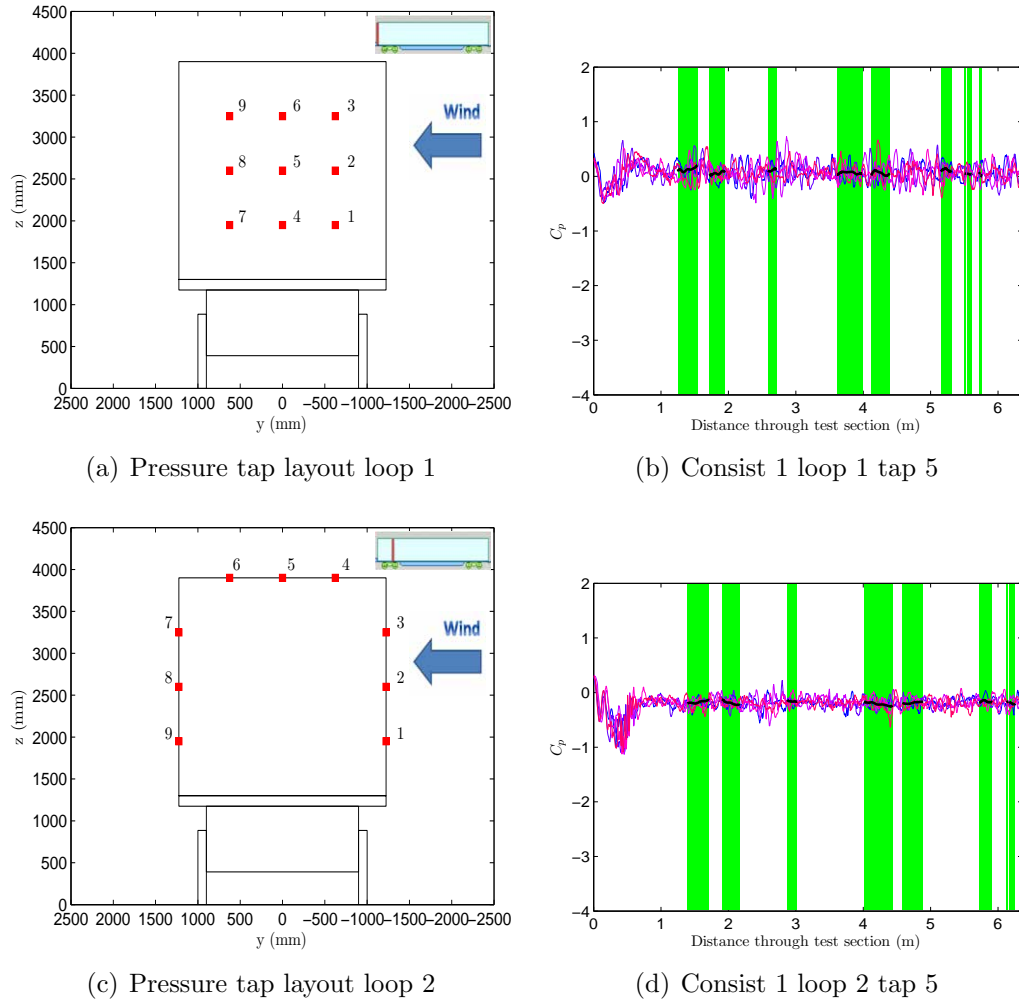
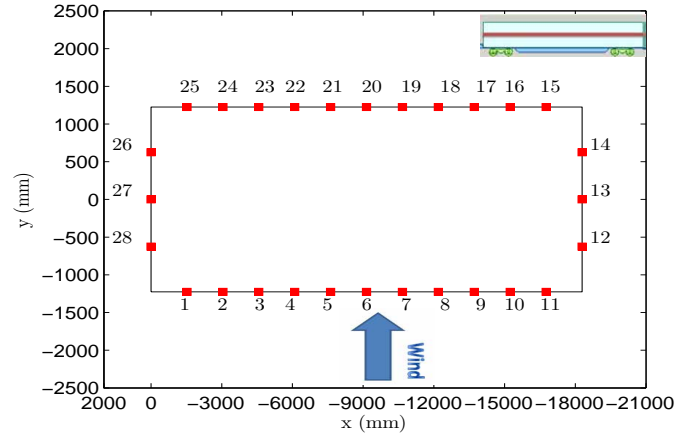
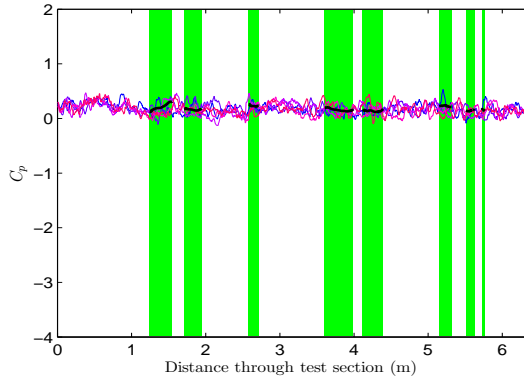


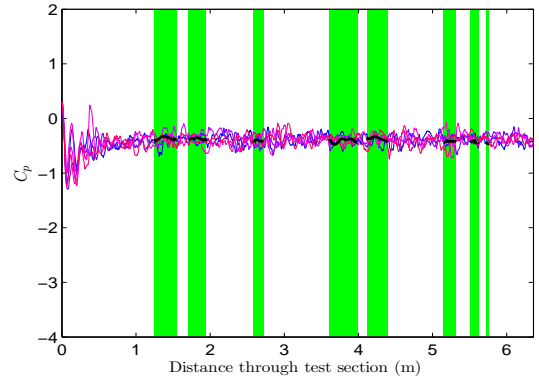
Figure C.3: Examples of the typical evolution of pressure coefficient as the train travels within the crosswind generator. A series of 5 individual runs from the preliminary experiments are plotted with corresponding deconstructed ensemble average time series for consist 1 loops 1 and 2. Areas highlighted green are where the ensemble mean yaw angle $28^\circ < \overline{\theta}_{\text{ENS}} < 32^\circ$.



(a) Pressure tap layout loop 8



(b) Consist 1 loop 8 tap 1



(c) Consist 1 loop 8 tap 25

Figure C.4: Examples of the typical evolution of pressure coefficient as the train travels within the crosswind generator. A series of 5 individual runs from the preliminary experiments are plotted with corresponding deconstructed ensemble average time series for consist 1 loop 8. Areas highlighted green are where the ensemble mean yaw angle $28^\circ < \overline{\theta}_{\text{ENS}} < 32^\circ$.

container was shown to work well for the freight train.

C.4 General concluding remarks

The results collected in the preliminary experiments highlight the successfulness of undertaking additional experiments to analyse the suitability of an experimental methodology. A series of conclusions can be drawn from the results and analysis presented in this appendix:

1. Slipstream results highlight the unsuitability of reaching the limit of the Cobra probe operating range within the slipstream around the model nose. The outcome of no data recorded for half the runs completed was calculated to be inappropriate for an experiment campaign within the allotted time available at the TRAIN rig. To negate the problem of data acceptance in relation to the Cobra probe operating range, the train speed was further reduced to $V_{train} = 20 \pm 0.5\text{m/s}$.
2. Data measured using the light source and position finder in line with the Cobra probe heads proved the validity of the slipstream data processing methodology to align the data with respect to the pressure peaks at the Class 66 nose.
3. It is possible to present slipstream results as a series of flow regions, exhibiting clear differences in slipstream development for differing container loading configurations.
4. Comparison of slipstream development for consist 1 and 5 highlighted the lack of boundary layer transition, from growth to stability, for the poor loading efficiency of consist 5. The preliminary results were used as a point of development for the 181.25m eight wagon freight train.
5. Aerodynamic load experiment results show the methodology of using an on-board surface pressure monitoring system for the TRAIN rig freight model was accept-

able and provided results to develop an understanding of the forces subjected to a loaded container through open air and crosswind situations.

6. Analysis of results highlighted the need for additional light sources and position finders to align surface pressure data with respect to the crosswind generator.
7. Surface pressure results exhibit good consistency through the open air and crosswind sections. All results are shown to be within the pressure transducer range of operation.

Appendix D

Ensemble sensitivity analysis

D.1 Introduction

In this appendix the method of ensemble averaging will be discussed in relation to the slipstream and aerodynamic load experiments. By analysing Cobra probe velocity and static pressure data and the pressure transducer static pressure data, it is possible to assess the stability of ensemble averages with respect to an increasing ensemble size, and compare this with the ensemble requirements from the TSI standards. The method of ensemble averaging in relation to freight slipstreams is discussed at length in section 5.2. This discussion is developed further in section D.2, by analysing the process of ensemble averaging and the application through the TSI methodology. Ensemble stability analysis, developed in section 5.2, is further discussed in this appendix by applying a correlation coefficient analysis and the bootstrap method to a standard deviation analysis, focusing on results from the slipstream (section D.3) and aerodynamic load (section D.4) experiments. Finally, conclusions are drawn in section D.6 on the suitability of ensemble sizes in relation to model scale experiments and the relevance of a small ensemble size for full scale experiments.

D.2 Ensemble averaging methodology

Ensemble averaging is a method based on the assumption of the existence of independent statistical events (George, 2004). Experimental data may have considerable test to test differences, inhibiting averages to be taken by a normal method. Ensemble averaging is a method by which to overcome problems encountered due to these differences. Considering all r realisations of a variable c as independent, the ensemble average can be defined as (George, 2004),

$$C = \langle c \rangle \equiv \frac{1}{N} \lim_{N \rightarrow \infty} \sum_{r=1}^N c_r \quad (\text{D.1})$$

It is however impossible to ever obtain the ensemble average experimentally, as it is not possible to record an infinite number of independent realisations. Therefore, within experimental work it is only possible to calculate an estimate of the ensemble average, based on the mean of independent realisations (George, 2004). By calculating the stability of fluctuations in the experimental mean with respect to an increasing number of realisations in the mean calculation, it is possible to estimate the number of independent realisations needed to create a stable ensemble average.

Results gained from experiments can be non-dimensionalised and averages constructed using non-dimensional coefficients (Deeg et al., 2008). To non-dimensionalise velocity and pressure a standard reference speed can be used to resample data in relation to the varying local train speed, as in equations 4.3–4.6 (Deeg et al., 2008). By assuming a signal $c(x)$ is measured N times in respect to an axial coordinate position x , relating to a defined position along the train, the ensemble average $\bar{c}(x)$, variance $var(x)$ and standard deviation $\sigma(x)$ are then defined as (Deeg et al., 2008),

$$\bar{c}(x) = \frac{1}{N} \sum_{r=1}^N c_r(x), \quad \overline{c^2}(x) = \frac{1}{N} \sum_{r=1}^N c_r^2(x), \quad var(x) = \overline{c^2} - \bar{c}^2 \quad \sigma(x) = \sqrt{\overline{c^2} - \bar{c}^2}, \quad (\text{D.2})$$

where r is the r^{th} passage of a train and N denotes the number of independent mea-

surements, or the ensemble size.

Although equation D.2 provides an estimate to the ensemble average in equation D.1, since an infinite number of realisations are not possible, how many realisations are needed to create a mean capable of estimating the ensemble? In general, to be an estimator to the ensemble average, as the number of realisations is increased the mean should converge to the ensemble average value (George, 2004). Therefore, as the number of realisations is increased the variation in mean value should reduce. Figure 5.2 in section 5.2 illustrates the effect of an increasing ensemble size for an example of slipstream velocities. As the number of runs contained in the ensemble increases so the variability decreases. By creating an ensemble average it is possible to pick out key statistical events in the flow.

European TSI standards state an experiment should be conducted at least 20 times to validate results and create ensemble averages without the influence of run to run variability (TSI, 2008; Gil et al., 2008). It has however been shown in chapter 5 that achieving an ensemble size of 20 is difficult for full scale experiments, which are in general expensive and difficult to complete, with results highly susceptible to changes in ambient conditions. Model scale experiments offer a cheaper, easier option to create large data sets for an ensemble analysis approach to understanding slipstream development, but results need validation.

The ensemble size needed to create a stable ensemble average is dependent on the standard deviation of individual realisations to the mean. In relation to freight data, static pressure ensemble averages are more stable than velocity ensemble averages, and the stability of an ensemble average is dependent on container loading configuration.

In section 5.2 ensemble stability was assessed by calculating the percentage difference between ensemble averages at each time step for slipstream velocities and static pressure. This analysis is extended by calculating the change in correlation coefficient as the ensemble size is increased. A bootstrap method is also applied to assess the

standard deviation evolution with respect to an increasing ensemble size.

D.2.1 Correlation coefficient

The correlation coefficient is a measure of strength of a linear relationship (Derrick et al., 1994). By calculating the correlation coefficient between ensemble average time histories for an increasing number of runs, it is possible to examine whether the stability of the ensemble average increases as the number of runs contained in the ensemble increases. For the consists analysed, $N=25$ runs were carried out for the slipstream experiments and $N=20$ runs for the aerodynamic load experiments. For ease of presentation, the analysis technique definitions are considered in terms of a series of $N=25$ realisations. A series of ensemble averages are calculated for an ensemble size of $N=2$ to 25. The correlation coefficient is calculated between each pair of ensemble averages as,

$$(\gamma_i)_{N-1,N} \tag{D.3}$$

for $3 \leq N \leq 25$. To quantify the change in correlation coefficient between each pair of ensemble averages, the difference between pairs of correlation coefficients is calculated,

$$(\Delta\gamma_i)_N = (\gamma_i)_{N-1,N} - (\gamma_i)_{N-2,N-1} \tag{D.4}$$

for $4 \leq N \leq 25$. Low values of $(\Delta\gamma_i)_N$ indicate small changes occur between the pair of ensemble averages tested; values close to zero exhibit a high ensemble average stability.

D.2.2 Standard deviation method

In figure 5.2 as the ensemble size is increased the variation in the ensemble average decreases. To quantify this decrease it is possible to calculate the standard deviation about the ensemble average with respect to an increasing ensemble size. Dorigatti (2013) presented an analysis of standard deviation in relation to an ensemble average

with an increasing ensemble size. The method of analysis is adopted in this study for analysing slipstream, as well as, aerodynamic load results.

Considering a series of N experimental runs $c_r(x) = \{c_1(x), c_2(x), \dots, c_N(x)\}$ it is possible to define the ensemble average $\bar{c}_N(x)$ and standard deviation $\sigma_N(x)$. Dorigatti (2013) defines the standard deviation of the ensemble average time history as,

$$\sigma_{\bar{c}_N}(x) = \frac{\sigma_N(x)}{\sqrt{N}} = \frac{\sqrt{\frac{1}{N-1} \sum_{r=1}^N (c_r(x) - \bar{c}_N(x))^2}}{\sqrt{N}} \quad (\text{D.5})$$

In essence this parameter gives an estimate of the uncertainty relating to the ensemble average; therefore, a smaller value for $\sigma_{\bar{c}_N}(x)$ indicates a more accurate estimation of the ensemble average (Dorigatti, 2013). By calculating the time average value $\overline{\sigma_{\bar{c}_N}}$ and the standard deviation of $\sigma_{\bar{c}_N}(x)$ it is possible to analyse the uncertainty associated with the ensemble average, with respect to an increasing ensemble size.

To develop the robustness of this method of analysis in relation to the statistical calculation, Dorigatti (2013) cited that an increased sample size N was needed; thus by applying a bootstrap method 500 times to the N experiment runs it is possible to estimate the effects of an increased sample size (Efron and Tibshirani, 1994). The bootstrap method essentially randomly resamples the sample $c_r(x)$ of N runs, creating $B(= 500)$ new sample data sets $c_{b,r}(x)$ of size N runs (Efron and Tibshirani, 1994). Each bootstrap sample set $c_{b,r}(x)$ contains a random section of N time histories from the original sample $c_r(x)$. The standard deviation of the ensemble average time history can then be redefined in relation to the bootstrap method (Efron and Tibshirani, 1994; Dorigatti, 2013),

$$\sigma_{\bar{c}_N}(x) \equiv \sigma_{\bar{c}_N}^{BS}(x) = \frac{\sqrt{\sum_{b=1}^B \left(\bar{c}_{b,N}(x) - \frac{1}{B} \sum_{b=1}^B (\bar{c}_{b,N}(x)) \right)^2}}{\sqrt{B-1}} \quad (\text{D.6})$$

Similarly by calculating the time average value $\overline{\sigma_{\bar{c}_N}^{BS}}$ and the standard deviation of $\sigma_{\bar{c}_N}^{BS}(x)$ it is possible to analyse the uncertainty associated with the ensemble average

with respect to an increasing ensemble size for a bootstrap sample size of 500 sample data sets.

D.3 Cobra probe ensemble analysis

Throughout the Cobra probe ensemble stability analysis, results from consists 1 and 5 are presented. Consist 1 and 5 have been chosen to represent the extremes of loading efficiency for this analysis. Individually, consist 1 presented the most stable results from all loading configurations and can be considered similar to a passenger train for analysis purposes. Consist 5 was chosen for this analysis as the largest variations in velocities and pressure are witnessed for this loading configuration, and thus can be considered the most extreme configuration tested, providing a base case for all other loading configurations. For all cases the largest variations in velocities and pressure are observed close to the train side; this analysis will focus on probe positions 1 and 2 (table 3.1). The analysis is undertaken for the region $-100\text{m} \leq x \leq 300\text{m}$, which includes the upstream, nose, boundary layer, tail and wake regions.

D.3.1 Correlation coefficient results

Figure D.1 illustrates the correlation coefficient differences for an increasing ensemble size for consists 1 and 5, measured for the 181.25m freight train at probe positions 1 and 2. For all cases the change in correlation coefficient $(\Delta\gamma_i)_N$ tends to zero, exhibiting good stability in the ensemble average. For U and C_p the values of $(\Delta\gamma_i)_N$ tend to zero rapidly, whereas values for V and W do decrease but at a slower rate. This analysis indicates that to create a stable ensemble average an ensemble size of at least 15 realisations is needed; however, an ensemble size of 20 realisations, in line with TSI methodology provides a highly stable ensemble average for all cases analysed. The influence of these findings in relation to a moving ensemble size adopted within this

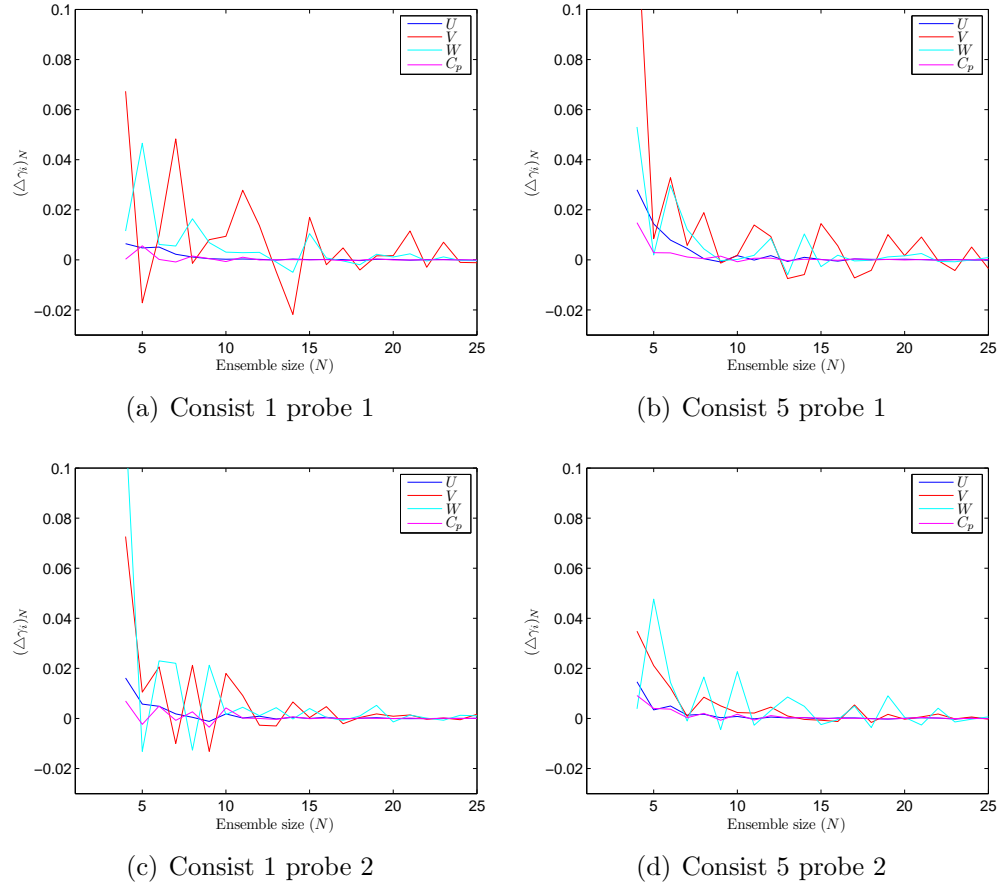


Figure D.1: Correlation coefficient differences relative to a changing ensemble size. Analysis is undertaken for consists 1 and 5 at probe positions 1 and 2 for U (blue), V (red), W (cyan) and C_p (magenta).

study is discussed further in section D.6.1.

D.3.2 Standard deviation results

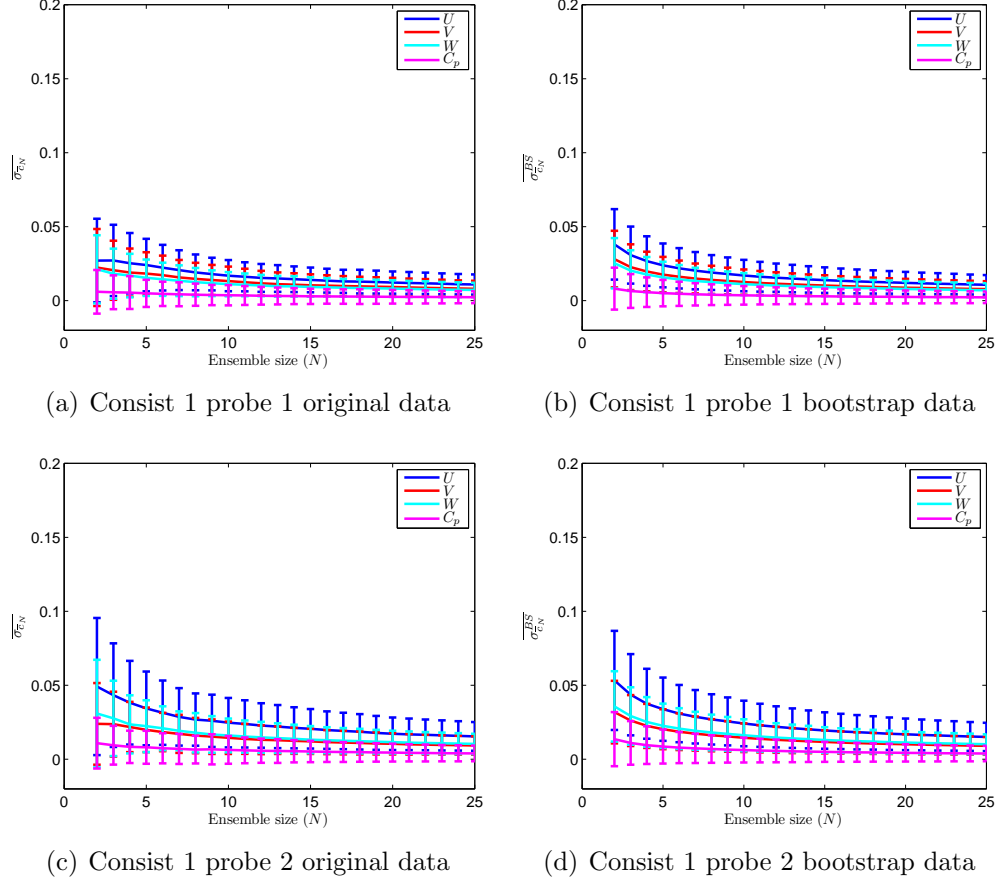


Figure D.2: Standard deviation analysis results for original data set $\overline{\sigma_{\bar{c}_N}}$ and the bootstrap method $\overline{\sigma_{\bar{c}_N}^{BS}}$. Analysis is undertaken for consist 1 at probe positions 1 and 2 for U (blue), V (red), W (cyan) and C_p (magenta).

The time average values for $\overline{\sigma_{\bar{c}_N}}$ and $\overline{\sigma_{\bar{c}_N}^{BS}}$ are shown in figures D.2-D.3, plotted with the associated error bars, calculated as the standard deviation. Good agreement is observed between the original sample size of $N = 25$ and the bootstrap method. As the ensemble size increases the time average values for standard deviation and the error bars decrease to zero, exhibiting stability of the ensemble average. The analysis agrees with results from section D.3.1, indicating an ensemble size of at least 15 realisations is needed to create a stable ensemble average. Therefore, the TSI methodology of 20

realisations provides a highly stable ensemble average.

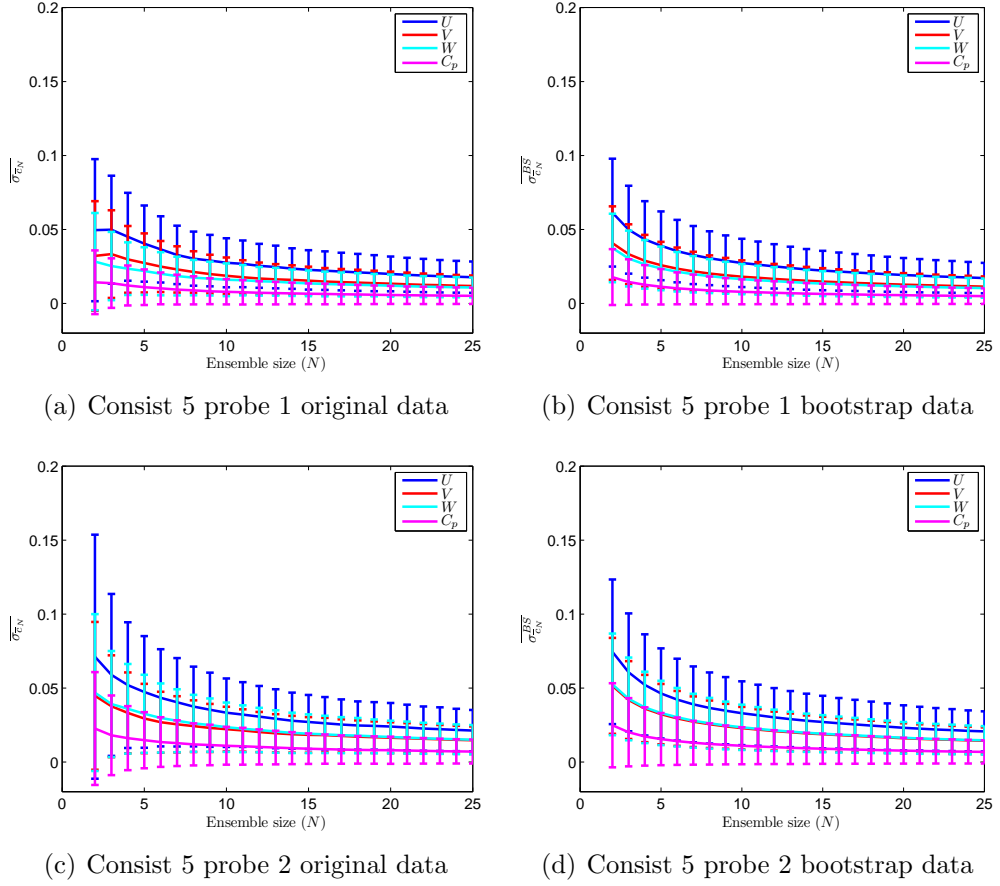


Figure D.3: Standard deviation analysis results for original data set $\overline{\sigma_{\bar{c}_N}}$ and the bootstrap method $\overline{\sigma_{\bar{c}_N}^{BS}}$. Analysis is undertaken for consist 5 at probe positions 1 and 2 for U (blue), V (red), W (cyan) and C_p (magenta).

D.4 Pressure transducer ensemble analysis

Due to time constraints it was not possible to make many additional experiment runs for the aerodynamic load experiments. Dorigatti (2013) showed, from carrying out ensemble stability analysis, that 15 experimental runs were necessary to create a stable ensemble average; therefore for the majority of aerodynamic load tests in this study 15 runs were undertaken. To complete a comparable test with Dorigatti (2013), an additional 5 runs were carried out for a series of pressure taps on consist 1. The largest variations in pressure are observed close to the container leading end and across the

roof. The following analysis will focus on pressure tap loops 1 and 2 (figures 6.14-6.17). The analysis is conducted for the region when the train is in the crosswind section.

D.4.1 Correlation coefficient results

The correlation coefficient differences observed for an increasing ensemble size tend to zero for all pressure taps tested. This finding exhibits good stability in the ensemble average for every pressure tap. Figure D.4 indicates to create a stable ensemble average, an ensemble size of at least 10 realisations is needed. An ensemble size of 15 realisations, as adopted by Dorigatti (2013), provides a highly stable ensemble average for all cases.

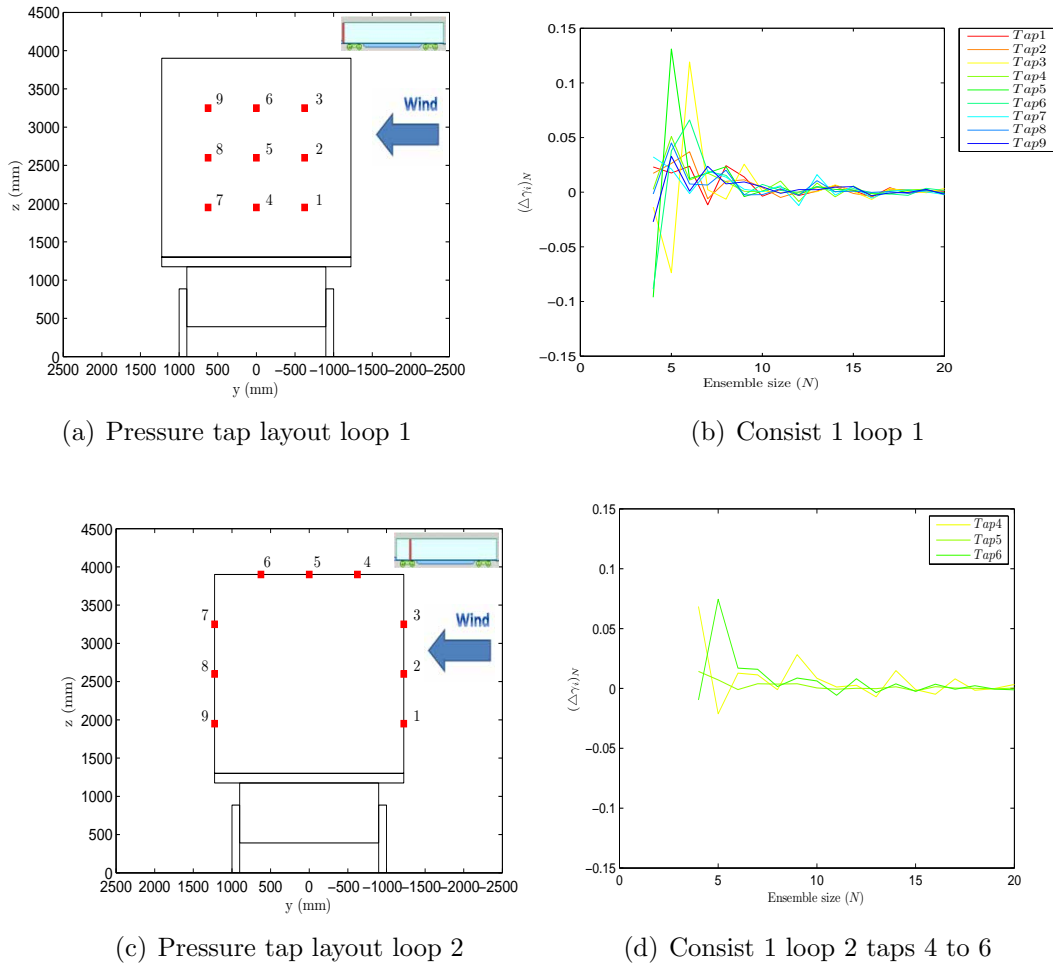


Figure D.4: Correlation coefficient differences relative to a changing ensemble size. Analysis is undertaken for consists 1 at loops 1 and 2.

D.4.2 Standard deviation results

The time average values for $\overline{\sigma_{\bar{c}_N}}$ and $\overline{\sigma_{\bar{c}_N}^{BS}}$ for consist 1 loops 1 and 2 are shown in figure D.5, plotted with the associated error bars, calculated as the standard deviation. The loop and pressure tap arrangements are shown in figure D.4. Good agreement is observed again between the original and the bootstrap methods. The results exhibit increasing stability in the ensemble average as the ensemble size increases. The standard deviation values exhibit relative stability after 13 realisations, indicating that an ensemble size of at least 13 realisations is needed to create a stable ensemble average. Therefore, an ensemble size of 15 realisations, as suggested by Dorigatti (2013), provides a highly stable ensemble average.

D.5 Full scale ensemble analysis

The Uffington full scale data analysed consisted of eight Class 66 hauled freight trains, with differing wagon types and loading configurations. As the Class 66 locomotive was the only constant for each data sample, it was only possible to create an ensemble average within the train nose region; defined in the analysis as $\pm 18.75\text{m}$. The standard deviation analysis with respect to a changing ensemble size, using a bootstrap method, is applied to the full scale data. The analysis is carried out for the pressure probes positioned 2m from the centre of track and 1m above the top of the rail, a distance of 39.5m apart and an ultrasonic anemometer at the TSI equivalent position 3m from the centre of track and 0.7m above the top of the rail. As the pressure probes were at a repeated position the maximum ensemble size for static pressure is 16 samples; whereas for the TSI velocity measurements only 8 samples are available. The analysis is carried out for both the full and model scale experiments, focusing on data from the Class 66 nose region, defined as $\pm 18.75\text{m}$.

The time average values for $\overline{\sigma_{\bar{c}_N}}$ and $\overline{\sigma_{\bar{c}_N}^{BS}}$ suggest good agreement between model and

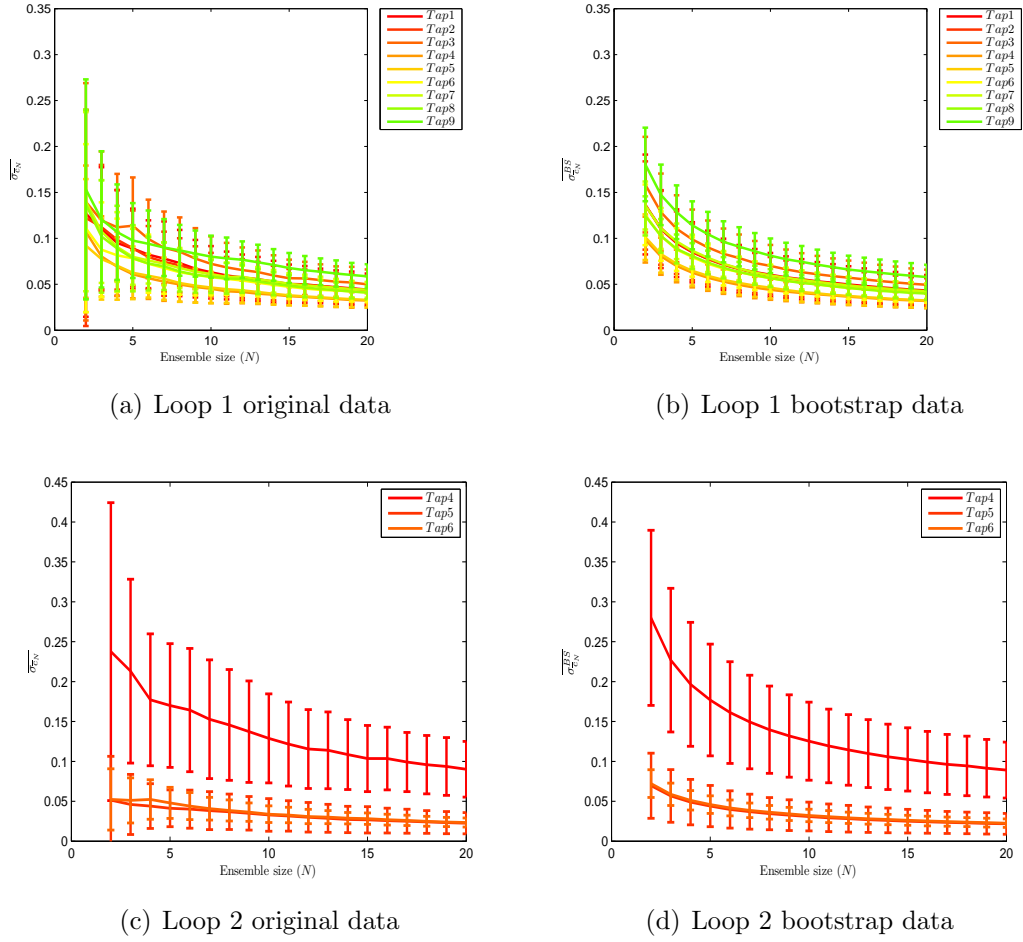
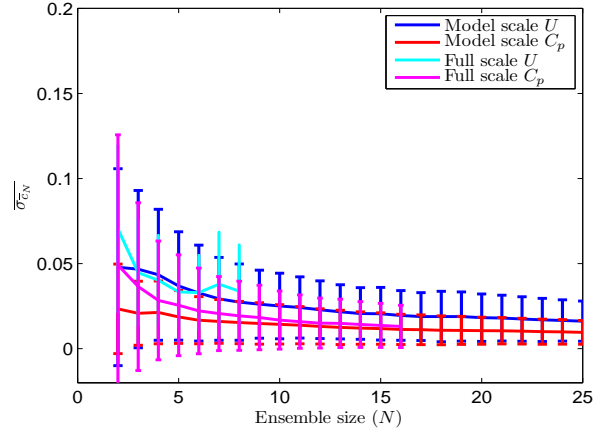
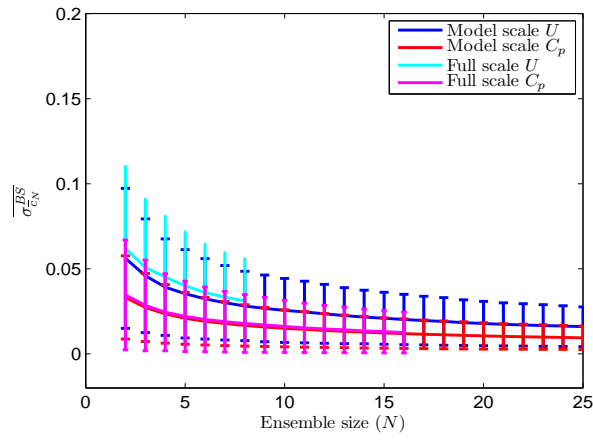


Figure D.5: Standard deviation analysis results for original data set $\overline{\sigma_{\bar{c}_N}}$ and the bootstrap method $\overline{\sigma_{\bar{c}_N}^{BS}}$. Analysis is undertaken for pressure taps in consist 1 loops 1 and 2.



(a) Full and model scale original data



(b) Full and model scale bootstrap data

Figure D.6: Standard deviation analysis results for original data set $\overline{\sigma_{\bar{c}_N}}$ and the bootstrap method $\overline{\sigma_{\bar{c}_N}^{BS}}$ for the full and model scale nose region data for U and C_p .

full scale data, and between the original and bootstrap method of calculation. Full scale data exhibits an increasing stability in the ensemble average as the ensemble size is increased, and is generally limited within the model scale error bounds. Analysis indicates that a similar number of realisations are needed to create a stable ensemble average in the full scale data as in the model scale data.

D.6 Discussion

D.6.1 Moving ensemble size

An issue associated with the ensemble averaging process and Cobra probe results is the $\pm 45^\circ$ cone of influence, which if exceeded creates a zero in the outputted time series. To eliminate the Cobra probe cone of influence issue in relation to the ensemble average, the zero data is disregarded in the ensemble calculation. Therefore a moving ensemble size at each time step is employed. If a zero is recorded for every run at a time step, the measured region is considered individually; either the region is in still air before the train, or the region is highly turbulent and a possible flow reversal has occurred. Analysis of the influence of a moving ensemble size, in section 5.2, showed the ensemble size varies dramatically with position. The average ensemble size is much smaller in the upstream region in comparison to the train and wake regions. As the distance along the train is increased the ensemble size increases. An analysis of the percentage of time steps with ensemble size greater than or equal to 20 indicated the influence of a moving ensemble size. For all regions the percentage of time steps greater than or equal to 20 is 53.5%, however if the upstream region is removed this increases to 75%. Altering the ensemble size criteria revealed over 80% of the time steps in the train region have an ensemble size of 17 or greater. Analysis highlighted the difference between the ensemble average for an ensemble size of 17 and 20 to be minimal ($\pm 2\%$), similar to the error associated with the Cobra probe.

In comparison to the Cobra probe analysis undertaken in this appendix, it is shown in sections D.3.1-D.3.2 that an ensemble size of 15 realisations for all components of velocity and the static pressure are needed to create a stable ensemble average. As discussed, applying the TSI methodology with an ensemble size of 20 is shown to provide a highly stable ensemble average. In relation to the moving ensemble size it is shown the difference in ensemble stability between 17 and 20 runs, as shown in section 5.2, is minimal and within the Cobra probe error range. It is concluded that the method of applying a moving ensemble size, to account for dropouts in the Cobra probe data, is appropriate for this study.

D.6.2 Full scale vs model scale

In chapter 5 a discussion regarding the suitability of the TRAIN rig to carry out model scale freight slipstream measurements to create an understanding of the flow development around a container freight train was carried out. Results found that although the magnitude of key flow features was replicated, it is suggested that finer turbulent scales may not be modelled accurately and further full scale measurements are needed to provide suitable comparisons.

Full scale measurements are in general difficult and expensive to carry out, and to create an ensemble size with the same freight train configuration in line with TSI standards is not possible. The analysis in section D.5 suggests a similar degree of variation between individual runs at both model and full scale, with the full scale data presented falling to within similar error bounds of the model scale data. Good agreement between model and full scale data is observed for the original and bootstrap method of calculation; exhibiting an increasing stability in the ensemble average as the ensemble size is increased. As the analysis matches closely it is possible to use the model scale results for larger ensemble sizes to predict the number of realisations needed at full scale to create good ensemble stability. Analysis in section D.6.1 suggests an ensemble size of

15 runs is needed to create a stable ensemble average in both U and C_p . Although this ensemble size is only 5 runs smaller than that suggested within the TSI methodology, it reduces the number of independent realisations needed to be undertaken, given the difficulty of conducting full scale measurements. Applying an experiment methodology with multiple probes at one measuring position, as for the pressure probes in the Uffington data (chapter 3), would allow for numerous measurements to be taken for one train passage, reducing the number of individual train passes needed.

D.6.3 General concluding remarks

A series of conclusions can be drawn from the results and analysis presented in this appendix:

1. Correlation coefficient and standard deviation analysis for slipstream and aerodynamic load experiments has shown good stability in ensemble averages for all results tested.
2. Ensemble average stability increases as the ensemble size increases.
3. The associated error bars to the standard deviation analysis are shown to decrease in size as the ensemble size increases.
4. Results indicate to create a stable ensemble average an ensemble size of at least 15 realisations for Cobra probe measurements and 13 for pressure transducer measurements are needed.
5. Analysis indicates good agreement between full and model scale data, suggesting an ensemble of at least 15 realisations is needed to create stable ensemble averages in U and C_p at full scale.
6. The moving ensemble size adopted within the slipstream study is shown to be a suitable method to account for dropouts in the Cobra probe data.

7. Analysis has shown the ensemble size suggested by the TSI methodology will lead to a stable ensemble average.

Appendix E

Author's publications

E.1 Introduction

In this appendix the following conference papers written by the author in relation to the work discussed in this PhD study are presented:

David Soper, Prof Chris Baker, Prof Mark Sterling: The slipstream development of a container freight train. European and African Conference on Wind Engineering, Cambridge, UK, 2013.

David Soper, Prof Chris Baker, Prof Mark Sterling, Dr Andrew Quinn: A comparison of model and full scale experimental data to assess the suitability of analysing slipstream development of a container freight train using the TRAIN rig facility. First international conference in numerical and experimental aerodynamics of road vehicles and trains (Aerovehicles 1), Bordeaux, France, June 23-25, 2014.

David Soper, Prof Chris Baker, Prof Mark Sterling: Assessing crosswind effects

on a container freight train with differing container loading configurations. First international conference in numerical and experimental aerodynamics of road vehicles and trains (Aerovehicles 1), Bordeaux, France, June 23-25, 2014.

The first paper presents preliminary results relating to the model scale slipstream experiments discussed in chapter 5. The paper includes a preliminary validation of results from the model scale slipstream experiment by making comparisons to full scale experiment data, as discussed in chapter 5. The second paper includes a more detailed discussion of the validation of model scale slipstream experimental data. The third paper contains a preliminary version of the results for aerodynamic loads measured within a crosswind, as presented in chapter 8.

The slipstream development of a container freight train

David Soper¹, Chris J. Baker¹ and Mark Sterling¹

¹ Department of Civil Engineering, School of Engineering,

The University of Birmingham, Edgbaston, Birmingham, B15 2TT, UK.

DXS020@bham.ac.uk

Abstract

Slipstreams associated with freight trains can have large pressure and velocity magnitudes, potentially creating a danger to the public on platforms and trackside workers. Open air moving model aerodynamic experiments were undertaken using a 1/25th scale container freight train at the TRAIN rig facility to develop an understanding and characterise slipstream development for different container loading configurations. Results highlighted effects of loading configuration on pressure and slipstream velocities. Model scale results are validated against full scale freight data. Comparisons to passenger slipstream velocities at UK safety positions are made and conclusions drawn on suitability in relation to container freight passage.

1 Introduction

The UK rail freight industry is a growing sector with increasing volumes of international trade coupled with a gradual return from road to rail transportation. Efficiency studies into increased volumes of freight trains within an already overstretched network, primarily focused on passenger transportation, recommend developing faster and longer trains. This however has implications on efficiency and safety, as the movement of a vehicle causes deformation in the surrounding air, creating so called transient aerodynamic effects. The airflow around a moving vehicle is called a slipstream (Baker et al., 2001). Induced slipstream forces can interact with trackside objects, potentially destabilising such objects and people. In the last forty years there have been twenty four train slipstream incidents, the majority caused by freight trains. In one incident a braked pushchair was drawn by the slipstream 3m towards a freight train, hitting the moving train and thrown across the platform into two passengers (Temple and Johnson, 2008).

Concerns over the possibility of slipstream induced incidents have led to a number of studies into the effects of slipstreams, mainly for high speed passenger trains (Baker et al., 2001; Sterling et al., 2008). Although some freight research has been included, a thorough study of freight slipstream development is yet to be undertaken. This experimental study will focus on assessing slipstream development of a container freight train by undertaking a series of open air experiments at the University of Birmingham owned TRAIN (TRAnsient Aerodynamic INvestigation) rig facility in Derby.

2 TRAIN Rig Experiment Development

The TRAIN rig is a purpose built testing facility for examining the transient aerodynamics of moving vehicles (Baker et al., 2001). The advantage of using a moving model rig over a typical stationary wind tunnel is the ability to correctly simulate relative motion between the vehicle and the ground/structures or crosswind simulation.

A moving model was developed to simulate container loading configurations seen at full scale. An existing Class 66 model was modified to include a long flat plate to simulate four flatbed wagons, with bogies modelled using balsa wood. There are six scale 6.096m containers, and four 12.192m containers arranged in five configurations to represent a cross section of different loading efficiencies and provide data for comparison to full scale results; the fully loaded and a partially loaded consist are seen in figure 1.

Slipstream and wake velocities are measured using Cobra probes (Turbulent Flow Instrumentation) at various TSI and UK safety positions. Cobra Probes are four-hole pressure probes capable of measuring three components of velocity and the local static pressure in real time. A drawback to the probe is a ± 45 degree cone of acceptance, limiting the range of flow detection. For flow outside the cone of acceptance, data outputted is replaced by a zero, thus the ensemble size varies with distance. To be within the capable working range of the Cobra probes a train speed of 20m/s was chosen, with 25 repeats undertaken to create ensemble averages in line with TSI standards (Hemida et al., 2010). A sampling frequency of 2500Hz was chosen to avoid signal aliasing and provide measurements every 8mm along the TRAIN rig model, corresponding to every 0.2m at full scale. A coordinate system is used such that the x-axis is aligned in the direction of travel, with the origin taken to be when the train nose passes the measuring point. The y-axis is the horizontal plane perpendicular to the track direction, measured from the centre of track and the z-axis is in the vertical direction measured from the top of the rail.



Figure 1: TRAIN rig freight model and Cobra probe set up. Figure 1a) shows the fully loaded consist with 100% loading efficiency and b) shows a partially loaded consist with 33% loading efficiency.

3 Experiment Results

The TRAIN rig experimental data presented here focuses on two loading configurations (see figure 1), to analyse the influence of container loading efficiency. The data was aligned with the train nose passing at the origin, indicated by the point at which pressure crosses the x-axis between the maximum positive and negative pressure peaks created about the train nose, see figure 2. The aligned data was normalised with respect to train speed u_{train} ,

$$c_u(x) = \frac{u(x)}{u_{train}}, \quad c_p(x) = \frac{p(x) - p_0}{0.5 \rho u_{train}^2} \quad (1)$$

where p_0 denotes ambient pressure. Ensemble averages for normalised velocities and coefficient of pressure are created, defined as (Baker et al., 2001),

$$\bar{c}(x_k) = \frac{1}{n} \sum_{i=1}^n c_i(x_k) \quad (2)$$

where n denotes the ensemble size (number of nonzero values per x-position). All measurements are given in full scale values.

Figure 2 illustrates differences created by container loading configuration on the coefficient of pressure C_p . In the nose region a positive then negative peak is observed about the train nose passage. The peak magnitudes are unlike those witnessed in passenger studies (Hemida et al., 2010), it is hypothesised that this is due to train nose shape. For the fully loaded consist (figure 2a)), following the nose region C_p stabilises about zero, with only small changes due to small gaps between containers. The fully loaded case exhibits a similar pattern to a passenger train with inter-carriage gaps (Hemida et al., 2010). In figure 2b) the influence of space between containers is clearly visible. A similar flow pattern to the nose region occurs about the leading face of each container. At the rear face a smaller negative peak is observed. Between loaded containers C_p increases to the maximum peak seen before the face of the following container. In the wake C_p quickly stabilises to zero.

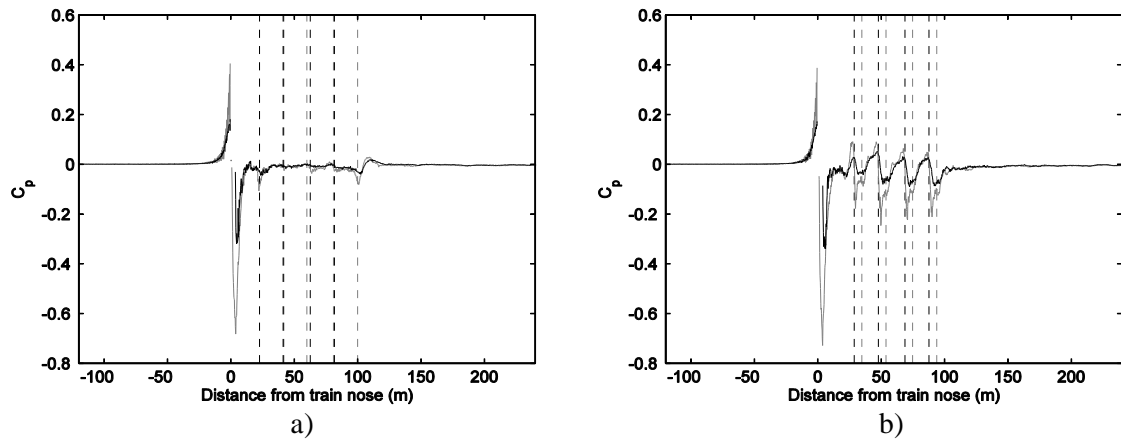


Figure 2: A comparison of ensemble coefficients of pressure for fully loaded a) and partially loaded b) consists, measured at height 2.25m and distance 1.75m (grey) and 3m (black) from the centre of track. The vertical dashed lines indicate the front (black) and rear (grey) faces of the containers.

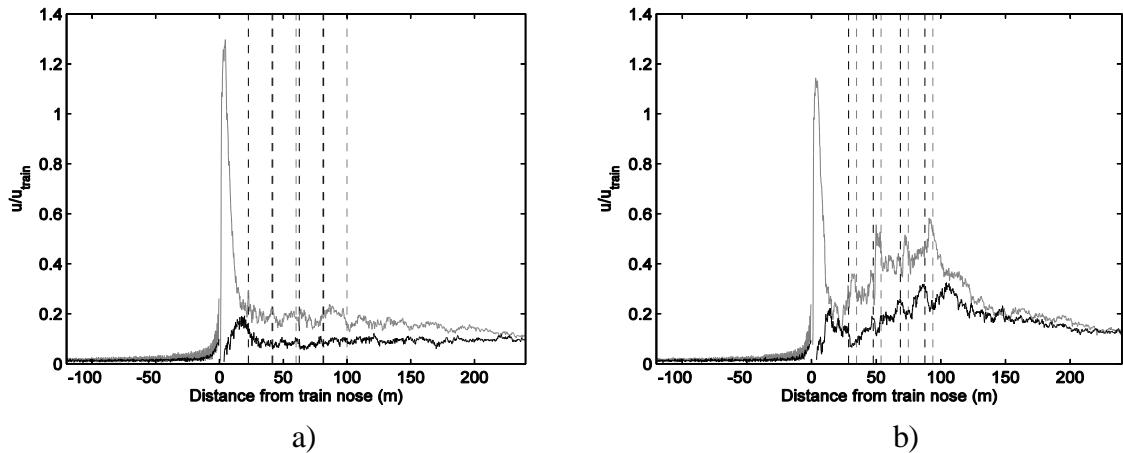


Figure 3: A comparison of normalised ensemble longitudinal velocity U for fully loaded a) and partially loaded b) consists, measured at height 2.25m and distance 1.75m (grey) and 3m (black) from the centre of track. The vertical dashed lines indicate front (black) and rear (grey) faces of containers.

Figure 3 illustrates the corresponding normalised ensemble longitudinal component of velocity U . In the nose region there is a velocity peak corresponding to the change in C_p . The velocity in this region reaches 120% of train speed at 1.75m from train side, much higher than previously witnessed in passenger studies, and is hypothesised to be related to train nose shape. For the fully loaded consist the boundary layer stabilises rapidly after the train nose due to relatively smooth train sides, however for the partially loaded case the boundary layer continues to grow until the train tail where velocities fall away. In figure 3b) the influence of spaces between containers causes pulse peaks in velocity within the boundary layer at the container leading faces. For both loading configurations as the measuring distance from the centre of track is increased the magnitude of slipstream velocities decrease.

Further analysis of the boundary layer region has shown the influence of spaces between loaded containers increases turbulence intensity. The fully loaded case exhibits little change in turbulence intensity, similar to previous passenger studies with inter-carriage gaps (Hemida et al., 2010). The displacement thickness for the partially loaded consist continually increases unlike the fully loaded consist which remains constant. Although the displacement thickness has been calculated using the two-dimensional definition, which for these highly three dimensional flows may not be appropriate, it is felt to be a useful indicator of boundary layer development.

4 Full Scale Validation

Full scale freight data was collected as part of the RAPIDE project and a Network Rail project on the West Coast Mainline, UK, using Class 66 or Class 92 hauled partially loaded container trains (Temple

and Johnson, 2008; Sterling et al., 2008). Results were analysed using the methodology described in section 3 and comparisons made with model scale results at similar measuring positions.

In the nose region of the full scale data, velocity peak magnitudes of individual runs are similar to those seen at model scale, suggesting good reproducibility between full and model scale in the nose region. There is however a lack of Class 66 hauled data to create ensemble averages, thus further analysis is needed. Following the nose region there is a period of boundary layer growth then stabilisation until the train tail where velocity falls away in the wake. In full scale data, boundary layer growth is seen to stabilise after 150m, whereas the model scale boundary layer slipstreams for partially loaded consists show continual growth for the entire train length. At full scale the rig model is 101.25m long, indicating that a possible increase in rig model length is needed to capture the transition from boundary layer growth to stability.

5 Discussion

The UK platform yellow line safety position is specified as 1.5m from the platform edge for a passenger train passing at speeds up to 125mph creating a maximum 1 second moving average slipstream velocity of 15m/s 1m above the platform at this position (Temple and Johnson, 2008). By comparing full scale container freight maximum slipstream velocities a scaling is created with passenger data, allowing the calculation of yellow line placement and train speed for freight in respect to current safety positions.

Analysis has shown that over 70% of container freight trains tested exceed the maximum 1 second moving average slipstream velocity of 15m/s at the yellow line position. Results imply that the yellow line should be moved further to 2m from the platform edge or train speed reduced below 58mph. Similarly for the trackside safety position analysis found that all container freight trains tested exceeded safety limits. Comparison of maximum values in individual runs and 1 second moving averages found a difference of nearly 50%, highlighting whether the use of maximum 1 second moving averages as a measure for safety is appropriate.

6 Conclusions

This paper introduces an initial series of open air model experiments conducted at the TRAIN rig facility to understand slipstream development of a container freight train for different loading efficiencies. Results show clear differences between full and partially loaded consists. Analysis indicates to increasing model length to allow the transition between boundary layer growth and stability to be observed. A fundamental comparison of freight and passenger maximum velocities in relation to safety positions highlighted the need to review current safety positions and train speeds.

References

- Baker, C., S. Dalley, T. Johnson, A. Quinn, and N. Wright, (2001): The slipstream and wake of a high-speed train. *Proceedings of the Institution of Mechanical Engineers, Part F: Journal of Rail and Rapid Transit*, **215** (2), 83–99.
- Temple, J. and T. Johnson, (2008): Effective management of risk from slipstream effects at trackside and on platforms. Tech. rep., A report produced for Rail Safety and Standards Board.
- Sterling, M., C. Baker, S. Jordan, and T. Johnson (2008). A study of the slipstreams of high speed passenger trains and freight trains. *Proceedings of the Institution of Mechanical Engineers, Part F: Journal of Rail and Rapid Transit* Volume 222 (2), 177–193.
- Hemida, H., N. Gil, and C. Baker (2010). LES of the Slipstream of a Rotating Train. *Journal of Fluids Engineering* Volume 132.

A comparison of model and full scale experimental data to assess the suitability of analysing slipstream development of a container freight train using the TRAIN rig facility

D. Soper*, C. Baker*, M. Sterling* and A.D. Quinn*
Corresponding author: dxs020@bham.ac.uk

*School of Civil Engineering, University of Birmingham, Edgbaston, Birmingham, UK

Abstract: Slipstreams associated with freight trains can have large pressure and velocity magnitudes, potentially creating a danger to the public on platforms and trackside workers. Open air moving model and full scale aerodynamic experiments were undertaken using a Class 66 hauled container freight train to develop an understanding slipstream development. Results show good agreement between model and full scale data. A discussion of the suitability of model scale experiments to analyse slipstream development is carried out.

Keywords: Aerodynamics, freight trains, slipstreams, experiments, full scale, model scale.

1 Problem Statement

The UK rail freight industry is a growing sector with increasing volumes of international trade coupled with a gradual return from road to rail transportation. Efficiency studies into increased volumes of freight trains within an already overstretched network, primarily focused on passenger transportation, recommend developing faster and longer trains. This, however, has implications on efficiency and safety, as the movement of a vehicle causes deformation of the surrounding air, creating transient aerodynamic effects. The airflow around a moving vehicle is called a slipstream [1]. Induced slipstreams can interact with trackside objects creating forces which potentially can destabilise such objects and people.

Concerns over the possibility of slipstream induced incidents have led to a number of studies into the effects of slipstreams, mainly for high speed passenger trains [1,2]. Results from these studies have led to the development of the Technical Specifications for Interoperability (TSI); a series of standards on train aerodynamics giving limiting values for slipstream velocities, allowing for interoperability of trains across national boundaries in Europe [3]. Although some research covering freight has been included in these studies, a thorough study of freight slipstream development and appropriate guidelines written in relation to rail freight is yet to be undertaken. Furthermore, the calculation of these limit values relies on full scale experimental data which is expensive and difficult to collect. This study will compare full and model-scale experimental results to assess the suitability of analysing slipstream development of a container freight train using model-scale data collected at the University of Birmingham's TRAIN (TRAnsient Aerodynamic INvestigation) rig facility.

2 Experiment Development

The TRAIN rig is a purpose built testing facility for examining transient aerodynamics of moving vehicles [1]. The advantage of using a moving model rig over a typical stationary wind tunnel is the ability to correctly simulate relative motion between the vehicle and the ground/structures or

crosswind simulation. An existing EMD/BR Class 66 1/25th scale model was modified to include a long flat plate to simulate eight trailing flatbed wagons, with bogies modelled using balsa wood. Twelve 1/25th scale 6.096m containers and eight 12.192m containers were arranged in different configurations to represent a variety of loading efficiencies, providing data for comparison to full scale results. Slipstream and wake velocities were measured using Cobra probes (Turbulent Flow Instrumentation) at TSI equivalent positions.

Full-scale freight data was collected as part of a Network Rail project on the Western Mainline, UK, using Class 66 hauled partially loaded container trains. Data were collected using R3-50 ultrasonic anemometers (Gill Instruments) and static pressure probes at TSI positions. All results were aligned to the Class 66 nose passing the measuring instrumentation, resampled and normalised to the maximum UK freight train speed of 33.5m/s and an ensemble average created for analysis purposes.

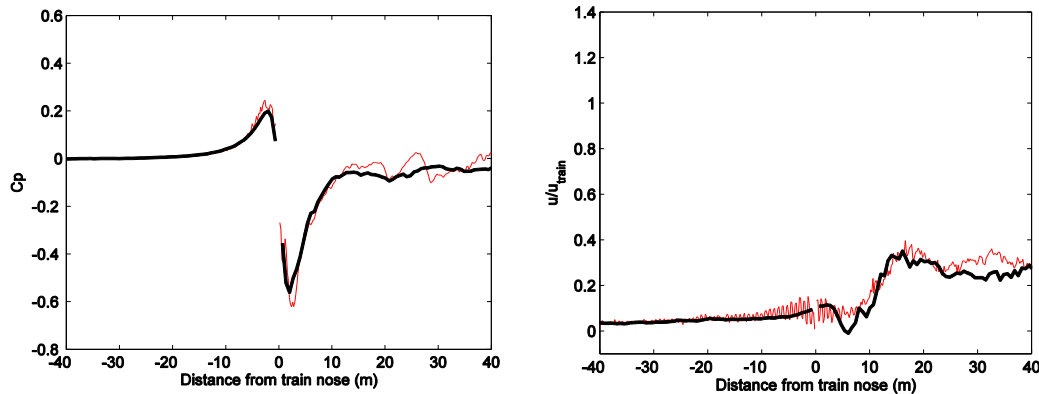


Figure 1: A comparison of coefficient of pressure C_p and normalised ensemble longitudinal component of velocity U for model (red) and full scale (black) Class 66 nose region data.

3 Results and discussion

Figure 1 illustrates the ensemble coefficient of pressure C_p and normalised ensemble longitudinal component of velocity U in the nose region of the Class 66 locomotive at both full- and model-scale. At full-scale an ensemble of 8 runs was available, whereas at model-scale an ensemble size of 75 runs was chosen. A comparison of data was undertaken to validate model-scale results and analyse Reynolds number independence. Both figures suggest good reproducibility in the nose region, with C_p and U exhibiting similar peak magnitudes at both model- and full-scale. Results indicate the validity of model-scale experiments and Reynolds number independence for magnitudes. It is, however, possible that although key flow characteristics and the overall magnitudes of velocities and pressures created are similar, smaller turbulent scales cannot be accurately modelled. Therefore further full-scale experiments are needed to provide data for comparisons with model scale data.

The lack of consistent full-scale Class 66 hauled data inhibits the creation of ensemble averages for the entire train length. Analysis of individual runs shows that following the nose region there is a period of boundary layer growth, then stabilisation until the train tail where velocity decreases in the wake. At both full- and model-scale boundary layer growth is seen to stabilise after 150m for partially loaded consists of loading efficiency less than 50%.

References

- [1] Baker, C.J., The flow around high speed trains. *Journal of Wind Engineering and Industrial Aerodynamics*. 98, 277-298, 2010.
- [2] Sterling M., Baker C.J., Jordan S.C., Johnson T., A study of the slipstreams of high speed passenger trains and freight trains, *Proc. Institute of Mechanical Engineers Part F: Journal of Rail and Rapid Transport*. 222, 177-19, 2008.
- [3] EU Technical Specification for Interoperability Relating to the 'Rolling Stock' Sub-System of the Trans-European High-Speed Rail System (HS RST TSI), 2008/232/EC, 2008.

Assessing crosswind effects on a container freight train with differing container loading configurations

D. Soper*, C. Baker* and M. Sterling*
Corresponding author: dxs020@bham.ac.uk

*School of Civil Engineering, University of Birmingham, Edgbaston, Birmingham, UK

Abstract: Relative crosswinds when coupled with transient aerodynamic effects associated with freight trains can have large velocity magnitudes, potentially affecting the stability of loads. Moving model crosswind experiments are undertaken using a Class 66 hauled container freight train fitted with an on-board surface pressure monitoring system. By altering container loading efficiency it is possible to develop an understanding of influencing factors on forces subjected to a loaded container.

Keywords: Aerodynamics, freight trains, crosswind, slipstreams, forces, experiments, model scale.

1 Problem Statement

On the 1st March 2008, in two separate incidents, a total of seven containers were blown from flatbed freight wagons travelling along the West Coast Mainline, UK. The effect of slipstream velocities coupled with strong gusty crosswind conditions and a failure of equipment was found to be the incidents cause [1]. In America and Australia a number of similar incidents have occurred with double stack container freight trains travelling in strong crosswind conditions or through exposed routes. Although such incidents are rare these examples highlight the importance of understanding air flows around freight trains.

The UK government has set aims to double the volume of rail freight cargo on the UK rail network by 2030. Efficiency studies into increased volumes of freight trains within an already overstretched network, primarily focused on passenger transportation, recommend developing faster and longer trains. This however has implications on the magnitude and incident angle of relative crosswinds (see figure 1). The effect of increasing train speeds and lengths also increases slipstream velocities and transient aerodynamic effects created by vehicle movement. These effects when coupled with a crosswind are increased and potentially affect the relative stability of loaded containers.

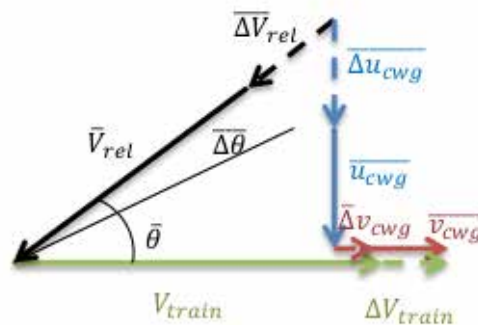


Figure 1: An illustration of relative crosswind magnitude and angle of incidence.

A number of studies have assessed crosswind effects on isolated containers [2,3] or within an infinite consist [2]. Results show the largest forces occur at angle of incident close to 30 degrees and to correctly model a train at least four wagons are needed. These studies however negate the trains relative motion and container loading configuration. In this study moving model scale crosswind experiments are undertaken at the University of Birmingham owned TRAIN rig facility using a purpose built Class 66 hauled container freight train. Pressure fluctuations are monitored on a container surface by a specifically designed surface pressure monitoring system. Integrating average pressure data over the container surface allows forces acting on the container to be calculated. It is possible to identify key influencing factors on force magnitudes by altering container loading configurations.

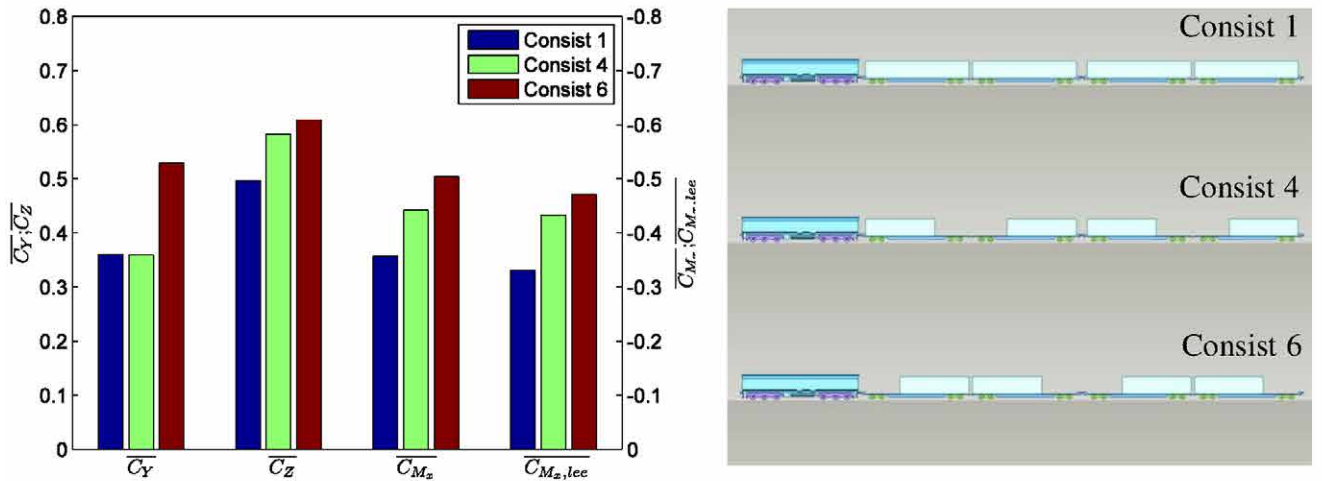


Figure 2: An illustration of side and lift force coefficients and roll moments measured on the 3rd container of consists 1, 4 and 6.

2 Results and discussion

Figure 2 illustrates clear differences in force and roll moment coefficients as container loading configuration varies. Larger magnitudes are observed as container loading efficiency is reduced. Although consists 4 and 6 have the same loading efficiency, the variation in loading pattern creates differences in force coefficients. Consists 6 has a large space before the measuring container in comparison to consist 4, which is relatively shielded by a container on the wagon in front. Forces acting on the measuring container in consist 6 have a greater influence from slipstream velocities within the boundary layer around the train. Side force coefficients for consists 1 and 4 have similar magnitude. It is hypothesised that the container loaded on the wagon in front has a shielding effect on the measuring container, reducing side force magnitude in relation to consist 6, for which container leading edges are more susceptible to large flow separations.

References

- [1] Spacey, S., Detachment of containers from freight wagons near Cheddington and Hardendale 1 March 2008. Technical report, DfT Accident Investigation, 2009.
- [2] Hemida, H. and Baker, C., Large-eddy simulation of the flow around a freight wagon subjected to a crosswind. Computers & Fluids Volume 39, Issue 10, 1944–1956, 2010.
- [3] Johnson, T., Investigation of freight vehicle aerodynamic performance in accordance with GM/RT 2142 Resistance of Railway Vehicles to Roll-over in Gales. Technical report, RSSB, 2012.